STRENGTH ANALYSIS OF CONCRETE-ENCASED CELLULAR STEEL COLUMNS

Mr. Worakarn Anuntasena

จุฬาลงกรณ์มหาวิทยาลัย
CHULALONGKORN UNIVERSITY
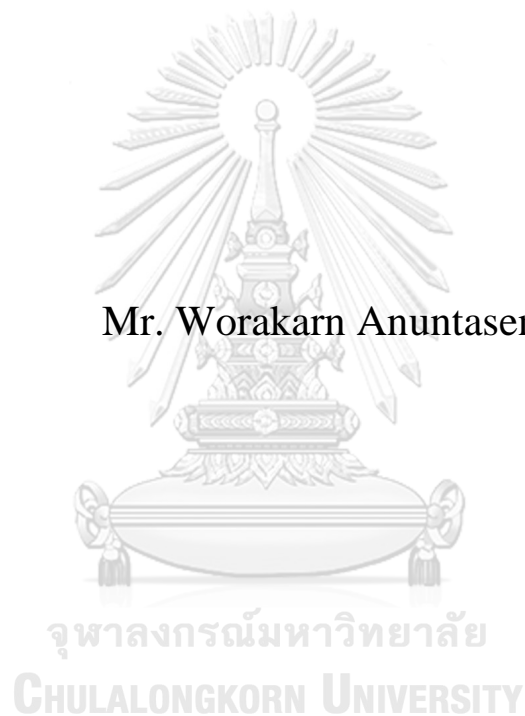
A Dissertation Submitted in Partial Fulfillment of the Requirements
for the Degree of Doctor of Philosophy in Civil Engineering
Department of Civil Engineering
FACULTY OF ENGINEERING
Chulalongkorn University
Academic Year 2019
Copyright of Chulalongkorn University

การวิเคราะห์กำลังของเสาเหล็กเซลลูลาร์หุ้มด้วยคอนกรีต

นายวรการ อนันตเสนา

Thesis Title	STRENGTH ANALYSIS OF CONCRETE-ENCASED CELLULAR STEEL COLUMNS
By	Mr. Worakarn Anuntasena
Field of Study	Civil Engineering
Thesis Advisor	Associate Professor Akhrawat Lenwari, Ph.D.

Accepted by the FACULTY OF ENGINEERING, Chulalongkorn University in Partial Fulfillment of the Requirement for the Doctor of Philosophy

.... Dean of the FACULTY OF
ENGINEERING
(Professor SUPOT TEACHAVORASINSKUN, D.Eng.)

DISSERTATION COMMITTEE

.... Chairman
(Professor Thaksin Thepchatri, Ph.D.)
.... Thesis Advisor
(Associate Professor Akhrawat Lenwari, Ph.D.)
.... Examiner
(Professor Teerapong Senjuntichai, Ph.D.)
.... Examiner
(Assistant Professor Pitcha Jongvivatsakul, Ph.D.)
.... External Examiner
(Assistant Professor Aphinat Ashakul, Ph.D.)

จุฬาลงกรณ์มหาวิทยาลัย

CHULALONGKORN UNIVERSITY

วรการ อนันตเสนา : การวิเคราะห์กำลังของเสาเหล็กเซลลูลาร์หุ้มด้วยคอนกรีต. (STRENGTH ANALYSIS OF CONCRETE-ENCASED CELLULAR STEEL COLUMNS) อ.ที่ปรึกษาหลัก : รศ. ดร.อัครวัชร เล่นวารี

       งานวิจัยนี้ศึกษาเสาเหล็กเซลลูลาร์และเสาเหล็กเซลลูลาร์หุ้มด้วยคอนกรีตภายใต้น้ำหนักบรรทุกตรงศูนย์และเยื้องศูนย์ โดยเริ่มจากการศึกษาเสาเหล็กเซลลูลาร์และเสาเหล็กเซลลูลาร์หุ้มด้วยคอนกรีตโดยการทดสอบในห้องปฏิบัติการ จากการทดสอบเสาเหล็กเซลลูลาร์ภายใต้น้ำหนักบรรทุกตรงศูนย์ พบว่า เสาเหล็กเซลลูลาร์มีการวิบัติทั้งแผ่นเอวและแผ่นปีกที่หน้าตัดที่ผ่านจุดศูนย์กลางรูเจาะ โดยมีพฤติกรรมการครากและการแข็งตัวเนื่องจากความเครียดเหมือนกันกับเสาเหล็กทั่วไป มีกำลังรับน้ำหนักบรรทุกที่จุดครากต่ำกว่าเสาเหล็กเดิมก่อนที่จะนำมาตัดและเชื่อมประกอบเป็นเสาเหล็กเซลลูลาร์ 15 เปอร์เซ็นต์ จากการทดสอบเสาเหล็กเซลลูลาร์หุ้มด้วยคอนกรีตภายใต้น้ำหนักบรรทุกตรงศูนย์ พบว่า เสาเหล็กเซลลูลาร์หุ้มด้วยคอนกรีตมีรูปแบบการวิบัติและความสัมพันธ์ระหว่างน้ำหนักบรรทุกกับการเสียรูปเหมือนกันกับเสาเหล็กหุ้มด้วยคอนกรีตทั่วไป โดยมีการวิบัติที่คอนกรีตหุ้มร่วมกับการวิบัติของเหล็กเสริมทางยาวที่จุดน้ำหนักบรรทุกสูงสุดและกำลังรับน้ำหนักบรรทุกสูงสุดของเสาเหล็กเซลลูลาร์หุ้มด้วยคอนกรีตมีค่าน้อยกว่าเสาเหล็กหุ้มด้วยคอนกรีต 3 − 6 เปอร์เซ็นต์ จากการทดสอบเสาเหล็กเซลลูลาร์ภายใต้น้ำหนักบรรทุกเยื้องศูนย์ พบว่า เสาเหล็กเซลลูลาร์มีการวิบัติทั้งแผ่นเอวและแผ่นปีกที่หน้าตัดที่ผ่านจุดศูนย์กลางรูเจาะด้านที่รับแรงอัด มีกำลังรับน้ำหนักบรรทุกที่จุดครากน้อยกว่าเสาเหล็กเดิม 4 เปอร์เซ็นต์ จากการทดสอบเสาเหล็กเซลลูลาร์หุ้มด้วยคอนกรีตภายใต้น้ำหนักบรรทุกเยื้องศูนย์ พบว่า รูปแบบการวิบัติของเสาเกิดจากการวิบัติของคอนกรีตด้านรับแรงอัดที่กึ่งกลางความสูงเสาที่น้ำหนักบรรทุกสูงสุดตามด้วยการวิบัติของคอนกรีตด้านรับแรงดึง นอกจากนี้ งานวิจัยนี้ยังนำเสนอแบบจำลองสำหรับทำนายความสัมพันธ์ระหว่างน้ำหนักบรรทุกกับการเสียรูปในแนวแกนของเสาเหล็กเซลลูลาร์และเสาเหล็กหุ้มด้วยคอนกรีต และนำเสนอสมการสำหรับทำนายกำลังรับน้ำหนักบรรทุกของเสาเหล็กเซลลูลาร์และเสาเหล็กเซลลูลาร์หุ้มด้วยคอนกรีต โดยแบบจำลองที่เสนอได้นำไปตรวจสอบความถูกต้องกับผลทดสอบในงานวิจัยนี้ สุดท้ายนี้ งานวิจัยนี้ได้เสนอวิธีการสร้างเส้นโค้งปฏิสัมพันธ์กำลังของเสาเหล็กเซลลูลาร์และเสาเหล็กเซลลูลาร์หุ้มด้วยคอนกรีต จากการศึกษาพบว่าเสาเหล็กเซลลูลาร์และเสาเหล็กเซลลูลาร์หุ้มด้วยคอนกรีตมีกำลังสูงกว่าเสาเหล็กเดิมและเสาเหล็กหุ้มด้วยคอนกรีตภายใต้น้ำหนักบรรทุกเยื้องศูนย์ที่มีระยะเยื้องศูนย์มาก

จุฬาลงกรณ์มหาวิทยาลัย

CHULALONGKORN UNIVERSITY

สาขาวิชา	วิศวกรรมโยธา	ลายมือชื่อนิสิต ....
ปีการศึกษา	2562	ลายมือชื่อ อ.ที่ปรึกษาหลัก ....

iv

5971439821 : MAJOR CIVIL ENGINEERING
KEYWORD: CELLULAR STEEL COLUMNS, CONCRETE-ENCASED STEEL
COLUMNS, STRENGTH INTERACTION DIAGRAM
Worakarn Anuntasena : STRENGTH ANALYSIS OF CONCRETE-ENCASED
CELLULAR STEEL COLUMNS. Advisor: Assoc. Prof. Akhrawat Lenwari,
Ph.D.

This research investigates the compression behavior of bare cellular steel columns and concrete-encased cellular steel (CECS) columns subjected to concentric and eccentric loadings. First, the experimental study of the cellular steel and CECS columns was conducted in the laboratory. For the cellular steel columns subjected to concentric loading, the failure mode of the bare cellular steel columns was local buckling at both web and flanges at the hole section. All cellular steel columns exhibited yielding and hardening behavior. The cellular columns had the average yield loads less than the parent column by 15 %. For the CECS and CES columns subjected to concentric loading, the failure mode and load – deformation relationships were similar with the CES columns having a similar stirrup spacing. The failure of CECS and CES columns in this research was cover concrete spalling and buckling of the longitudinal rebars at the maximum loads. The CECS columns had the averaged maximum loads less than the CES column by 3 – 6 %. For the cellular steel columns subjected to eccentric loading, the failure mode was local buckling at compression web and flange at the hole section. The cellular columns had the yield loads slightly less than the parent column by 4 % for large eccentricity in this research. For the CECS and CES columns subjected to eccentric loading, the failure mode was concrete crushing at compression side at mid-height at the maximum loads followed by the failure of concrete at tension side. Second, the analytical models were proposed to predict the load – strain relationships of the cellular steel columns and CES columns. In addition, the equations were proposed to predict the yield load and axial stiffness of the cellular steel columns and the maximum loads and axial stiffness of the CECS columns. Finally, the plastic stress distribution and modified AISC 360-16 methods for the strength interaction diagram of the cellular steel and CECS columns were proposed. The proposed strength interaction diagrams show that the cellular and CECS columns had higher strength than the parent columns at high load eccentricity.

Field of Study: Civil Engineering   Student's Signature ....
Academic Year: 2019   Advisor's Signature ....

ACKNOWLEDGEMENTS

Worakarn Anuntasena

TABLE OF CONTENTS

LIST OF TABLES

LIST OF FIGURES

CHAPTER 1
INTRODUCTION

1.1 Background of research

At present, steel-concrete composite columns are widely used in high rise buildings. The main advantages of the composite columns are high load capacity, high ductility and high fire resistance. Nowadays, the steel-concrete composite columns are five types as shown in Figure 1.1. First, partially encased composite (PEC) column shows in Figure 1.1 (a). Second, concrete-encased steel (CES) column, as shown in Figure 1.1 (b). Third, concrete filled steel tube (CFT) columns, as shown in Figure 1.1 (c). Forth, concrete filled double-skin steel tube (CFDT) columns, as shown in Figure 1.1 (d). Fifth, steel reinforced-concrete filled-steel tube (SRCFT) columns, as shown in Figure 1.1 (e).
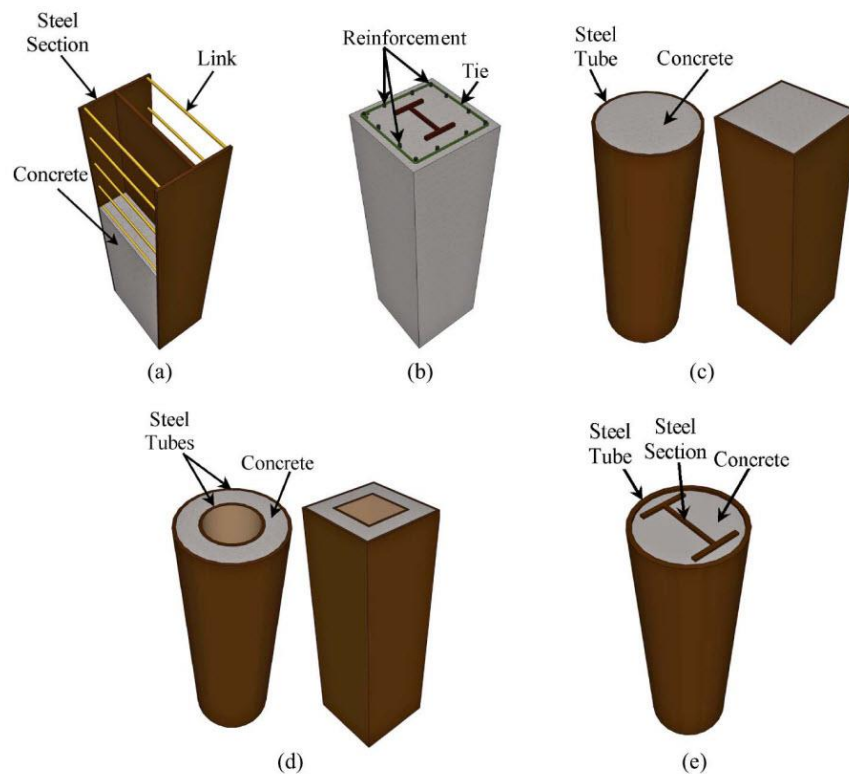
Figure 1.1 Five types of concrete-steel composite columns
(a) PEC column (b) CES column (c) CFT columns (d) CFDT columns
(e) SRCFT column (Karimi et al., 2011).

Two types of concrete-encased steel composite columns, the PEC and CES columns, are popular type of composite columns. The composite columns consist of a wide flange steel and filled concrete, as shown in Figure 1.1 (a-b). The main advantages of the PEC and CES columns are higher load capacity and ductility than reinforced concrete (RC) columns and higher fire resistance than steel columns. There are many researches investigated the PEC and CES columns, as presented in chapter 2.

On the other hand, cellular steel members (cellular beams and columns) are popular for in residential and nonresidential building. Cellular steel members are wide flange steel members with circular web openings. The cellular member produced by cutting and re-welding a standard wide flange steel member along longitudinal axis, as shown in Figure 1.2. The main advantages of the cellular members are high major axis moment capacity, cost saving and passageway of pipe and other service systems.

Generally, the cellular members are used as beams. However, the cellular members become used as columns in the present. The main advantage of the cellular columns is high major axis moment capacity. In addition, there are many researches investigating on the cellular columns in the past, as presented in chapter 2.

Typical Cut of Castellated Members

Castellated Members after Welding

Computerized Cut of Cellular Members

Cellular Members after Welding
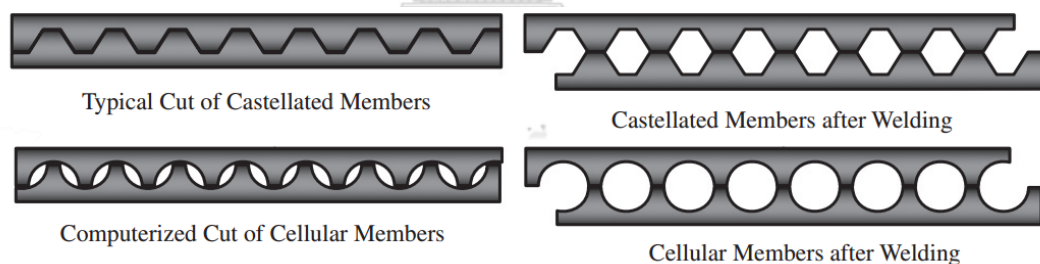
Figure 1.2 Fabrication of castellated and cellular steel member
(Sweedan et al., 2009).

1.2 Motivation and significance of research

Literature reviews show that there have been many researches investigated the PEC, CES and cellular steel columns in the past. Fewer researches investigated composite columns with web opened steel member. However, the concrete-encased steel columns with cellular steel member have not been investigated yet.

This research investigates the concrete-encased cellular steel (CECS) columns. The new composite column is concrete-encased steel column using cellular steel member instead of traditional wide flange steel member. Expectation of researcher is the combined advantages of CES columns and cellular steel columns. The main expected advantages of the CECS columns are high axial load capacity from CES columns and high major axis moment capacity and cost saving from cellular steel columns. In addition, the weak web of the cellular steel columns is protected by encased concrete.

The main contributions of this research are to study structural behaviors of the CECS columns subjected to concentric and eccentric loads, to develop analytical models for predicting axial compressive capacity of the CECS columns, and to develop strength interaction diagrams of the CECS columns to show the advantages of the CECS columns. In addition, other objectives are to study structural behaviors of the cellular steel columns subjected to concentric and eccentric loads, and to develop strength interaction diagram of the cellular steel columns.

It is expected that the CECS columns will be used instead of the traditional CES columns in the future, and PEC columns with cellular steel member will be investigated in the future.

1.3 Research objectives

The main purposes of this research are as follows:

1. To develop an analytical model to predict the load-deformation of the CES columns.
2. To develop an analytical model to predict the load-deformation of the CECS columns.
3. To experimentally investigate structural behaviors of the cellular steel columns subjected to concentric and eccentric loads.
4. To experimentally investigate structural behaviors of the CECS columns subjected to concentric and eccentric loads.
5. To develop strength interaction diagrams of the cellular steel columns.
6. To develop strength interaction diagrams of the CECS columns.

7. To study the effects of design parameters on the strength interaction diagrams of the cellular steel columns.

8. To study the effects of design parameters on strength interaction diagrams of the CECS columns.

1.4 Scope of research

The scope of this research is listed below:

1. Studied columns are stub columns.

2. Studied columns are square and rectangular sections.

3. Studied wide flange steel members are hot-rolled steel.

4. Structural behaviors are studied by experimental studies.

5. Studied structural behaviors are as follows:

   - Failure mode

   - Deformed shape

   - Load-deformation relation

   - Concrete confinement

6. The proposed analytical models predict axial load-strain relations of cellular steel and CECS columns.

7. Strength interaction diagrams are developed by analysis models.

8. Effect of design parameters are studied by experimental studies and analysis models.

9. Studied design parameters are as follows:

   - Hole diameter of the cellular member

   - Hole spacing of the cellular member

   - Stirrup spacing

   - Concrete strength

10. Failure of weld is not considered.

1.5 Expected benefits of research

The expected benefits of this research are as follows:

1. The advantages of the cellular steel and CESC columns are proposed.
2. The proposed analytical models are used to predict axial load-deformation of the cellular steel, CES, and CECS columns.
3. The proposed strength interaction diagrams are used to design the cellular steel and CECS columns.
4. The effects of design parameters on strength interaction diagrams of the cellular steel and CECS columns are investigated.

1.6 Research methodology

The methodologies of this research are listed below:

1. Review literatures and theories.
2. Define research objectives, scopes, and specify research methodology.
3. Develop the analytical model of the CES columns.
4. Provide experimental specimens of the cellular steel, CES and CECS columns.
5. Perform specimens testing of the cellular steel columns.
6. Perform specimens testing of the CES and CECS columns.
7. Develop the analytical model of the cellular steel and CECS columns.
8. Develop interaction diagrams of the cellular steel columns.
9. Develop interaction diagrams of the CES and CECS columns.
10. Study the effect of design parameters to strength interaction diagrams of the cellular steel columns.
11. Study the effect of design parameters to strength interaction diagrams of the CECS columns.
12. Discuss and conclude research findings.

1.7 Organization of dissertation

The outline of this research is as follows,

Chapter 1 presents background, motivation and significance, objectives, scope, expected benefits, and methodology of this research.

Chapter 2 collects the reviews of previous studies about the PEC columns, CES columns, steel columns with web openings and composite columns with web opened steel member.

Chapter 3 describes the theoretical backgrounds of concrete confinement models, analytical models to predict axial load-deformation relation of CES column, simplified methods to predict axial compression of CES column. strength interaction diagram of CES column, design of CES column by AISC 360-16, analytical models to predict axial load-deformation relation of steel column with web opening, design of steel beam with web opening by AISC design guide 2 (1992), and design of cellular steel beam by AISC design guide 31 (2016).

Chapter 4 presents the experimental program of this research. This chapter consists of experimental specimens, material properties, and test setup.

Chapter 5 reports the experimental results of cellular steel columns subjected to concentric loads, CECS columns subjected to concentric loads, cellular steel columns subjected to eccentric loads, and CECS columns subjected to eccentric loads.

Chapter 6 proposes analytical models to predict axial load-deformation relation of cellular steel, CES, and CECS columns. In addition, the simplified and modified simplified equations to predict axial compressive strength of CES, and CECS columns are proposed.

Chapter 7 proposes strength interaction diagram of cellular steel columns, and CECS columns. The plastic stress distribution method, and modified AISC 360-16 section I and section H method were proposed in this chapter.

Chapter 8 presents the research conclusions and proposes recommendations for future works.

CHAPTER 2
LITERATURE REVIEW

From the literature review, PEC or CES columns with web-opened steel member have not been investigated. This chapter reviews the investigations of PEC columns, CES columns, castellated and cellular steel columns, and composite columns with web-opened steel member.

2.1 Partially encased composite columns

In this section, the previous investigations of the PEC columns subjected to concentric and eccentric loadings are summarized.

In 1991, Elnashai et al. investigated the PEC columns strengthening with transverse links under cyclic and pseudo-dynamic loadings. The main purposes of additional transverse links restrained local buckling at large displacements and increase interaction between concrete and steel. A sections of modified PEC column with transverse links and conventional PEC column was compared. The test results showed that the transverse links significant restrain local buckling, increase interaction between concrete and steel, and increase concrete confinement. The deflection ductility of the modified columns increasing 50-80%.

In 1993, Elnashai and Elghazouli investigated the PEC columns strengthening with transverse links subjected to dynamic and cyclic loads. An analytical model of the PEC beam-column considering nonlinearity geometry and inelastic material. The model considers confinement effect of concrete and local buckling effects of steel. The model was validated with experimental data of PEC columns by Elnashai et al. in 1991. In addition, parameter studies were presented in a companion paper.

In the companion paper, Elghazouli and Elnashai (1993) presented parametric studies of PEC columns strengthening with transverse links subjected to dynamic and cyclic loads. The results showed that confinement of concrete influences the ultimate moment capacity and no effect to yield moment capacity of partially encased composite columns. Moment capacity equations based on a linear curvature

distribution were found to give conservative results. In addition, an adopted approach about the concrete model in Eurocode 8 was shown to be viable for design.

In 1994, Hunaiti and Fattah investigated the PEC columns subjected to eccentric loadings. Nineteen full-scale PEC columns with a length 2.4 m were tested under minor axis bending and compared with twentieth bare steel columns. The results showed that the tested PEC columns had full flexural strength of section and had not local and overall buckling. Next, effects of eccentricity, concrete strength and shear studs were investigated. The results showed that shear studs had not affect to strength of the tested PEC columns, but shear studs will be required in actual design because a bond between concrete and steel was affected by several factor, such as age of concrete. And increasing of the concrete strength more than three times made the strength of PEC columns increase 30%. In addition, design considerations of PEC columns were proposed in this paper. A design calculations of bridge code - BS5400 (1979) were good agreement with the tested results in case of equal end eccentricities and high strength concrete, but were conservatively in case of unequal end eccentricities and low strength concrete.

In 2001, Uy investigated local and post local buckling behaviors of PEC columns fabricated from very slender steel plates. Eight specimens of welded box and wide flange columns filled with concrete were tested under axial compressive loads and compared with eight bare steel columns. Four specimens of wide flange were slenderness limit values vary from 20 to 35 filled with concrete which nominal strength 20 MPa. The results showed that the filled concrete increase strength and local buckling stress of the columns. Next, a finite strip method was proposed to calculate an initial local buckling stress by considering residual stress of the welded columns. The finite strip method considered residual compressive stresses up to 30% of the yield stress. In addition, an effective width model existing in international code was used to calibrate and determine axial compressive strength of the welded columns.

In 2002, Chicoine et al. investigated the built-up PEC short columns with transverse links. Welded steel in the PEC columns were slender wide flange section. Five large-size 600 x 600 mm were tested under axial compressive loads. All columns had a height 5d which controlled uniform transverse links over the central 3d segment

(d was column depth). The results showed that the failure of specimens was concrete crushing together with local buckling of steel flange. High stress occurred in transverse links from lateral expansion of the filled concrete. In addition, the results showed that closer link spacing can improve load capacity in post peak behavior. In case of link spacing equal to column depth, steel flange of the specimens buckled at around 75% of the peak loads. In case of link spacing equal to half of column depth, steel flange of the specimens did not occur local buckling before the peak loads. Moreover, the results showed that the additional reinforcement bars improve post peak capacity and ductility of the columns, but the additional reinforcement bars did not improve concrete confinement of the columns.

In 2003, Chicoine et al. investigated the long-term behavior of built-up PEC short columns with transverse links. Welded steel in the PEC columns were slender wide flange section. Five 300 x 300 mm and two 450 x 450 mm were tested under axial compressive loads. Four specimens were tested about 150 days, and five specimens were tested until failure. All columns had a height 5d which controlled uniform transverse links over the central 3d segment (d was column depth). A load sequence of the test had 3 stages. At first stage, construction loads were applied in the steel. At second stage, service loads were applied in the concrete and steel and hold the loads about 150 days. At third stage, the columns were tested until failure. The results showed that the failure mode of the specimens subjected to long-term loadings were same as the specimens subjected to short-term loadings. The failure of specimens under long-term loads were concrete crushing together with local buckling of steel flange. In addition, the results showed that an existing model to evaluate the ultimate loads under short-term loadings had an accurate prediction in the ultimate loads under long-term loadings.

In 2007, Begum et al. investigated the PEC columns with transverse links by numerical method. The finite element models of PEC columns were proposed by considering effect of rapid volumetric expansion of concrete and local buckling of steel flange. A concrete damage plasticity and a formulation of dynamic explicit were used in the model. The model results were in good agreement with the experimental data at maximum loads, failure modes and post-peak behaviors of the PEC columns subjected to concentric and eccentric loadings. The numerical results showed that the

effect of the transverse links spacing equal to half of column depth is slowly failure than transverse links spacing equal to column depth.

In the same year, Marinopoulou et al. investigated simulation of PEC columns with steel columns. The presented method was proposed for purposed of linear elastic analysis. The fictitious cross-section consists of actual steel cross-section and two additional pairs of plates, the additional plates were added at the web of actual steel cross-section. The new fictitious cross-section was represented the actual section and material properties of the PEC columns. The advantage of this proposed method is widely available to model the PEC columns in linear elastic steel analysis software.

In 2012, Kim et al. investigated the CES and PEC columns with high strength steel and high strength concrete. Seven CES columns were tested under eccentric axial compressive loads. The yield stress of structural steel was 913 and 806 MPa and the compressive strength of concrete cylinder are 94 and 113 MPa. Because of high strength of structural steel, the yield strain (≈ 0.004) higher than crushing strength of concrete (≈ 0.003), the investigation focused on early crushing of concrete and the tested columns showed ductile flexural behavior. In the CES specimens, the structural steel start to yield after the concrete crushing and the column loads increase to second peak load. In the PEC specimen, the transverse links welding failure and the steel flange local buckling occurred after the first peak and the column loads continued to decrease. In addition, ACI 318-08 method and Eurocode 4 (2005) method to calculate the strength capacity of CES and PEC columns were discussed in this investigation. The result showed that ACI 318-08 method underestimate load capacity of the specimens. The Eurocode 4 (2005) method overestimate load capacity of the specimens.

In 2013, Begum et al. investigated the PEC columns with transverse links and high strength concrete by numerical method. The steel of the PEC columns was built-up slender section. All columns had a height 5d which controlled uniform transverse links over the central 3d segment (d was column depth). A finite element model by software ABAQUS was developed to predict behavior of the PEC columns subjected to concentric and eccentric loadings. In the model, material property of the steel used tri-linear elasto-plastic model including strain hardening, and material property of concrete used damage plasticity model in ABAQUS. The contact pair algorithm in

ABAQUS was used to model the steel-concrete interface in the composite columns. The load-deformation relationship and failure mode from finite element analysis were accurately verified with existing experimental results. Finally, the finite element model was used to parametric study. The results showed that the axial capacity of the PEC columns with slender steel section and transverse links is very increased in case of high strength concrete (60 MPa) instead of normal strength concrete (30 MPa) by average increasing 55%.

In 2016, Pereira et al. investigated the PEC columns which replacing steel bars by welded wire mesh by experimental and numerical methods. Four PEC columns were tested under axial compressive loads. The results showed that the PEC columns reinforced by welded wire mesh no significant difference failure mode and crack pattern with the PEC columns reinforced by steel bars. Next, software DIANA was used to develop finite element models. The models have assumption that perfect bone between concrete and steel and not considering on local buckling of steel. The finite element models were verified with experimental results in both capacity and deformation of PEC columns. The analysis results showed good agreement with the experimental data. In addition, the finite element models were used to study design parameters. The results showed that thickness of steel profile and steel strength no significant change to behavior of PEC columns, but concrete strength significant change to post peak behavior of PEC columns.

In the same year, Song et al. (2016) investigated local and post-local behavior of PEC columns with transverse links by numerical method. The steel of the PEC columns was built-up slender section. Nonlinear finite element models were developed to predict strength and buckling behaviors of steel plates and the PEC columns which considering residual stress of the steel shapes. The finite element models by software ABAQUS with Explicit module were verified with existing experimental results. Because of the steel web of the PEC column was supported by concrete encasement, the steel flanges which supported by transverse links were focused to study local buckling and post local buckling behaviors. Two modeling formats used in this investigation were overall model which modeling whole PEC column and single plate model which modeling symmetric partition separated from overall model. The separated model consisted of half of the steel flange and a quarter

of the concrete encasement. In the finite element models, shell elements (S4R) were applied to be steel plates, brick elements (C3D8R) were applied to be concrete and linear beam element (B31) were applied to be transverse links. The results showed that smaller transverse links spacing and width-to-thickness ratio made higher critical stress in steel flange. Finally, two formulas for predict critical stress of steel flanges for analytical and design were proposed in this investigation. The formulas were accurately verified with finite element and experimental results.

Piquer and Hernandez-Figueirido (2016) investigated fire performance of PEC columns. Comparison of the fire resistance of the PEC columns with steel columns with and without fire protection was proposed. The results showed that the most protected steel columns were resist before column collapse around 120 min. In case of the PEC columns, the columns had good performance subjected to fire. In addition, the PEC columns had more saving cost around 50% than other protected steel columns.

In 2019, Jamkhaneh et al. investigated the octagonal PEC columns under axial and bending loads by experimental study. The main parameters were failure modes and reinforcement details. The results showed that the local buckling and concrete crushing occurred at the ultimate stage. In addition, finite element analysis of the octagonal PEC columns under combined axial-torsional loads were investigated in this study.

In 2020, Jamkhaneh et al. investigated concrete confinement factors, partially and highly confined concrete, in PEC columns. 3D nonlinear finite element analysis of PEC columns was developed based on the dynamic explicit method. The load-displacement relation and bearing capacity of the models were verified with experimental results from the literatures. The parametric study which using finite element models consisted of concrete strength, structural steel shape and transverse link spacing. The results showed that structural steel section had greatly influences on partially and highly confined area.

2.2 Concrete-encased steel columns

In this section, previous investigations of the CES columns subjected to concentric and eccentric loadings are summarized.

In 1979, the SSRC council proposed a specification for composite columns design. The design of concrete-encased steel (CES) columns and concrete filled steel tube (CFT) columns subjected to concentric and eccentric loading were included. General requirements recommended for design the steel-concrete columns were cross-section area of structural steel shape at least 4% of total cross-section area, compressive strength of concrete between 3000 to 8000 psi, yield stress of structural steel less than 55 ksi and others. In addition, design of axial compressive loads and eccentric loads of the composite columns were proposed by considering columns slenderness. The recommended design was compared safety with experimental data reported from several laboratories.

In 1991, Mirza and Skrabek investigated the strength interaction diagram of CES short beam-columns. This study focused on variability of the ultimate strength of CES columns by considering concrete confinement. Strength ratio (Theoretical strength model divided by ultimate strength by ACI Standard 318-89) was proposed to represent the variability of the CES columns. The results showed that structural steel ratio, concrete strength and load eccentricity ratio had effect on strength of CES columns, but steel grade had not effect on the strength of CES columns. In addition, the CES columns with slenderness ratio near ACI Building code limit had lower strength than cross-section calculation.

In 1992, Mirza and Skrabek investigated the strength interaction diagram of CES slender beam-columns. This study focused on variability of the ultimate strength of CES slender columns by considering concrete confinement. Strength ratio was proposed to represent the variability of the CES columns. The results showed that structural steel ratio, load eccentricity ratio and slenderness ratio had effect on strength of CES columns, and Concrete strength had effect on strength of CES columns only non-slender columns, but steel grade had not effect on the strength of CES columns.

In 1994, Ricles and Paboojian investigated the CES columns under seismic loads by experimental study. Eight specimens were tested under simulated seismic loading conditions. The tested specimens had flange shear studs for shear resistance mechanism. The behavior of concrete confinement was included in this study. The results showed that CES columns were excellent strength and ductility under cyclic loads if longitudinal reinforcement buckling was inhibited. The shear studs had not effect on the strength of CES columns. The proposed analytical models of CES columns under combine axial loads and moments were good agreement with experimental results. In addition, ultimate strength predicted by ACI and AISC standard had conservative results with experimental results.

In 1996, Kato investigated the buckling strength of CFT and CES columns subjected to concentric loadings. Buckling strength design formulas by Eurocode4 and ISO standard for structural steel were applied for the CFT and CES columns. And Columns curves of the composite columns were proposed in this studied. The results showed that the applied buckling curve of Eurocode4 and ISO standard could be used for design CFT and CES columns. In addition, suggested design formulas for CFT and CES columns were proposed in this study.

In the same year, Mirza et al. investigated the CES beam-columns axial loads and moments by experimental and analytical. Sixteen specimens were tested which loaded to failure. The tested CES columns had steel rib connector at the top and bottom flanges. The results showed that strain at ultimate loads of tested specimens close to 0.003 which strain at maximum compression of concrete of ACI Standard 318. The prediction strength of ACI318 and Eurocode4 were adequately estimate strength of the tested columns. In addition, nonlinear finite element analysis by ABAQUS program of CES beam-columns were developed in this study. The results showed that ultimate strength and load-deflection relation from finite element analysis were good agreement with experimental results.

In 1999, Wang investigated the slender CFT and CES slender columns. Eight specimens of CFT columns and seven specimens of CES columns were test under eccentric loads. This paper focused on comparison of ultimate strength of test result with ultimate strength calculated from Eurocode4, BS5400 and applied BS5950 method. The result showed that these methods given conservative results. Eurocode4

predicted closer than BS5400. The applied BS5950 method predicted similar to Eurocode4 and closer than BS5400. Moreover, the applied BS5950 method had easier calculated than Eurocode4 and BS5400.

In 2002, Weng and Yen investigated design provisions of CES columns by AISC specification (LRFD, 1993) and ACI code (ACI318-99). Comparison of strength calculated by design provisions and 78 experimental results by previous studies were investigated. The comparison was proposed inform of maximum strength and interaction diagrams of the CES columns. The results showed that ACI code predicted closer the experimental results than AISC specification. The mean value of predicted-to-tested strength ratios were 0.9 and 0.73 for ACI code and AISC specification respectively.

In 2003, Al-Shahari investigated behavior of the CES columns with lightweight aggregate concrete subjected to eccentric loadings. Sixteen full-scale specimens were tested under axial loads and bending moments about major axis. This study focused on verifying and checking in predicting strength of AISC (LRFD, 1993) and BS5400 specification of the CES columns with lightweight aggregate concrete. The tested results showed that the lightweight aggregate concrete provided perfect bond between concrete and steel up to failure of the CES columns, improved load capacity of the steel section but decreased ductility of the steel section. In addition, the investigation showed that the AISC (LRFD) and BS5400 could to predicting the strength of the CES columns with lightweight aggregate concrete.

In 2006, Chen and Lin proposed an analytical model for predicting axial compressive strength of CES stub columns. The model was developed for predicting loads-strain relation of the CES stub columns with various structural steel and reinforcement steel condition. The strength model was determined from strength assembled of concrete, structural steel and reinforcement steel by considering confinement effect of concrete and buckling effect of structural steel. The model showed good agreement with previous experimental results, could provide axial-strain relation, maximum axial strength and post-peak behavior of the CES columns. Details of the analytical model will be shown in Chapter 3.

In 2011, Ellobody and Young investigated the CES columns subjected to axial loads by numerical analysis. Nonlinear 3D finite element models by ABAQUS

programs were developed by considering confinement behavior of concrete and inelastic behavior of steel. This study focused on using finite elastic to predict maximum loads and failure mode of the CES columns, study effect of design parameters and verify AISC360-05 and Eurocode4 (2004). The results showed that AISC360-05 given conservative results for all CES specimens and Eurocode4 given accurately results in limited material properties of the code.

In the same year, Ellobody et al. investigated CES columns subjected to eccentric loadings by numerical analysis. Nonlinear 3D finite element models by ABAQUS programs were developed by considering confinement behavior of concrete and inelastic behavior of steel. The eccentricity was varied between 0.125-0.375 of total depth of the sections. The finite element results were used to study effect of design parameters and verify an interaction diagram from Eurocode4 (2004). The results showed that Eurocode4 given accurately results for CES columns subjected to eccentric loadings in limited material properties of the code.

In 2015, Ky et al. investigated post-collapse behavior of CES columns subjected to concentric loadings by numerical method. Fiber element model with additional additive technique were proposed. The proposed models provided confinement effect of concrete, buckling effect of reinforcement steel and local buckling of structural steel of the CES columns. The results showed that the proposed models were good agreement with previous experimental results. In addition, effects of design parameters were proposed in this study. Increasing concrete strength was increase column strength but decrease column ductility. Closer spacing of stirrups was increase column ductility only stub columns.

In 2016, Zhu et al. investigated the CES columns by experimental study. Total 21 CES columns with high strength concrete were tested under axial compressive load and cyclic lateral loads with constant axial load. The studied design parameters consisted of stirrup arrangement, axial load level, structural steel details and studs. The results showed that the CES with high strength concrete with multiple stirrups and normally structural steel ratio show excellent seismic behavior. Stirrups had little effect on stiffness. Structural steel is obviously effective in significant axial loads. Studs did not significantly effect on stiffness in early stage; but, it's effect on energy dissipation.

In 2017, Chen and Wu proposed an analytical model for predicting axial compressive strength of CES columns with cross shape steel section. The strength model was determined from strength assembled of concrete, structural steel and reinforcement steel by considering confinement effect of concrete. The concrete confinement zone divided into 3 parts as highly confined concrete, partially confined concrete and unconfined concrete. In case of highly confined concrete, the confined mechanism of structural steel was proposed. In case of partially confined concrete, the confined mechanism of stirrups was proposed. The proposed model was verified with experimental results of CES and PEC columns with cross shape steel section. In addition, a simplified method for estimated real stress in stirrups of the CES columns. Details of the analytical model of the CES and PEC will show in chapter 3.

Next, Lai et al. (2019a) proposed a unified approach to evaluate strength interaction diagram of CES columns which made of different concrete and steel grade. The compressive strength of concrete varies from 20 to 104 MPa and the yield stress of structural steel varies from 280 to 913 MPa. Analytical study was based on material strain compatibility principle. The proposed approach was validated with test results. In addition, the existing EC4 methods, plastic design method, was predicting un-conservatively the strength interaction diagrams of CES columns with high strength steel and high strength concrete.

In the same year, Lai et al. (2019b) investigated the CES columns with high strength concrete by experimental study. Six CES specimens with high strength concrete were tested by axial compressive loads. The studied structural behaviors consisted of failure mode, load-deformation relation, load-carrying capacity and post peak behavior. The results showed that the failure mode of the CES columns with high strength concrete was concrete covering spalling, and the compressive loads suddenly dropped when the loads reaching the peak loads. The experimental results indicated that the concrete with 0.5% volume of steel fiber was able to prevent the concrete cover spalling. Moreover, two analytical methods were proposed for design CES columns with high strength concrete in this study.

Lai et al. (2019c) investigated the CES stub columns with S690 steel and C130 concrete by experimental study. The studied structural behaviors consisted of failure mode, load-deformation relation, load-carrying capacity and post peak behavior.

A total of 14 CES specimens with high strength steel and concrete were tested by axial compressive loads. Two steel grades (S500 and S690) and two concrete grades (C90 and C130) were used to prepare the specimens. Steel fiber (0.5% of volume) was added into the concrete for reducing the inherent brittleness of high strength concrete. The results showed that the existing design codes had inability to estimate CES columns with high strength concrete. In addition, the parametric study showed that the steel contribution ratio had effect on the ductility of the CES columns, whereas, increasing of steel fiber and hoop reinforcement ratio had negligible effect. Finally, a simplified formula was proposed to evaluate ductility of the CES columns with high strength concrete.

Lai et al. (2019d) investigated the buckling behavior of CES columns with high strength concrete by experimental, numerical and analytical analysis. Three long CES columns with high strength concrete C100 and S355 steel member were tested axial compressive loads. The load capacities of the tested specimens were compared with the load capacity predicting from EN 1994-1-1, ACI 318-08 and AISC 360-10. Nonlinear finite element analysis was used to predict the load-displacement behavior and the buckling resistance of these columns. The results showed that EC4 and AISC methods predicted conservatively the buckling resistance compared with these tested results. AISC method, ACI method and Tikka's model conservatively predicted effective flexural stiffness of CES columns. EC4 method closely predicted effective flexural stiffness of CES columns than other methods.

In 2020, Lai et al. investigated the CES columns with high strength concrete and steel. Fourteen CES specimens with different steel section and material properties were tested under axial compressive loads. Compared with EN 1994-1-1 and JGJ 138-2016 design methods show that the design methods predicted overestimate axial compressive loads of CES columns with high strength concrete. In addition, a new test database consisting of 51 PEC columns and 82 CES columns were established. For PEC columns, a simplified method was proposed to compute the enhanced concrete strength based on regression analysis. For CES columns, a concrete strength reduction factor was proposed to predict the compressive strength.

In the same year, Lai and Liew (2020) investigated the axial-moment interaction diagram of CES columns with high strength concrete by numerical

method. Nonlinear numerical model is developed by considering concrete confinement effect, concrete cover spalling, buckling of longitudinal bars and strain-hardening of structural steel. The load-deformation relation, moment curvature relation, and strength interaction diagram were predicted from the model. The model was validated with experimental results in the companion paper and literatures test data. The parametric study performed the effect of yield stress of structural steel, compressive strength of concrete, steel area ratio, and load eccentricity. In addition, a simplified method to construct the strength interaction diagram of CES columns, which it could be used for CES columns with steel grade up to S960 and concrete grade up to C100, was proposed.

2.3 Cellular and castellated steel columns

In this section, previous investigations of cellular members, castellated members and steel members with web openings under axial compressive loads or axial compressive loads and moments are summarized.

In 2009, Sweedan et al. investigate the elastic buckling capacity of cellular steel columns under axial compressive loads. The investigation focuses on elastic buckling load capacity about major axis of the cellular columns. Finite element models by ANSYS software were developed and used to calculate a dimensionless reduction factor, β-factor. The models were developed as 3D structural models by using solid element SOLID45 in the ANSYS software. The reduction factor was investigated under various support condition. And the reduction factor from finite element models was compared with a dimensionless reduction factor from a proposed buckling load capacity equation. In addition, a simplified method to evaluate elastic buckling load of cellular columns with various column support conditions were proposed.

In the same year, Sawy et al. investigated the elastic buckling capacity of castellated steel columns under axial compressive loads. The investigation focuses on elastic buckling load capacity about major axis of the castellated columns. Finite element models by ANSYS software were developed and used to determine the

buckling load reduction due to combined flexural and shear deformation. In addition, the numerical results were used to calculate a dimensionless buckling modification factor (η). The models were developed as 3D structural models by using solid element SOLID45 in the ANSYS software. In addition, a simplified method to evaluate elastic buckling load of cellular columns with various column support conditions were proposed.

In 2011, Sweeden and El-Sawy investigated the elastic local buckling capacity of perforated web of cellular columns under axial and flexural stress. Finite element (FE) models by ANSYS software were developed and used to study design parameters of the web of cellular columns. The FE models were developed as 2D structural models by modeling web of the cellular columns only and using shell element SHELL63 in the ANSYS software. The considered parameters in this investigation are length of the web, width of the web, diameter of the opening and spacing of the opening. The studied showed that when hole spacing-to-web width ratio to be 1.5, the elastic buckling stress are peak value. When hole spacing-to-diameter ratio exceeds 3.5, the elastic buckling loads are not change and converges to the elastic buckling loads of solid web columns.

In the same year, Sonck et al. (2011) investigated the weak-axis flexural buckling of cellular members. A design approach of buckling load of cellular columns was proposed. The design approach was adopted from a design approach of buckling load of traditional steel member in EC3. In addition, Numerical simulations of cellular column were proposed. Finite element models of the column were developed by ABAQUS programs. Nonlinear geometry, nonlinear material properties, geometry imperfection and residual stress of the cellular column were considered. Column buckling curves from the proposed design approach and numerical simulation were compared. The comparison showed that the weak-axis flexural buckling load of cellular columns from numerical simulation was higher than proposed design approach. As a result, the proposed design approach was conservative to design cellular columns.

In 2012, Sonck et al. investigated the global buckling loads of cellular columns under compression and bending. The buckling modes in these cases were lateral torsional buckling and weak-axis flexural buckling. In bending moment case,

existing design approaches were examined. In compression case, a new design approach was proposed and examined. These approaches based on plain-web design beam existing in Eurocode3. The results of these approaches were compared. In addition, parametric studies of cellular member geometries were investigated and the design approaches which have the best results were proposed. The results showed that 2T approach combined with buckling curve of the parent sections had very satisfactory results in compression case. In bending moment case, 2T approach combined with buckling curve b and c of the parent sections had the best approximate the numerical results.

In 2014, Sonck et al. investigated the residual stresses of cellular and castellated steel members by experimental method. It was expected that the residual stresses in the cellular and castellated members was different than the traditional steel members, because of the effect of cutting and welding processes. And it was expected that the additional residual stresses are influence on global buckling behaviors of cellular and castellated steel members. The investigation studies residual stresses of cellular and castellated steel members compared with their parent steel members. A section method which a destructive relaxation method was used to measure the residual stresses in each member sections. The residual stresses ware calculated from metered relaxation strain attached in the tested members. The investigate results showed that the compressive residual stresses in web post and tee section of the castellated steel member are increased. In cellular steel member, the residual stresses in the flange are increased and became totally in compression, because of heat from cutting are close to the steel flange. As a result, the residual stresses of cellular and castellated steel members are influence on global buckling resistance than the residual stresses of traditional steel members.

In the same year, Yuan et al. (2014) investigated the buckling capacity of castellated steel columns under axial compressive loads. An analytical model to predict critical buckling loads about major axis of castellated columns was proposed. The model which considering web shear deformation was derived by using stationary principle of potential energy. The analytical results were validated with numerical results publishes by other. The result showed that the web shear deformations significantly reduces the buckling capacity about major axis of the castellated

columns. In addition, buckling capacity calculation by not considering web shear deformation has overestimate up to 25%.

In 2016, Serror et al. investigated the influence of design parameters to elastic and inelastic buckling of steel web of cellular and castellated steel members. The parameters were opening shape, opening size, opening spacing, end distance to first opening, plate slenderness ratio, steel grade and initial imperfection. Finite element method with ANSYS software was used in this study, and the finite element models were verified with both experimental and numerical results in literatures. In addition, a buckling stress modification factor (β-factor) which present as a ratio of buckling stress of web plate with opening and solid web plate was proposed. The results showed that the minimum of the β-factor was 0.9 for web plates with opening under axial compression and 0.7 for web plates with opening under bending moment. The web plate with circular opening has closely same behavior with the web plate with square opening. The recommended ratio of web opening size and web height are greater than 0.5 for circular and rectangular opening and less than or equal to 0.7 for non-square opening.

In the same year, Sonck and Belis (2016) investigated the weak-axis flexural buckling of cellular and castellated steel members by taking into effect of modified geometry and modified residual stress pattern. Numerical models by ABAQUS program were used in this study. The residual stresses of cellular and castellated members from production were measured and considered in the models. A 2T approach combined with European buckling curve in Eurocode3 was proposed for calculating flexural buckling resistance of the cellular and castellated columns. The preliminary best fit curves of European buckling curves were buckling curve c and d which depending on a ration of height and width of the members.

Gu and Cheng (2016) investigated the major-axis buckling loads of cellular columns which considering shear deformation. An analytical model to predict critical buckling loads of cellular columns was derived by using stationary principle of potential energy. The derived model was validated with numerical results from finite element method with ANSYS software. The results from verified analytical model

showed that the effect of shear deformation was significantly reduce the buckling loads of cellular columns.

In the same year, Najafi and Wang (2017) investigated the steel members with web openings under combined bending, shear and compression. This investigation developed analytical models to evaluate strength capacity of steel members with web openings under pure compression, pure bending, combined compression and bending and combined compression, bending and shear by including buckling behavior of T-section of the members. The analytical models were compared with numerical models which using finite element model by ABAQUS program. The finite element models were validated with experimental results of castellated beams and steel beams with web openings by others. The results showed that the comparison between the analytical results and numerical results are very good agreement. Details of the analytical models for calculate strength capacity of steel members with web openings will show in chapter 3.

In 2019, Panedpojaman et al. investigated the elastic buckling of cellular columns subjected to concentric loadings. A simplified calculation method for predicting elastic buckling loads about major axis of cellular column with pin-ended supports. This method based on column geometry and considered on shear effect. The proposed loads were validated with finite element analysis results. The parameter study consisted of the section ratio, the spacing ratio, the opening ratio and the slenderness. The results showed that the spacing ratio effect on the buckling loads more than the opening ratio.

2.4 Composite members using steel members with web openings

In this section, previous investigations of composite members with steel members with web openings are summarized.

In 2014, Junus et al. investigated the castellated beam-column and castellated beam-column with concrete under seismic loads. Experimental results of traditional steel beam-column, castellated beam-column and castellated beam-column with concrete under cyclic loadings were compared. The comparison showed that the castellated member had higher energy absorption and flexural capacity than the

traditional member about 74.3% and 100.5% respectively, but the castellated member had lower partial ductility and full ductility than traditional member about 12.6% and 18.1% respectively. In addition, the disadvantage of the castellated member was accelerating the degradation rate of stiffness ratio about 31.4% and decrease resistance ratio about 29.5%. On the contrary, the result of the castellated member with filled concrete showed that the castellated member with filled concrete had higher energy absorption, flexural capacity, partial ductility, full ductility and resistance ratio than the castellated member without concrete about 217.1%, 184.8%, 27.9%, 26% and 52.5% respectively. Moreover, the advantage of the castellated member with filled concrete slow the rate of degradation of the stiffness ratio 55.1%

In 2017, Farajpourbonab et al. investigated the concrete filled steel tube (CFT) columns with castellated steel members. The structural steel in the composite columns are castellated cruciform steel members. Four small size and short columns as shown in Figure 2.1 were tested under concentric loadings. A comparison of compressive strength of CFT columns with a traditional steel member and a castellated steel member fabricated from the traditional steel member were proposed. The results showed that the CFT columns with castellated steel members have higher maximum strength and post yield stress than CFT columns with traditional steel members. Moreover, this paper presented numerical study of traditional and castellated steel columns. Finite element model of the columns was developed by using ANSYS software. In addition, an equation for predict maximum axial compressive loads of castellated steel columns were proposed. And the maximum loads from numerical studies were good agreement with proposed equation.

In the same year, Ahmad et al. investigated the PEC beams with web openings. PEC beams with web openings were tested and compared with PEC beams without web openings. The tested specimens of the beam with web openings had similar steel-to-concrete volumetric ratios to beam without web openings, but had not similar dimension. The steel to concrete volumetric ratios proposed in this study were 1%, 2% and 3%, and all tested specimens had not shear studs. The results showed that the tested beams with web openings provided higher maximum loads and stiffness than tested beams without web openings for all steel ratios. And the tested beams with web opening provided full bond interaction between concrete and steel section.

In addition, finite element models by ABAQUS program were proposed in this study. The numerical results were good agreement with the experimental results.

(a)   (b)

Figure 2.1 Steel reinforced-concrete filled with (a) castellated cruciform steel section; and (b) traditional cruciform steel section (Farajpourbonab et al., 2017).

2.5 Conclusions

The literature reviews of partially encased composite (PEC) columns show that the PEC columns have been widely investigated. The PEC columns were investigated by both experimental and numerical methods. In the experimental studies, the PEC was tested under concentric loads, eccentric loads and dynamic loads. In the numerical studies, analytical models and numerical models of the PEC columns were proposed. Some models were used to predict the local and post local behaviors of the PEC columns. The investigation showed that the PEC columns have high strength and ductility. Moreover, some research showed that the PEC columns had good performance subjected to fire resembling steel columns with fire protection. In addition, the PEC columns were investigated in many forms, the PEC columns with standard sections, the PEC columns with thin-walled built-up sections and the PEC columns with thin-walled built-up sections strengthened by transverse links. However, the PEC columns with cellular steel member have not been investigated.

The literature reviews of concrete-encased steel (CES) columns show that the CES columns have been widely investigated. The CES columns were investigated by both experimental and numerical methods. In the experimental studies, the CES were

tested under concentric loads and eccentric loads. In the numerical studies, analytical models and numerical models of the CES columns were proposed. Some models predicted the confinement behaviors of the CES columns. The investigation showed that the CES columns have high strength, high ductility and high fire resistance. In addition, some results were compared with predictions by design provision. Moreover, the CES columns were investigated with many steel shapes. However, the CES columns with cellular steel member have not been investigated.

The literature reviews of cellular columns show that the cellular columns are new type of steel columns. The investigations on cellular columns range from 2009 to 2019. All cellular columns were investigated by numerical methods. Analytical models and finite element models of the cellular columns were proposed. These models predicted local buckling behavior of the cellular columns. Moreover, the cellular columns were investigated with many steel shapes. However, using cellular columns with PEC and CES have not been investigated.

The literature reviews of the composite members with steel members with web openings show that this is a new type of composite members. The reviews show three investigations in 2014 and 2017. The first research investigated castellated beam-column filled with concrete. The second research investigated concrete filled steel tube columns with castellated steel members. The third research investigated PEC beams with web openings. All researches show that using cellular member in composite member had more efficiency than using traditional steel member. However, PEC and CES columns with cellular members have not been investigated.

Therefore, this research investigates concrete-encased cellular steel (CECS) columns. It is expected that the CECS columns combines the advantages of composite columns and cellular members. In addition, the partially concrete-encased cellular steel columns will be investigated in the future.

CHAPTER 3
THEORETICAL CONSIDERATIONS

3.1 Concrete confinement models for reinforced concrete columns

In this section, concrete confinement models of reinforced concrete columns of Mander et al. (1988) and Cusson and Paultre (1995) are proposed.

3.1.1 Concrete confinement model of Mander et al. (1988)

In the investigation of Mander et al. (1988), a model to predict stress-strain relation of confined concrete was proposed. This research focus on the model of confined concrete of reinforced concrete columns subjected to concentric loadings.

The stress-strain relation of confined concrete in reinforced concrete columns subjected to concentric loadings shown in Figure 3.1 was developed by Popovics (1973). The stress-strain relation of confined concrete is

$$f_c = \frac{f_{cc}' x r}{r - 1 + x^r} \tag{3.1}$$

Where

$$x = \frac{\varepsilon_c}{\varepsilon_{cc}} \tag{3.2}$$

$$\varepsilon_{cc} = \varepsilon_{co} \left[1 + 5 \left(\frac{f_{cc}'}{f_{co}'} - 1 \right) \right] \tag{3.3}$$

$$r = \frac{E_c}{E_c - E_{sec}} \tag{3.4}$$

$$E_c = 5000 \sqrt{f_{co}'} \text{ MPa} \tag{3.5}$$

$$E_{sec} = \frac{f_{cc}'}{\varepsilon_{cc}} \tag{3.6}$$

E_c = elastic modulus of concrete;

E_{sec} = secant modulus of concrete at peak strength of confined concrete;

f_{cc}' = compressive strength of confined concrete;

f_{co}' = compressive strength of concrete cylinder;

ε_c = corresponding strain of concrete;

ε_{co} = corresponding strain at compressive strength of concrete cylinder.
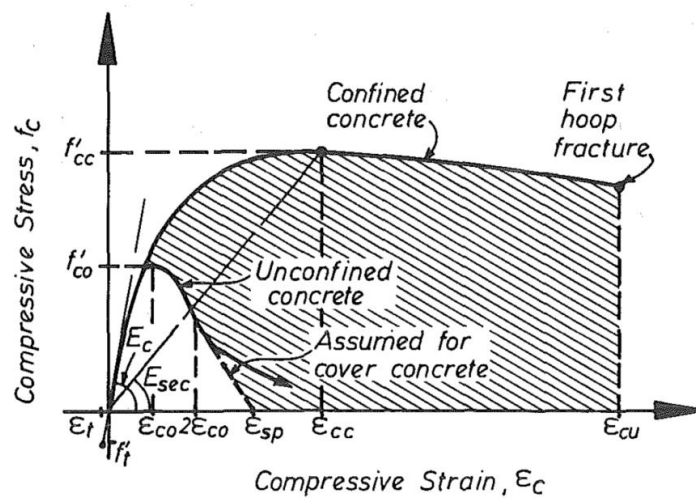
Figure 3.1 Stress-strain relation of confined concrete of reinforced concrete columns subjected to concentric loadings (Mander et al., 1988).

For concrete confined by active hydrostatic fluid pressure, the compressive strength and corresponding strain of confined concrete is

$$f_{cc}' = f_{co}' + k_1 f_l \tag{3.7}$$

$$\varepsilon_{cc} = \varepsilon_{co}\left(1 + k_2 \frac{f_l}{f_{co}'}\right) \tag{3.8}$$

Where

k_1 and k_2 = coefficients of confined concrete;

f_l = lateral pressure.

Richart et al. (1928) proposed the value of k_1 to be 4.1 and $k_2 = 5k_1$, and Balmer (1949) proposed the average value of k_1 to be 5.6.

For concrete confined by circular hoop stirrups or circular spiral stirrups, the confined core of reinforced concrete columns with circular hoop stirrups or circular spiral stirrups, as shown in Figure 3.2. The compressive strength of confined concrete is

$$f_{cc}' = f_{co}'\left(-1.254 + 2.254\sqrt{1 + \frac{7.94 f_l'}{f_{co}'}} - 2\frac{f_l'}{f_{co}'}\right) \tag{3.9}$$

Where

$$f_l' = f_l k_e \tag{3.10}$$

$$k_e = \frac{A_e}{A_{cc}} \tag{3.11}$$

$$A_e = \frac{\pi}{4}\left(d_{sr} - \frac{s}{2}\right)^2 \tag{3.12}$$

$$A_{cc} = A_{c,core}\left(1 - \rho_{cc}\right) = \frac{\pi}{4}d_{sr}^{~2}\left(1 - \rho_{cc}\right) \tag{3.13}$$

$$f_l = \frac{1}{2}\rho_s f_{ysh} \tag{3.14}$$

$A_{c,core} = $ cross-sectional area of concrete core bounded by closed stirrup;

$A_e \quad = $ effective area of confined concrete;

$d_s \quad = $ diameter of spiral;

$f_{ysh} \quad = $ specified minimum yield stress of stirrup;

$s \quad = $ longitudinal spacing of stirrup;

$\rho_{cc} \quad = $ ratio of longitudinal reinforcement area to core section area;

$\rho_s \quad = $ ratio of stirrups volume to concrete core volume.
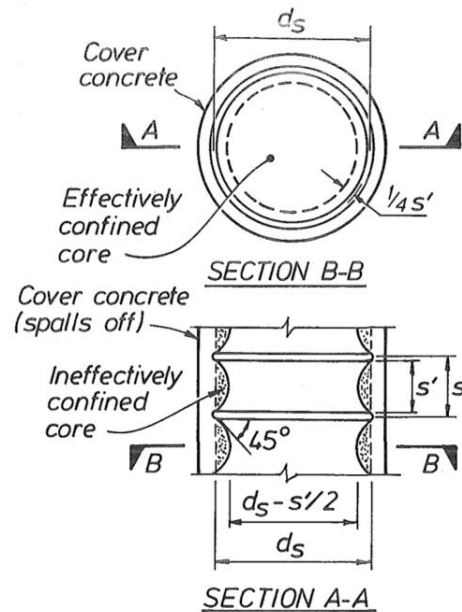
Figure 3.2 Area of confined concrete by circular hoop stirrups or circular spiral stirrups (Mander et al., 1988).

For concrete confined by rectangular hoop stirrups, the confined core of reinforced concrete columns with rectangular hoop stirrups is shown in Figure 3.3. The compressive strength of confined concrete which it's depends on effective lateral pressure was presented in Figure 3.4. The effective lateral pressure is

$$f_{lx}^{'} = k_e \rho_x f_{ysh} \tag{3.15}$$

$$f_{ly}^{'} = k_e \rho_y f_{ysh} \tag{3.16}$$

Where

$$k_e = \frac{\left(1 - \sum_{i=1}^{n} \frac{\left(w_i^{'}\right)^2}{6b_c d_c}\right)\left(1 - \frac{s^{'}}{2b_c}\right)\left(1 - \frac{s^{'}}{2d_c}\right)}{\left(1 - \rho_{cc}\right)} \tag{3.17}$$

$$\rho_x = \frac{A_{sx}}{sd_c} \tag{3.18}$$

$$\rho_y = \frac{A_{sy}}{sb_c} \tag{3.19}$$

A_{sx} = area of stirrups in the x direction;

A_{sy} = area of stirrups in the y direction;

b_c = diameter of stirrups in x direction;

d_c = diameter of stirrups in y direction;

s' = clear longitudinal spacing of stirrup;

w_i' = clear distance between adjacent longitudinal bars.
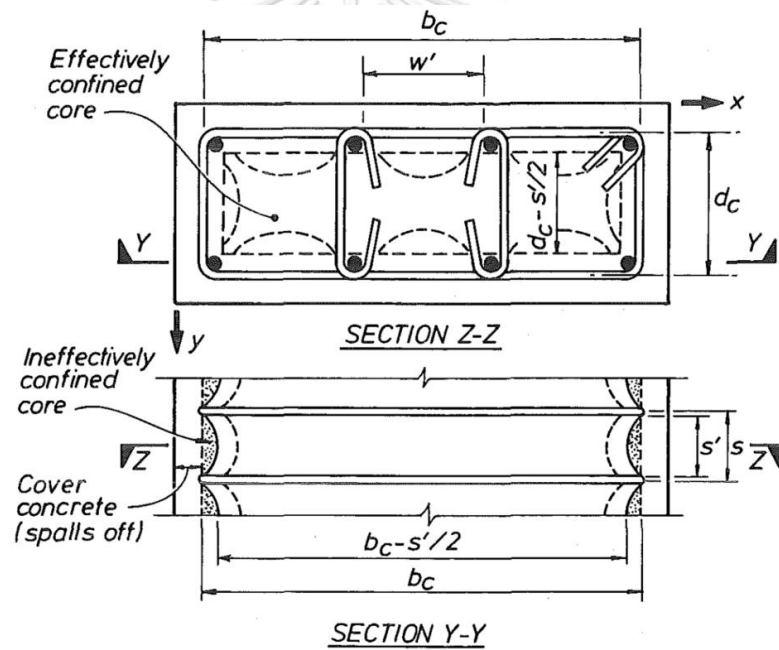
Figure 3.3 Area of confined concrete by rectangular hoop stirrups
(Mander et al., 1988).
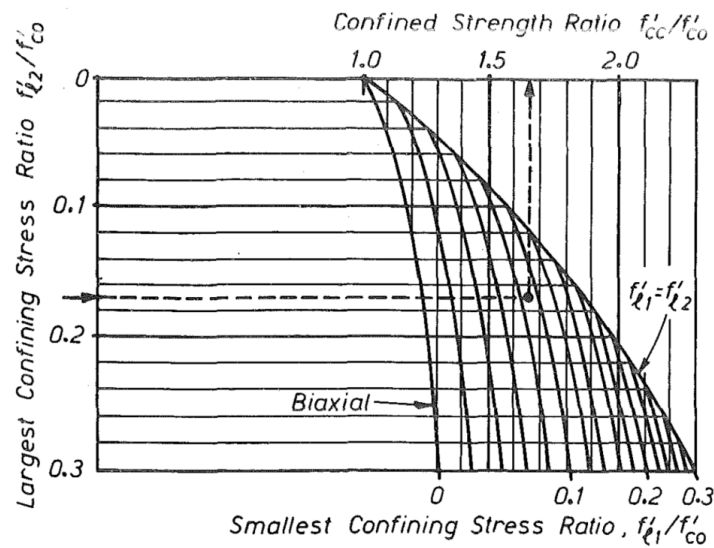
Figure 3.4 Factor of compressive strength of confined concrete of rectangular hoop stirrups (Mander et al., 1988).

3.1.2 Concrete confinement model of Cusson and Paultre (1995)

In the investigation of Cusson and Paultre (1995) a concrete confinement model for reinforced concrete columns with high-strength concrete and a method to compute the stress in stirrup were proposed.

The proposed stress-strain relation of unconfined and confined concrete was shown in Figure 3.5. The stress-strain curve of confined concrete in ascending part (OA) was proposed by Popovic (1973); and, the curve in descending part (ABC) was proposed by Fafitis and Shah (1985). The stress-strain relation of confined concrete of was given as follows,

For the ascending part (OA)

$$f_c = f_{cc}' \left[\frac{k(\varepsilon_c/\varepsilon_{cc})}{k - 1 + (\varepsilon_c/\varepsilon_{cc})^k} \right] \tag{3.20}$$

Which $\quad \varepsilon_c \leq \varepsilon_{cc}$

$$k = \frac{E_c}{E_c - (f_{cc}'/\varepsilon_{cc})} \tag{3.21}$$

$$\varepsilon_{co} = 0.002$$

For the descending part (ABC)

$$f_c = f_{cc}' \cdot \exp\left[k_1\left(\varepsilon_c - \varepsilon_{cc}\right)^{k_2}\right] \tag{3.22}$$

Which $\varepsilon_c \geq \varepsilon_{cc}$

$$k_1 = \frac{\ln 0.5}{\left(\varepsilon_{C50C} - \varepsilon_{cc}\right)^{k_2}} \tag{3.23}$$

$$k_2 = 0.58 + 16\left(\frac{f_l'}{f_{co}'}\right)^{1.4} \quad \text{as shown in Figure 3.6} \tag{3.24}$$

ε_{C50C} = longitudinal strain of confined concrete at 50% of the maximum compressive stress.

The ratio of compressive strength on confined concrete to unconfined concrete (strength ratio) was given to be

$$f_{cc}'\Big/f_{co}' = 1.0 + 2.1\left(f_l'\Big/f_{co}'\right)^{0.7} \quad \text{as shown in Figure 3.7} \tag{3.25}$$

The peak strain of confined concrete was given to be

$$\varepsilon_{cc} = \varepsilon_{co} + 0.21\left(f_l'\Big/f_{co}'\right)^{1.7} \quad \text{as shown in Figure 3.8} \tag{3.26}$$

The Longitudinal strain of confined concrete at 50% of the maximum compressive stress was given to be

$$\varepsilon_{C50C} = \varepsilon_{C50U} + 0.15\left(f_l'\Big/f_{co}'\right)^{1.1} \quad \text{as shown in Figure 3.9} \tag{3.27}$$

ε_{C50U} = longitudinal strain of unconfined concrete at 50% of the maximum compressive stress (= 0.004).
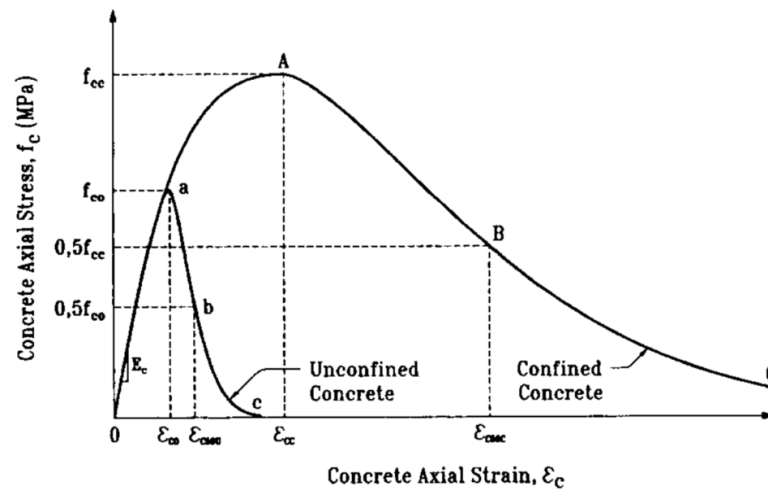
Figure 3.5 Stress-strain relation of confined concrete of reinforced concrete columns subjected to concentric loadings (Cusson and Paultre, 1995).
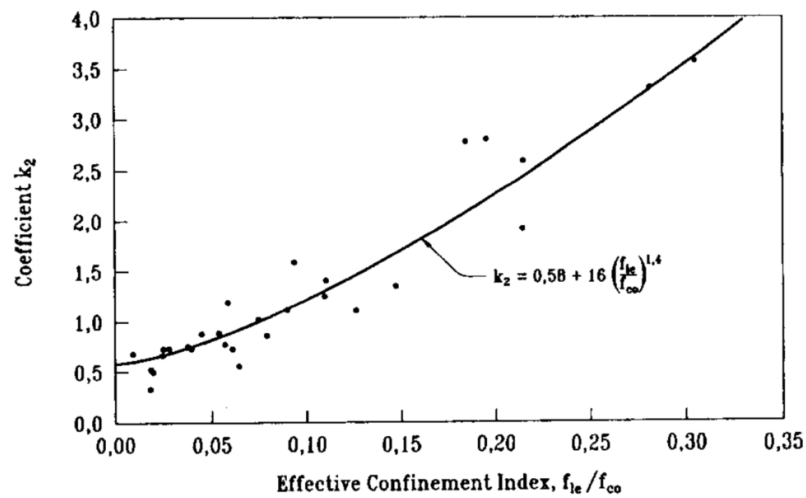
Figure 3.6 Effect of effective confinement index on coefficient k_2
(Cusson and Paultre, 1995).
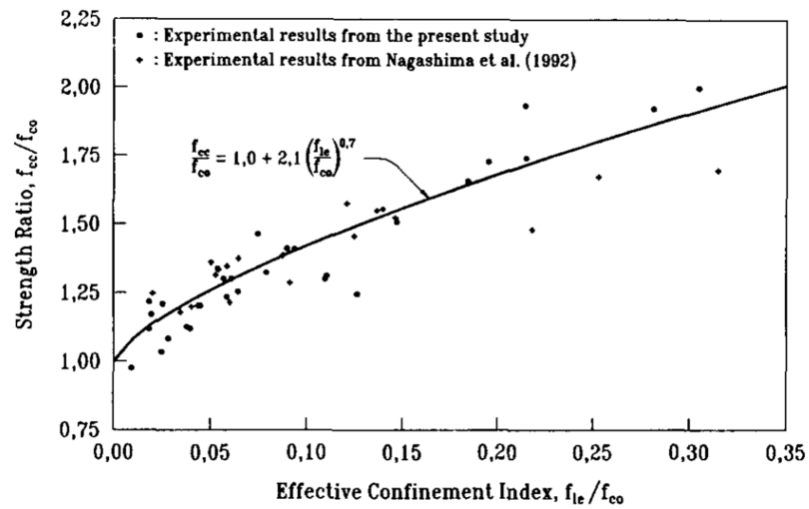
Figure 3.7 Effect of effective confinement index on strength ratio
(Cusson and Paultre, 1995).
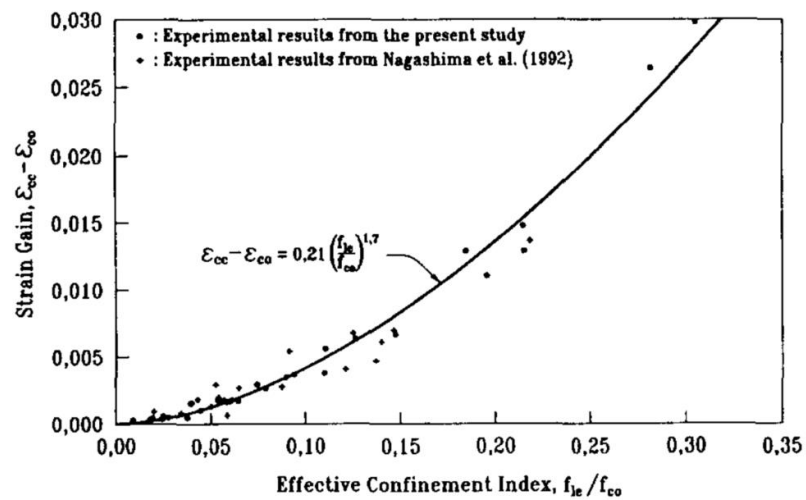
Figure 3.8 Effect of effective confinement index on peak strain of confined concrete
(Cusson and Paultre, 1995).
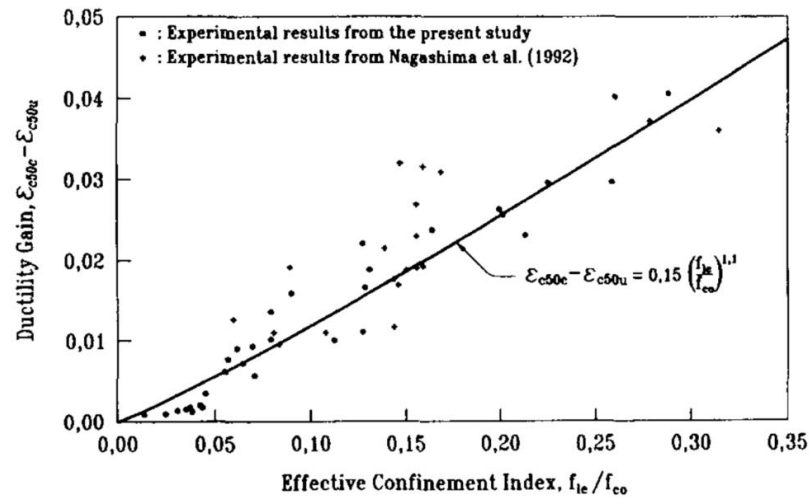
Figure 3.9 Effect of effective confinement index on Longitudinal strain of confined concrete at 50% of maximum compressive stress (Cusson and Paultre, 1995).

The effective confinement pressure was given to be

$$f_l' = K_e f_l \tag{3.28}$$

Where

$$f_l = \frac{f_{hcc}}{s}\left(\frac{A_{shx} + A_{shy}}{b_c + d_c}\right) \tag{3.29}$$

$$K_e = \frac{\left(1 - \sum_{i=1}^{n}\frac{\left(w_i'\right)^2}{6b_c d_c}\right)\left(1 - \frac{s'}{2b_c}\right)\left(1 - \frac{s'}{2d_c}\right)}{\left(1 - \rho_{cc}\right)} \tag{3.30}$$

A_{shx} = area of stirrups in the x direction;

A_{shy} = area of stirrups in the y direction;

f_{hcc} = stress in the transverse reinforcement at the maximum strength of confined concrete.

The stress in the lateral reinforcement was determined from the corresponding stirrups strain which assuming the lateral strain of stirrups equal to lateral concrete strain. The lateral strain of stirrups was determined to be

$$\varepsilon_{hcc} = \nu_c \varepsilon_{cc} - \frac{(1-\nu_c)f_l'}{E_{sec}}$$ (3.31)

Where

ν_c = Poisson's ratio of concrete.

When used Poisson's ratio of concrete to be 0.5

$$\varepsilon_{hcc} = 0.5\varepsilon_{cc}\left[1 - \frac{f_l'}{f_{cc}}\right]$$ (3.32)

In this investigation, the Poisson's ratio of concrete was used to be 0.5. In addition, above equation had three unknowns: the peak strain of confined concrete (ε_{cc}), the effective confinement pressure (f_l') and the compressive strength of confined concrete (f_{cc}) which all variables were function of stress in the transverse reinforcement at the maximum strength of confined concrete (f_{hcc}). The method to compute the variables followed an iterative procedure as follows,

1. Assume $f_{hcc} = f_{yh}$ and compute f_l'.
2. Compute f_{cc} and ε_{cc}.
3. Estimate ε_{hcc}.
4. Find new value of f_{hcc} from estimated ε_{hcc}.
5. Reevaluate f_l'.
6. Repeat step 2 to 5 until the values are convergence.

3.2 Analytical load-deflection models for concrete-encased steel columns

In this section, analytical models for predicting the axial load-deformation of CES stub columns of Chen and Lin (2006) and Chen and Wu (2017) are proposed. The effect of concrete confinement and buckling of steel are considered in these models.

3.2.1 An analytical model of Chen and Lin (2006)

In the investigation Chen and Lin (2006), the axial load-deformation model was proposed based on strain compatibility method of the composite cross-section. The axial loads of the CES columns were computed from assembled the axial stress of structural steel, longitudinal reinforcement steel and concrete in the CES columns. Assumptions of the model were as follows: (1) the model assumed uniform distribution on the cross-section; (2) axial stress of each materials used uniaxial stress-strain relationships; (3) the model considered confinement effect of concrete; (4) the model assumed local buckling of structural steel and reinforcement steel.
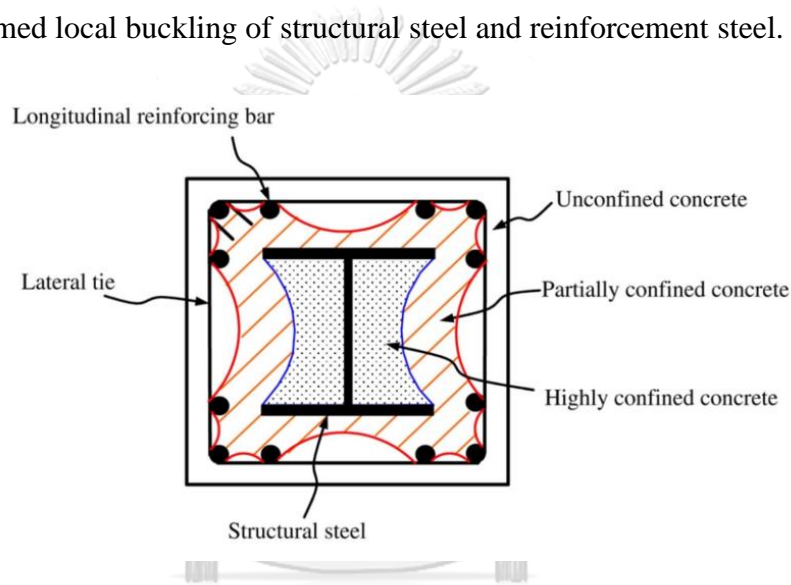
Figure 3.10 Materials and concrete confinement zone of concrete-encased steel columns (Chen and Lin, 2006).

The concrete in the CES columns was divided into three parts as unconfined concrete, partially confined concrete and highly confined concrete, as shown in Figure 3.10. The confined areas are assumed as parabolic arching referenced confinement areas of reinforced concrete columns. The unconfined concrete zone is outside the parabolic arching formed by reinforcement steel. The highly confined zone is inside the parabolic arching formed by flange of structural steel. The partially confined zone is outside the highly confined zone and inside the unconfined zone.

The axial load-deformation of the CES columns was proposed in terms of the axial loads and axial strain relationships. The axial loads from the model were determined by assembling axial capacity of all materials in the CES columns, as shown in Figure 3.11. The analytical axial loads were given to be

$$P_{ana} = f_s A_s + f_{sr} A_{sr} + f_{uc} A_{uc} + f_{pc} A_{pc} + f_{hc} A_{hc} \qquad (3.33)$$

Where

A_{hc} =   cross-sectional area of highly confined concrete;

A_{pc} =   cross-sectional area of partially confined concrete;

A_{uc} =   cross-sectional area of unconfined concrete;

$f_{cc,h}'$ =   compressive strength of highly confined concrete;

$f_{cc,p}'$ =   compressive strength of partially confined concrete;

$f_{cc,u}'$ =   compressive strength of unconfined concrete.
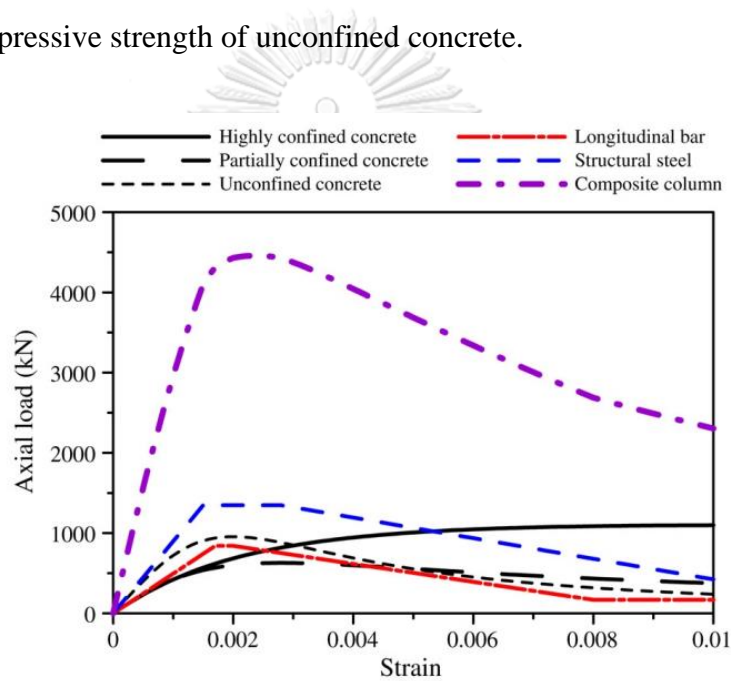
Figure 3.11 Axial loads of CES columns by analytical model of Chen and Lin (2006).

The concrete referenced model of unconfined and confined concrete by Mander et al. (1988), but the compressive strength of partially and highly confined concrete defined as follows,

For partially confined concrete

$$f_{cc,p}' = K_p f_{co}' \qquad (3.34)$$

For highly confined concrete

$$f_{cc,h}' = K_h f_{co}' \qquad (3.35)$$

Where

K_h = confinement factor of highly confined concrete;

K_p = confinement factor of partially confined concrete.

The stress-strain relationships of unconfined, partially confined and highly confined concrete were shown in the Figure 3.12. The strain at maximum compressive stress of unconfined concrete was assumed to be 0.002. In addition, the concrete confinement factors of partially confined and highly confined concrete were proposed, as shown in Figure 3.13.
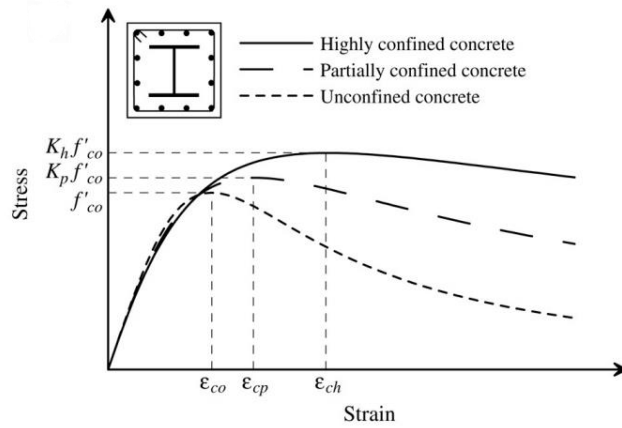
Figure 3.12 Stress-strain relationships of unconfined, partially confined and highly confined concrete (Chen and Lin, 2006).
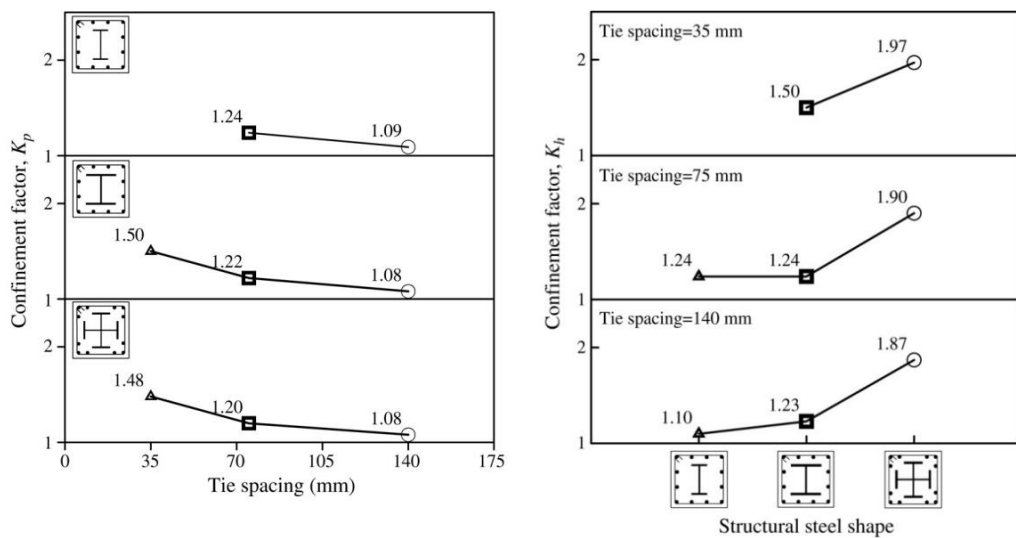
Figure 3.13 Concrete confinement factors of partially confined and highly confined concrete (Chen and Lin, 2006).
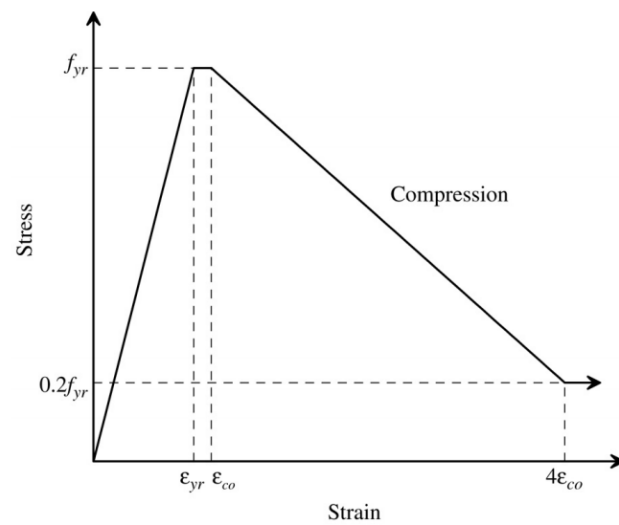
Figure 3.14 Stress-strain relationships of longitudinal reinforcement steel
(Chen and Lin, 2006).

The steel models considered buckling behavior of steel in compression. The stress-strain relationships of structural steel and longitudinal reinforcement steel were assumed, as shown in Figure 3.14-3.15. The structural steel and reinforcement steel reached the yield stress of steel. After that, the reinforcement steel was assumed to buckle after spalling of the unconfined concrete, and the stress of the longitudinal reinforcement steel became degrade. Moreover, the structural steel was assumed to buckle after crushing of the partially confined concrete.
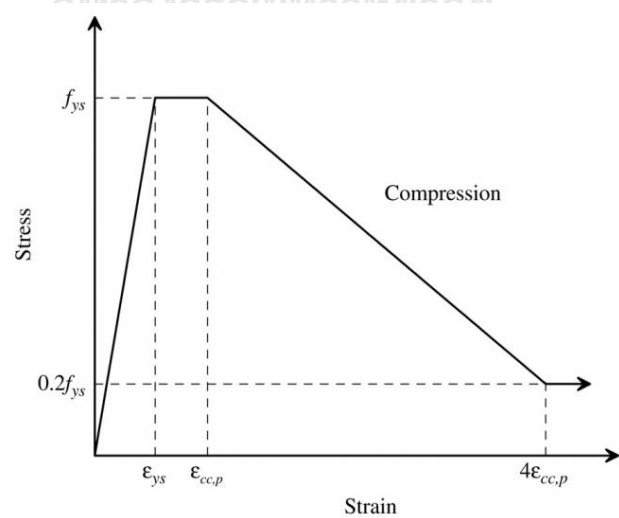
Figure 3.15 Stress-strain relationships of structural steel (Chen and Lin, 2006).

3.2.2 An analytical model of Chen and Wu (2017)

In the investigation Chen and Wu (2017), the axial load-deformation model was proposed based on strain compatibility method of the composite cross-section as same as Chen and Lin (2006), but the equation to compute the lateral confinement pressure were thoroughly proposed. The axial loads of the CES columns were computed from assembled the axial stress of structural steel, longitudinal reinforcement steel and concrete in the CES columns. The concrete in the CES and PEC columns were divided into three parts and two parts respectively, as shown in Figure 3.16. Definition of the concrete confinement zone in this model was similar to the concrete confinement zone of Chen and Lin (2006).

(a) SRC column.　　　　　　　　　　　　(b) PSRC column.
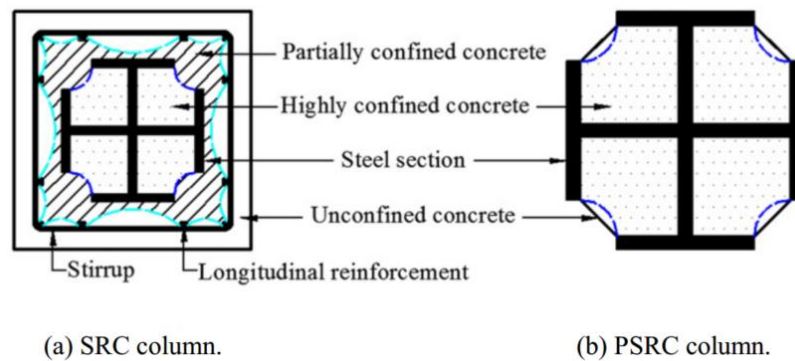
Figure 3.16 Materials and concrete confinement zone of concrete-encased steel columns (Chen and Wu, 2017).

The highly confined concrete of the PEC columns was confined by structural steel only, but the highly confined concrete of the CES columns was confined by structural steel and reinforcement steel. The effective lateral confining pressure of PEC and CES columns were defined as follows,

For partially encased composite columns

$$f_{l,h}' = f_{l,s}' \tag{3.36}$$

For highly concrete-encased steel columns

$$f_{l,h}' = f_{l,s}' + f_{l,p}' \tag{3.37}$$

Where

$f'_{l,s}$ = the effective lateral confining pressure from structural steel;

$f'_{l,p}$ = the effective lateral confining pressure from stirrups.

The effective lateral confining pressure from structural steel ($f'_{l,s}$) was determined from lateral confining pressure, stress effectiveness coefficient and confinement effectiveness coefficient. The lateral confining pressure are determined from the pressure by the expansion of the concrete to the structural steel flange. The stress effectiveness coefficient is the coefficient considering uneven distribution of confining pressure. The confinement effectiveness coefficient is the coefficient different confining states. The effective lateral confining pressure from structural steel pressure could be determined to be

$$f'_{l,s} = k_{es} k_{ea} f_{l,s} \tag{3.38}$$

Where

k_{ea} = confinement effectiveness coefficient;

k_{es} = stress effectiveness coefficient;

$f_{l,s}$ = lateral confining pressure.

The lateral confining pressure was determined from the pressure by the expansion of the concrete to the structural steel flange. The edge of steel flange was assumed to yield. The biaxial ellipse theory was used to calculate the maximum tensile stress at the edge of the steel flange. And experimental found that the nonlinear expansion of concrete occurred at 0.75 times of the yielding strength of PEC columns. From calculated of the biaxial ellipse theory, the maximum tensile stress of the steel flange against the lateral expansion of concrete to be 0.375 times of yielding of structural steel, as shown in Figure 3.17. The lateral confining pressure was determined to be

$$f_{l,s} = \frac{2}{3} q_u \tag{3.39}$$

Where

q_u =   maximum lateral confining pressure;

$$q_u = \frac{t_f^2}{4b^2} f_y \tag{3.40}$$

b =   clear width of steel flange.
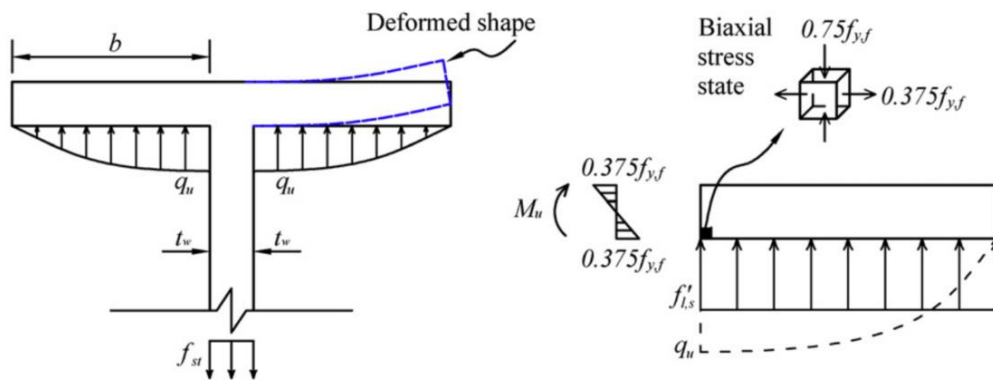
Figure 3.17 Lateral confining pressure from structural steel (Chen and Wu, 2017).

      The stress effectiveness coefficient was used to adjust the direct confining pressure to the average confining pressure ($f'_{lu,s}$), as shown in Figure 3.18. The equations to calculate the stress effectiveness coefficient was given to be

$$k_{es} = \frac{f'_{lu,s}}{f'_{l,s}} = \frac{3\lambda}{2\lambda + 1} \tag{3.41}$$

Where

$$\lambda = \frac{b}{h} \tag{3.42}$$

b =   clear width of steel flange;

h =   clear height of steel web.
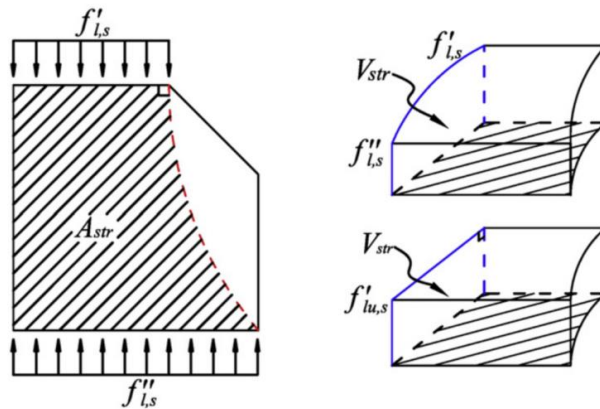
Figure 3.18 Average confining pressure of highly confined concrete
(Chen and Wu, 2017).

The cross-section of the PEC columns with cross-shape structural steel is shown in Figure 3.19.

Quater-concrete model
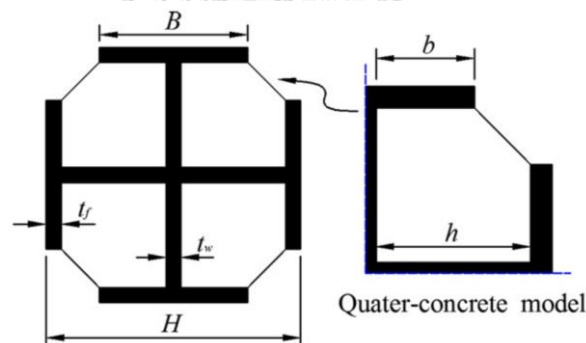
Figure 3.19 Cross-section of PEC columns with cross-shape structural steel
(Chen and Wu, 2017).

The confinement effectiveness coefficient was used to adjust the total area of concrete to area of effective highly confined zone, as shown in Figure 3.20. The equation to calculate the confinement effectiveness coefficient was given to be

$$k_{ea} = \frac{4A_e}{A_c} = \frac{1 - \dfrac{\lambda}{4}\left(1 - \dfrac{\lambda}{3}\right)^2}{1 - \dfrac{1}{2}(1-\lambda)^2} \tag{3.43}$$

Where

A_e =   area of effective highly confined zone.

(a) Real confining state   (b) Effectively confining state
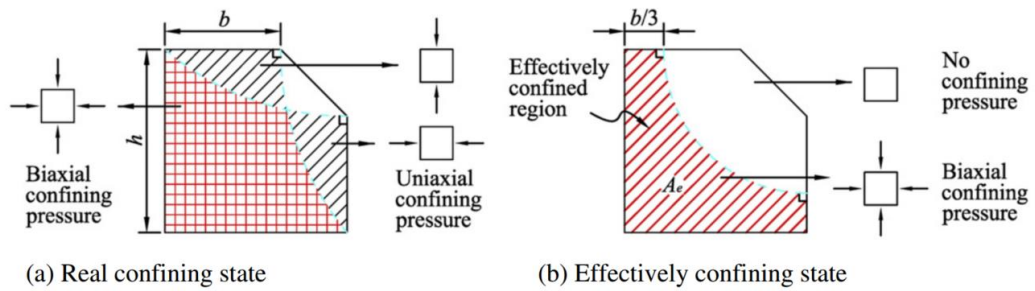
Figure 3.20 Adjustment of highly confined concrete zone (Chen and Wu, 2017).

The effective lateral confining pressure from stirrups which confining lateral pressure to both highly confined concrete and partially confined concrete was determined based on lateral confining pressure of Mander model in 1988. But, Mander model assumed yielding of stirrups which the stirrups may not yield in some case. In 1995, Cusson and Paultre proposed an iterative procedure to determine real stress in stirrups which proposed in section 3.1. The effective lateral confining pressure from stirrups was defined to be

$$f_{l,p}' = k_e \rho_{sh} f_{rh} \tag{3.44}$$

Where

k_e =   area ratio of effectively confined area of partially confined concrete;

ρ_{sh} =   effective volume ratio of stirrups;

f_{rh} =   real stress in stirrups which determined based on Cusson and Paultre iterative procedure.

The stress-strain of all part of concrete referred the stress-strain relation of confined and unconfined concrete of Mander et al. (1988) as shown in Figure 3.21 which the maximum compressive stress of highly confined, partially confined and unconfined concrete was defined to be

$$f_{cc,h}' = K_h f_{co}' = \left(-1.254 + 2.254\sqrt{1 + \frac{7.94 f_{l,h}'}{f_{co}'}} - 2\frac{f_{l,h}'}{f_{co}'} \right) f_{co}' \tag{3.45}$$

$$f_{cc,p}{}' = K_p f_{co}{}' = \left(-1.254 + 2.254\sqrt{1 + \frac{7.94 f_{l,p}{}'}{f_{co}{}'}} - 2\frac{f_{l,p}{}'}{f_{co}{}'} \right) f_{co}{}' \qquad (3.46)$$

$$f_{cc,u}{}' = f_{co}{}' \qquad (3.47)$$

Where

$f_{l,h}{}' =$ effective lateral confining pressure of highly confined concrete;

$f_{l,p}{}' =$ effective lateral confining pressure of partially confined concrete.
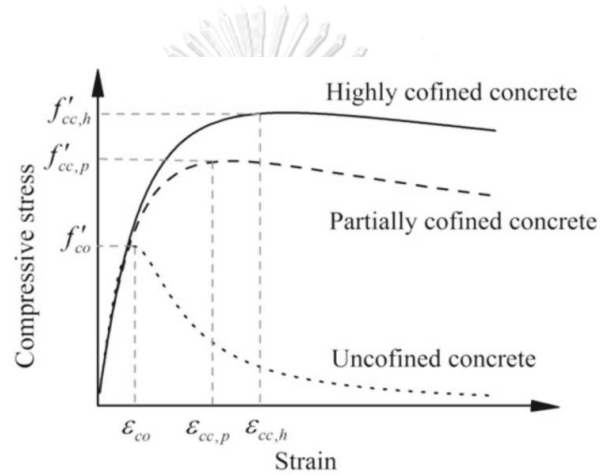
Figure 3.21 Stress-strain relation of highly, partially confined and unconfined concrete (Chen and Wu, 2017).

For structural steel, biaxial stress ellipse theory was adeptly used for web plate of structural steel. The biaxial stress ellipse theory was defined as follows,

$$f_{st}^2 + f_{sv}^2 - f_{st}f_{sv} = f_y^2 \qquad (3.48)$$

Where

f_{st} = maximum lateral tensile stress in web;

f_{sv} = maximum vertical stress in web.

For the structural steel web, the maximum lateral tensile stress was determined from force equilibrium of steel section, as shown in Figure 3.17. The maximum lateral tensile stress was defined to be

$$f_{st} = \frac{4b}{3t_w} q_u \qquad\qquad (3.49)$$

Where

b = clear width of steel flange;

q_u = maximum lateral confining pressure.

For the stress-strain relation of steel, the Giuffre-Menegotto model without considering hardening effect was adapted for the structural steel web and flange, as shown in Figure 3.22. Radius of transition part between elastic range and hardening branch was to be 10, $R = 10$. For the steel flange of structural steel, buckling effect of steel flange due to lateral expansion of concrete was not considered.
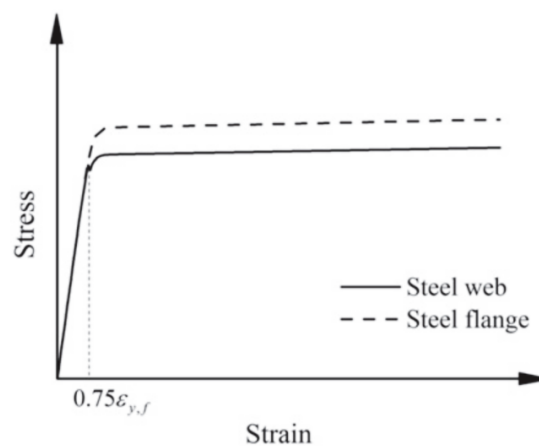
Figure 3.22 Stress-strain relation of structural steel (Chen and Wu, 2017).

For stress-strain relation of longitudinal reinforcement steel, the stress-strain model of Chen and Lin (2006) as shown in Figure 3.23 was used in this model. The longitudinal reinforcement bars were assumed to buckle after the unconfined concrete crushing. And the strength of longitudinal reinforcement bars was decreased to 20% of the yield stress. The stress-strain relation of longitudinal reinforcement bars was shown as follows,
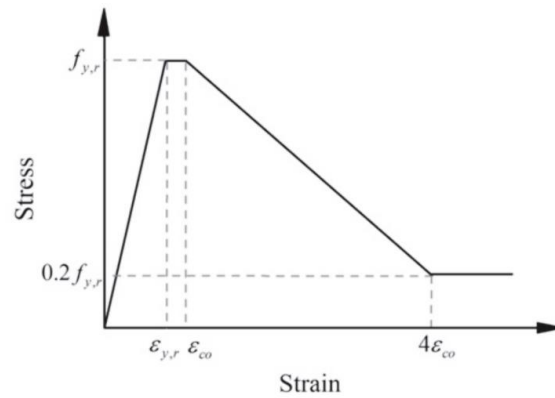
Figure 3.23 Stress-strain relation of longitudinal reinforcement bars
(Chen and Wu, 2017).

Finally, the examples of the predicted load-strain relation of this model were shown in Figure 3.24. The axial loads from the model were determined by assembled axial capacity of all materials in the CES columns similar to model of Chen and Lin (2006).
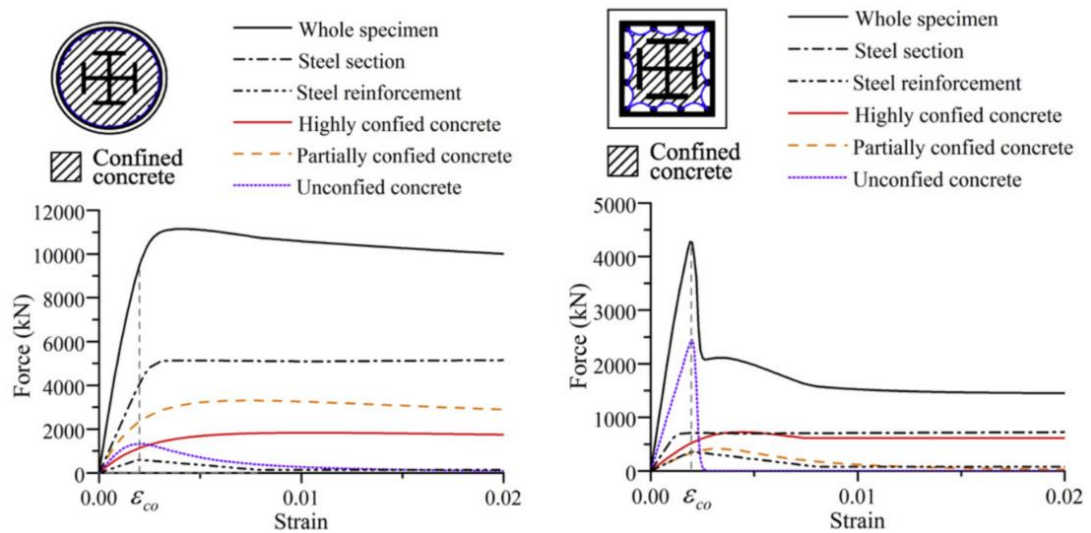
Figure 3.24 Axial loads of concrete-encased steel columns by analytical model of (Chen and Wu, 2017).

3.3 Simplified methods to predict axial compression of concrete-encased steel columns

In this section, squash load and simplified methods of Lai et al. (2019) are proposed.

3.3.1 Squash load method

Squash load method is a simplified method for predicting axial compressive load of stub columns. The model defined by assuming all material reaches its ultimate strength. The squash load method of CES columns defined to be

$$P_{squash} = A_s f_y + A_{sr} f_{ysr} + 0.85 A_c f_{co}'$$ (3.50)

Where

A_c = cross-sectional area of concrete;

A_s = cross-sectional area of structural steel;

A_{sr} = cross-sectional area of longitudinal rebar;

f_{co}' = compressive strength of concrete cylinder;

f_{ys} = yield stress of structural steel;

f_{ysr} = yield stress of longitudinal rebar.

3.3.2 Simplified methods of Lai et al. (2019)

In case of CES columns with high-strength concrete, Lai et al. (2019) found that the concrete cover had failure before the columns reaches peak load. The squash load method was adopts as shown to be

$$P_{squash} = A_s f_y + A_{sr} f_{ysr} + 0.85 A_{c,core} f_{co}'$$ (3.51)

Where

$A_{c,core}$ = cross-sectional area of core concrete.

3.4 Strength interaction diagram of CES columns

In this section, a unified approach of Lai et al. (2019) for developing the strength interaction diagram of CES columns based on strain compatibility method is proposed. Strength interaction diagram based on plastic stress distribution method is described in section 3.5.3.

3.4.1   A unified approach of Lai et al. (2019)

The section analysis by strip element method was performed, which was the same approach as ACI 318-14 method. The nonlinear material properties of concrete and steel were used. The CES section was discretized into a number of equally thickness strip element, as shown in Figure 3.25. Assumption of strain compatibility and linear strain distribution over the cross-section were used in this model. The longitudinal stress of each material components was obtained by using material constitutive relation. Axial force and bending moment capacity were calculated by combining the axial force and the bending moment about the geometric centroid of each strips. In addition, several assumptions used in strip element method were

1. Perfectly bonds about concrete and steel materials.
2. Plane section remains plane after deformation.
3. Tensile strength of concrete is small which can be neglected.
4. Initial residual stressed of steel is small which can be neglected.
5. Shear deformation of CES columns is small which can be neglected.
6. Effect of concrete confinement is carefully evaluated and include in analysis for well-confined CES columns, as shown in Figure 3.26.
7. Failure of the CES columns occurred when concrete reaches crushing strain.
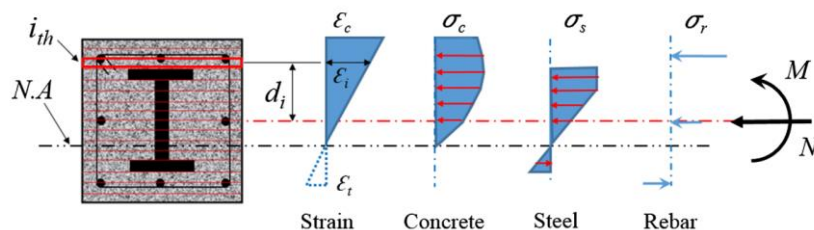
Figure 3.25 Determination of strength interaction diagram based on strip element method (Lai et al., 2019).
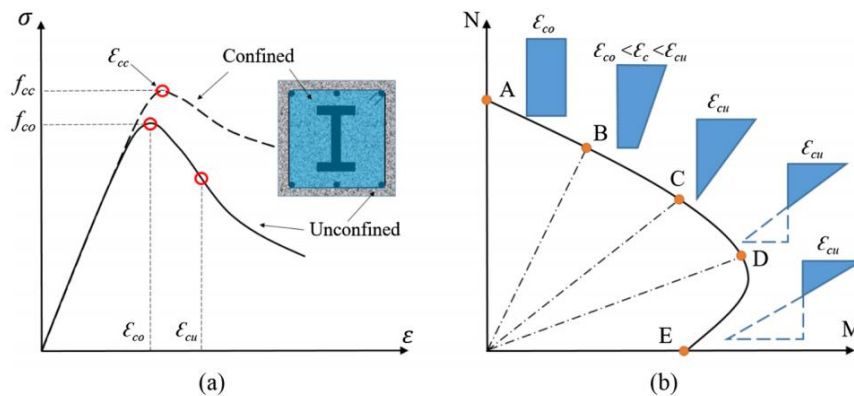
Figure 3.26 Concrete model used in strip element method (a) stress-strain relation of unconfined and confined concrete; (b) Different of strain gradient of concrete (Lai et al., 2019).

3.5 Design of concrete-encased steel columns by AISC 360-16

In this section, design of composite members by AISC 360-16 which reference some part of ACI 318-14 are proposed. This review focus on concrete-encased steel (CES) columns only.

3.5.1 General provision

The design provisions had limitations of material and section properties. The limitation of compressive strength of concrete is not less than 21 MPa (210 ksc) nor more than 69 MPa (700 ksc). The minimum yield stress of steel shall less than 525 MPa (5350 ksc) for structural steel and 550 MPa (5600 ksc) for reinforcement steel. The limitation of minimum longitudinal reinforcement steel section area is 0.4% of total section area. But the limitation of minimum longitudinal reinforcement steel section area is 1% of total section area in the ACI 318-14. The maximum spacing of transverse reinforcement steel is 300 mm for bar diameter to be 10 mm and 400 mm for bar diameter equal or larger than 13 mm. Minimum clear spacing between structural steel and longitudinal reinforcement steel shall be more than 1.5 of reinforcement bar diameters, but not less than 38 mm.

Nominal cross-section strength of the composite members is predicted by 4 methods as follows: plastic stress distribution method, strain compatibility method, elastic stress distribution method and effective stress-strain method.

The plastic stress distribution method is a general method for compact section. Material properties of concrete and steel are assumed to be rigid-plastic behavior under uniaxial force. The yield stress of steel material is to be yield stress in compression and tension. The compressive stress of concrete to be 0.85 of specified compressive strength in compression for CES columns and to be zero in tension.

The strain compatibility method is an alternative method for compact section. Strain in the cross-section is assumed to be a linear distribution. The maximum compressive strain of concrete is assumed to be 0.003 mm/mm. Material properties, stress-strain relationships of steel and concrete, shall be get from test results. Guidelines of the strain compatibility method are shown in AISC Design Guide 6 (1992) and ACI 318-14.

The elastic stress distribution method is a general method for composite beam with noncompact web. The nominal strength is determined from superposition of elastic stress of each material properties.

The effective stress-strain method is added method in this AISC 360-16 for noncompact and slender section. This method referenced strain compatibility method, but used effective stress-strain relationships of steel and concrete which considering effect of confinement of concrete and local buckling of steel.

3.5.2 Compressive strength

The nominal compressive strength of CES columns with double symmetric section and axially loaded is determined by considering flexural buckling behavior based on slenderness ratio of the columns as follows,

When $P_{no} / P_e \leq 2.25$

$$P_n = P_{no} \times 0.658^{P_{no} / P_e} \tag{3.52}$$

When $P_{no} / P_e > 2.25$

$$P_n = 0.877 P_e \tag{3.53}$$

Where

$$P_{no} = A_s f_y + A_{sr} f_{ysr} + 0.85 A_c f_{co}' \tag{3.54}$$

$$P_e = \pi^2 EI_{eff} / (KL)^2 \tag{3.55}$$

$$EI_{eff} = EI_s + E_s I_{sr} + C_1 E_c I_c \tag{3.56}$$

$$C_1 = 0.25 + 3\left(\frac{A_s + A_{sr}}{A_g}\right) \le 0.7 \tag{3.57}$$

A_g = total cross-sectional area;

E_c = elastic modulus of concrete;

E_s = elastic modulus of structural steel;

E_{sr} = elastic modulus of reinforcement bars;

EI_{eff} = effective flexural rigidity;

I_c = moment of inertia of concrete section about elastic neutral axis of composite section;

I_s = moment of inertia of structural steel section about elastic neutral axis of composite section;

I_{sr} = moment of inertia of longitudinal rebars about elastic neutral axis of composite section;

L = column length.

3.5.3 Strength interaction diagram

Four methods to determine the nominal strength of the CES columns subjected to combined axial and flexural force include interaction equations of section H1 of AISC 360-16, interaction curves from the plastic stress distribution method, method by design guide 6 and direct interaction method for noncompact and slender filled

sections. In this study, the interaction curves from the plastic stress distribution method is proposed because it is high accurate and appropriate with CES columns which does not consider local buckling of structural steel.

The interaction curves from the plastic stress distribution method is a section approach for double symmetric columns which determined by plastic stress distribution method. The interaction diagram of this method constructed by interpolated four points, point A – D, as shown in Figure 3.27. Point A is defined by pure axial compressive strength of composite columns. Point B is defined by flexural strength of composite columns. Point C is defined by corresponds to a plastic neutral axis location that determined by point B, but considering axial compression. Point D is defined by corresponds to one-half of axial compressive strength that determined by Point A.
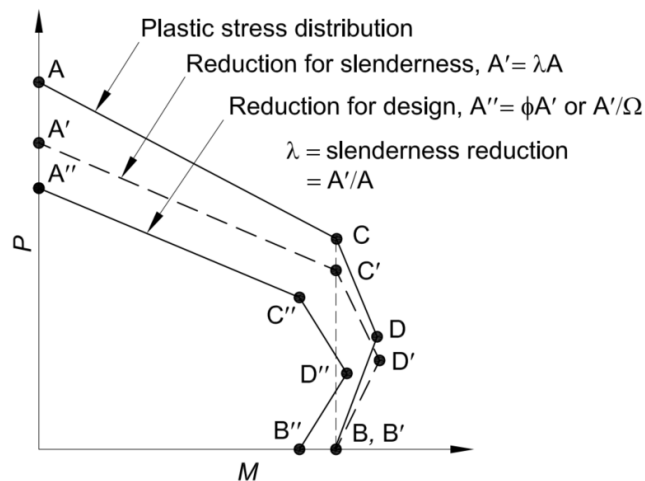
Figure 3.27 Interaction diagram by plastic stress distribution method of AISC 360-16.

3.6 Analytical load-deformation models of cellular steel columns

In this section, analytical models to predict behavior of steel columns with web openings under non-combined axial compression and bending moment, and under combined axial compression and bending of Najafi and Wang (2017) is described.

3.6.1 An analytical model of steel columns with web openings under axial compression and bending moment

For steel columns with web openings, section properties of a tee-section which it's a cross-section at the centerline of the opening as shown in Figure 3.28 (a) was used to calculate the axial compression and bending moment capacities. Three types of openings were proposed including circular, rectangular and elongated circular openings, as shown in Figure 3.28 (b).

(a)   (b)
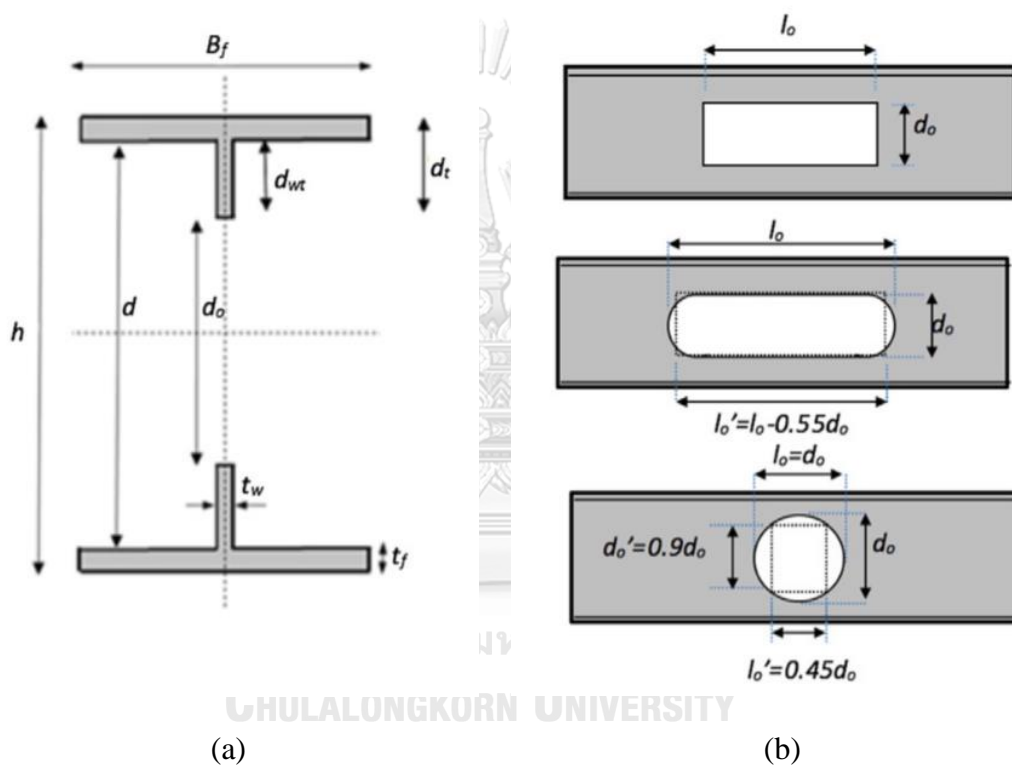
Figure 3.28 Tee-section, rectangular opening, elongated circular opening and circular opening (Najafi and Wang, 2017).

In case of steel columns with circular web openings, the tee-section of the circular openings was very short. Therefore, failure of the columns was plastic capacity of the tee-section. The plastic axial compressive capacity and plastic bending moment capacity of the steel columns with circular openings were given as follows, For plastic axial compressive capacity

$$N_{o,pl} = A_{s,net} f_y \qquad (3.58)$$

For plastic bending moment capacity

$$M_{o,pl} = Z_{x,o} f_y = \left(Z_x - \frac{D_o^2 t_w}{4} \right) f_y = M_{pl} - \frac{D_o^2 t_w}{4} f_y \tag{3.59}$$

Where

$A_{s,net}$ = cross-section area of tee-section;

$Z_{s,o}$ = plastic section modulus of cross-section at opening about x axis.

3.6.2 An analytical model of steel columns with web openings under combined axial compression and bending moment

In case of steel columns with web openings under combined axial compression and bending moment as shown in Figure 3.29, plastic neutral axis (P.N.A.) of the cross-section of the tee-section was changed by the magnitude of the axial forces, as shown in Figure 3.30. The bending moment capacity was reduced by according to increasing of the axial force. The equations to compute the reduced plastic bending moment capacity were given as follows,

For P.N.A is in bottom web of tee-section

$$M_{sd} = M_{o,pl} \left[1 - \frac{A_{s,net}^2}{4 t_w Z_{x,o}} \left(\frac{N_{sd}}{N_{o,pl}} \right)^2 - \frac{A_o D_o}{2 Z_{x,o}} \left(\frac{N_{sd}}{N_{o,pl}} \right) \right] \tag{3.60}$$

For P.N.A is in bottom flange of tee-section

$$M_{sd} = M_{o,pl} \frac{A_{s,net} \left(0.5 d_g - 0.5 t_f \right)}{Z_{x,o}} \left[1 - \frac{N_{sd}}{N_{o,pl}} \right] \tag{3.61}$$

Where

$$N_{sd} = \left(\left(d_g - D_o \right) t_w - 2 d_{Nf} b_f \right) f_y \tag{3.62}$$

d_{Nf} = height of flange thickness subjected to axial compressive force;

M_{sd} = reduced plastic bending moment capacity;

N_{sd} = axial compressive force.
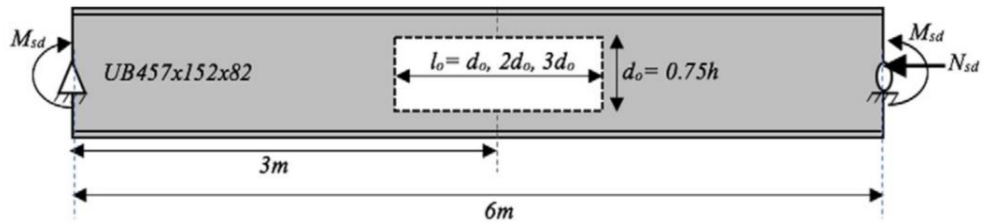
Figure 3.29 Column with web opening under combined axial compression and moment (Najafi and Wang, 2017).

Details of derived reduced plastic bending moment capacity were shown in Najafi and Wang (2017). Examples of strength interaction diagrams shown in Figure 3.30. The figure shown that the prediction had high accuracy in circular opening.
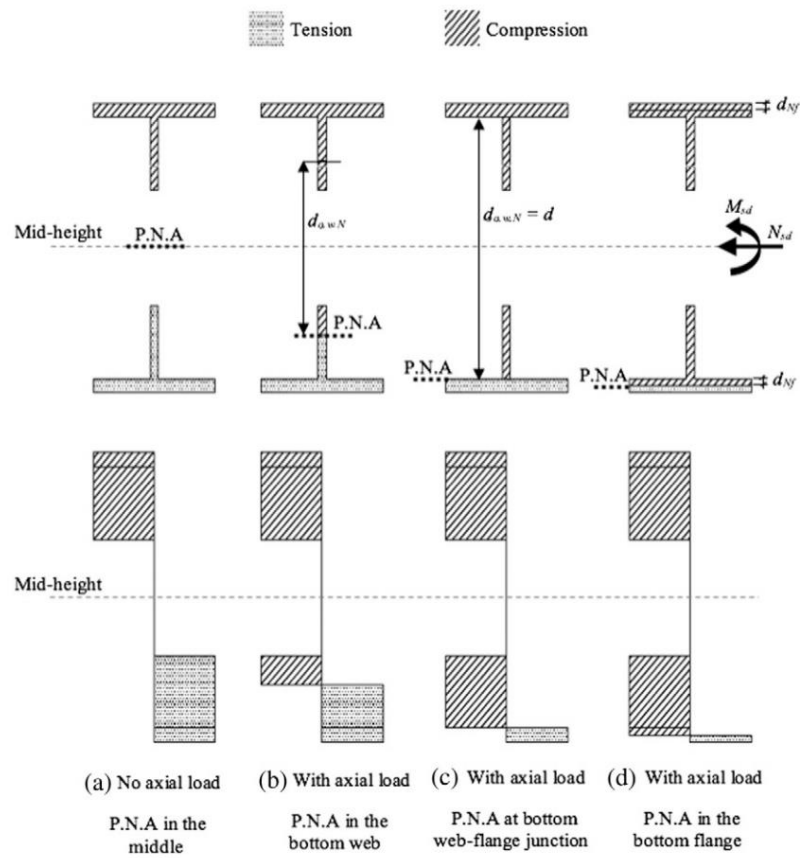
Figure 3.30 Plastic interaction of axial force and bending moment in tee-section (Najafi and Wang, 2017).
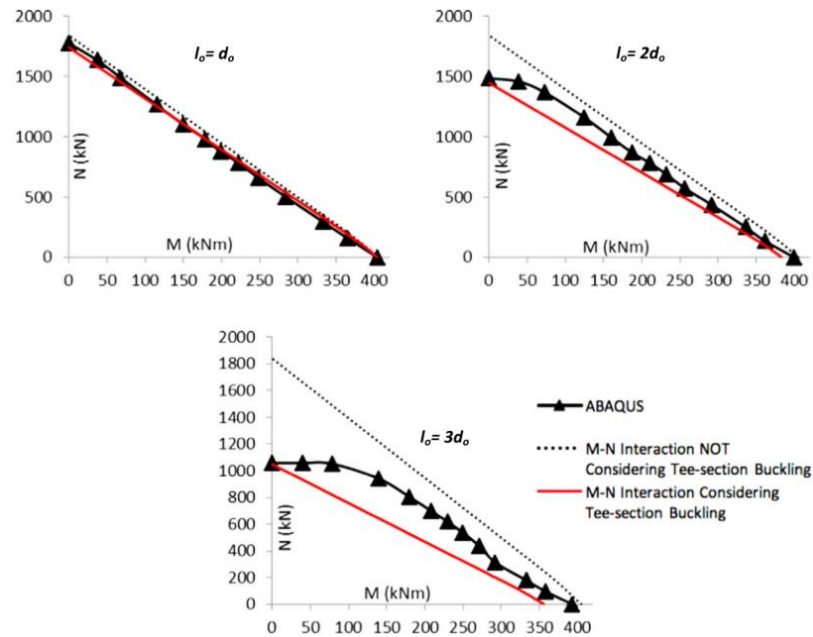
Figure 3.31 Interaction diagrams of section UB457x152x82 (Najafi and Wang, 2017).

3.7 Design of cellular steel beams by AISC design guide 2 (1992)

In this section, design of steel beam with web opening by AISC design guide 2 (1992) is proposed. Bending moment capacity of bare steel beam with circular web opening is described in this part.

3.7.1 Maximum moment capacity of steel beam with web opening

The bending moment capacity of a steel beam with web opening is to be

$$M_n = M_{pl} \left[1 - \frac{A_{s,hole}\left(\dfrac{D_o}{4} - e\right)}{Z_{s,g}} \right] \tag{3.63}$$

Where

$$A_{s,hole} = D_o t_w \tag{3.64}$$

$$M_{pl} = f_y Z_{s,g} \tag{3.65}$$

D_o = hole diameter of cellular column;

e = eccentricity of opening;

t_w = web thickness of structural steel;

f_y = specified minimum yield stress of steel;

$Z_{s,g}$ = plastic section modulus of gross section about x axis.

3.8 Design of cellular steel beams by AISC design guide 31 (2016)

In this section, design of cellular steel members by AISC design guide 31 was proposed. The proposed design guide was focus on cellular steel beam. At present, the proposed design guide was lack of method to design of cellular steel columns. Therefore, the proposed design guide of cellular steel beam was proposed.

The cellular beams had limit states as follows,

1. Vierendeel moment of tee
2. Local buckling and compactness
3. Axial compression and tension
4. Flexural strength of Beam
5. Buckling of web post
6. Horizontal shear
7. Vertical shear
8. Lateral-torsional buckling

This review focused on Vierendeel moment of tee, axial compressive strength, axial tensile strength, flexural strength, and combined flexural and axial force of non-composite cellular beam only.

3.8.1 Vierendeel moment

Vertical global shear force at the openings was the cause of Vierendeel moment. The shear force increases the internal moment in the top and bottom tee-sections. This failure occurred from plastic hinges at the comers of the openings and checked from global moment and shear in all openings. Three steps to check the Vierendeel moment failure was given as follows,

1. Calculate axial forces in the top and bottom tees due to global moment; and, calculate Vierendeel moment at each opening due to global shear.

2. Calculate axial tensile and compressive strength of the tees using Chapter D and E of AISC360-16 and calculate flexural strength of the tee section using Chapter F of AISC360-16.

3. Check the failure of combined axial force and Vierendeel moment using Chapter H of AISC360-16.

Equations to calculate the axial forces in the top and bottom tees due to global moment, as shown in Figure 3.32, and Vierendeel moment at each opening due to global shear, as shown in Figure 3.33, were given as follows,

For axial forces due to global moment

$$P_r = \frac{M_r}{d_{effec}}$$
(3.66)

For Vierendeel moment due to global shear

$$M_{vr} = V_r \left(\frac{A_{tee}}{A_{s,net}} \right) \left(\frac{D_o}{2} \right)$$
(3.67)

Where

A_{tee} = area of tee-section;

d_{effec} = distance between centroids of bottom and top tee;

M_r = require flexural strength;

V_r = require shear strength.
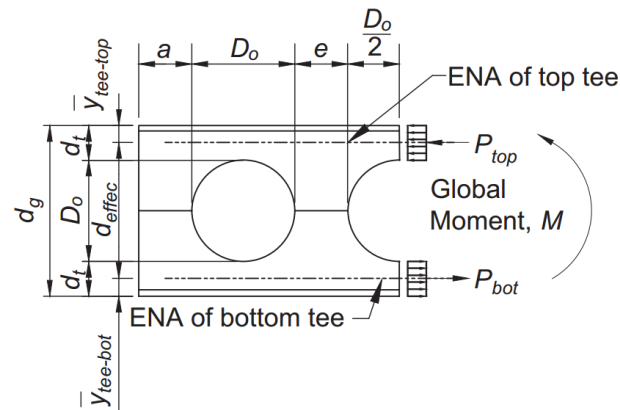
Figure 3.32 Axial forces in the top and bottom tees due to global moment
(AISC design guide 31, 2016).
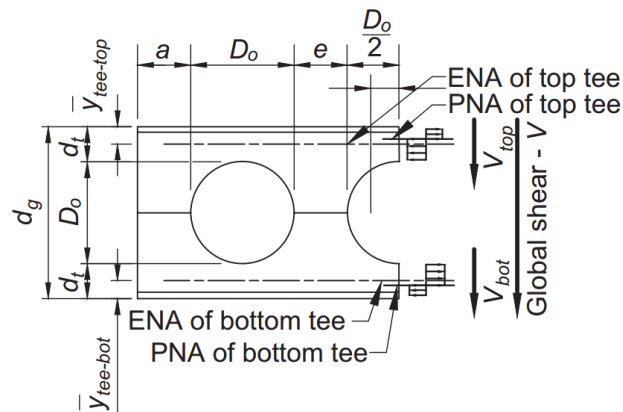
Figure 3.33 Vierendeel moment at each opening due to global shear
(AISC design guide 31, 2016).

3.8.2 Axial compressive strength of tee

Nominal compressive strength of tee section was lowest of limit states of flexural buckling and flexural-torsional buckling. This section focuses on calculation of nominal compressive strength for checking Vierendeel failure. Section properties of the tee-sections were given as follows,

E_s = 200,000 MPa.

G_s = 77,200 MPa.

K_x = 0.65 (Fixed-free condition).

K_y = 1.0

L =   Lateral unbraced length.

$$L = {D_o}\big/{2} \tag{3.68}$$

L_c =   Effective length.

$$L_c = \begin{cases} K_x L \\ K_y L \end{cases} \tag{3.69}$$

For limit states of flexural buckling, the nominal compressive strength of tee-section depended on slenderness of elements of the tee-section. If the tee-section member without slender element, the calculations using section E3 of AISC360-16 were given as follows,

$$P_n = F_{cr} A_g \tag{3.70}$$

$$A_g = A_{s,net} \tag{3.71}$$

When $\dfrac{L_c}{r} \leq 4.71\sqrt{\dfrac{E_s}{f_y}}$ or $\dfrac{f_y}{F_e} \leq 2.25$

$$F_{cr} = \left(0.658^{\frac{f_y}{F_e}}\right) f_y \tag{3.72}$$

When $\dfrac{L_c}{r} > 4.71\sqrt{\dfrac{E_s}{f_y}}$ or $\dfrac{f_y}{F_e} > 2.25$

$$F_{cr} = 0.877 F_e \tag{3.73}$$

$$F_e = \frac{\pi^2 E_s}{\left(\dfrac{L_c}{r}\right)^2} \tag{3.74}$$

Where

r = minimum of r_x and r_y.

If the tee-section member with slender element, section E3 of AISC360-16 was used to calculate critical stress.

For limit states of flexural-torsional buckling, section E4 of AISC360-16 was used to calculate nominal compressive strength of tees. The nominal compressive strength (P_n) was calculated according to Equation 3.70 and critical stress (F_{cr}) according to Equation 3.72-3.73. The equations to calculate flexural-torsional buckling stress (F_e) were given as follows,

$$F_e = \left(\frac{F_{ey} + F_{ez}}{2H} \right) \left[1 - \sqrt{1 - \frac{4F_{ey}F_{ez}H}{\left(F_{ey} + F_{ez}\right)^2}} \right] \tag{3.75}$$

$$F_{ey} = \frac{\pi^2 E_s}{\left(\dfrac{L_{cy}}{r_y} \right)^2} \tag{3.76}$$

$$F_{ez} = \left[\frac{\pi^2 E_s C_w}{L_{cz}^2} + G_s J \right] \frac{1}{A_g \overline{r_o}^2} \tag{3.77}$$

$$H = 1 - \frac{x_o^2 + y_o^2}{\overline{r_o}^2} \tag{3.78}$$

$$L_{cx} = K_x L \tag{3.79}$$

$$L_{cy} = K_y L \tag{3.80}$$

$$L_{cz} = K_z L \tag{3.81}$$

$$\overline{r_o}^2 = x_o^2 + y_o^2 + \frac{I_x + I_y}{A_g} \tag{3.82}$$

Where

J =   torsion constant;

K_x and K_y = effective length factor about x and y axis;

K_z =   effective length factor about longitudinal axis;

x_o and y_o = coordinates in x and y axis of the shear center and centroid.

3.8.3   Axial tensile strength of tee

Section D2 in AISC360-16 was referred to determined nominal strength of tee-section. Equation to calculate the nominal tensile strength were given to be

$$P_n = f_y A_{s,net} \tag{3.83}$$

3.8.4   Flexural strength of tee

Nominal flexural strength (M_n) of tee section was lowest of limit states of yielding, local buckling of flange, local buckling of tee stems and lateral-torsional buckling. This section focuses on calculation of nominal compressive strength for checking Vierendeel failure. Section properties of the tee-sections were given as follows,

$$L_b = D_o \big/ 2 \tag{3.84}$$

Where

L_b =   Unbraced length.

E_s =   200,000 MPa.

G_s =   77,200 MPa.

For limit states of yielding, the nominal flexural strength of tee-section using section F9.1 of AISC360-16 was given to be

$$M_n = M_{pl} \tag{3.85}$$

Where

$$M_{pl} = M_y \tag{3.86}$$

$$M_y = f_y S_{x-tee} \tag{3.87}$$

$S_{x-tee} = $ modulus of elastic of tee-section about the x-axis.

    For limit states of lateral-torsional buckling, the nominal flexural strength of tee-section using section F9.2 of AISC360-16 was given as follows,

When $L_b \leq L_p$

$$M_n = M_{pl} \tag{3.88}$$

When $L_b < L_b \leq L_r$

$$M_n = M_{pl} - \left(M_{pl} - M_y\right)\left(\frac{L_b - L_p}{L_r - L_p}\right) \tag{3.89}$$

When $L_b < L_b \leq L_r$

$$M_n = M_{cr} \tag{3.90}$$

Where

$$L_p = 1.76 r_y \sqrt{\frac{E_s}{f_y}} \tag{3.91}$$

$$L_r = 1.95 \left(\frac{E_s}{f_y}\right) \frac{\sqrt{I_y J}}{S_x} \sqrt{2.36 \left(\frac{f_y}{E_s}\right) \frac{d_{tee} S_x}{J} + 1} \tag{3.92}$$

$$M_{cr} = \frac{1.95 E_s}{L_b} \sqrt{I_y J} \left(B + \sqrt{1 + B^2}\right) \tag{3.93}$$
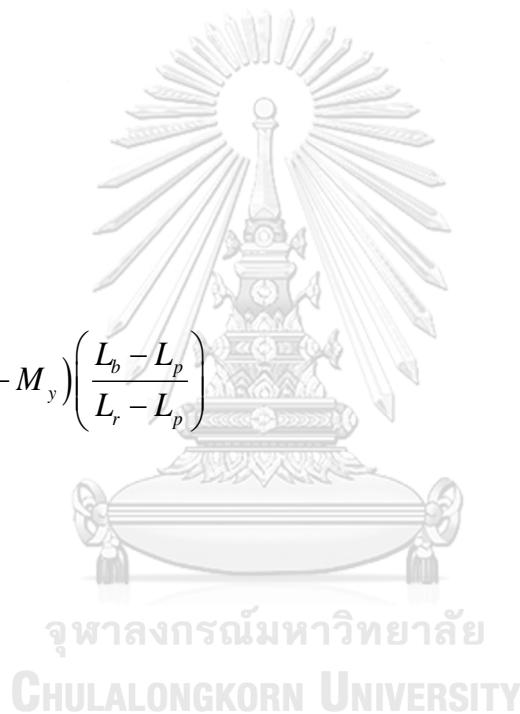
$$B = 2.3\left(\frac{d_{tee}}{L_b}\right)\sqrt{\frac{I_y}{J}} \tag{3.94}$$

For limit states of local buckling of flange, the nominal flexural strength of tee-section using section F9.3 of AISC360-16 is given as follows,

When flange section is a compact

$$M_n = M_y \tag{3.95}$$

When flange section is a noncompact

$$M_n = \left[M_{pl} - \left(M_{pl} - 0.7f_y S_{xc}\right)\left(\frac{\lambda - \lambda_{pf}}{\lambda_{rf} - \lambda_{pf}}\right)\right] \le 1.6M_y \tag{3.96}$$

When flange section is a slender section

$$M_n = \frac{0.7E_s S_{xc}}{\left(\dfrac{b_f}{2t_f}\right)} \tag{3.97}$$

Where

S_{xc} = elastic section modulus of compression flange about x-axis.

$$\lambda = \frac{b_f}{2t_f} \tag{3.98}$$

λ_{pf} = slenderness limit of compact flange;

λ_{rf} = slenderness limit of noncompact flange.

For limit states of local buckling of tee stems, the nominal flexural strength of tee-section using section F9.4 of AISC360-16 was given as follows,

$$M_n = F_{cr} S_x \tag{3.99}$$

When $\dfrac{d_{tee}}{t_w} \le 0.84 \sqrt{\dfrac{E_s}{f_y}}$

$$F_{cr} = f_y \tag{3.100}$$

When $0.84 \sqrt{\dfrac{E_s}{f_y}} < \dfrac{d_{tee}}{t_w} \le 1.52 \sqrt{\dfrac{E_s}{f_y}}$

$$F_{cr} = \left(1.43 - 0.515 \dfrac{d_{tee}}{t_w} \sqrt{\dfrac{f_y}{E_s}} \right) f_y \tag{3.101}$$

When $\dfrac{d_{tee}}{t_w} > 1.52 \sqrt{\dfrac{E_s}{f_y}}$

$$F_{cr} = \dfrac{1.52 E_s}{\left(\dfrac{d_{tee}}{t_w} \right)^2} \tag{3.102}$$

3.8.5 Check tees under combined flexural and axial force

For check tees under combined flexural and axial force, equation of interaction of combined flexural and axial force in section H1 of AISC360-16 was given as follows,

When $\dfrac{P_r}{P_c} \ge 0.2$

$$\dfrac{P_r}{P_c} + \dfrac{8}{9} \left(\dfrac{M_{rx}}{M_{cx}} + \dfrac{M_{ry}}{M_{cy}} \right) \le 1.0 \tag{3.103}$$

When $\dfrac{P_r}{P_c} < 0.2$

$$\frac{P_r}{2P_c} + \left(\frac{M_{rx}}{M_{cx}} + \frac{M_{ry}}{M_{cy}} \right) \leq 1.0 \tag{3.104}$$

Where

M_{cx} = available flexural strength about x axis;

M_{cy} = available flexural strength about y axis;

M_{rx} = flexural moment about x axis;

M_{ry} = flexural moment about y axis;

P_c = available axial strength;

P_r = axial force.

CHAPTER 4
EXPERIMENTAL PROGRAM

4.1 Experimental program

In the experimental program, the bare steel and composite columns were tested under concentric and eccentric loadings. The bare steel columns consisted of the cellular steel columns and hot-rolled wide-flange steel column, so-called "parent columns". The composite columns consisted of CECS columns and CES columns. The CES columns used the parent steel shape, while the CECS used the cellular steel shapes. The parent steel member was a hot-rolled wide-flange shape with the flange width (b_f) of 150 mm, total depth (d) of 150 mm, web thickness (t_w) of 7 mm, and flange thickness (t_f) of 10 mm. The length-to-width ratios (L/b) were 4 and 3 for steel and composite columns, respectively.

The experimental program was divided into 2 parts. First part proposed the bare steel and the composite columns under concentric loadings. The objectives of the first part are as follows: 1) study the axial compressive behavior of cellular steel and CECS columns, 2) compare the axial compressive behavior of the cellular steel columns with the parent columns, 3) compare the axial compressive behavior of the CECS columns with the CES columns, 4) compare the axial compressive behavior of bare steel columns with the composite columns, 5) study the effect of design parameters on the axial compressive behavior of cellular steel and CECS columns

Second part proposed the bare steel and the composite columns under eccentric loadings. The objectives of the second part are as follows: 1) study compressive behavior of cellular steel and CECS columns subjected to eccentric loadings, 2) compare the eccentric compressive behavior of the cellular steel columns with the parent columns, 3) compare the eccentric compressive behavior of the CECS columns with the CES columns, 4) compare the eccentric compressive behavior of bare steel columns with the composite columns, 5) study the effect of design parameters on the eccentric compressive behavior of cellular steel and CECS columns

The test variables included the concrete strength, spacing of stirrups and cellular steel shape for concentric loading columns, and the cellular steel shape and load eccentricity for eccentric loading columns.

4.2 Concentric loading columns

4.2.1 Cellular steel columns subjected to concentric loadings

Table 4.1 shows the geometric properties of all tested steel columns subjected to concentric loadings. The dimensions of three cellular steel columns (ST-C1, ST-C2 and ST-C3) and the parent steel column (ST-W) are shown in Figure 4.1. The cross-section properties were calculated at the net section at the hole center and at the gross section (solid section). The column length (or height) was 600 mm.

Table 4.1 Geometric properties of cellular and parent steel columns subjected to concentric loadings.

Steel column	Nominal dimensions of steel column							Cross-sectional properties		Comparison $\left(\dfrac{\text{Cellular}}{\text{Parent}}\right)$	
	Hole diameter	Hole spacing	Loss	Total depth	Hole Spacing / Hole diameter	Total depth / Hole diameter	Weight per length	Net area	Gross area	Net area	Gross area
	D_o	S	$loss$	d_g	$\dfrac{S}{D_o}$	$\dfrac{d_g}{D_o}$	W_s	$A_{s,net}$	$A_{s,g}$	$A_{s,net}$	$A_{s,g}$
	mm	mm	mm	mm	-	-	N/m	cm^2	cm^2	-	-
	(1)	(2)	(3)	(4)	$\dfrac{(2)}{(1)}$	$\dfrac{(4)}{(1)}$	(5)	(6)	(7)	$\dfrac{(6)}{(6)^a}$	$\dfrac{(7)}{(7)^a}$
ST-W	-	-	-	150	-	-	309	40.15	40.15	-	-
ST-C1	90	126	10.0	185	1.40	2.06	300	36.30	42.60	0.90	1.06
ST-C2	75	126	22.5	165	1.68	2.20	298	35.95	41.20	0.90	1.03
ST-C3	90	108	10.0	185	1.20	2.06	296	36.30	42.60	0.90	1.06

[a] Based on the parent steel column (ST-W)
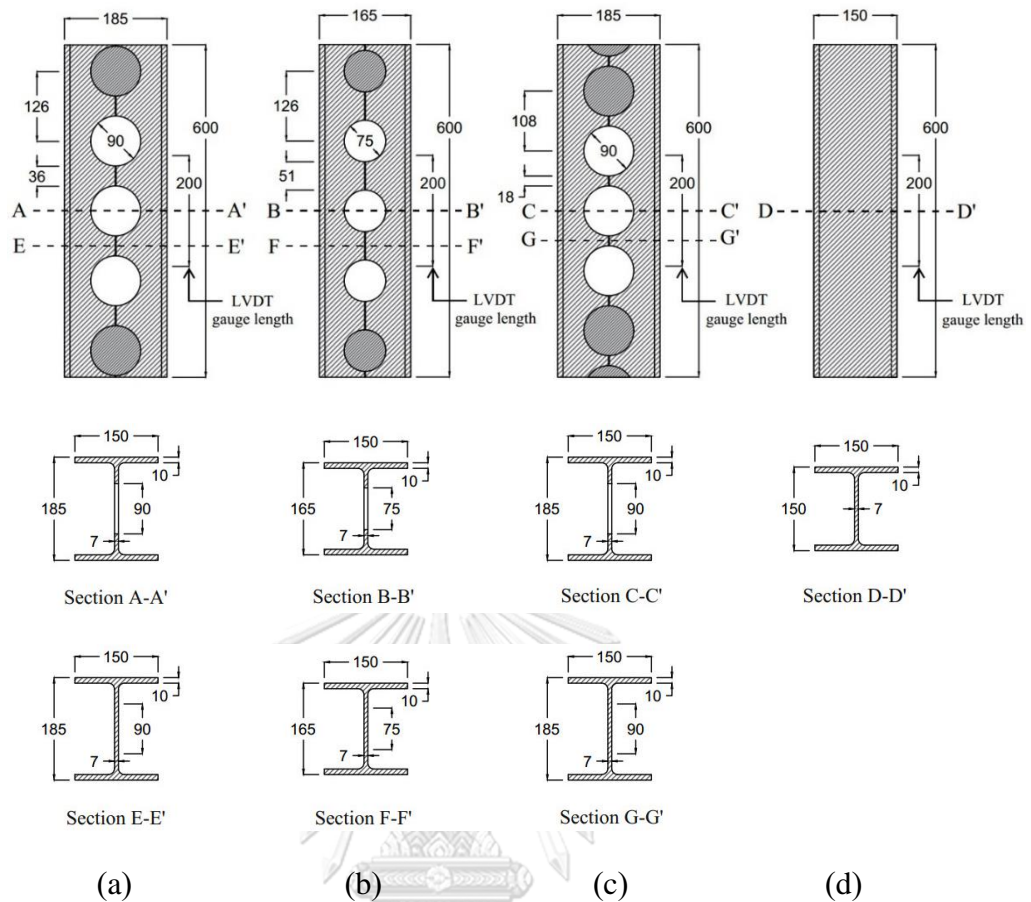
Figure 4.1 Tested steel columns (a) ST-C1; (b) ST-C2; (c) ST-C3; and (d) ST-W
(dimensions in mm).

Figure 4.2 shows the symbols used for parameters of the cellular steel columns. Figure 4.3 shows a of cellular steel column after welding process. The loss value was designed to control the total depth and hole spacing. The total depth (d_g) of the cellular steel column is

$$d_g = d + \frac{D_o}{2} - loss \qquad (4.1)$$

Where

D_o = hole diameter of cellular column;

d = total depth of steel column;

d_g = total depth of cellular steel column;

$loss$ = loss from fabrication of cellular steel column.

The hole diameters (D_o) ranged from 75 to 90 mm. In this study, the total depth-to-hole diameter (d_g / D_o) ratio ranged from 2.06 to 2.20. The hole spacing-to-hole diameter (S / D_o) ratio ranged from 1.20 to 1.68. It should be noted that the AISC design guide no. 31 recommends the d_g / D_o ratio between 1.25 and 1.75, and S / D_o ratio between 1.08 and 1.50 for the web post buckling behavior. The weight per length, moment of inertia, net cross-sectional area, and gross cross-sectional area of the cellular steel column are calculated from

$$W_{s,cellular} = \rho_s A_{s,parent} + \rho_s \left(d_g - d \right) t_w - \rho_s \left(\frac{\pi D_o^2}{4} \right) \left(\frac{t_w}{S} \right) \tag{4.2}$$

$$A_{s,net} = A_{s,parent} - \left(d - \left(d_g - D_o \right) \right) t_w \tag{4.3}$$

$$A_{s,g} = A_{s,net} + D_o t_w \tag{4.4}$$

Where

$A_{s,g}$ gross cross-sectional area of cellular steel member (at solid web section);

$A_{s,parent}$ cross-sectional area of parent steel column;

$A_{s,net}$ critical cross-sectional area of cellular steel member (at critical section, i.e., double tee section at hole middle, of cellular steel member);

S center-to-center hole spacing of cellular column;

t_w web thickness of structural steel;

$W_{s,cellular}$ weight per length of cellular steel column;

ρ_s density of steel.

(a)   (b)
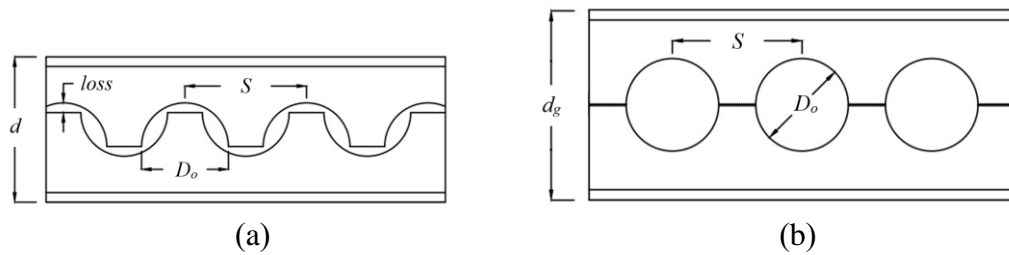
Figure 4.2 Parameters of cellular steel column (a) after cutting process;
and (b) after welding process.

Figure 4.3 Cellular steel column (specimen ST-C1) after welding process.

From Table 4.1, the weight per length of the cellular steel columns were slightly less than the parent column. The net and gross cross-sectional areas of three cellular columns were almost identical, i.e., 90 and about 106 % of the parent cross-sectional area. Therefore, the replacement of parent steel column with the cellular one reduces axial performance and slightly reduces the weight. However, the replacement of parent steel column with the cellular one can increase flexural performance, which discussed in section 4.3.1. The effects of hole configuration on the axial stiffness, yield load, and maximum loads under compression are discussed in section 5.1. In addition, the equivalent cross-sectional areas are proposed in section 6.1.

4.2.2 CECS columns subjected to concentric loadings

Table 4.2 shows the properties of all tested composite columns. The dimensions of all composite columns were 340×340 mm in cross section and 1100 mm in height. Figure 4.4 shows the typical reinforcement details of the CECS columns.

Four 15-mm-diameter round bars (RB15) were used as the corner longitudinal reinforcements. The longitudinal reinforcement ratio was 0.006. This value was slightly above the ANSI/AISC 360-16 minimum value of 0.004 for the CES columns. The 9-mm-diameter round bars (RB9) were used as the transverse reinforcements (closed stirrups). The maximum spacing used in this study was limited by the ANSI/AISC 360-16 maximum spacing requirement. The target compressive strength of concrete cylinders at 28 days was 21 MPa, the minimum limit specified by the ANSI/AISC360-16. The shear studs were not installed in all composite columns in this part. All sketches of tested composite columns are shown in Appendix A.

(a)   (b)
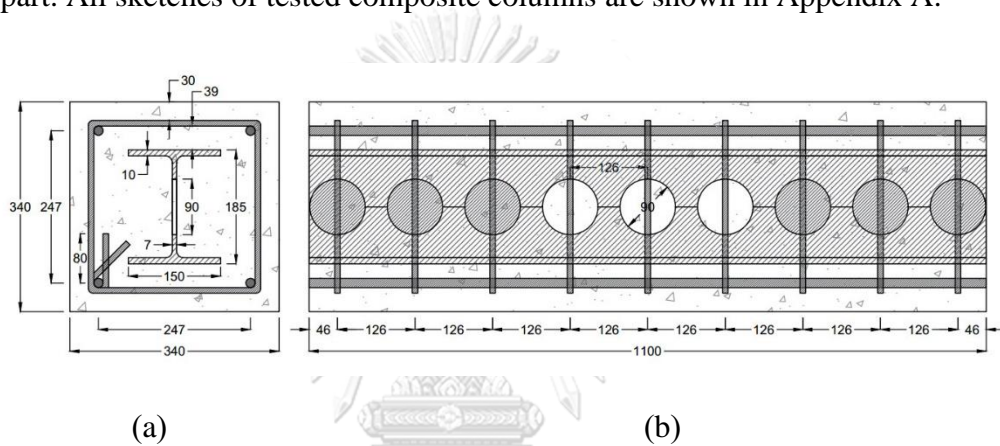
Figure 4.4 Typical reinforcement details of CECS column (column C1-126); (a) cross section; and (b) longitudinal section (dimensions in mm).

For the CECS composite columns (Figure 4.5), the parameters of cellular steel members were identical to the bare cellular steel columns in section 4.2.1. The cross-sectional properties were calculated at the net and gross section. As shown in section 4.2.1, the net and gross cross-sectional areas of three cellular members were almost identical, i.e., 90 and about 106 % of the parent cross-sectional area.

Figure 4.6 shows three components of the composite columns. All composite columns were prepared by casting concrete vertically. During the concrete casting into the timber formwork, a vibrator was used to remove air bubbles in the concrete and compact the concrete. After 24 hours, the formwork was dismantled. Subsequently, the columns were watered and covered with burlap. The standard concrete cylinders for the material property testing were also prepared using the same curing method.

Table 4.2 Properties of CECS and CES columns subjected to concentric loadings.

Composite columns	Geometric and material properties of composite column								Cross-sectional Properties	
	Structural steel	Hole diameter	Hole spacing	Total depth	Stirrup spacing	Concrete strength	Hole Spacing / Hole Diameter	Total depth / Hole diameter	Net area	Gross area
	-	D_o	S	d_g	s	f_{co}'	$\dfrac{S}{D_o}$	$\dfrac{d_g}{D_o}$	$A_{s,net}$	$A_{s,g}$
	mm	mm	mm	mm	mm	MPa	-	-	cm^2	cm^2
	(1)	(2)	(3)	(4)	(5)	(6)	$\dfrac{(3)}{(2)}$	$\dfrac{(4)}{(2)}$	(7)	(8)
W-170 (A)	W	-	-	150	170	20.1	-	-	40.15	40.15
C1-170 (A)	C1	90	90	185	170	20.1	1.40	2.06	36.30	42.60
C2-170 (A)	C2	75	75	165	170	20.1	1.68	2.20	35.95	41.20
C3-170 (A)	C3	90	90	185	170	20.1	1.20	2.06	36.30	42.60
W-170 (B)	W	-	-	150	170	18.3	-	-	40.15	40.15
C1-170 (B)	C1	90	90	185	170	18.3	1.40	2.06	36.30	42.60
C2-170 (B)	C2	75	75	165	170	18.3	1.68	2.20	35.95	41.20
C3-170 (B)	C3	90	90	185	170	18.3	1.20	2.06	36.30	42.60
W-126	W	-	-	150	126	20.1	-	-	40.15	40.15
C1-126	C2	75	75	165	126	20.1	1.68	2.06	36.30	42.60
C2-126	C1	90	90	185	126	20.1	1.40	2.20	35.95	41.20
C3-108	C3	90	90	185	108	20.1	1.20	2.06	36.30	42.60
W-63	W	-	-	150	63	22.9	-	-	40.15	40.15
C1-63	C1	90	90	185	63	22.9	1.40	2.06	36.30	42.60
C2-63	C2	75	75	165	63	22.9	1.68	2.20	35.95	41.20
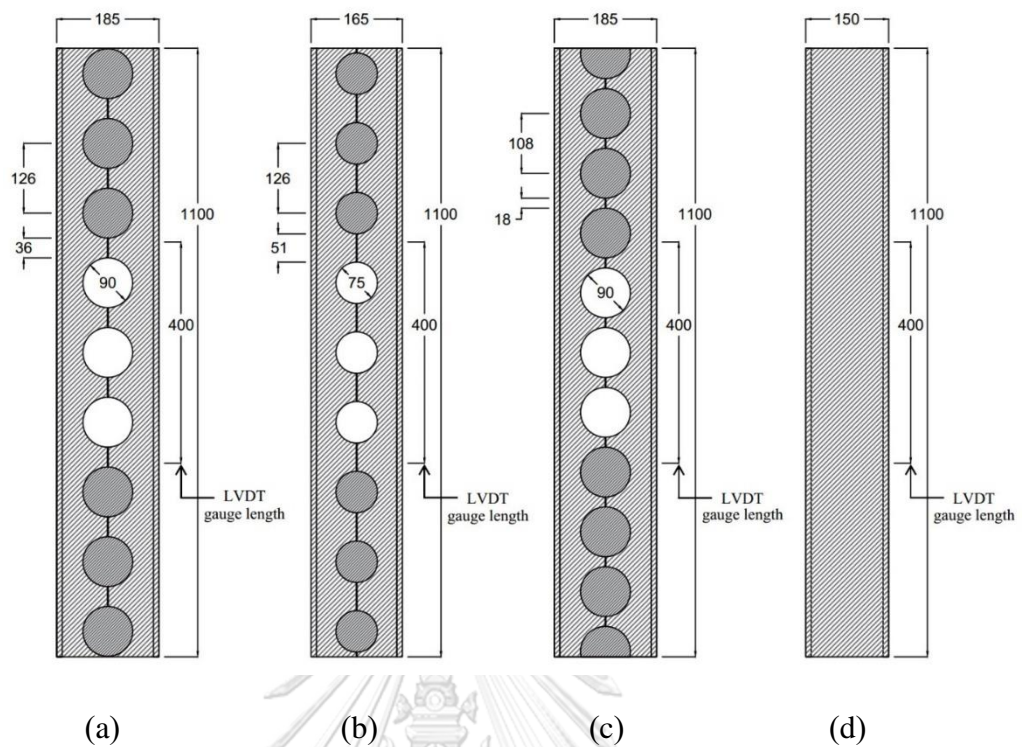
Figure 4.5 Dimensions of steel members in tested composite columns (a) C1; (b) C2; (c) C3; and (d) W (dimensions in mm).

Figure 4.6 Components of CECS composite column (a) cellular steel; (b) steel reinforcements; and (c) composite column after concrete encasement.

In addition, four reinforced concrete (RC) columns (RC-170, RC-126, and RC-63) were tested for comparing the axial compressive properties with the composite columns. Figure 4.7 shows the typical reinforcement details of the RC columns. The dimension, longitudinal reinforcement, and transverse reinforcement of

the RC columns were similar to the composite columns. The stirrup spacings of RC-170, RC-126, and RC-63 were 170, 126, and 63 mm, respectively. The concrete strength of RC-170, and RC-126 were 20.1 MPa. The concrete strength of RC-63 was 22.9 MPa. All sketches of tested composite columns are shown in Appendix A.

(a)   (b)
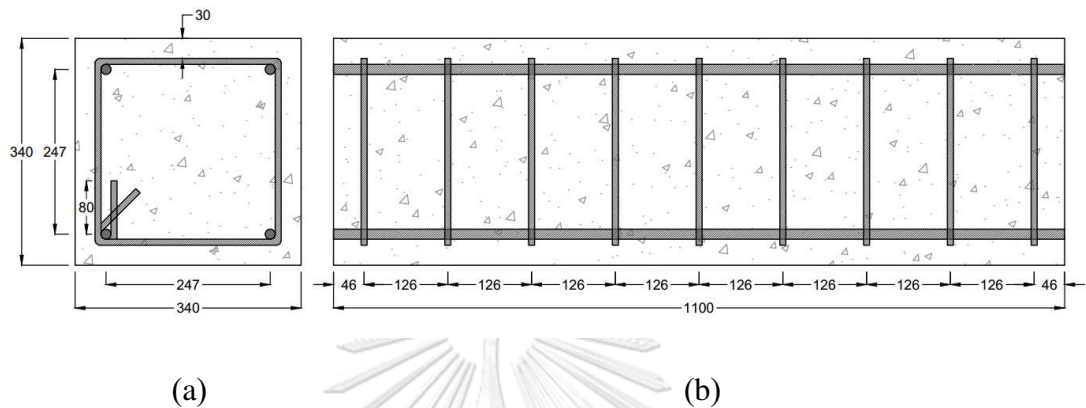
Figure 4.7 Typical reinforcement details of RC column (column RC-126);
(a) cross section; and (b) longitudinal section (dimensions in mm).

4.2.3 Material properties of concentric loading columns

A ready-mixed concrete with the maximum aggregate size of ¾ inch was used. The target compressive strength of concrete cylinder at 28 days was 21 MPa. The standard concrete cylinders with diameter of 150 mm and height of 300 mm, as shown in Figure 4.8 (a), were used. The average compressive strengths of the first batch concrete cylinders at 14 and 28 days were 18.3 and 20.1 MPa, respectively. The average compressive strength of the second batch concrete at 14 days was 22.9 MPa.

The structural steel column was the hot-rolled wide-flange steel shape. The chemical and mechanical properties conformed to TIS 1227, grade SS400. The tensile steel specimens were cut from both flange and web of the structural steel, as shown in Figure 4.8 (b). RB9 and RB15 were hot-rolled steel bars conformed to TIS 20, grade SR24. Three samples, as shown in Figure 4.8 (c), were tested. Table 4.3 shows the measured tensile properties of structural steel and rebars including the elastic modulus, yield stress, and ultimate tensile strength.

The butt welding was used to produce the cellular steel columns. The size of weld wire was 1.2 mm according to AWS A5.20 (E71T-1). The measured weld size was 10 mm.

(a)   (b)

(c)
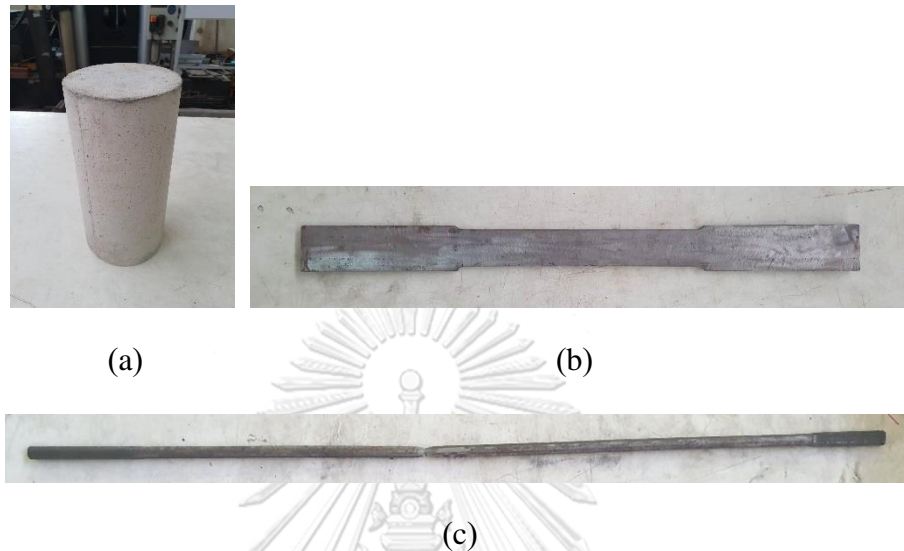
Figure 4.8 Material property testing; (a) concrete; (b) steel plate;
and (c) reinforcement bar.

Table 4.3 Measured tensile properties of structural steel and rebars.

Structural steel	Nominal thickness (mm)	Elastic modulus (GPa)	Yield stress (MPa)	Yield strain	Tensile strength (MPa)
Flange	10	204	306	0.00150	472
Web	7	211	311	0.00148	482
Rebars	Nominal diameter (mm)	Elastic modulus (GPa)	Yield stress (MPa)	Yield strain	Tensile strength (MPa)
$\phi15$	15.0	210	332	0.00158	522
$\phi9$	9.0	213	328	0.00154	471

4.2.4   Test setup and instrumentation of concentric loading columns

Figure 4.9 shows the test setup of the composite columns under concentric loadings. The 500-ton-capacity testing machine was used. An applied load was continuously recorded with the load cell positioned on the loading plate at the top of the tested column. Three Linear Variable Displacement Transducers (LVDTs) were used to measure the deformation response of the tested columns. The LVDT no.1 and

no.2 at front and back sides of each tested column were used to record the axial deformation over a gauge length of 400 mm at mid height. The LVDT no.3 was used to record the crosshead movement. The crosshead rate was controlled to be 0. 3 mm/min from the start to maximum loads, and 1.5 mm/min from the maximum loads to termination of the testing. The test was terminated when the applied load dropped to 70% of the maximum loads. The test setup of the bare steel columns (cellular and parent steel columns) was identical to the composite columns, except that the gauge length used for LVDT no.1 and no.2 was 200 mm, as shown in Figure 4.10.
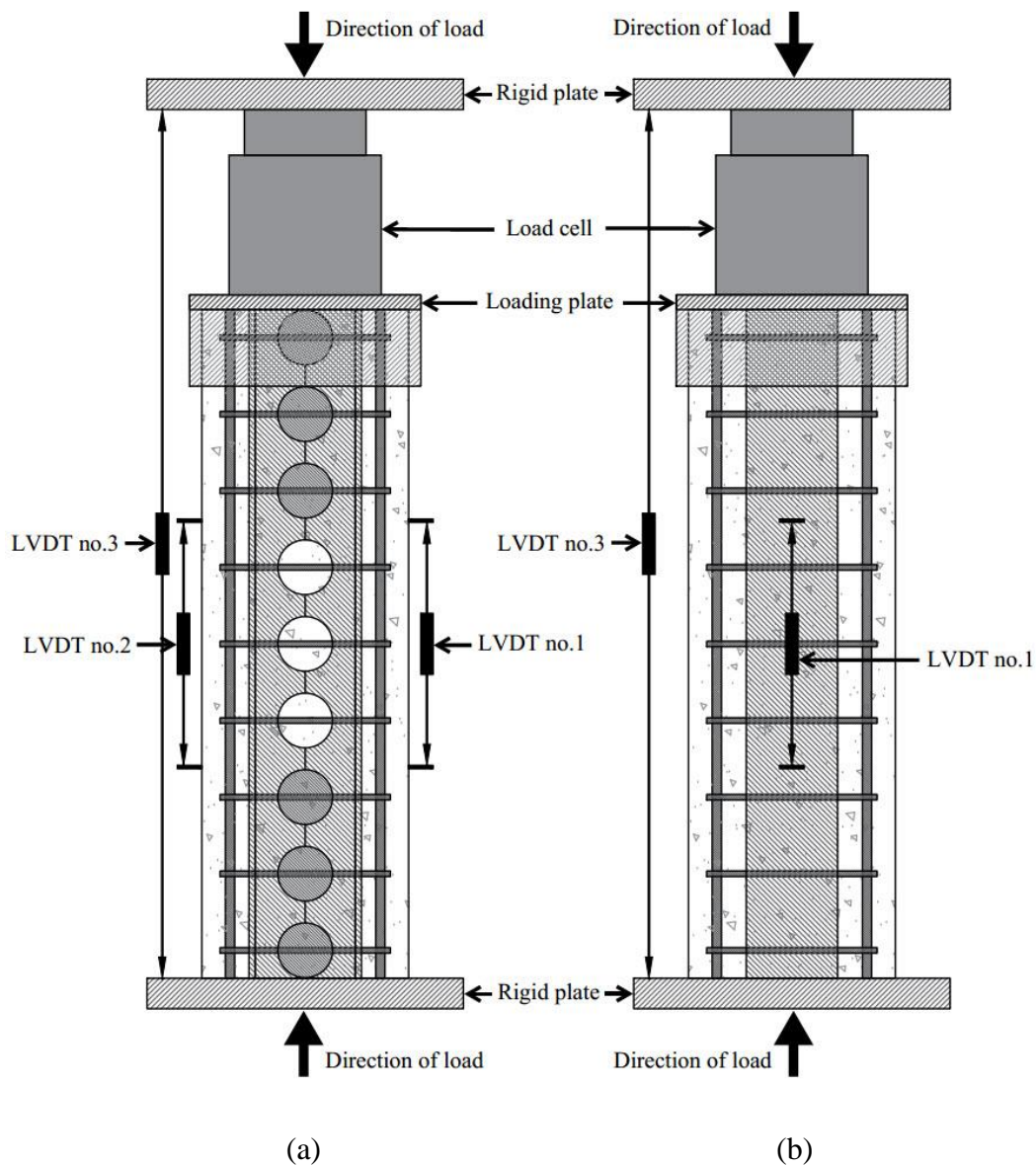
Figure 4.9 Static test setup of composite column under concentric loads;
(a) side view; and (b) front view.
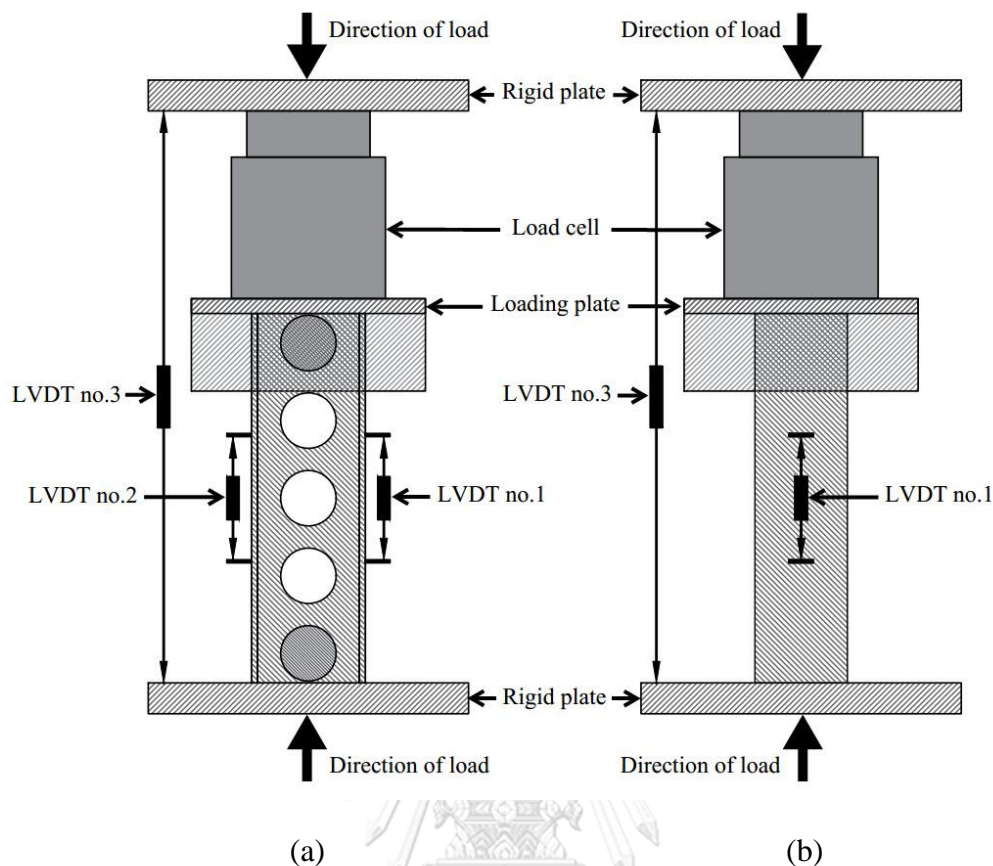
Figure 4.10 Static test setup of steel column under concentric loads;
(a) side view; and (b) front view.

Figure 4.11 (a) shows the location of strain gauges installed to capture the local strain response in both longitudinal and transverse directions of the steel columns (cellular and parent steel columns). In each column, eight strain gauges were installed. Four strain gauges in the longitudinal direction included SG1 and SG4 at the outside of both steel flanges and SG2 and SG3 at the steel web. Another four strain gauges in the transverse direction included SG5 and SG6 at the steel web; SG7 at the outside steel flange; and SG8 at the inside of the steel flange.

Figure 4.11 (b) shows the location of strain gauges in the composite column (CECS and CES columns). Twelve strain gauges were installed in each column. Four strain gauges in the longitudinal direction included SG1 and SG2 at outside of steel flange and SG3 and SG4 at outside of the longitudinal rebars. Another eight strain gauges in the transverse direction included SG7 and SG8 at the steel web; SG5, SG6, SG9, and SG10 at outside and inside of the steel flanges; and SG11 and SG12 at outside of the closed stirrup.

(a)

(b)
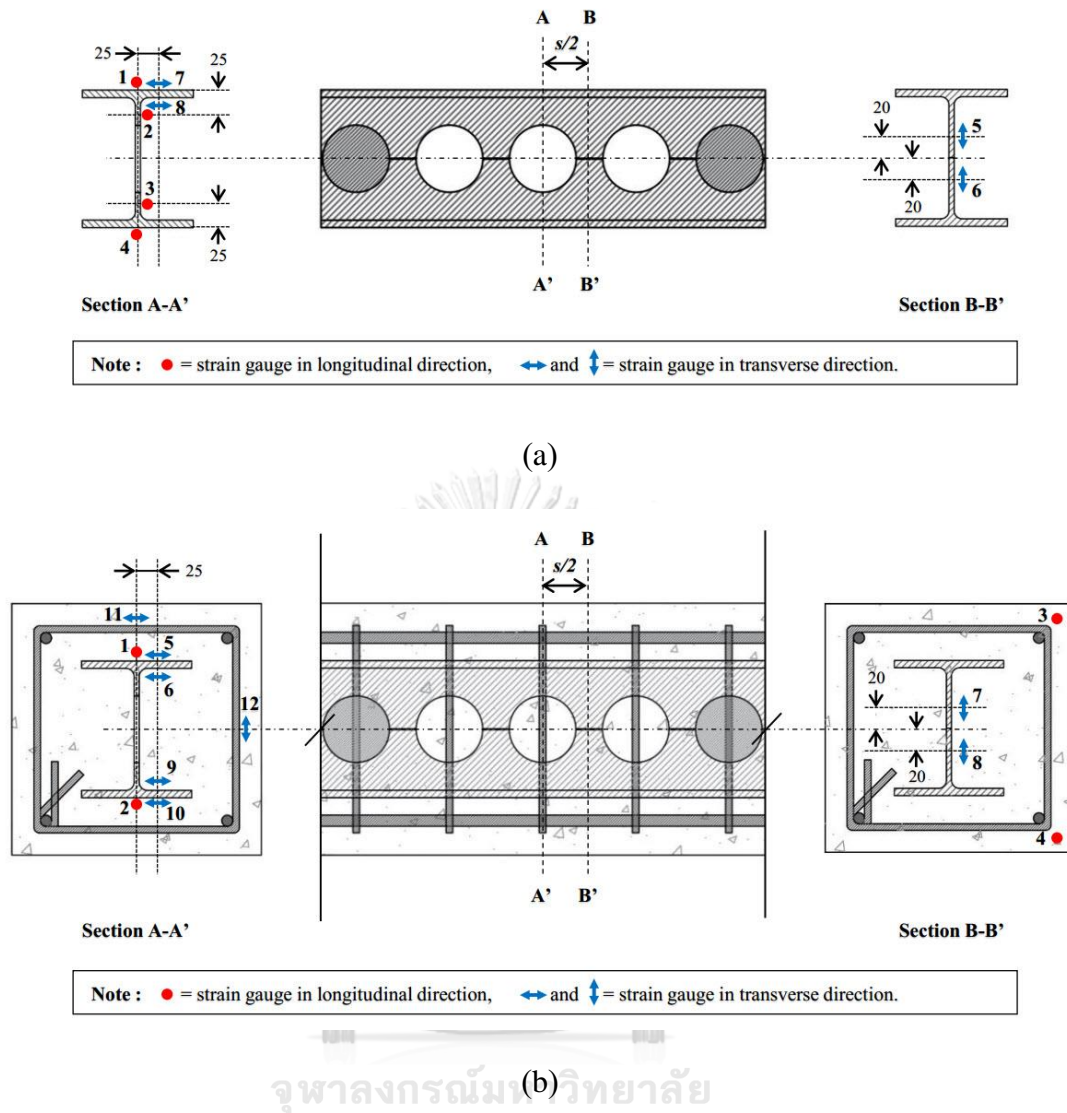
Figure 4.11 Location of strain gauges (a) cellular steel column; and (b) CECS
composite column subjected to concentric loadings (dimensions in mm).

4.3 Eccentric loading columns

4.3.1 Cellular steel columns subjected to eccentric loadings

In this part, three types of cellular steel columns and a parent steel column
were tested under two load eccentricity values (E1 and E2). All column properties
(hole diameter, hole spacing, hole spacing to diameter ratio, total depth to hole
diameter ratio and weight per length) are similar with the bare steel columns in
section 4.2.1. The load eccentricity E1 and E2 are 17.5 and 35 mm, respectively.

Table 4.4 shows the geometric properties of all tested steel columns subjected to eccentric loadings. The column length (or height) was 600 mm.

The moment of inertia of the cellular steel column, which the cross-section property was calculated at the net section at the hole center, are calculated from

$$I_{sx,cellular} = 2\left(\frac{b_f t_f^{\,3}}{12} + b_f t_f \left(\frac{d_g}{2} - \frac{t_f}{2} \right)^2 \right) + \left(\frac{t_w \left(d_g - 2t_f \right)^3}{12} \right) - \left(\frac{t_w D_o^{\,3}}{12} \right) \tag{4.5}$$

Table 4.4 Geometric properties of cellular and parent steel columns subjected to eccentric loadings.

Steel column	Nominal dimensions of steel column						Loading condition	Cross-sectional properties	Comparison $\left(\dfrac{\text{Cellular}}{\text{Parent}} \right)$
	Hole diameter	Hole spacing	Total depth	Hole Spacing / Hole diameter	Total depth / Hole diameter	Weight per length	Load eccentricity	Moment of inertia	Gross area
	D_o	S	d_g	$\dfrac{S}{D_o}$	$\dfrac{d_g}{D_o}$	W_s	E	I_{sx}	I_{sx}
	mm	mm	mm	-	-	N/m	mm	cm^2	-
	(1)	(2)	(3)	$\dfrac{(2)}{(1)}$	$\dfrac{(3)}{(1)}$	(4)	(5)	(6)	$\dfrac{(6)}{(6)^a}$
ST-W-E1	-	-	150	-	-	309	17.5	1640	-
ST-C1-E1	90	126	185	1.40	2.06	300	17.5	2519	1.54
ST-C2-E1	75	126	165	1.68	2.20	298	17.5	1958	1.19
ST-C3-E1	90	108	185	1.20	2.06	296	17.5	2519	1.54
ST-W-E2	-	-	150	-	-	309	35	1640	-
ST-C1-E2	90	126	185	1.40	2.06	300	35	2519	1.54
ST-C2-E2	75	126	165	1.68	2.20	298	35	1958	1.19
ST-C3-E2	90	108	185	1.20	2.06	296	35	2519	1.54

[a] Based on the parent steel column (ST-W-E1 and ST-W-E2)

From Table 4.4, the weight per length of the cellular steel columns were slightly less than the parent column. However, the tested cellular columns had the major-axis moment of inertia higher than the parent steel column from 19 to 54 %. Therefore, the replacement of parent steel column with the corresponding cellular one can increase the flexural performance and slightly reduce the weight. The effects of hole configuration and load eccentricity on the stiffness, yield load, and maximum loads of the cellular steel columns subjected to eccentric loadings are discussed in section 5.2.

4.3.2 CECS columns subjected to eccentric loadings

In this part, two types of CECS columns and one type of CES column were tested under two load eccentricity values (E1 and E2). The load eccentricity E1 and E2 were 35 and 70 mm, respectively. The typical reinforcement details of the CECS and CES are shown in Figure 4.12. The dimensions of all composite columns were 340×340 mm in cross section and 1100 mm in height. Four 15-mm-diameter round bars (RB15) were used as the corner longitudinal reinforcements. The 9-mm-diameter round bars (RB9) were used as the transverse reinforcements (closed stirrups). The spacing used in this study was 63 mm. The target compressive strength of concrete cylinders at 28 days was 21 MPa. The cellular and parent steel members used in this part were similar with the cellular and parent steel member in section 4.2.2. The shear studs were installed in all composite columns in this part.

Table 4.5 shows the geometric properties of all tested CECS and CES columns subjected to eccentric loadings. All sketches of tested composite columns are in Appendix A. The effective flexural rigidities of CECS and CES columns are calculated using the ANSI/AISC360-16 equations as follows,

$$EI_{eff} = E_s I_s + E_{sr} I_{sr} + C_1 E_c I_c \tag{4.6}$$

$$C_1 = 0.25 + 3\left(\frac{A_s + A_{sr}}{A_g}\right) \le 0.7 \tag{4.7}$$

Where

A_s = cross-sectional area of structural steel;

A_{sr} = cross-sectional area of longitudinal rebar;

A_g = total cross-sectional area;

E_c = elastic modulus of concrete;

E_s = elastic modulus of structural steel;

E_{sr} = elastic modulus of reinforcement bars;

I_c = moment of inertia of concrete section about elastic neutral axis of composite section;

I_s = moment of inertia of structural steel section about elastic neutral axis of composite section;

I_{sr} = moment of inertia of longitudinal rebars about elastic neutral axis of composite section;
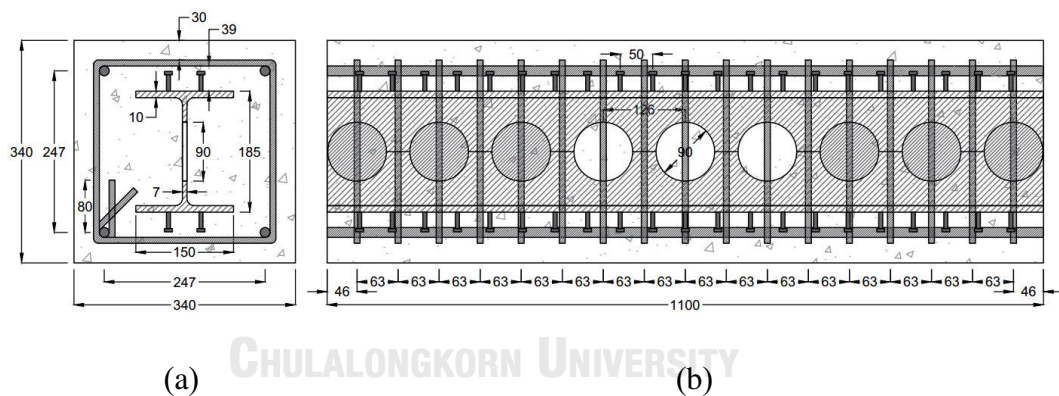
Figure 4.12 Typical reinforcement details of CECS column (column C1s-63);
(a) cross section; and (b) longitudinal section (dimensions in mm).

From Table 4.5, the tested CECS columns had the major-axis flexural rigidities higher than the CES columns from 2 to 12 %. Therefore, the replacement of CES with CECS columns can increase the moment capacity. The effects of hole configuration and load eccentricity on the stiffness, yield load and maximum loads of the cellular steel columns subjected to eccentric loadings are discussed in section 5.2.

The methods of welding process of the cellular specimens and preparing process of the composite specimens were similar with the specimens in section 4.2.

Table 4.5 Properties of CECS and CES columns subjected to eccentric loadings.

Composite column	Geometric and material properties of composite column								Loading condition	Cross-sectional properties
	Structural steel	Hole diameter	Hole spacing	Total depth	Stirrup spacing	Concrete strength	Hole Spacing / Hole Diameter	Total depth / Hole diameter	Load eccentricity	Effective flexural rigidity
	-	D_o	S	d_g	s	f_{co}'	$\dfrac{S}{D_o}$	$\dfrac{d_g}{D_o}$	E	EI_{eff}
	mm	mm	mm	mm	mm	MPa	-	-	cm2	cm2
	(1)	(2)	(3)	(4)	(5)	(6)	$\dfrac{(3)}{(2)}$	$\dfrac{(4)}{(2)}$	(7)	(8)
Ws-63	W	-	-	150	63	22.9	-	-	0	13657
C1s-63	C1	90	90	185	63	22.9	1.40	2.06	0	15112
C2s-63	C2	75	75	165	63	22.9	1.68	2.20	0	13992
Ws-63-E1	W	-	-	150	63	22.9	-	-	35	13657
C1s-63-E1	C1	90	90	185	63	22.9	1.40	2.06	35	15112
C2s-63-E1	C2	75	75	165	63	22.9	1.68	2.20	35	13992
Ws-63-E2	W	-	-	150	63	22.9	-	-	70	13657
C1s-63-E2	C1	90	90	185	63	22.9	1.40	2.06	70	15112
C2s-63-E2	C2	75	75	165	63	22.9	1.68	2.20	70	13992

4.3.3   Material properties of eccentric loading columns

In this part, used ready-mixed concrete, structural steel members and reinforced concrete members were similar to the specimens in the section 4.2. The target compressive strength of concrete cylinder at 28 days was 21 MPa. The standard concrete cylinders with diameter of 150 mm and height of 300 mm were used. The average compressive strength of the concrete cylinders at 14 days was 22.9 MPa. The structural steel column was the hot-rolled wide-flange steel shape. The chemical and mechanical properties conformed to TIS 1227, grade SS400. The RB9 and RB15 were hot-rolled steel bars conformed to TIS 20, grade SR24.

Because the used steel members in this research were small size members, the small size shear studs were specially ordered. Figure 4.13 shows the used shear stud. The shear studs were produced by lathing steel round bars, grade SS400. From measured properties, the yield stress was 439 MPa and tensile strength was 527 MPa.
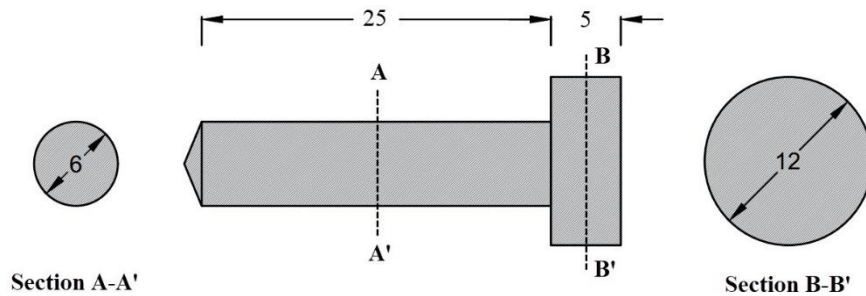
Figure 4.13 Sketch of shear stud (a) section A-A'; (b) longitudinal section; and (c) section B-B' (dimensions in mm).

4.3.4 Test setup and instrumentation of eccentric loading columns

Figure 4.14 and 4.15 show the test setup of the composite and steel columns under eccentric loadings, respectively. The 500-ton-capacity testing machine was used. An applied load was continuously recorded with the load cell positioned on the loading plate at the top of the tested column. Ball joints were added to apply the load eccentricity to the columns. For the tested steel columns, three Linear Variable Displacement Transducers (LVDTs) were used to record the crosshead movement. The LVDT no.1 and no.2 at front and back sides of each tested column were used to record the axial deformation over a gauge length of 200 mm at mid height. The LVDT no.3 was used to record the crosshead movement. For the tested composite columns, the only LVDT no.3 was used to record the crosshead movement. Because of safety of instruments, LVDT no.1 and no.2 were not used. The crosshead rate was controlled to be 0.3 mm/min from the start to maximum loads, and 1.5 mm/min from the maximum loads to termination of the testing. The test was terminated when the applied load dropped to 70% of the maximum loads.

(a)   (b)
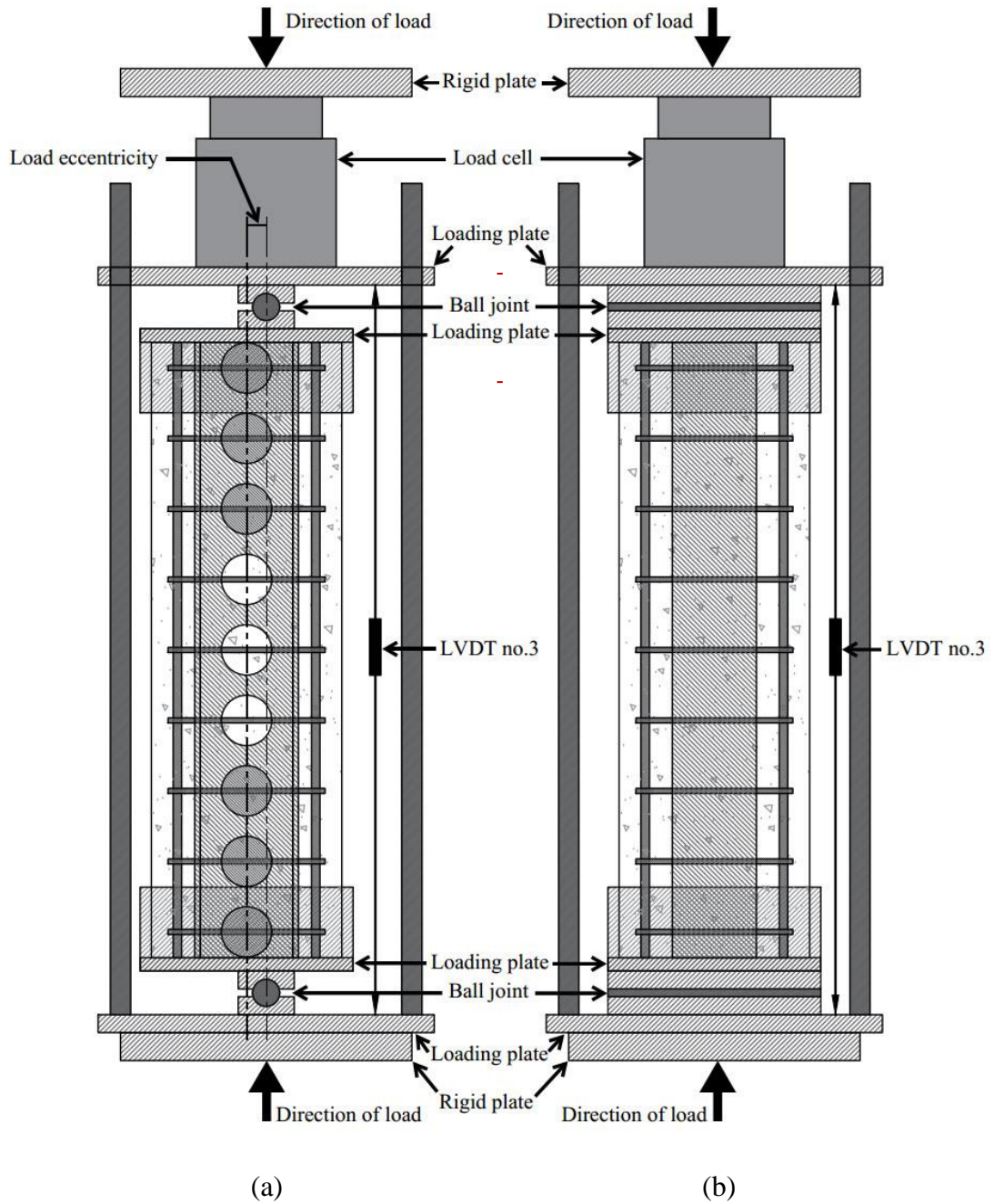
Figure 4.14 Static test setup of composite column under eccentric loads;
(a) side view; and (b) front view.
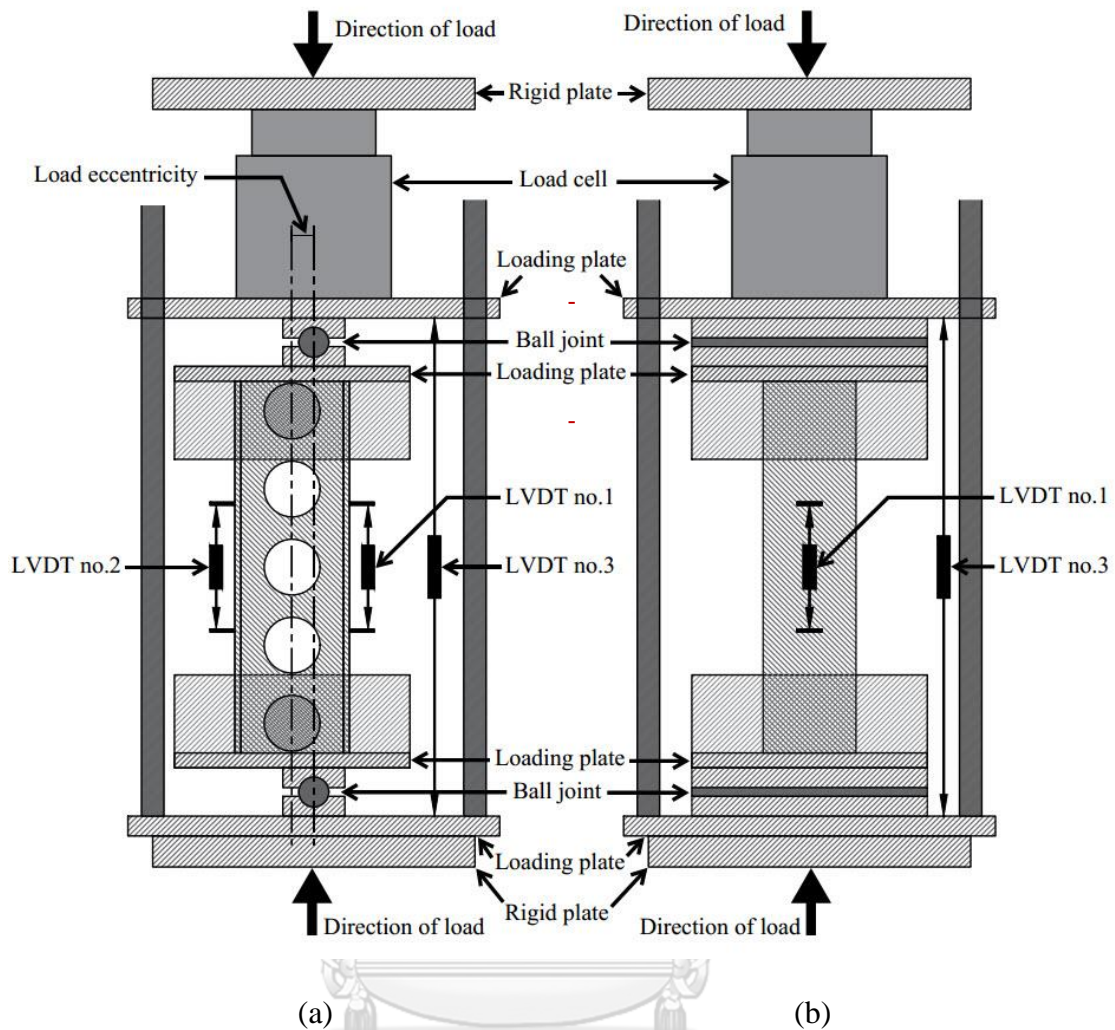
Figure 4.15 Static test setup of steel column under eccentric loads;
(a) side view; and (b) front view.

Figure 4.16 (a) shows the location of strain gauges installed to capture the local strain response in both longitudinal and transverse directions of the steel columns (cellular and parent steel columns). In each column, four strain gauges were installed. Two strain gauges in the longitudinal direction included SG1 and SG2 at the outside of both steel flanges. Another two strain gauges in the transverse direction included SG3 and SG4 at the steel web.

Figure 4.16 (b) shows the location of strain gauges in the composite column (CECS and CES columns). Fifteen strain gauges were installed in each column. Eight strain gauges in the longitudinal direction included SG1, SG2, SG3, and SG4 at outside of steel flanges and SG5, SG6, SG7, and SG8 at outside of the longitudinal rebars. Another five strain gauges in the transverse direction included SG9 and SG10

at the steel web and SG11, SG12, and SG13 at outside of the closed stirrup. Two strain gauges in the longitudinal direction included SG14 and SG15 at concrete surfaces.

(a)

(b)
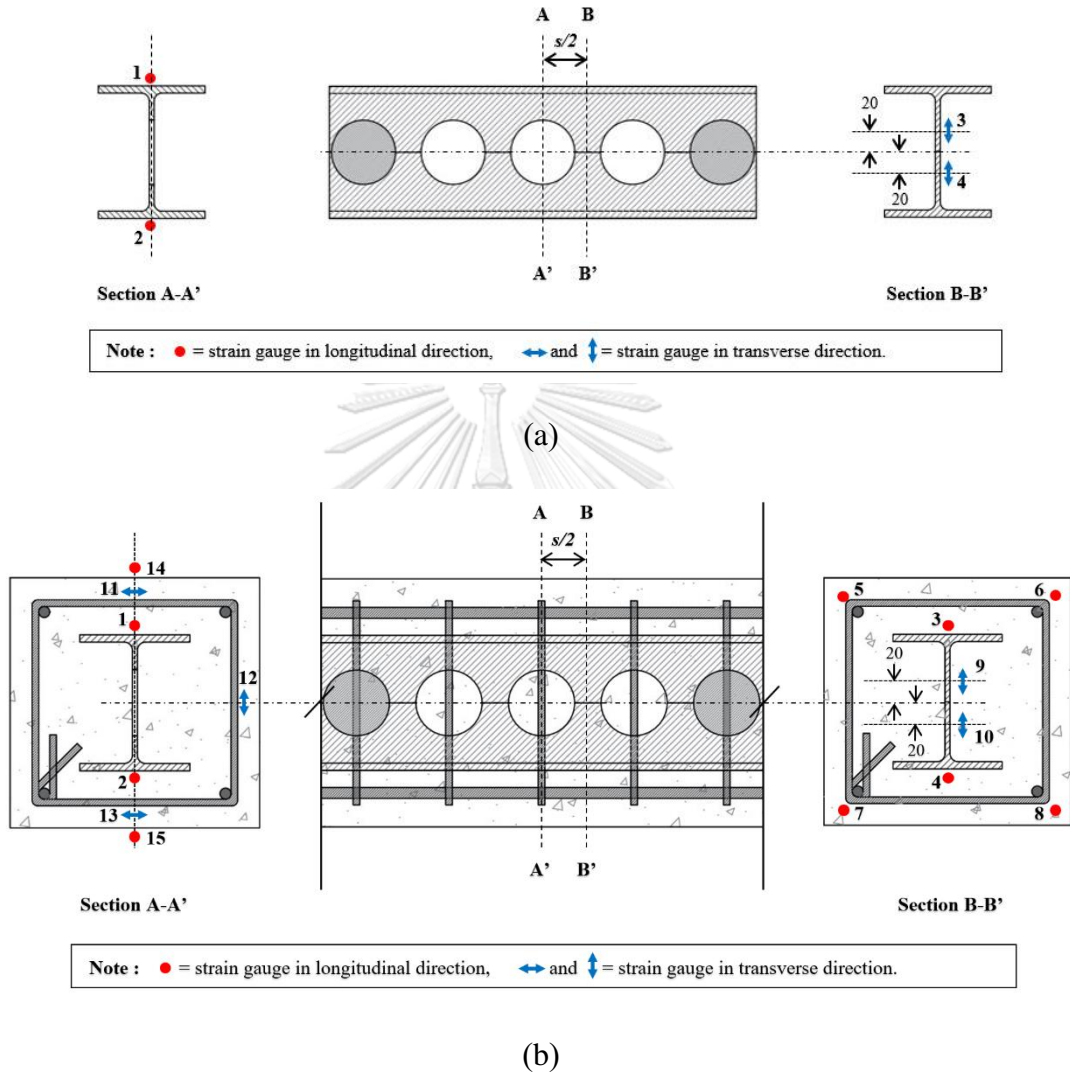
Figure 4.16 Location of strain gauges (a) cellular steel column; and (b) CECS composite column subjected to eccentric loadings (dimensions in mm).

CHAPTER 5
EXPERIMENTAL RESULTS

5.1 Experimental results of cellular steel columns subjected to concentric loadings

In this section, failure mode, load – deformation curves, load – axial strain curves, and load – transverse strain curves on axial compressive load of cellular steel columns subjected to concentric loadings are discussed.

5.1.1 Failure mode

Figure 5.1 shows the failure characteristics of bare steel columns. In the parent steel column (ST-W), the local buckling at the steel flanges occurred near mid-height after the yield point. In all cellular steel columns (ST-C1, ST-C2, ST-C3), both web and flange local buckling occurred at the hole section. No failure of weldment was observed.

| (a) | (b) | (c) | (d) |

Figure 5.1 Failure of steel columns (a) ST-C1; (b) ST-C2; (c) ST-C3; and (d) ST-W.

5.1.2 Load – deformation curves

Figure 5.2 shows a comparison of the load – deformation curves of the cellular steel columns (ST-C1, ST-C2 and ST-C3) with the parent steel column (ST-W). Similar to the parent column, all cellular steel columns exhibited yielding and hardening behavior. However, the hardening behavior became less obvious as hole

size increased. In addition, effect of residual stress on load – deformation curves are obvious in cellular steel columns with closely hole spacings only, as shown in zoom of Figure 5.2. The axial stiffness of cellular and parent steel calculated by initial slope of these curves are shown in Table 5.1. The comparison shows that the cellular steel columns have axial stiffness similar to the parent steel column.
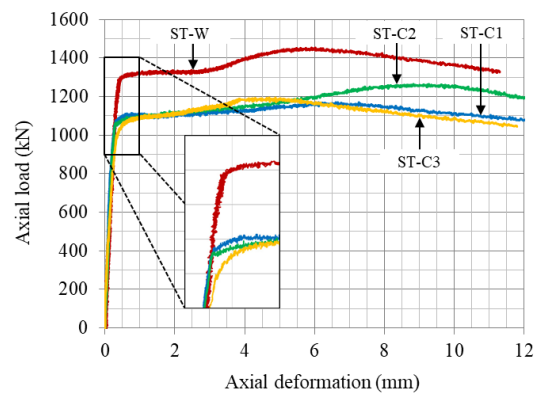
Figure 5.2 Load – deformation curves of bare steel columns ST-W, ST-C1, ST-C2, and ST-C3.

Table 5.1 Test results of bare steel columns subjected to eccentric loadings.

Columns	Experimental results				Comparison (Cellular / Parent)			
	Axial stiffness	Proportional limit load	Yield load	Maximum load	Axial stiffness	Proportional limit load	Yield load	Maximum load
	$(EA/L)_{exp}$	P_p	$P_{y, exp}$	P_{max}	$(EA/L)_{exp}$	P_p	$P_{y, exp}$	P_{max}
	MN/m	kN	kN	kN	MN/m	kN	kN	kN
	[1]	[2]	[3]	[4]	[1] / [1][a]	[2] / [2][a]	[3] / [3][a]	[4] / [4][a]
ST-W	4175	1214	1292	1453	-	-	-	-
ST-C1	4477	995	1094	1170	1.07	0.82	0.85	0.81
ST-C2	4114	994	1099	1264	0.99	0.82	0.85	0.87
ST-C3	4193	1035	1103	1194	1.00	0.85	0.85	0.82
Average					1.02	0.83	0.85	0.83

[a] Based on the parent steel column (ST-W).

5.1.3 Load – axial strain curves

Figure 5.3 shows the load – axial strain curves of the cellular steel columns (ST-C1, ST-C2 and ST-C3) and parent steel column (ST-W). The axial strain was measured from the strain gauges at steel flanges (SG 1 and SG 4), the strain gauges at steel web (SG 2 and SG 3) and LVDT (averages of LVDT 1 and LVDT 2).

From the strain gauges located at steel flanges, unlike the parent steel column, all cellular steel columns experienced a sudden reduction in axial strain at the hole center, i.e., the minimum (net) section, at the yield point. The sudden reduction indicates the onset of flange local buckling at the holes of the cellular steel columns.

From the strain gauges located at the steel web (SG 2 and SG 3), the captured strain of the web is more than the steel flanges at same load level. The difference levels are small in the parent column and are large in the cellular columns.

From the LVDT (averages of LVDT 1 and LVDT 2) curves, the measured axial deformation is transformed axial strain for comparing with the strain gauges. The initial slope measured by LVDT is similar to the strain gauges located at the steel flanges. In addition, the curves obtained from LVDT shows effect of residual stress more than the ones from strain gauges.

Because strain gauges SG 1 and SG 4 at the steel flanges were at the same position with those in the composite columns, they were chosen to evaluate the load at proportional limit, and yield load of all columns. In this study, the proportional limit denoted the point at 5% deviation from the initial slope. The yield point was based on the yield strain of steel specimens. Table 5.1 summarizes the test results of all bare steel columns.

From Table 5.1, the loads at proportional limit of all cellular columns ranged from 90 to 94 % of the yield load, while it was 94 % in a case of the parent column. This implies a comparable magnitude between residual stresses in the cellular steel columns and that in the parent column. A change in magnitude of residual stresses due to the cutting and welding processes was minimal. Also, the cellular columns had the proportional limit load, yield load, and maximum loads lower than the corresponding values of the parent column. The cellular columns ST-C1 (90-mm-diameter holes and 126-mm-spacing holes) had the proportional limit, yield, and

maximum loads less than the corresponding values of the parent column by 18, 15, and 19 %, respectively. The cellular column ST-C2 (75-mm-diameter holes and 126-mm-spacing holes) had the proportional limit, yield and maximum loads less than the corresponding values of the parent column by 18, 15, and 13 %, respectively. The cellular column ST-C3 (90-mm-diameter holes and 108-mm-spacing holes) had the proportional limit, yield and maximum loads less than the corresponding values of the parent column by 15, 15, and 18 %, respectively. Therefore, the axial stiffness or strength of the cellular column was not sensitive to the different hole diameter and spacing values used in this study. A comparison between the axial stiffness and strength of the bare steel columns and composite columns is discussed in section 5.2.6.
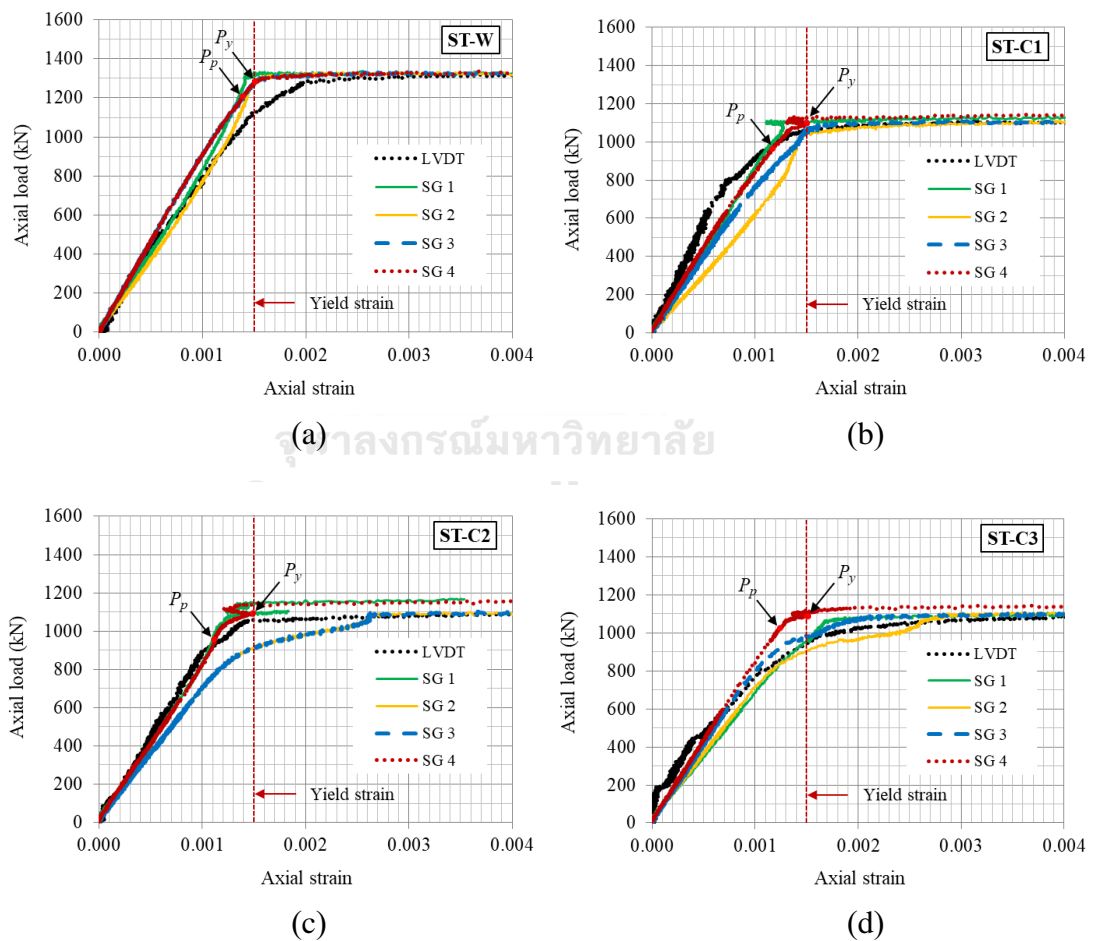
Figure 5.3 Loads at proportional limit and yield point of steel columns (a) ST-W; (b) ST-C1; (c) ST-C2; and (d) ST-C3.

5.1.4 Load – transverse strain curves

Figure 5.4 shows the load – axial and transverse strain curves of the cellular and parent steel columns. In a case of the parent column, the transverse tensile strain at the web increased proportionally to the axial compressive strain. A ratio between the transverse and axial strains was 0.30 at the proportional limit. After the yield point, the transverse strain at the web suddenly increased in tension.
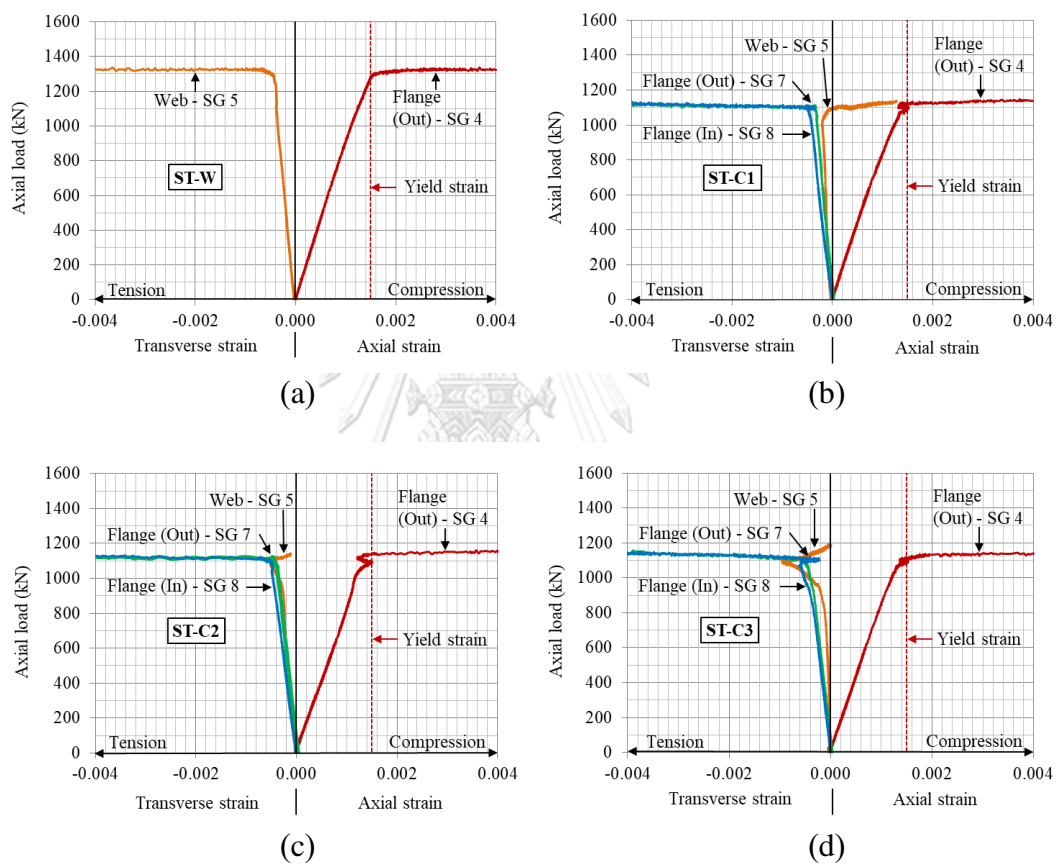
Figure 5.4 Load – axial and transverse strain curves (a) ST-W; (b) ST-C1; (c) ST-C2; and (d) ST-C3.

In case of the cellular columns: for the steel flange, the transverse tensile strain increased proportionally to the axial compressive strain. A ratio between the transverse and axial strains was 0.30 at the proportional limit. After the yield point, the transverse strain at the web suddenly increased in tension. For the steel web, the transverse tensile strain increased proportionally to the axial compressive strain. A ratio between the transverse and axial strains was less than 0.30 at the proportional

limit. After that, the transverse strain at the web reversed into compression due to flange local buckling. A visual inspection confirmed that the flange local buckling at the opened section did push the steel web into compression.

5.1.5 Conclusions

The conclusions of the experimental results of the cellular steel columns subjected to concentric loadings are as follows,

- Failure mode of the cellular steel columns are both web and flange local buckling occurred at the hole section. No failure of weldment was observed.
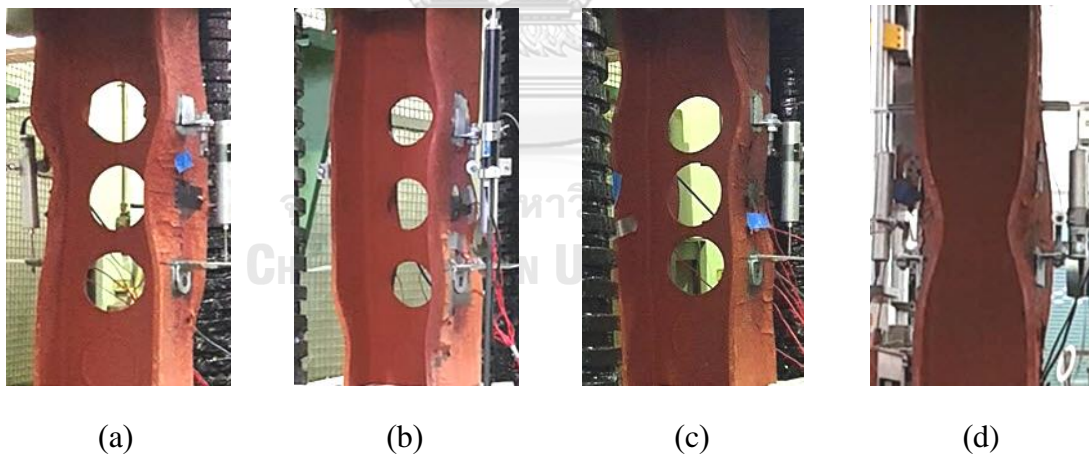- Load – deformation curves of the cellular steel columns are similar to the parent column. All cellular steel columns exhibited yielding and hardening behavior. However, the hardening behavior became less obvious as hole size increased.
- Load – axial strain curves of the cellular steel columns are mainly similar to the parent column with a few differences. For the strain gauges at the steel flange, the strain is suddenly reduced after the yield point corresponding to the observed local buckling failure. The measured strain at steel web is greater than the measured strain of the steel flanges at same load level.
- Load – transverse strain: for the steel flange, the transverse tensile strain increased proportionally to the axial compressive strain. A ratio between the transverse and axial strains was 0.30 at the proportional limit. After the yield point, the transverse strain at the web suddenly increased in tension. For the steel web, the transverse tensile strain increased proportionally to the axial compressive strain. A ratio between the transverse and axial strains was less than 0.30 at the proportional limit. After that, the transverse strain at the web reversed into compression due to flange local buckling.
- Axial stiffness of the cellular steel columns is close to the axial stiffness of the parent steel column.

- The cellular columns had the averaged proportional limit, yield and maximum loads less than the corresponding values of the parent column by 17, 15 and 17, respectively.

5.2 Experimental results of CECS and CES columns subjected to concentric loadings

In this section, failure mode, load – deformation curves, load – axial strain curves, load – transverse strain curves, ductility, and effect of design parameters of CECS and CES columns subjected to concentric loadings are discussed. In addition, the RC columns, which have column properties similar to the composite columns, were tested for comparing with the composite columns. The experimental results of RC columns are shown in Appendix B.

5.2.1 Failure mode

Figures 5.5 to 5.8 show the tested columns with stirrup spacing of 63, 108, 126, and 170 mm, respectively, at different stages as follows: (a) before testing, (b) at proportional limit, (c) at maximum loads, and (d) post peak of the composite columns. Both CECS and CES columns exhibited similar failure characteristics.

| (a) | (b) | (c) | (d) |
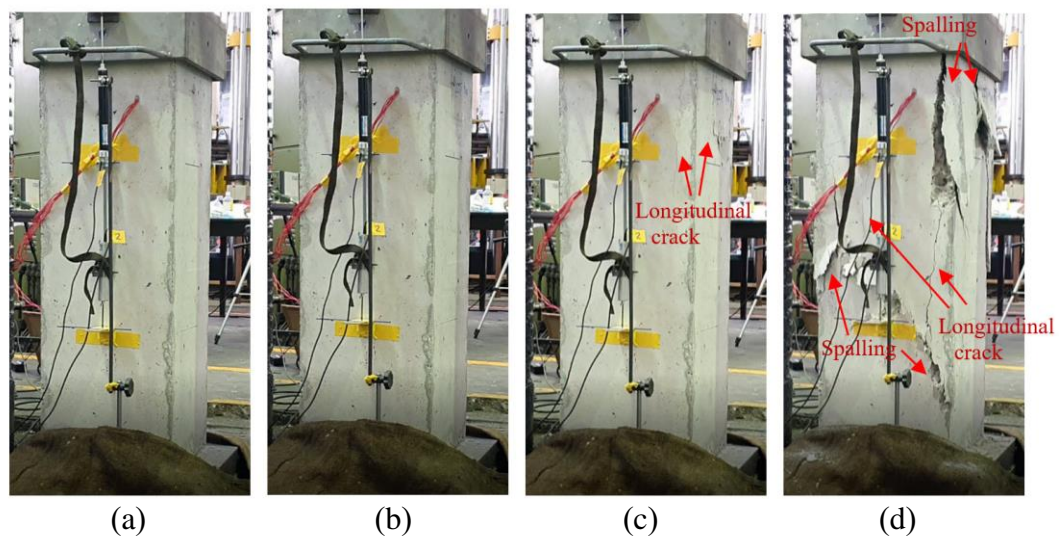
Figure 5.5 Failure of CECS column W-63 (a) before test; (b) at proportional limit load; (c) at maximum load; and (d) post peak.
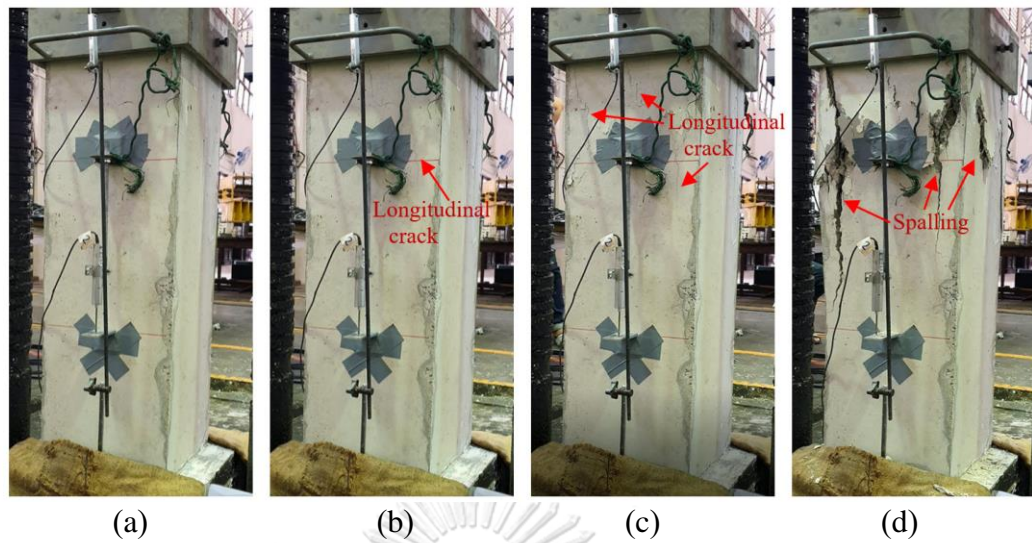
Figure 5.6 Failure of CECS column C3-108 (a) before test; (b) at proportional limit load; (c) at maximum load; and (d) post peak.
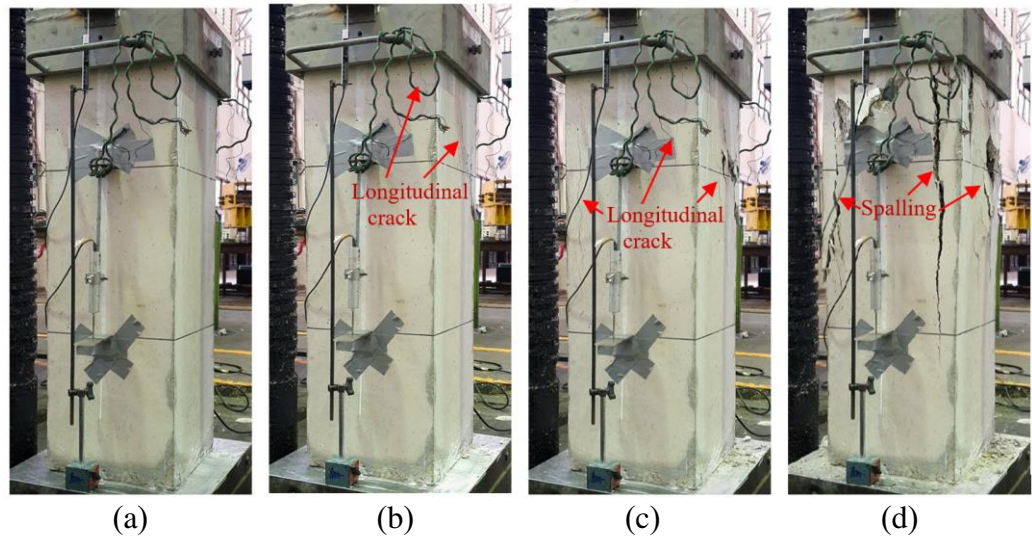
Figure 5.7 Failure of CECS column C1-126 (a) before test; (b) at proportional limit load; (c) at maximum load; and (d) post peak.

A combination of concrete spalling and buckling of longitudinal rebars was observed. Except in the columns with the smallest stirrup spacing (63 mm), the longitudinal cracks formed at the proportional limit in the columns with larger stirrup spacings (108, 126, and 170 mm). These cracks then extended rapidly as the maximum loads was approached.

(a)   (b)   (c)   (d)
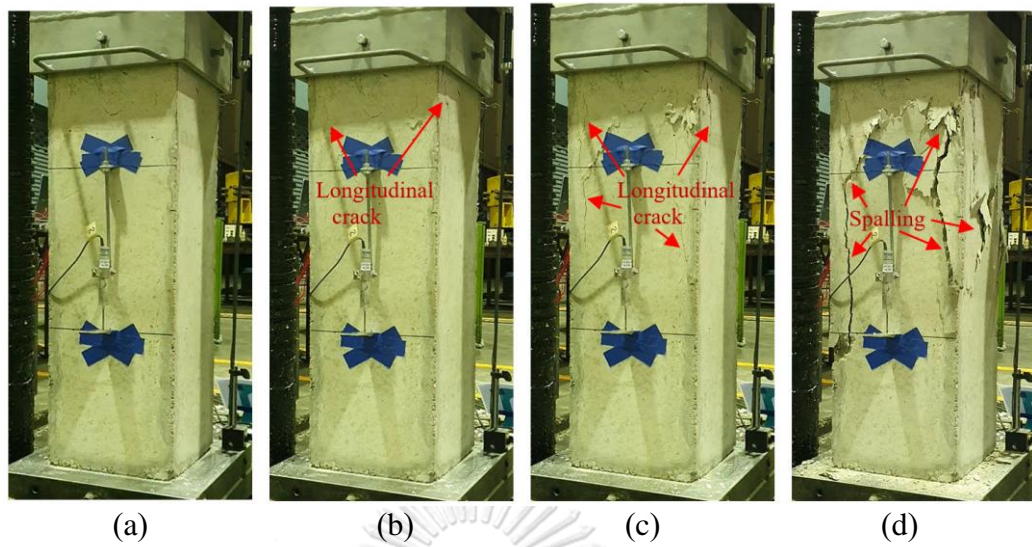
Figure 5.8 Failure of CECS column C2-170 (A) (a) before test; (b) at proportional limit load; (c) at maximum load; and (d) post peak.

Figure 5.9 shows the failure characteristics of the tested columns with different stirrup spacings after removal of the spalling concrete. The buckling of longitudinal rebars was evident in the columns with large stirrup spacing. A widening at hooks of the closed stirrups was also observed in columns with stirrup spacing of 108, 126, and 170 mm.

(a)   (b)   (c)   (d)
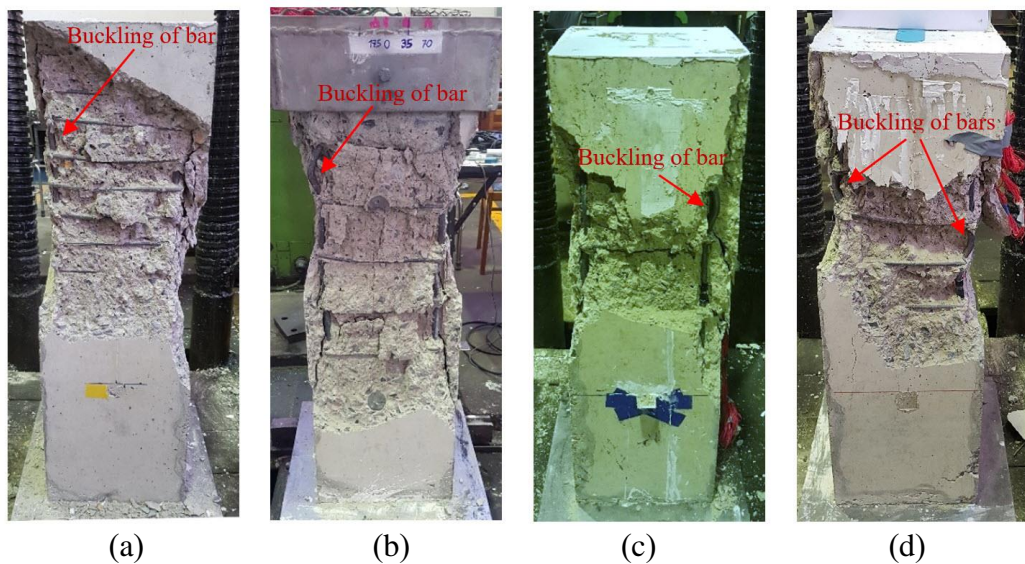
Figure 5.9 Failure of composite columns with different stirrup spacings after removal of spalling concrete (a) W-63; (b) C1-126; (c) C2-170 (A); and (d) C3-108.

5.2.2 Load – deformation curves

Figure 5.10 shows the typical load – deformation curves of the composite columns up to the proportional limit. Because the longitudinal LVDTs were attached to the concrete surface, the measured deformations were found to be unreliable after the concrete cracking at the proportional limit. Therefore, all load-deformation curves were truncated at this load level. Up to the proportional limit, a good agreement between an average strain over the 200 mm gauge length (from the LVDT reading) and local strain measured from the strain gauge at the structural steel was observed. With the same stirrup spacings, the axial stiffness of the CECS columns were slightly higher than the CES columns, as shown in Figure 5.10 (a). With the same cellular steel, the stiffness reduced as stirrup spacing increased, as shown in Figure 5.10 (b). The axial stiffness of CECS and CES are shown in Table 5.2. The comparison shows that the CECS columns have axial stiffness similar to the CES column; and, the CECS columns have greater axial stiffness than the CES columns in the closely stirrup spacings.

(a)   (b)
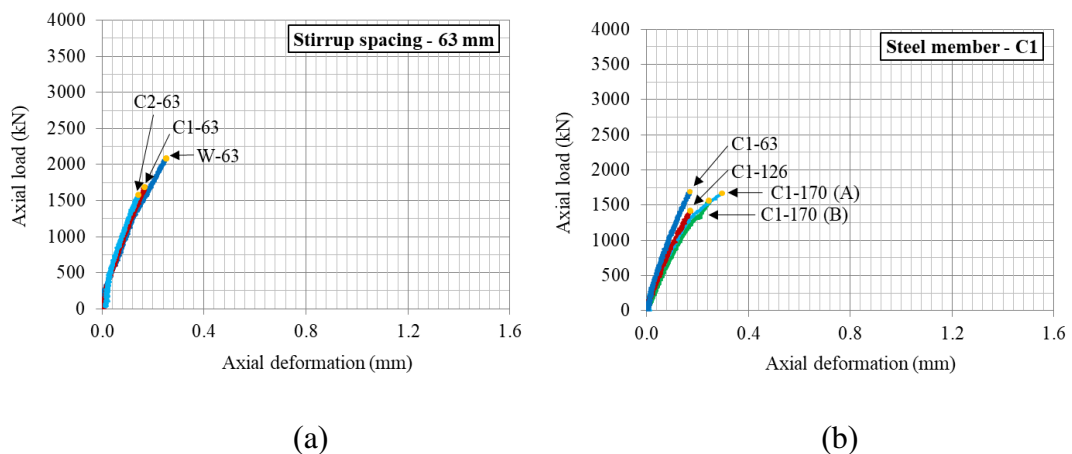
Figure 5.10 Load – deformation of curves; (a) columns with stirrup spacing at 63 mm; and (b) C1 columns.

Table 5.2 summarizes the test results of all composite columns. The proportional limit was defined as the point at 20 % deviation from the initial slope based on the strain gauges at the structural steel. The loads at the proportional limit ranged from 50 to 60 % of the maximum loads. In this study, the CECS columns had

slightly less compressive strength values than the CES columns with the average ratio of 0.94 – 0.97.

Table 5.2 Test results of composite columns subjected to concentric loadings.

Composite columns	Experimental result				Comparison (CECS / CES)		
	Axial stiffness	Proportional limit load	Maximum load	Ductility index	Axial stiffness	Proportional limit load	Maximum load
	$(EA/L)_{exp}$	P_{prop}	P_{max}	DI	$(EA/L)_{exp}$	P_{prop}	P_{max}
	MN/m	kN	kN	-	MN/m	kN	kN
	[1]	[2]	[3]	[4]	[1] / [1][a]	[2] / [2][a]	[3] / [3][a]
W-170 (A)	8228	1744	2744	3.28	-	-	-
C1-170 (A)	8175[b]	1673	2636	2.64	0.99	0.96	0.96
C2-170 (A)	8236[b]	1536	2572	3.30	1.00	0.88	0.94
C3-170 (A)	9151[b]	1496	2637	3.14	1.11	0.86	0.96
	Average				1.04	0.90	0.95
W-170 (B)	7626	1322	2632	3.30	-	-	-
C1-170 (B)	7896[b]	1561	2478	3.17	1.04	1.18	0.94
C2-170 (B)	8164[b]	1519	2480	3.45	1.07	1.15	0.94
C3-170 (B)	8095[b]	1418	2493	3.16	1.06	1.07	0.95
	Average				1.06	1.13	0.94
W-126	8402	1567	2868	3.29	-	-	-
C1-126	8974[b]	1426	2809	2.78	1.07	0.91	0.98
C2-126	8601[b]	1652	2782	2.63	1.02	1.05	0.97
	Average				1.05	0.98	0.97
C3-108	9319[b]	1538	2906	3.98	-	-	-
	Average				-	-	-
W-63	8807	2081	3469	1.65	-	-	-
C1-63	10250[b]	1761	3307	2.63	1.16	0.85	0.95
C2-63	10644[b]	1589	3270	3.19	1.21	0.76	0.94
	Average				1.19	0.80	0.95

[a] Based on the CES columns; [b] Based on the actual LDVT gauge.

5.2.3   Load – axial strain curves

Figure 5.11 shows the typical load – axial strain curves of the CES or CECS columns with stirrup spacing of 63, 108, 126, and 170 mm, respectively. With the same stirrup spacings, both CES and CECS columns had similar load – axial strain curves. The axial strains were measured with the strain gauges installed at the flanges of structural steel and longitudinal rebars. The curve can be divided into three stages: (1) linear elastic stage (from origin to the proportional limit) where the initial slope was the axial rigidity. This load level also corresponded to the stage at which the longitudinal cracks started to develop in the composite columns. Up to the proportional limit, the compressive strains at the structural steel flange and longitudinal rebar were identical; (2) nonlinear elastic stage (from the proportional limit to the maximum load). The structural steel flange started to exhibit higher compressive strains than the longitudinal rebars due to buckling of the longitudinal rebars. The difference between structural steel and rebar strains was obvious in the CECS columns with large stirrup spacings. The strain gauges positioned at outside of the longitudinal rebars also detected the outward buckling that reduced the compressive strains in the rebars. At the maximum loads, the strain in structural steel almost achieved the coupon yield strain. Meanwhile, the strain in reinforcement bars did not achieve the yield strain of rebars; and (3) post-peak stage (beyond the maximum load), the strain in structural steel suddenly dropped, but the columns were capable of sustaining 80% of the maximum loads until steel strain at about 0.004.

Figure 5.11 Load – strain curves (a) W-63; (b) C3-108; (c) C1-126; and (d) C2-170 (A).

5.2.4 Load – transverse strain curves

Figures 5.12 to 5.15 show the load – axial and transverse strain curves of all CECS and CES columns. In both CECS and CES columns, the transverse strain (in tension) at the steel flange increased as axial strain (in compression) increased. The Poisson's ratio was constant at about 0.3 up to 60 – 80 % of the maximum loads. Beyond this load level, the confinement effect from the steel web and flanges was triggered. The steel web and flanges started to resist the concrete expansion and provided the confining pressure to the inner concrete. In effect, the transverse strain at the inner face of the steel flange continued to increase, while one at the outer face did not increase or turned into compression. Meanwhile, the transverse strains at the steel web also increased.
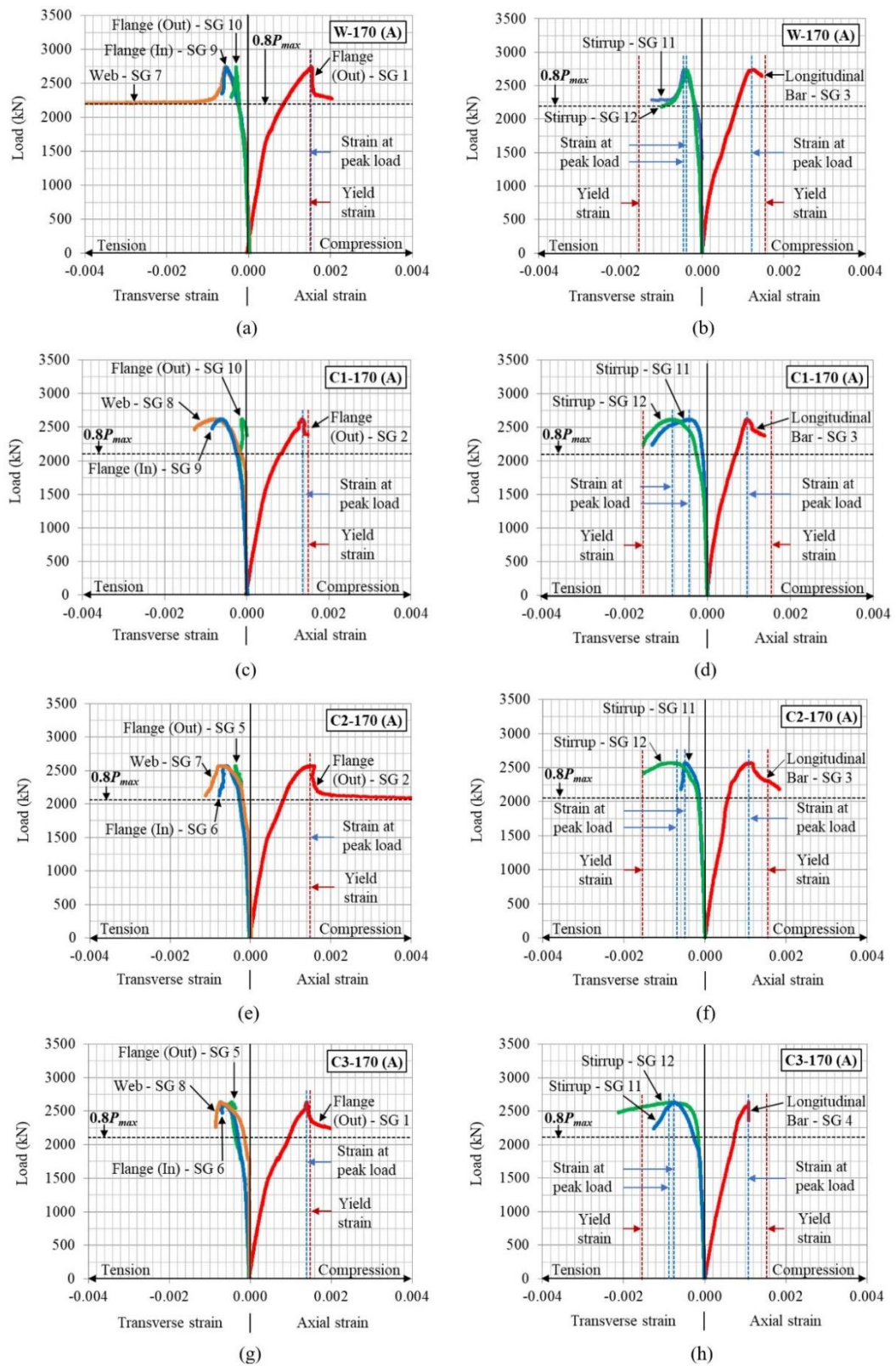
Figure 5.12 Load – axial and transverse strain curves (a-b) W-170 (A); (c-d) C1-170 (A); (e-f) C2-170 (A); and (g-h) C3-170 (A).
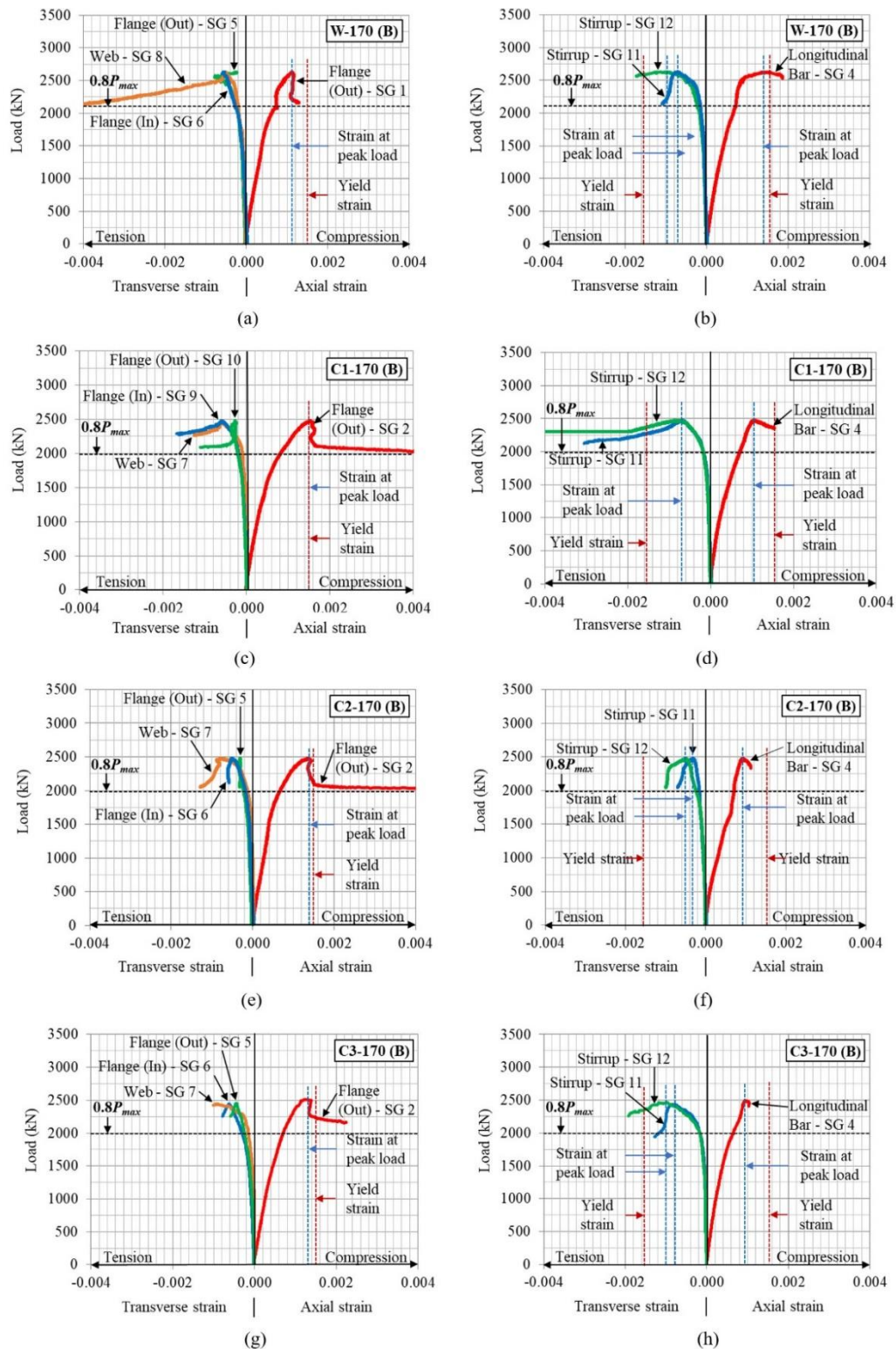
Figure 5.13 Load – axial and transverse strains (a-b) W-170 (B); (c-d) C1-170 (B);
(e-f) C2-170 (B); and (g-h) C3-170 (B).
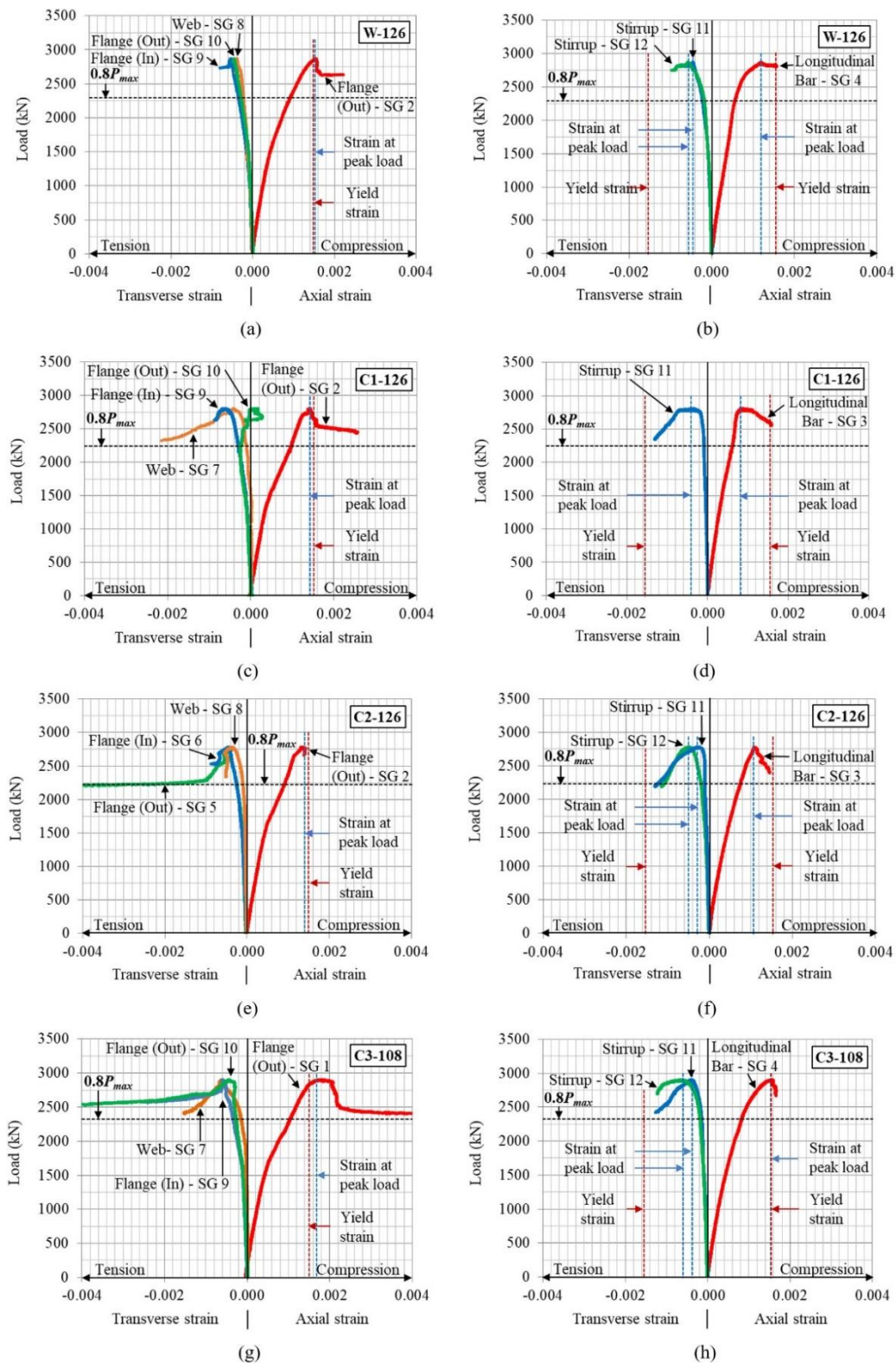
Figure 5.14 Load – axial and transverse strain curves (a-b) W-126; (c-d) C1-126; (e-f) C2-126; and (g-h) C3-108.
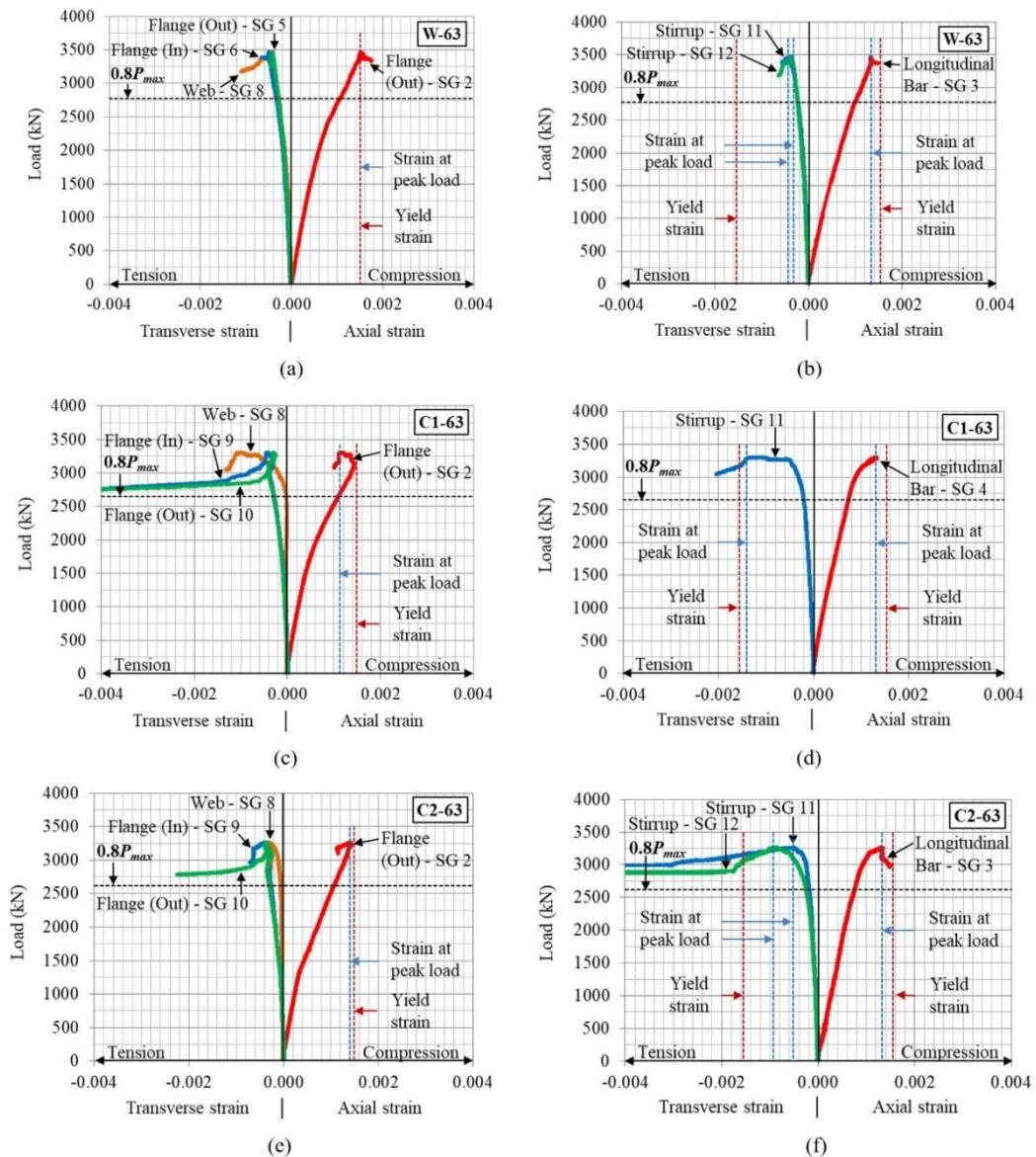
Figure 5.15 Load – axial and transverse strain curves (a-b) W-63; (c-d) C1-63; and (e-f) C2-63.

In addition, the closed stirrups provided the confining pressure to the enclosed concrete. A sudden increase in stirrup strain occurred at 60 – 80 % of the maximum loads. The maximum transverse strains in the closed stirrups increased as spacing of the stirrups increased. However, no yielding of the stirrups in all columns occurred at the maximum loads.

5.2.5 Ductility

The ductility index was defined to investigate the range from the onset of concrete cover cracking to the maximum loads. Because of the LVDT readings were not reliable after the proportional limit, the ductility index was defined in terms of the axial strain at structural steel as follows,

$$DI = \frac{\varepsilon_{max}}{\varepsilon_p} \qquad (5.1)$$

The measured ductility indexes of all tested composite columns are shown in Table 5.2. An average ductility index of the CECS and CES columns was about 3.

5.2.6 Effect of design parameters

Figure 5.16 shows a comparison between the compressive strength of bare steel columns and composite columns. The composite design enhanced the compressive strength of the CES and CECS columns with respect to the bare steel columns by 104 – 168 % and 126 – 202 %, respectively. Also, it increased the axial stiffness by 76 – 159 %. The effects of design parameters including the concrete strength, cellular steel configuration, and stirrup spacing on the compression properties of the CES and CECS columns can be summarized as follows,

Effect of concrete strength: a comparison of columns W-170 (A), C1-170 (A), C2-170 (A), and C3-170 (A) with columns W-170 (B), C1-170 (B), C2-170 (B), and C3-170 (B) showed that the compressive strength of CECS and CES columns increased by 3.7 – 6.4 % as concrete strength increased from 18.3 to 20.1 MPa (9.8 %).

Effect of stirrup spacings: a comparison of columns W-170 (A), C1-170 (A), C2-170 (A), and C3-170 (A) with columns W-126, C1-126, C2-126, and C3-108 showed that the compressive strength of CECS and CES columns increased by 4.5 – 10.2 % as stirrup spacing decreased.

The combined effect of concrete strength and stirrup spacing: a comparison of columns W-63, C1-63, and C2-63 with columns W-126, C1-126, and C2-126 showed that increase concrete strength from 20.1 to 22.9 MPa (13.9 %) and reducing stirrup spacing by a half increased the strength of CECS and CES columns by 17.5 – 21.0 %.

Effect of hole diameter: a comparison of column series C1 with column series C2 showed that the compressive strength of the CECS and CES columns decreased slightly as hole diameter increased.

Effect of hole spacing: a comparison of column series C1 with column series C3 showed that different hole spacings used in the study did not significantly influence the compressive strength of the CECS columns.
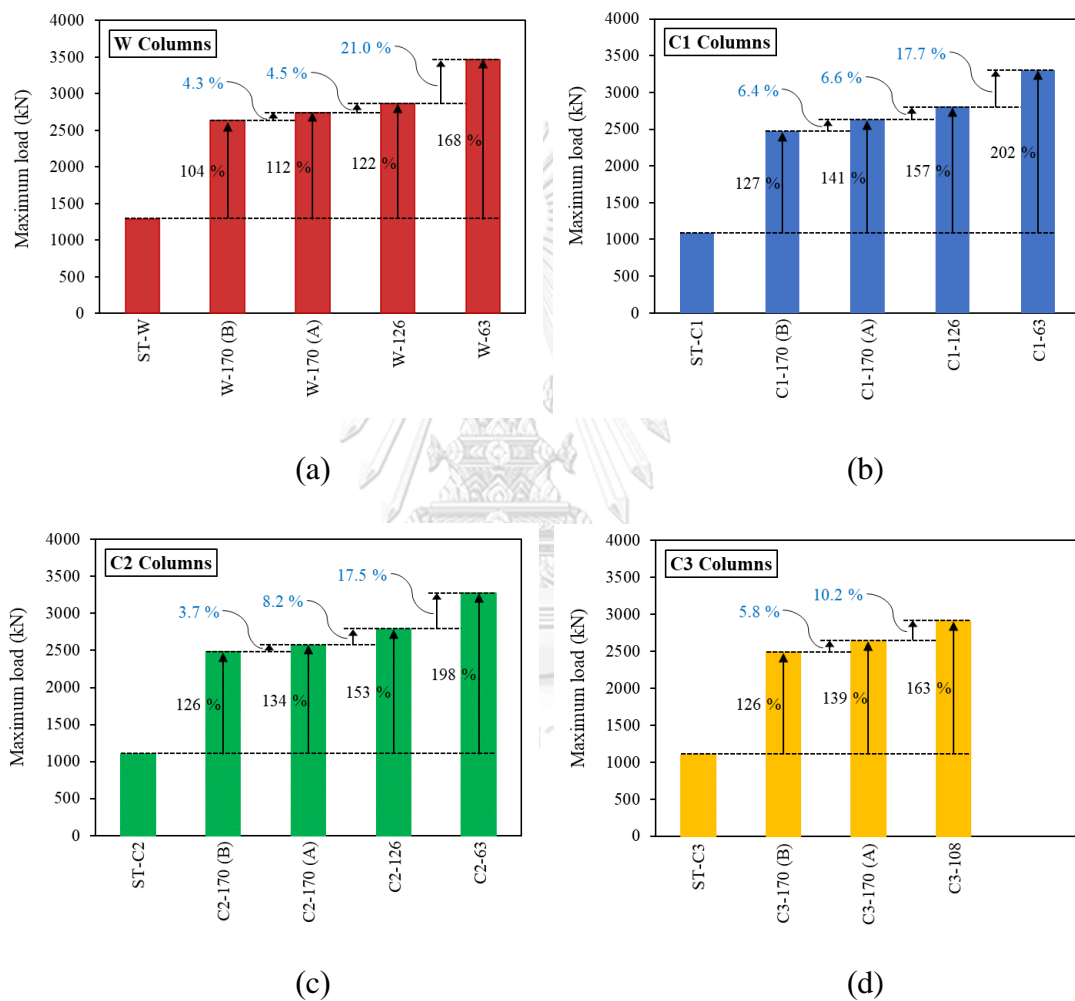
Figure 5.16 Comparison of compressive strength of concentric loading columns;
(a) W columns; (b) C1 columns; (c) C2 columns; and (d) C3 columns.

5.2.7   Conclusions

The conclusions of the experimental results of the CECS columns subjected to concentric loadings are as follows,

- Failure mode: with similar stirrup spacing, failure mode of the CECS columns are similar to the CES columns. Failure of CECS and CES columns in this research are cover concrete spalling and buckling of the longitudinal rebars at maximum loads.

- Load – deformation curves: with similar stirrup spacing, the load – deformation curves of the CECS columns are similar to the CES columns. The initial slope of the curves of the CECS columns are slightly less than the slope of the curves of the CES columns.

- Load – axial strain curves: The curve can be divided into three stages: (1) linear elastic stage (from origin to the proportional limit) where the initial slope was the axial rigidity. (2) nonlinear elastic stage (from the proportional limit to the maximum load) . At the maximum loads, the strain in structural steel almost achieved the coupon yield strain. Meanwhile, the strain in reinforcement bars did not achieve the yield strain of rebars; and (3) post-peak stage (beyond the maximum loads), the strain in structural steel suddenly dropped. But the columns were capable of sustaining 80% of the maximum loads until steel strain at about 0.004.
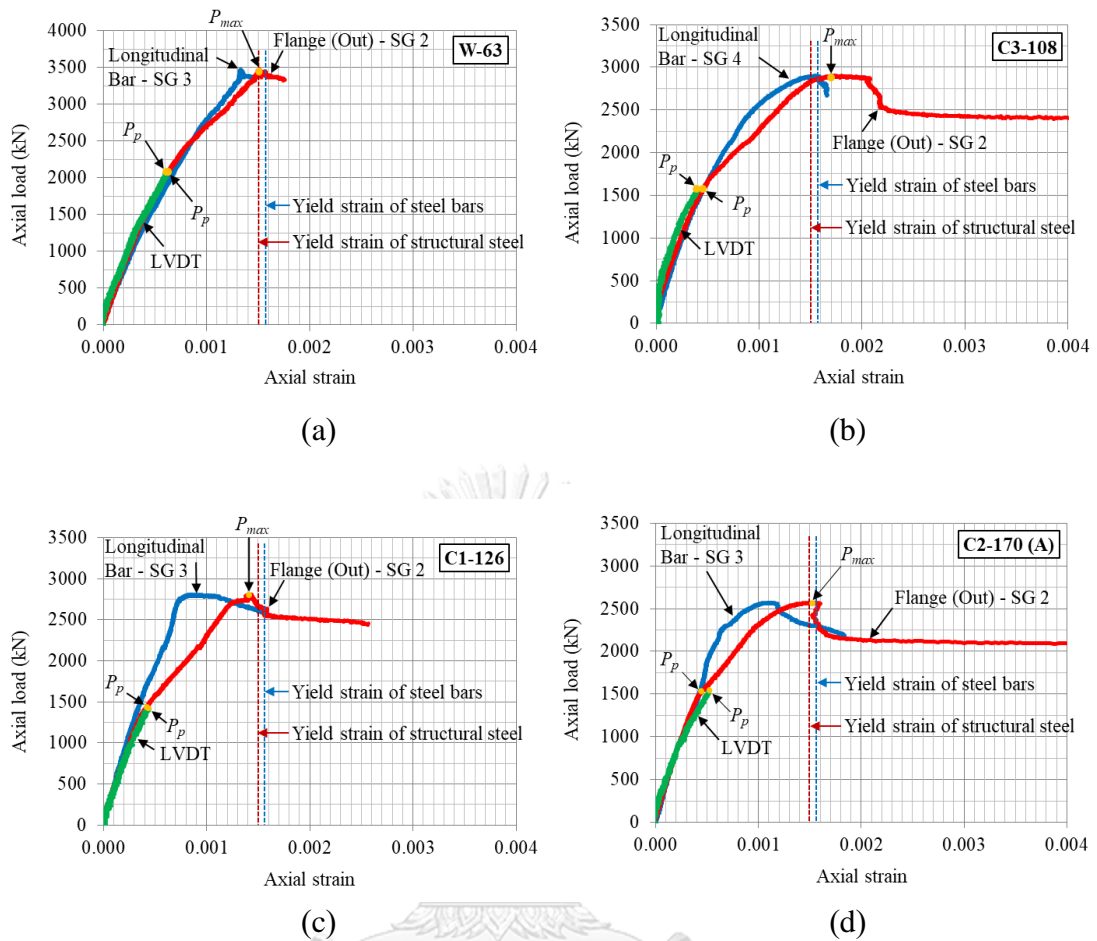
- Load – transverse strain curves: the transverse strain (in tension) at the steel flange increased as axial strain increased. The Poisson's ratio was constant at about 0.3 up to 60 – 80% of the maximum loads. Beyond this load level, the steel web and flanges started to resist the concrete expansion and provided the confining pressure to the inner concrete. However, no yielding of the stirrups in all columns occurred at the maximum loads.

- The measured ductility indexes of the CECS columns was about 3 similarly to the CES columns.

- Axial stiffness of the CECS columns is close to the axial stiffness of the CES columns.

- The CECS columns had the averaged maximum loads less than the CES columns by 3 – 6 %.
- Effect of increase concrete strength or decreasing stirrup spacing of CECS columns are increase strength of the CECS columns.

5.3 Experimental results of cellular steel columns subjected to eccentric loadings

In this section, failure mode, load – deformation curves, load – axial strain curves and load – transverse strain curves of cellular steel columns subjected to eccentric loadings are discussed.

5.3.1 Failure mode

Figures 5.17 and 5.18 show the failure characteristics of bare steel columns subjected to eccentric loadings E1 (17.5 mm) and E2 (35 mm), respectively. In the parent steel column (ST-W), the local buckling at the compression flanges occurred near mid-height after the yield point. In all cellular steel columns (ST-C1, ST-C2, and ST-C3), both compression web and flange local buckling occurred at the hole section. No failure of weldment was observed. The local buckling and bending failure of the specimen are obvious in eccentric loadings E2.

(a)	(b)	(c)	(d)
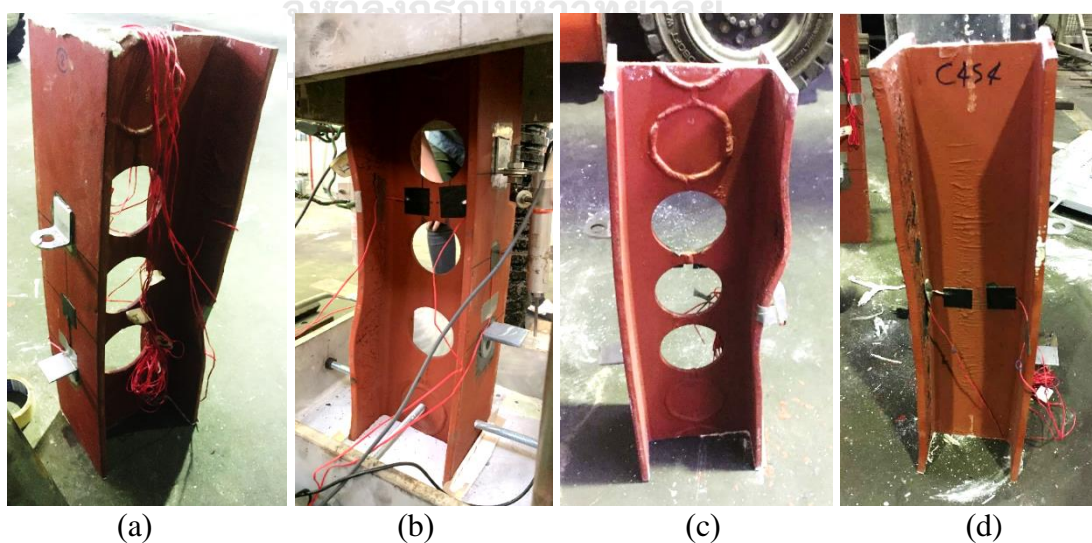
Figure 5.17 Failure of steel columns (eccentricity 17.5 mm); (a) ST-C1-E1;
(b) ST-C2-E1; (c) ST-C3-E1; and (d) ST-W-E1.

<p style="text-align:center">(a)   (b)   (c)   (d)</p>
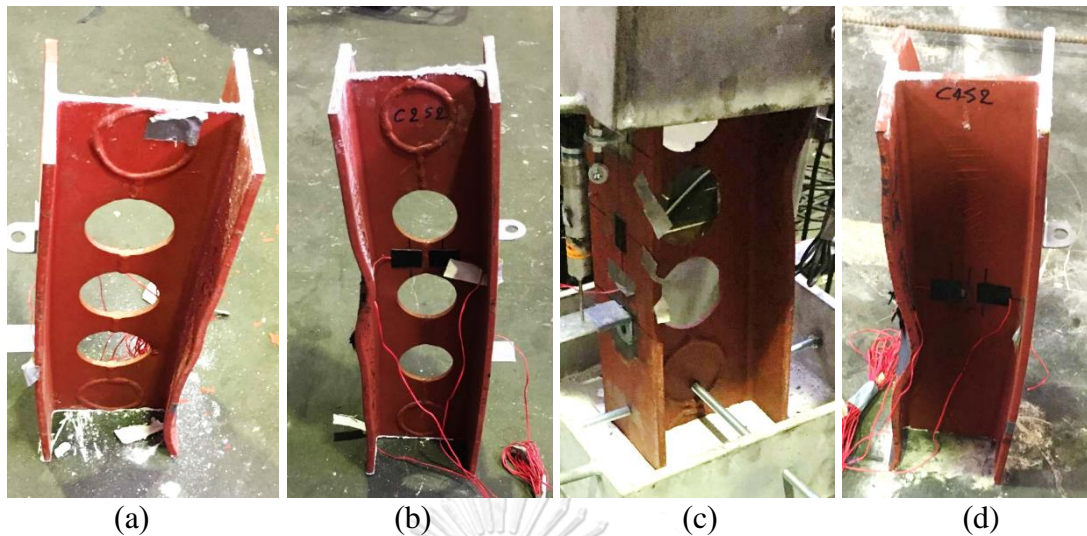
Figure 5.18 Failure of steel columns (eccentricity 35 mm); (a) ST-C1-E2;
(b) ST-C2-E2; (c) ST-C3-E2; and (d) ST-W-E2.

5.3.2 Load – deformation curves

Figures 5.19 and 5.20 show a comparison of the load – deformation curves of the cellular steel columns (ST-C1, ST-C2, and ST-C3) with the parent steel column (ST-W). Similar to the parent column, all cellular steel columns exhibited yielding and slight hardening behaviors. From the LVDT at compression flange, the curves of the bare steel columns subjected to eccentric loads is the same as the bare steel columns subjected to concentric loads. From the LVDT at tension flange, the curves of bare steel columns increased in compression in linear elastic state; and, the curves returned to tension at near yield point. In addition, increase the eccentricity has an effect on the curves of LVDT at tension flange only. The LVDT at tension flange of the bare steel columns with eccentric loading E2 are nearly to be zero in linear elastic state.
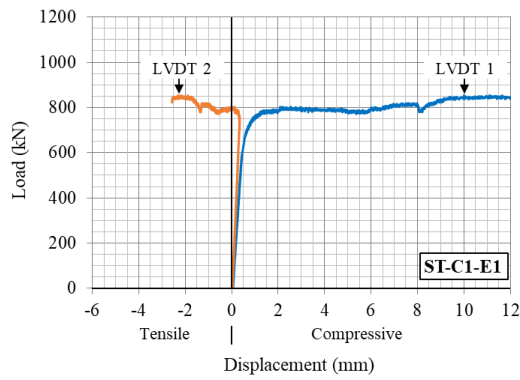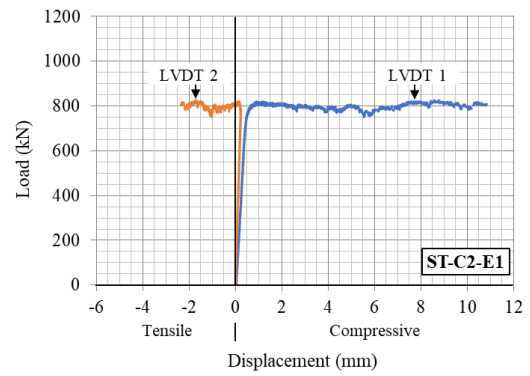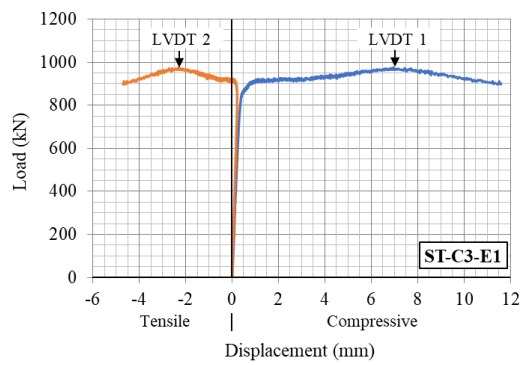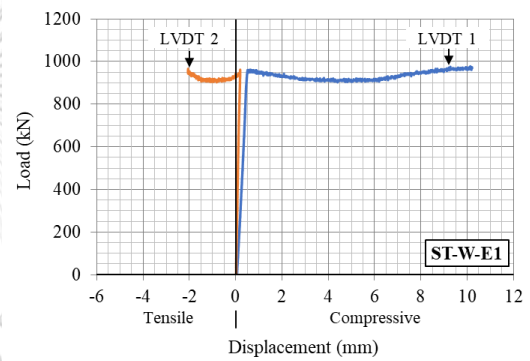
Figure 5.19 Load – deformation curves of (a) ST-C1-E1; (b) ST-C2-E1;
(c) ST-C3-E1; and (d) ST-W-E1.
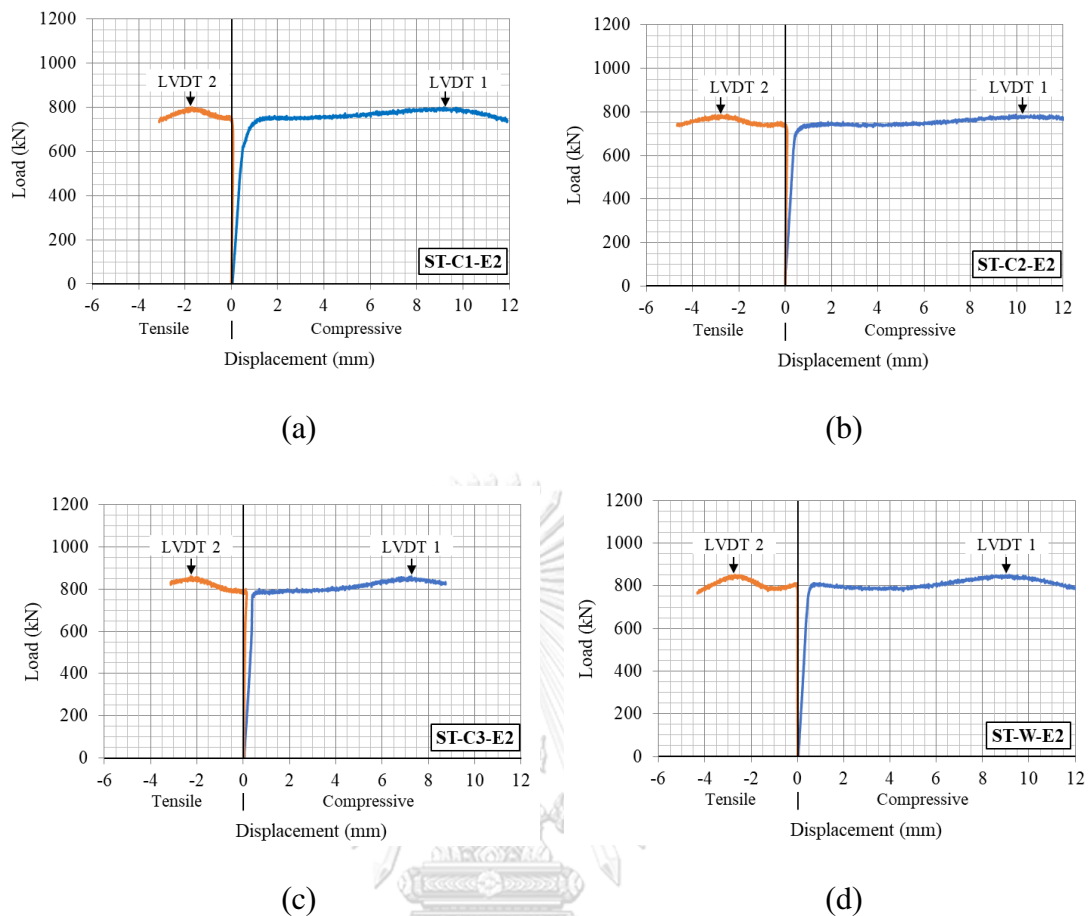
Figure 5.20 Load – deformation curves of (a) ST-C1-E2; (b) ST-C2-E2; (c) ST-C3-E2; and (d) ST-W-E2.

5.3.3 Load – axial strain curves

Figures 5.21 and 5.22 show the load – axial strain curves of the cellular steel columns (ST-C1, ST-C2, and ST-C3) and parent steel column (ST-W). The axial strain was measured from the strain gauges at steel flanges.

From the strain gauges located at compression flanges, the curves of the cellular steel columns subjected to eccentric loads are the same as the cellular steel columns subjected to concentric loads. Unlike the parent steel column, all cellular steel columns experienced a sudden reduction in axial strain at the hole center, i.e., the minimum (net) section, at the yield point. The sudden reduction indicates the onset of flange local buckling at the holes of the cellular steel columns.

From the strain gauges located at tension flanges, the curves of strain gauges are similar to the curves of LVDT at tension flanges. The curves increased in

compression in linear and nonlinear elastic state; and, the curves turned to in tension at near yield point. In addition, increase the eccentricity has effect on the curves of strain gauges at tension flanges only.
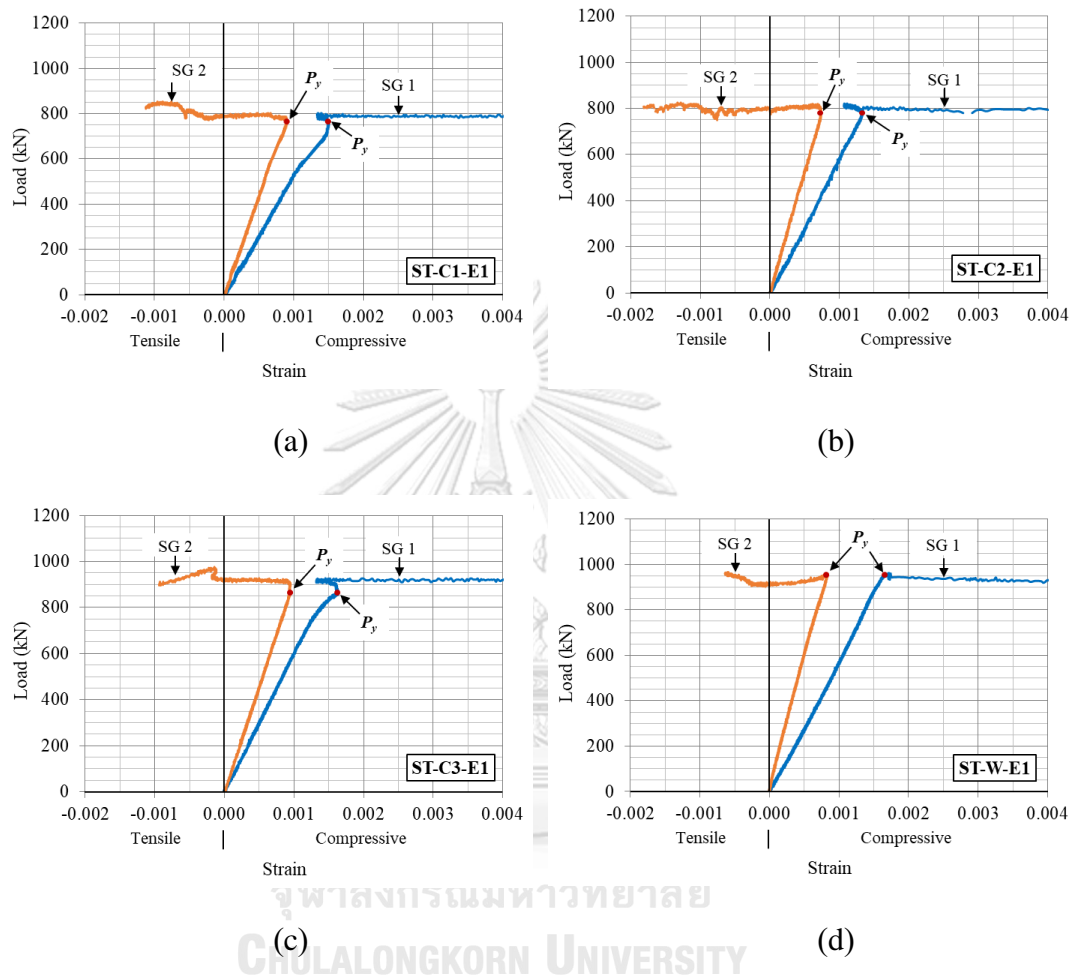
Figure 5.21 Load – axial strain curves of (a) ST-C1-E1; (b) ST-C2-E1;
(c) ST-C3-E1; and (d) ST-W-E1.
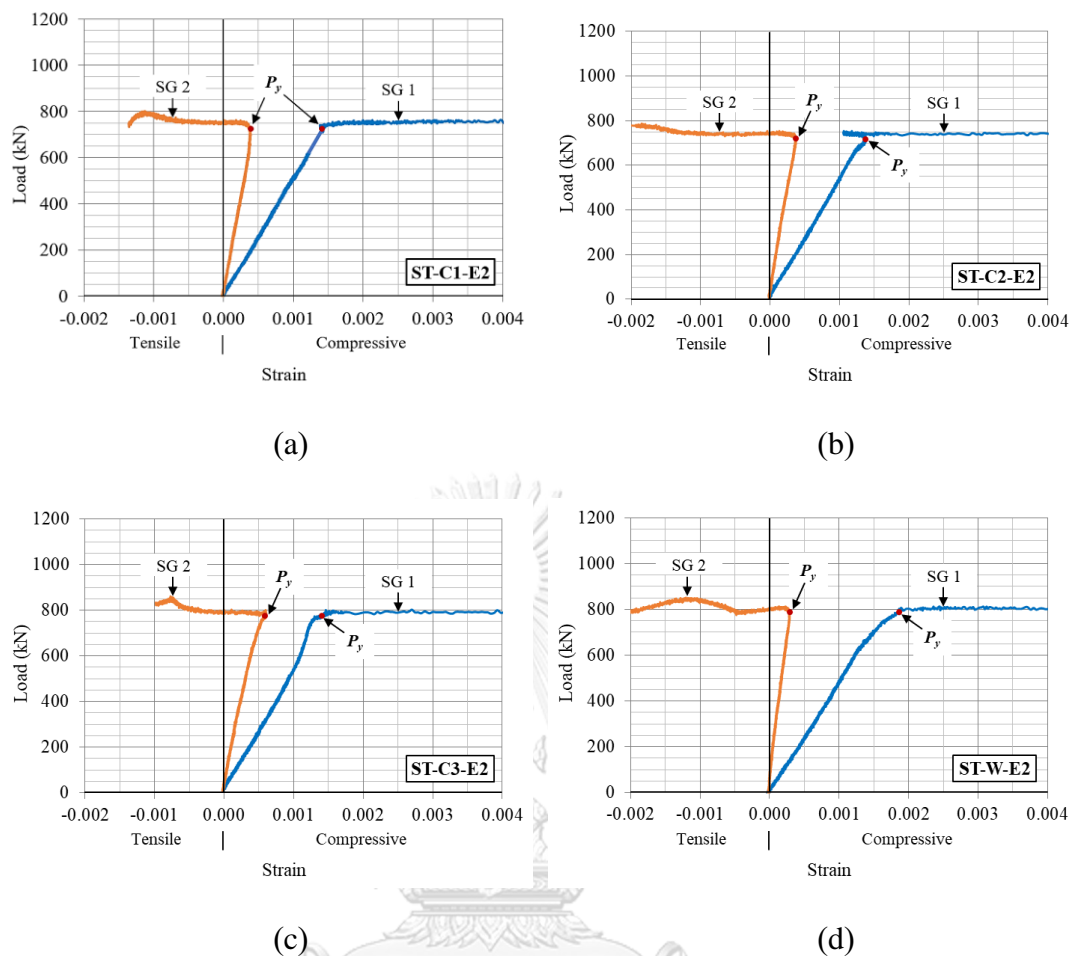
Figure 5.22 Load – axial strain curves of (a) ST-C1-E2; (b) ST-C2-E2;
(c) ST-C3-E2; and (d) ST-W-E2.

Observation shows that the compression flange and web local bucking occurred at yield point; and the strain in tension flange returned to tension at the moment. Therefore, the yield point was based on the return point, as shown in Figures 5.21 and 5.22. Table 5.3 summarizes the test results of all bare steel columns subjected to eccentric loadings.

From Table 5.3, the cellular columns had the lower yield and maximum loads than the parent column. The cellular columns under eccentric loads 17.5 mm (E1) had the yield and maximum loads less than the parent column by average 16 and 10 %, respectively. The cellular steel columns under eccentric loads 35 mm (E2) had the yield and maximum loads less than the parent column by average 4 and 4 %, respectively. Therefore, the strength cellular steel columns are close to the strength of the parent columns when the eccentricity is 35 mm. A comparison between the axial

stiffness and strength of the bare steel columns and composite columns is discussed in section 5.4.4.

Table 5.3 Test results of cellular steel columns subjected to eccentric loadings.

Columns	Experimental results		Comparison (Cellular / Parent)	
	Yield load	Maximum load	Yield load	Maximum load
	$P_{y, exp}$ kN [1]	P_{max} kN [2]	$P_{y, exp}$ kN [1] / [1][a]	P_{max} kN [2] / [2][a]
ST-W-E1	959	978	-	-
ST-C1-E1	772	853	0.81	0.87
ST-C2-E1	777	826	0.81	0.84
ST-C3-E1	861	976	0.90	1.00
Average			0.84	0.90
ST-W-E2	775	851	-	-
ST-C1-E2	738	801	0.95	0.94
ST-C2-E2	707	787	0.91	0.92
ST-C3-E2	787	861	1.02	1.01
Average			0.96	0.96

[a] Based on the CES columns.

5.3.4 Load – transverse strain curves

Figures 5.23 and 5.24 show the load – axial and transverse strain curves of the cellular and parent steel columns. In this part, the strain gauges were installed at steel web only, as shown in Figure 4.16. In a case of the parent column, the transverse tensile strain at the web increased proportionally to the axial compressive strain. A ratio between the transverse and axial strains was 0.30 at the proportional limit. After the yield point, the transverse strain at the web suddenly increased in tension.

In case of the cellular columns: the transverse tensile strain increased proportionally to the axial compressive strain. A ratio between the transverse and axial strains was less than 0.30 at the proportional limit. Because of SG 3 is installed at compression side, it captured larger value than SG 4. After the yield point, the transverse strain at the web reversed into compression due to flange local buckling. A

visual inspection confirmed that the flange local buckling at the opened section did push the steel web into compression.
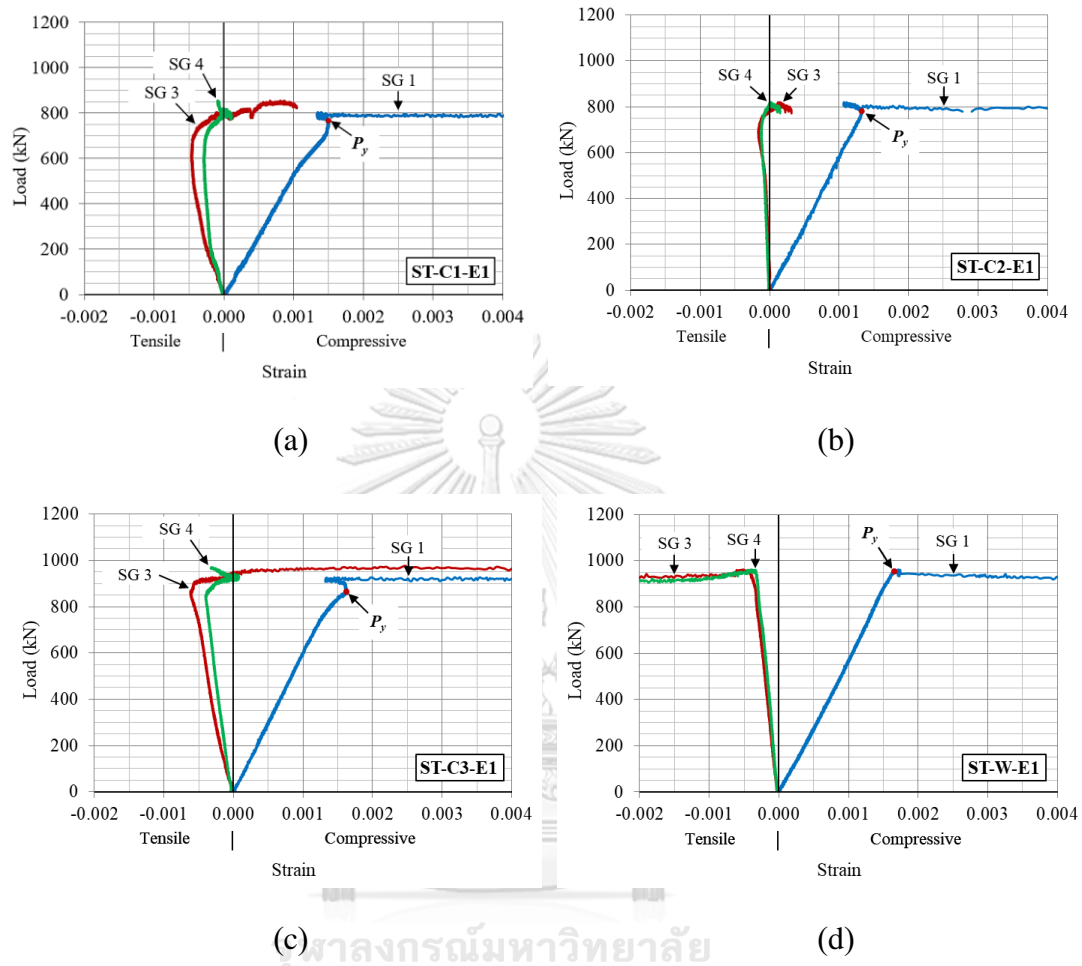
Figure 5.23 Load – transverse strain (SG 3 and SG 4) curves of
(a) ST-C1-E1; (b) ST-C2-E1; (c) ST-C3-E1; and (d) ST-W-E1.
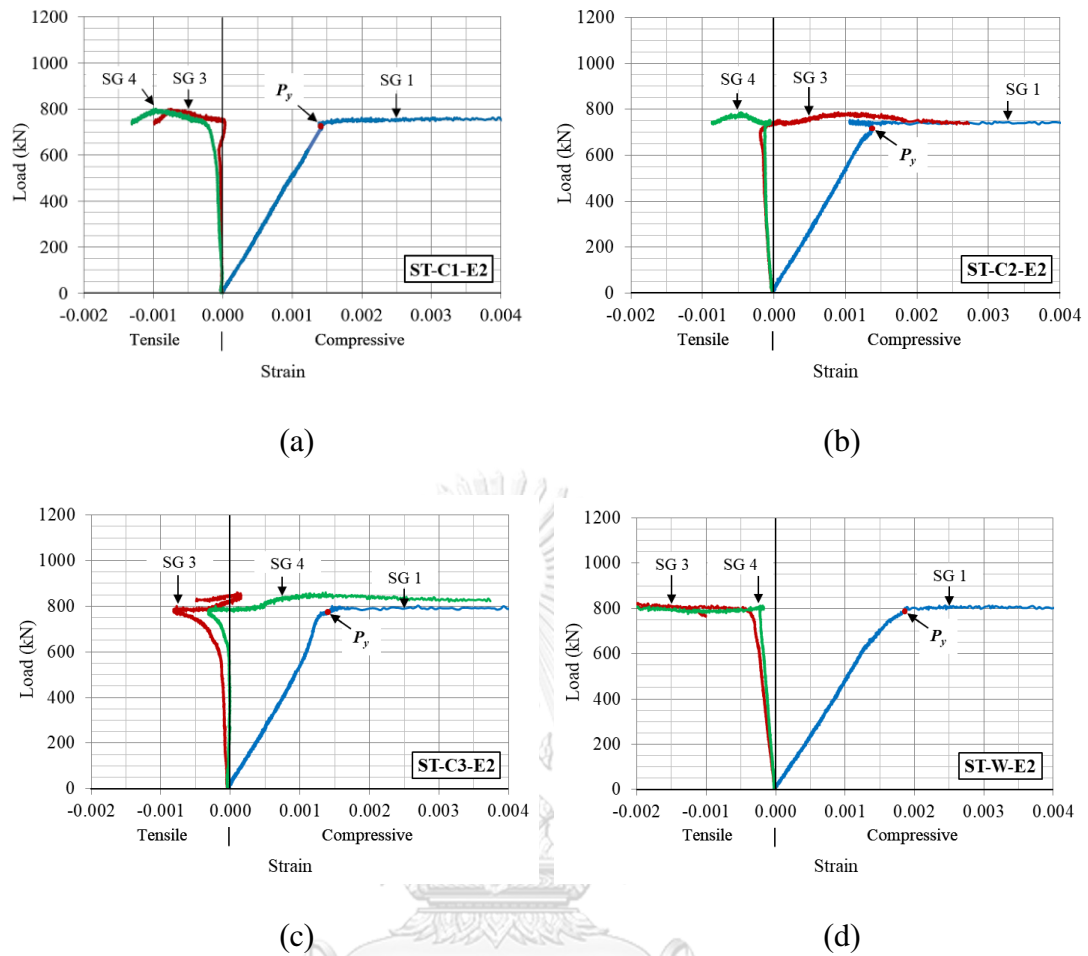
Figure 5.24 Load – transverse strain (SG 3 and SG 4) curves of
(a) ST-C1-E2; (b) ST-C2-E2; (c) ST-C3-E2; and (d) ST-W-E2.

5.3.5 Conclusions

The conclusions of the experimental results of the cellular steel columns subjected to eccentric loadings are as follows,

- Failure mode of the cellular steel columns were both compression web and compression flange local buckling occurred at the hole section. No failure of weldment was observed.

- Load – deformation curves: similar to the parent column, all cellular steel columns exhibited yielding and slight hardening behaviors. In the LVDT at compression flange, the curves are the same as the columns subjected to concentric loads. In the LVDT at tension flange, the curves of bare steel

columns increased in compression in linear elastic state; and, the curves returned to tension at near yield point.

- Load – axial strain curves: from the strain gauges located at compression flanges, the curves of the cellular steel columns subjected to eccentric loads are the same as the columns subjected to concentric loads. the cellular steel columns experienced a sudden reduction in axial strain at the hole center, i.e., the minimum (net) section, at the yield point. From the strain gauges located at tension flanges, the curves increased in compression in linear and nonlinear elastic state; and, the curves turned to in tension at near yield point.

- Load – transverse strain curves: the transverse tensile strain increased proportionally to the axial compressive strain. A ratio between the transverse and axial strains was less than 0.30 at the proportional limit. After the yield point, the transverse strain at the web reversed into compression due to flange local buckling. A visual inspection confirmed that the flange local buckling at the opened section did push the steel web into compression.

- The cellular columns had the averages yield and maximum loads less than the parent column by 16 % and 10 %, respectively, for eccentricity 17.5 mm and by 4 % and 4 %, respectively, for eccentricity 35 mm.

5.4 Experimental results of CECS and CES columns subjected to eccentric loadings

In this section, failure mode, load – axial strain curves, load – transverse strain curves and effect of design parameters of CECS and CES columns subjected to eccentric loadings are discussed. Shear studs were installed in these CECS and CES columns. In addition, the CECS and CES columns with shear studs subjected to concentric loadings are proposed in this section.

5.4.1 Failure mode

Figures 5.25 and 5.28 show the tested columns with load eccentricity E1 (35 mm) and E2 (70 mm), respectively: at different stages as follows (a) before testing, (b) at maximum loads and (c) post peak of the composite columns. For the concentric loading columns (C1s-63, C2s-63 and Ws-63), failure of the specimens was spalling of cover concrete and buckling of longitudinal bars, which similar to the specimens (C1-63, C2-63 and W-63), as shown in section 5.2.1.

For the composite columns subjected to eccentric loads E1: near the maximum loads, longitudinal crack occurred at the compression side and corner. At the maximum loads, concrete crushing occurred in the compression side at mid-height of the columns, as shown in Figure 5.26 (b). After that, transverse crack expanded rapidly from the compression side to the tension side. The load carrying capacity of the column reduced immediately. Finally, transverse crack occurred at the tension side; and, the column deformed as bending failure occurred as seen in Figure 5.26 (c). Figures 5.26 and 5.27 show failure of the specimens C1s-63-E1 and C2s-63-E1. Crushing of concrete occurred in the compression side; and, cracking of concrete occurred in the tension side.

(a) (b) (c)
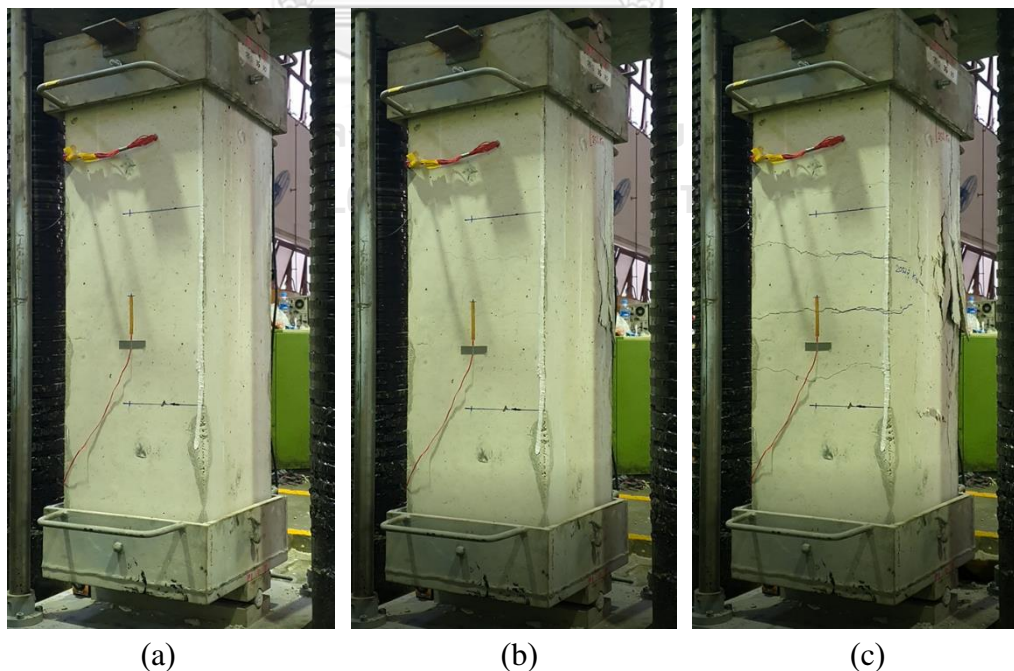
Figure 5.25 Failure of CECS column C1s-63-E1; (a) before test;
(b) at maximum loads; and (c) post peak.

(a) (b) (c)
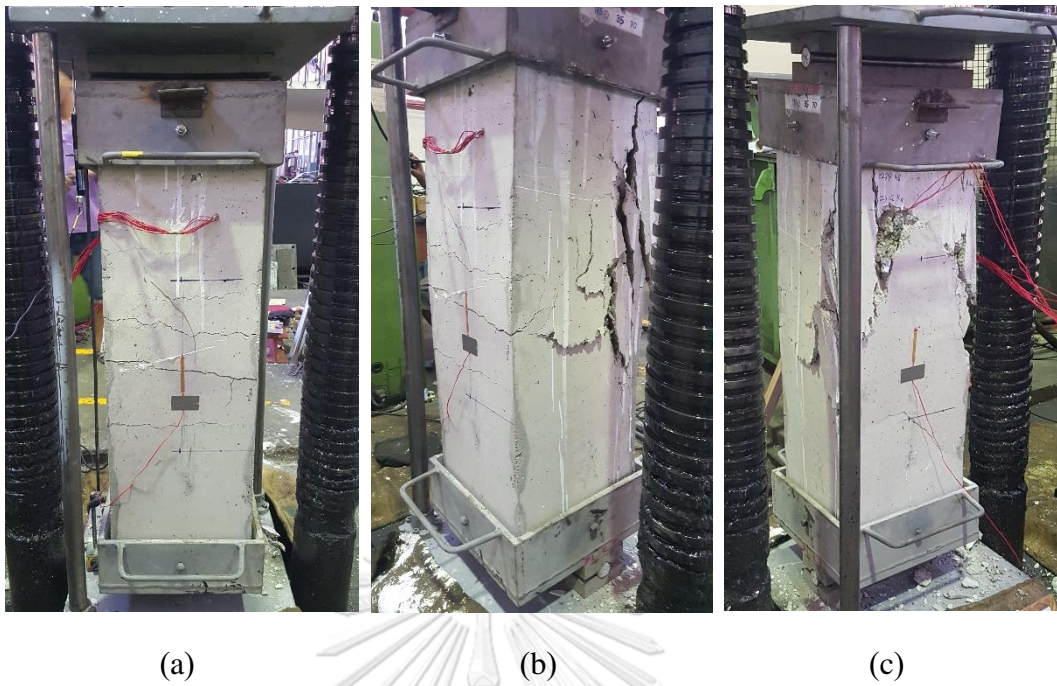
Figure 5.26 Failure of CECS column C1s-63-E1; (a) tension side; (b) side view; and (c) compression side.

(a) (b) (c)
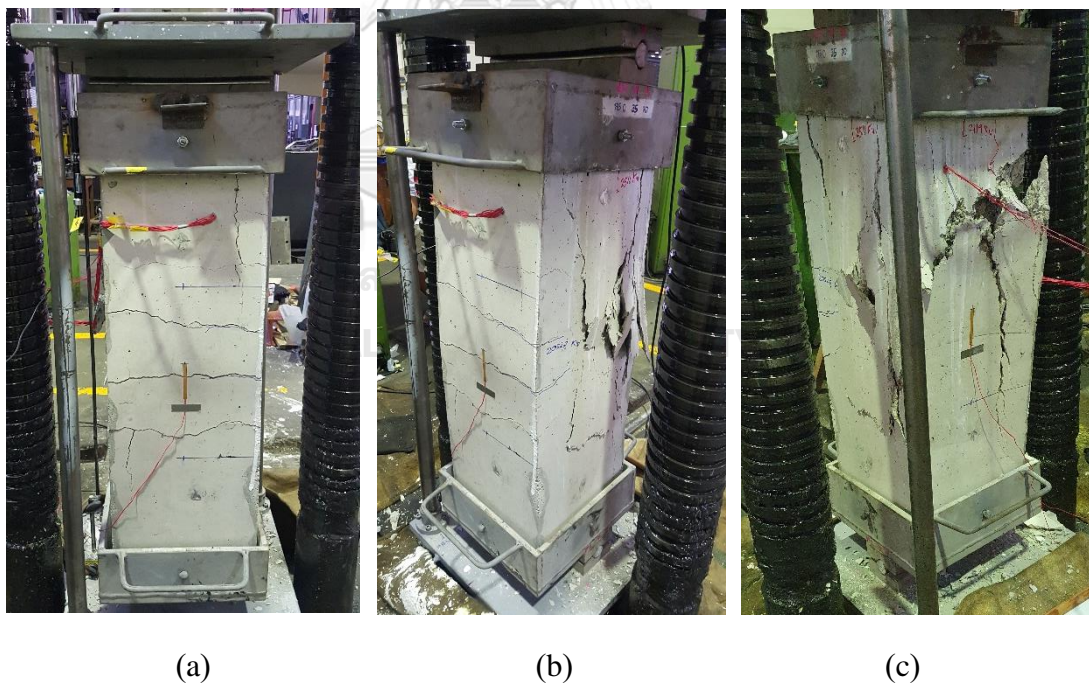
Figure 5.27 Failure of CECS column C2s-63-E1; (a) tension side; (b) side view; and (c) compression side.

For the composite columns subjected to eccentric loads E2: near the maximum loads, longitudinal crack occurred at the compression side; and, transverse crack occurred at the tension side at the same time. At the maximum loads, concrete crushing occurred in the compression side at mid-height of the columns, as shown in Figure 5.28 (b). After that, transverse crack expanded rapidly from the compression side to the tension side. The load carrying capacity of the column reduced immediately. Finally, transverse crack occurred at the tension side; and, the column deformed as bending failure occurred. Figures 5.29 and 5.30 show failure of the specimens C1s-63-E2 and C2s-63-E2.

Figures 5.31 and 5.32 show the comparison of the failure of the CECS and CES columns. Both CECS and CES columns exhibited similar failure characteristics. The failures on compression side of the columns with eccentric load E1 and E2 are similar. However, the failures on tension side have difference with an increase of the eccentricity. As the columns with eccentricity E2 have deep transverse crack than the columns with eccentricity E1.

(a)   (b)   (c)
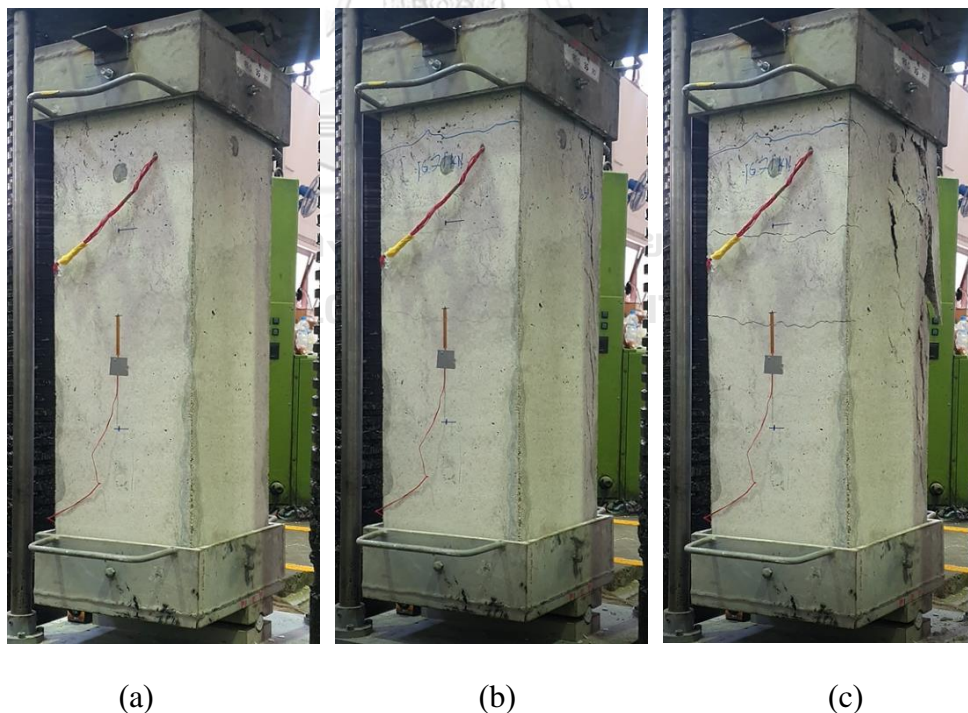
Figure 5.28 Failure of CECS column C1s-63-E2; (a) before test;
(b) at maximum loads; and (c) post peak.

(a)   (b)   (c)
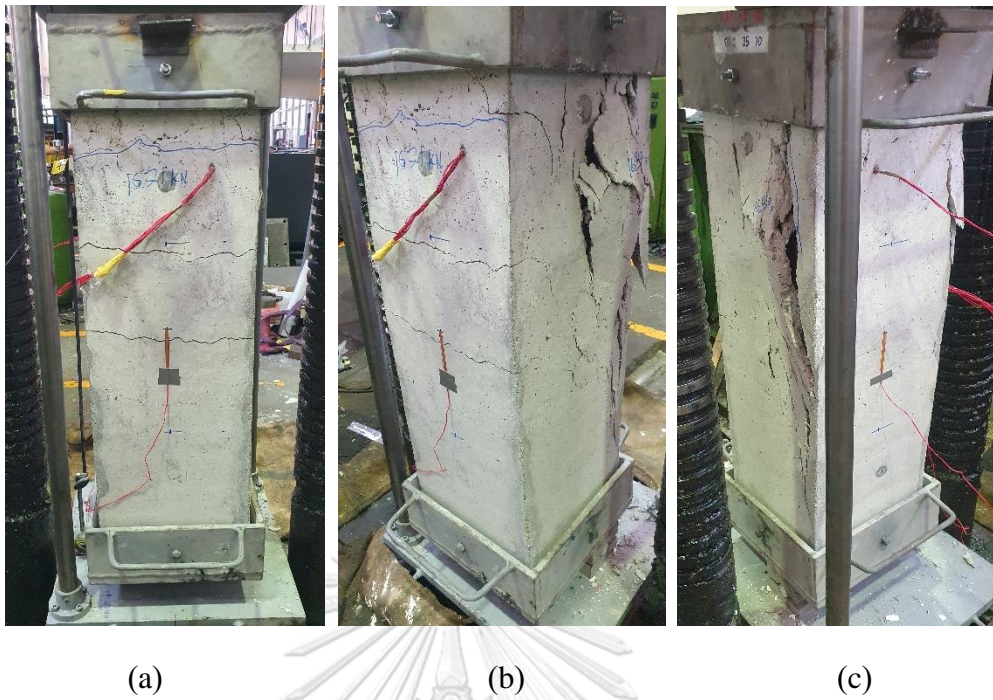
Figure 5.29 Failure of CECS column C1s-63-E2; (a) tension side; (b) side view;
and (c) compression side.

(a)   (b)   (c)
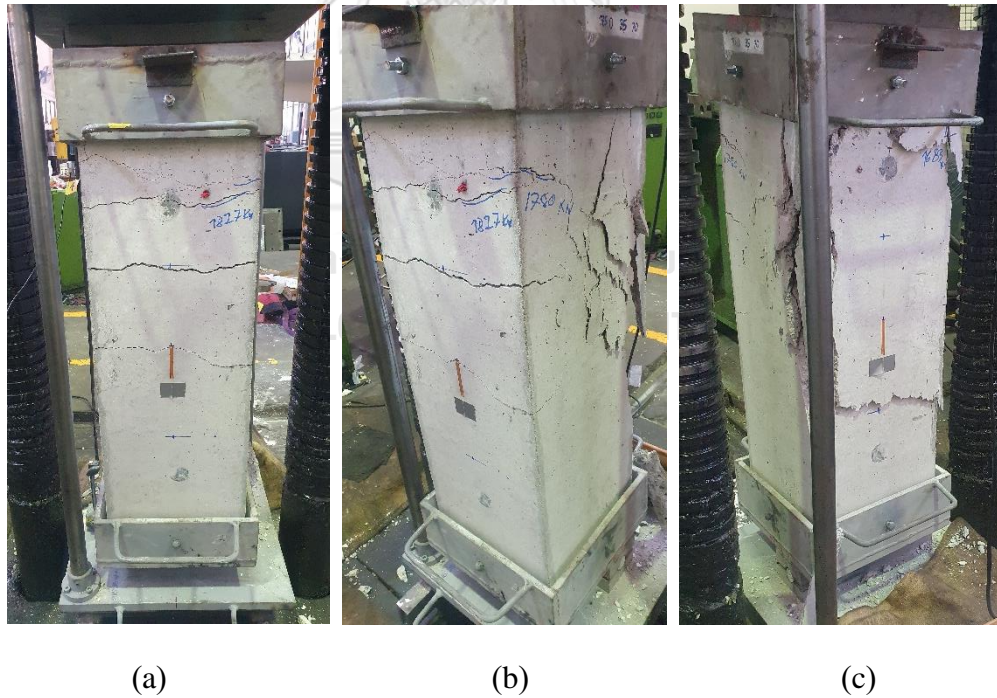
Figure 5.30 Failure of CECS column C2s-63-E2; (a) tension side; (b) side view;
and (c) compression side.

(a)   (b)   (c)
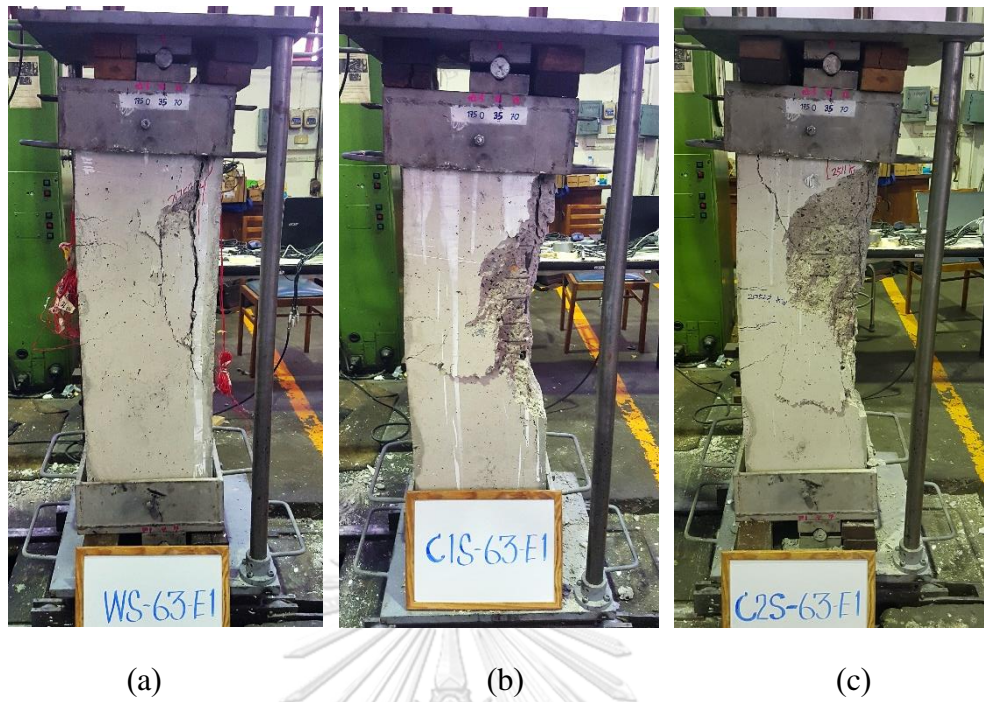
Figure 5.31 Failure of CECS column after tested; (a) Ws-63-E1; (b) C1s-63-E1; and (c) C2s-63-E1.

(a)   (b)   (c)
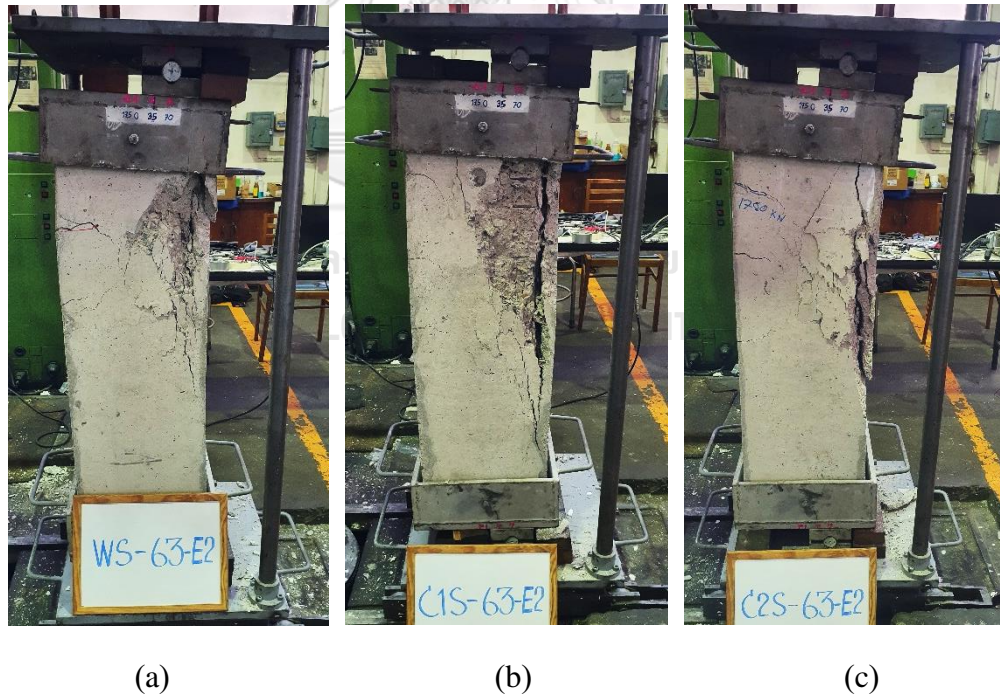
Figure 5.32 Failure of CECS column after tested; (a) Ws-63-E2; (b) C1s-63-E2; and (c) C2s-63-E2.

5.4.2   Load – axial strain curves

For the tested composite columns with shear studs subjected to concentric loadings, the axial compressive behavior of the columns is the same as the composite columns without shear studs as presented in section 5.2. However, the columns with shear studs have slightly higher axial compressive strength than the columns without shear studs. The maximum loads of C1s-63, C2s-63, and Ws-63 are 3482 kN, 3508 kN, and 3659 kN, respectively. Load – axial strain curves of the tested columns are shown in Figure 5.33.

(a)

(b)

(c)
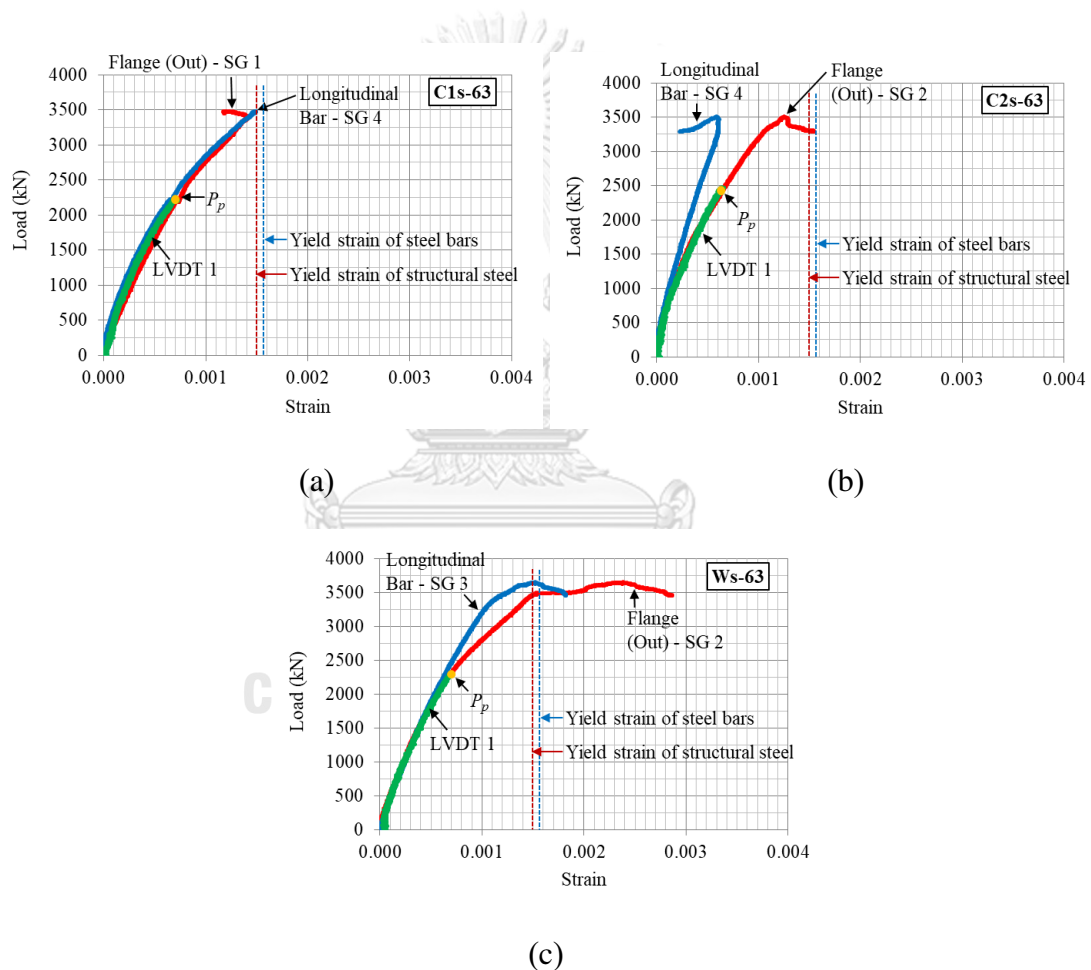
Figure 5.33 Load – strain curves; (a) C1s-63; (b) C2s-63; and (c) Ws-63.

For the tested composite columns with shear studs subjected to eccentric loadings, load – axial strain curves of the columns with eccentricity E1 and E2 are shown in Figures 5.34 and 5.35, respectively. The Figures 5.34 (a, c, and e) and

Figures 5.35 (a, c, and e) show the curves of strain gauges positioned at mid-height section (center of hole), as shown in Figure 4.16 (Section A-A'). Figures 5.34 (b, d and f) and 5.35 (b, d, and f) show the curves of strain gauges positioned at solid web section, as shown in Figure 4.16 (Section B-B').

For the load – axial strain curves of the columns with eccentricity E1, all strain increased in compression at initial state. However, the strain at different position depended on load distribution. For SG 15, which was positioned on concrete surface at compression side, the axial strain increased the most in compression from start to post-peak state. For SG 1 and SG 3, which were positioned on steel flange at compression side, the axial strain increased in compression from start to post-peak state. The curves showed that the compression steel yielded at maximum loads. For SG 2 and SG 4 which were positioned on steel flange at tension side, the axial strain increased in compression from start to maximum loads. After that, the strain returned to tension in post-peak state. For the SG 14, which was positioned on concrete surface at tension side, the axial strain increased in compression from start to maximum loads. After that, the strain returned to tension in post-peak state.

For the load – axial strain curves of the columns with eccentricity E2, most of the curves are similar to the columns with eccentricity E1 (except SG 14). For SG 14, which was positioned on concrete surface at tension side, the axial strain increased in tension from start to post-peak state.

(a)

(b)

(c)

(d)

(e)

(f)
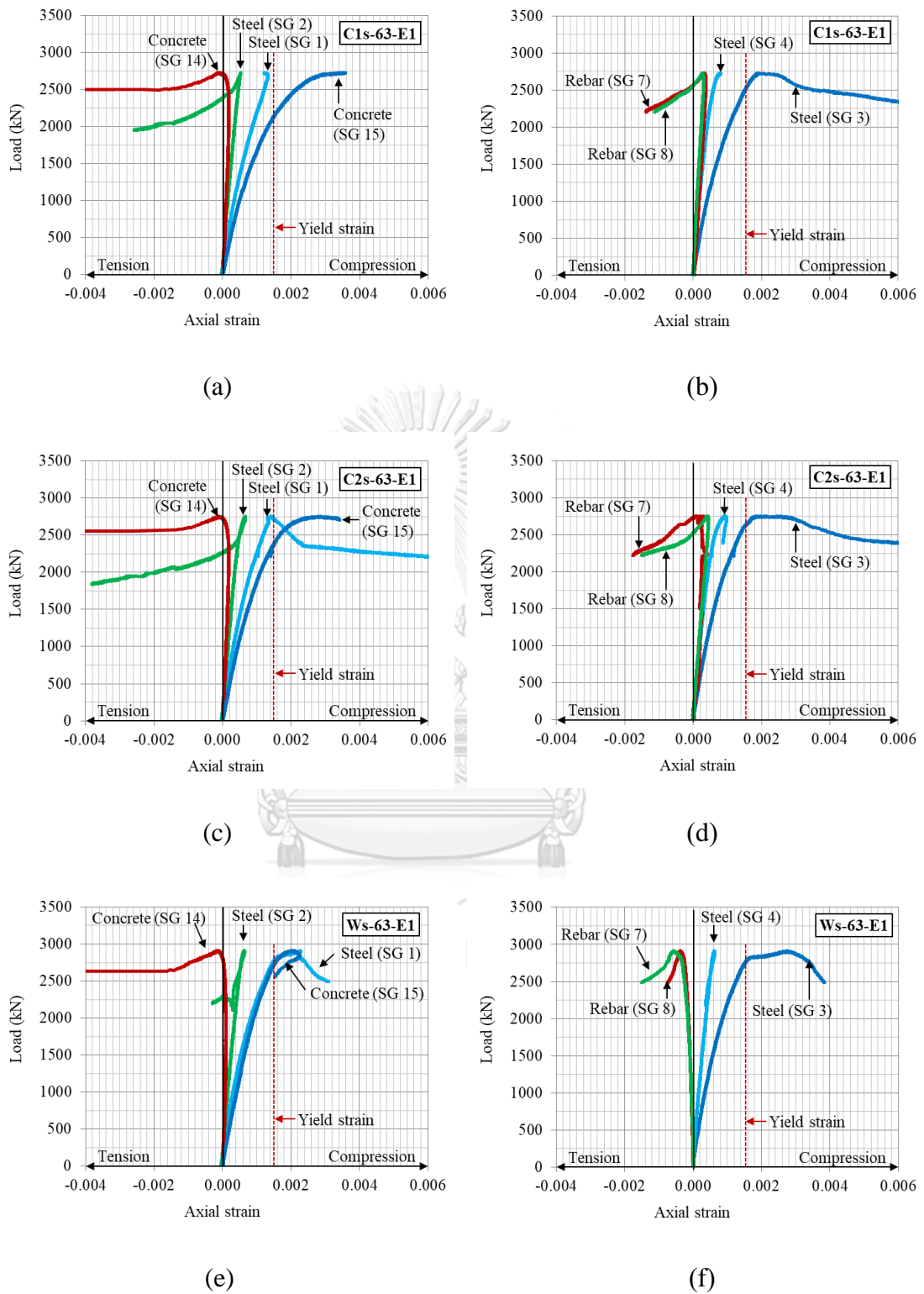
Figure 5.34 Load – axial strain curves; (a-b) C1s-63-E1; (c-d) C2s-63-E1; and (e-f) Ws-63-E1.
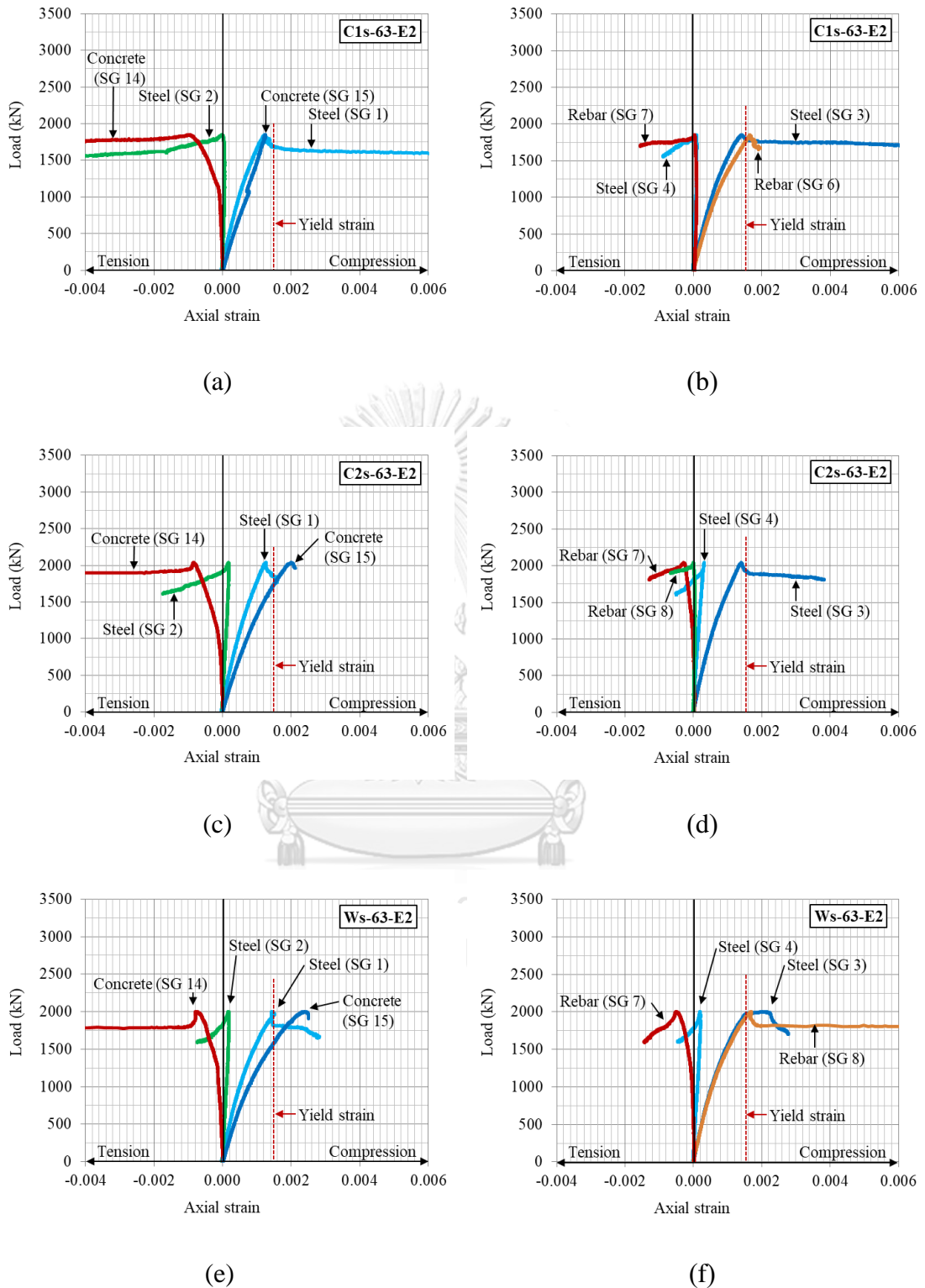
Figure 5.35 Load – axial strain curves; (a-b) C1s-63-E2; (c-d) C2s-63-E2; and (e-f) Ws-63-E2.

Figure 5.36 shows comparison of the curves of strain gauges positioned at solid web section and at center of hole section. The comparison shows that the strain gauges positioned at solid web section are slightly more axial strains than the strain gauges positioned at center of hole section. Because of specimens Ws-63-E1 and Ws-63-E2 have no openings, the strain gauges of two positions are similar.

Figure 5.37 shows axial strain contribution along column depth in each load state. The axial strain is collected by SG 1, SG 2, SG 14, and SG 15. The results showed that the strain distribution across the section remained linear up to over 80 % of maximum loads. The figure showed that the hypothesis plane-section remain plane is satisfied.

Table 5.4 shows maximum loads of the CES and CECS columns subjected to eccentric loadings. The CECS columns had slightly less compressive strength values than the CES columns with the average ratio of 0.96, 0.94, and 0.97 for concentric loadings, eccentric loadings E1, and eccentric loadings E2, respectively.
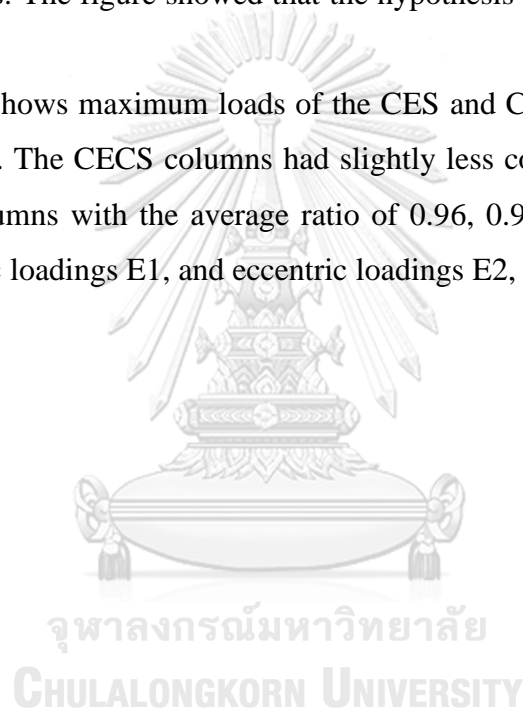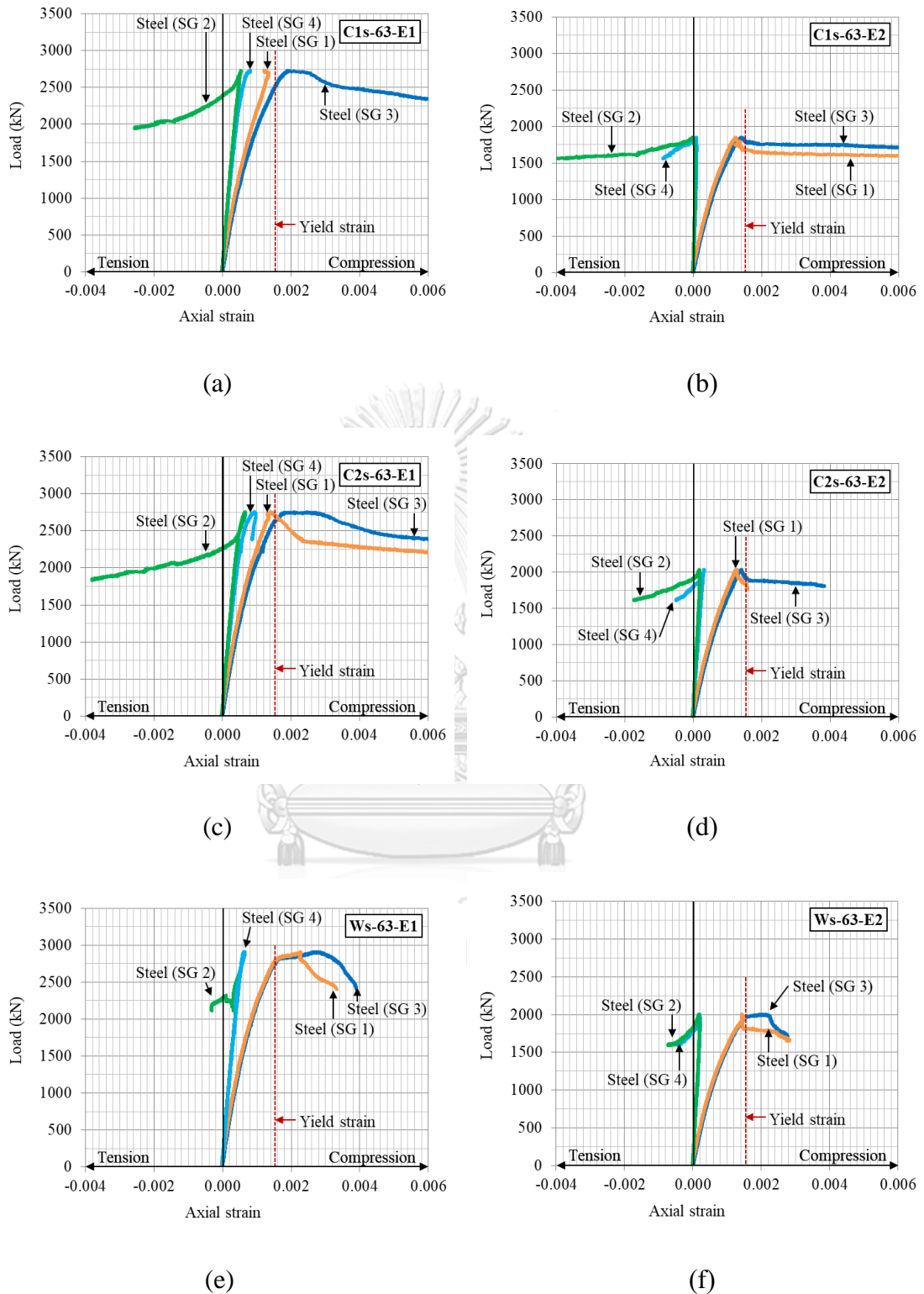
Figure 5.36 Comparison of load – axial strain curves between at solid web section and at center of hole section; (a) C1s-63-E1; (b) C1s-63-E2; (c) C2s-63-E1; (d) C2s-63-E2; (e) Ws-63-E1; and (f) Ws-63-E2.
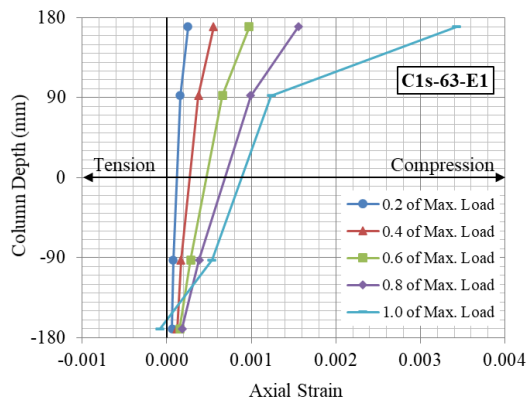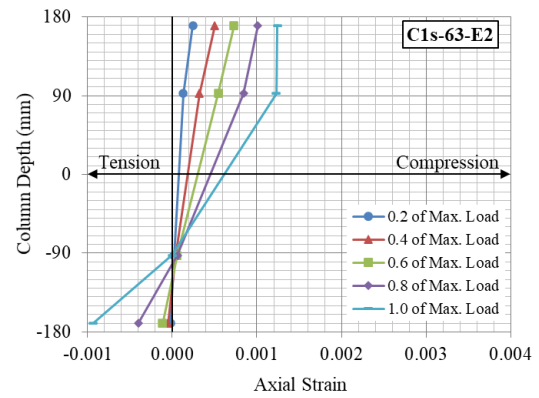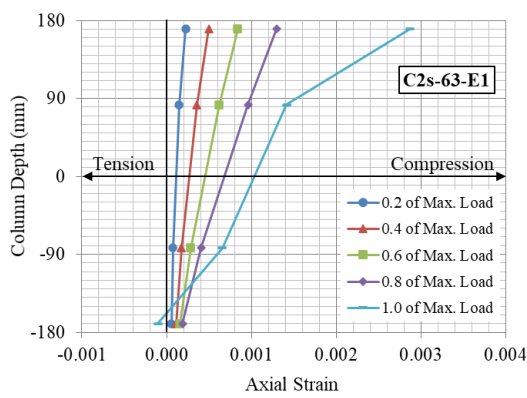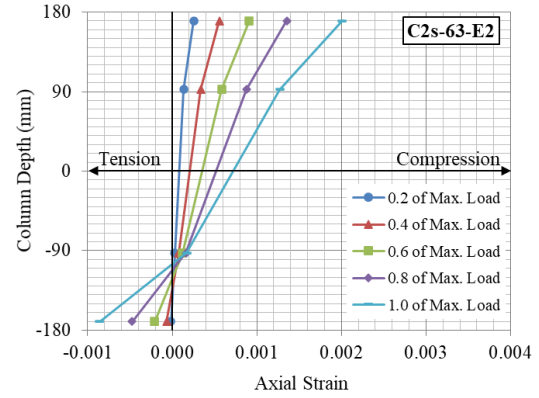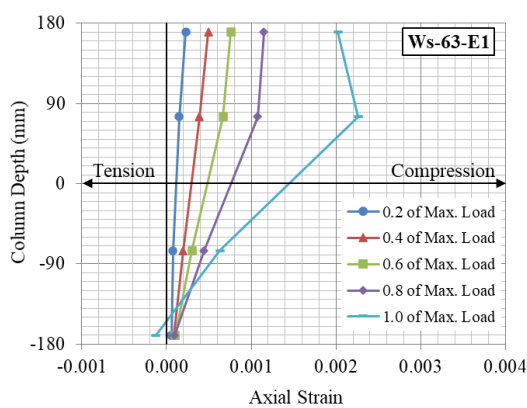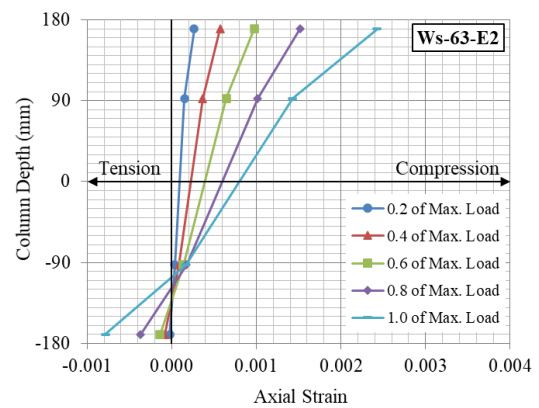
Figure 5.37 Axial strain at different load states of (a) C1s-63-E1; (b) C1s-63-E2; (c) C2s-63-E1; (d) C2s-63-E2; (e) Ws-63-E1; and (f) Ws-63-E2.

Table 5.4 Test results of cellular steel columns subjected to eccentric loadings.

Columns	Experimental results	Comparison (CECS / CES)
	Maximum load	Maximum load
	P_{max}	P_{max}
	kN	kN
	[1]	[1] / [1][a]
Ws-63	3659	-
C1s-63	3482	0.95
C2s-63	3508	0.96
Average		0.96
Ws-63-E1	2913	-
C1s-63-E1	2728	0.94
C2s-63-E1	2753	0.95
Average		0.94
Ws-63-E2	2003	-
C1s-63-E2	1852	0.92
C2s-63-E2	2042	1.02
Average		0.97

[a] Based on the CES columns.

5.4.3 Load – transverse strain curves

Figure 5.38 shows load – transverse curves of the tested composite columns with shear studs subjected to concentric loadings. The curves are similar to the curves of the composite columns without shear studs as presented in section 5.2.

Figure 5.39 shows load – transverse curves of the tested composite columns with shear studs subjected to eccentric loadings. All curves increased in tension from start to post-peak state. For SG 9 and SG 10, which were positioned on steel web compression and tension sides, the curves two different position are similar. For SG 11, SG 12, and SG 13, which were positioned on stirrup at different position, tension in the curves of compression side increased more than the curves of tension side.
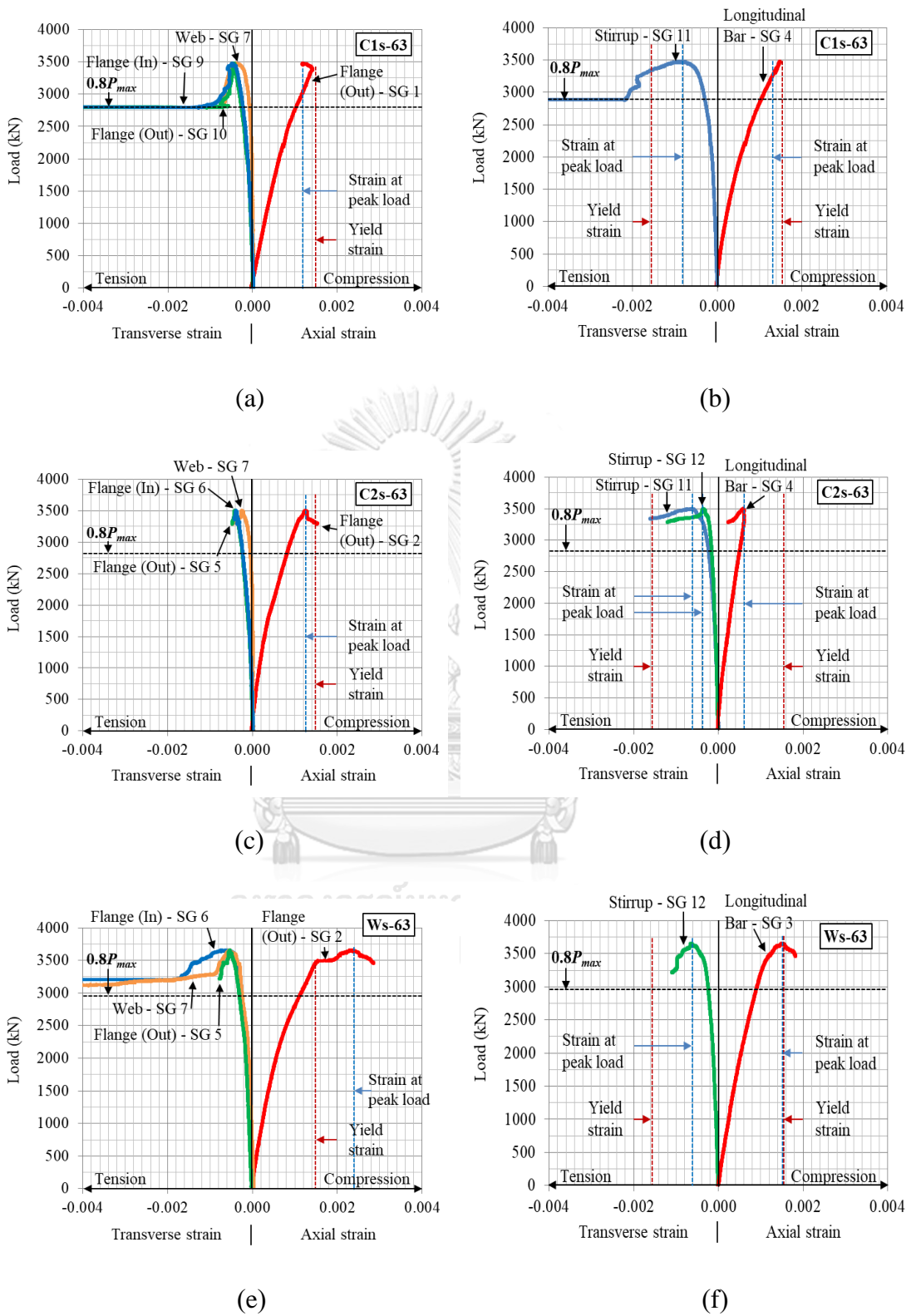
Figure 5.38 Load – axial and transverse strain curves; (a-b) C1s-63; (c-d) C2s-63; and (e-f) Ws-63.
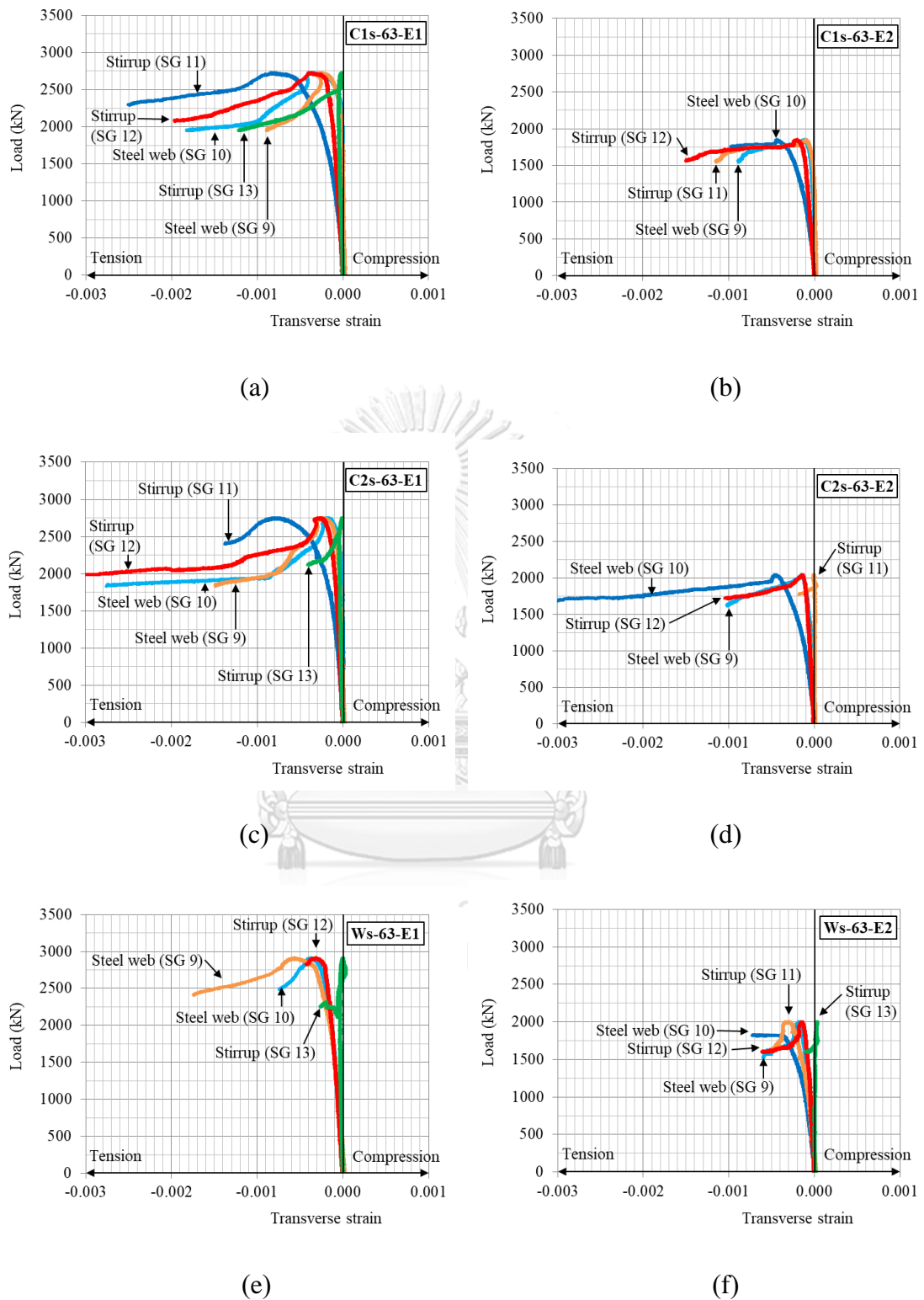
Figure 5.39 Load – transverse strain curves; (a) C1s-63-E1; (b) C1s-63-E2;
(c) C2s-63-E1; (d) C2s-63-E2; (e) Ws-63-E1; and (f) Ws-63-E2.

5.4.4 Effect of design parameters

Figure 5.40 shows a comparison between the compressive strength of bare steel columns and composite columns. The composite design enhanced the compressive strength of the CES and CECS columns with respect to the bare steel columns by 242 % and 241 – 250 %, respectively. The effects of eccentricity on the strength of bare steel and composite columns can be summarized as follows,

Effect of eccentricity on the strength of the bare steel columns: the strength of the parent steel column decreased by 13 % as eccentricity increased from 17.5 to 35 mm. On the other hand, the strength of the cellular steel columns decreased by 5 – 6 % as eccentricity increased from 17.5 to 35 mm.
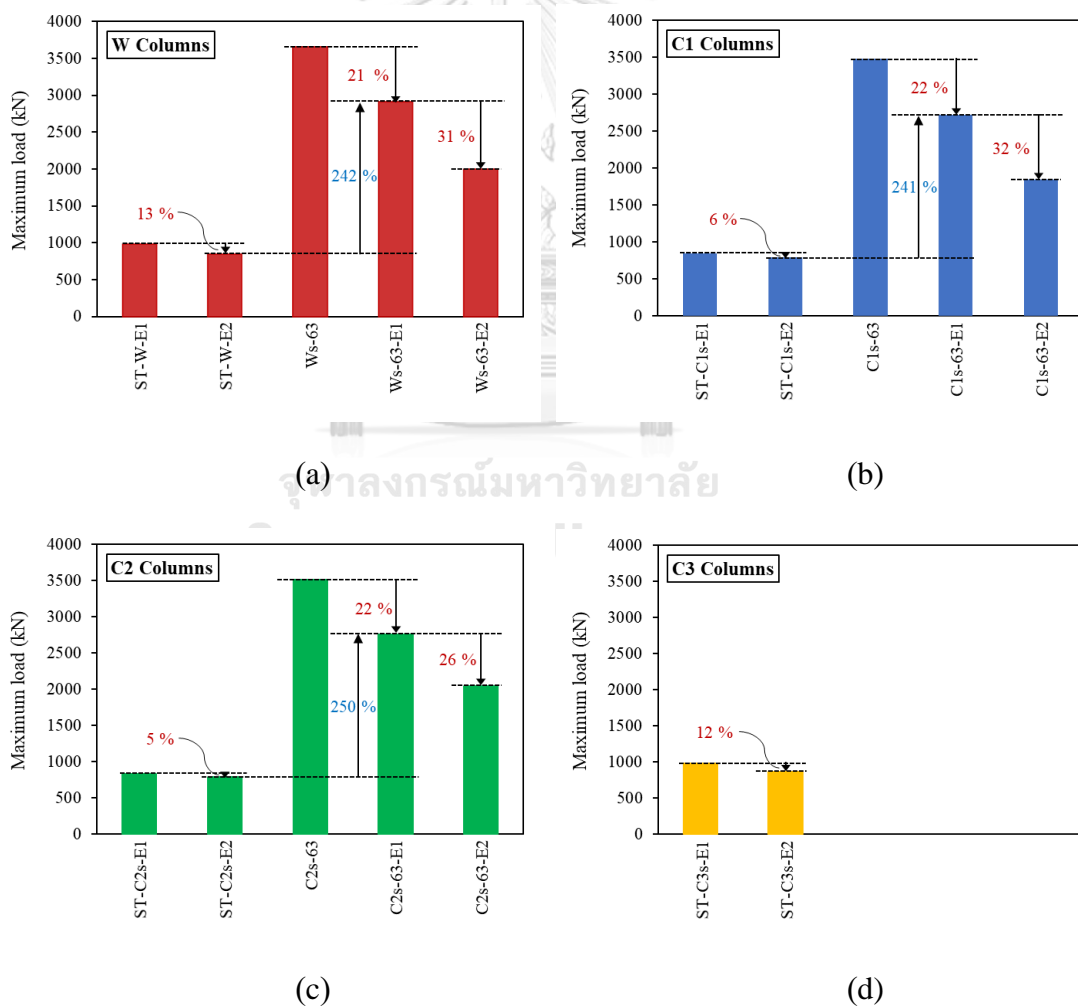
Figure 5.40 Comparison of compressive strength of eccentric loading columns;
(a) W columns; (b) C1 columns; (c) C2 columns; and (d) C3 columns.

Effect of eccentricity on the strength of the composite columns: the strength of the CES columns decreased by 20 % and 31 % as eccentricity increased from 17.5 to 35 mm and 35 to 70 mm. On the other hand, the strength of the CECS columns decreased by 22 % and 26 – 32 % as eccentricity increased from 17.5 to 35 mm and 35 to 70 mm.

5.4.5 Conclusions

The conclusions of the experimental results of the CECS columns subjected to eccentric loadings are as follows,

- Failure mode of the composite columns subjected to eccentric loads E1 (35 mm): near the maximum loads, longitudinal crack occurred at the compression side and corner. At the maximum loads, concrete crushing occurred on the compression side at mid-height of the columns. After that, transverse crack expanded rapidly from the compression side to the tension side. The load carrying capacity of the column reduced immediately. Finally, transverse crack occurred on the tension side.

- Failure mode of the composite columns subjected to eccentric loads E2 (70 mm): near the maximum loads, longitudinal crack occurred on the compression side; and, transverse crack occurred on the tension side at the same time. At the maximum loads, concrete crushing occurred on the compression side and large transverse crack occurred on the tension side at the same time at mid-height of the columns.

- Load – axial strain curves of the columns with eccentricity E1 (35 mm): all strain increased in compression at initial state. For the strain gauges positioned on concrete surface on compression side, the axial strain increased the most in compression from start to post-peak state. For the strain gauges positioned on steel flange on compression side, the axial strain increased in compression from start to post-peak state. The curves showed that the compression steel yielded at maximum loads. For the strain gauges positioned on steel flange on tension side, the axial strain increased in compression from start to maximum loads. After that, the strain returned to tension in post-peak state. For the strain gauges positioned on concrete surface on tension side, the axial strain increased in compression from start

to maximum loads. After that, the strain returned to tension in post-peak state.

- Load – axial strain curves of the columns with eccentricity E2 (70 mm): most of the curves are similar to the columns with eccentricity E1. Except strain gauge positioned on concrete surface on tension side, the axial strain increased in tension from start to post-peak state.

- Axial strain contribution along column depth: the strain distribution across the section remain linear up to over 80 % of maximum loads. The hypothesis plane-section remain plane is satisfied.

- Maximum loads of the CES and CECS columns: The CECS columns had slightly less compressive strength values than the CES columns with the average ratio of 0.96, 0.94, and 0.97 for concentric loadings, eccentric loadings E1 (35 mm) and eccentric loadings E2 (70 mm), respectively.

- Load – transverse strain curves: All curves increased in tension from start to post-peak state. For the strain gauges positioned on steel web compression and tension sides, the curves from two different position are similar. For the strain gauges positioned on stirrup at different position, the curves of compression side increased in tension more than the curves of tension side.

- Comparison between the compressive strength of bare steel columns and composite columns: the composite design enhanced the compressive strength of the CES and CECS columns with respect to the bare steel columns by 242 % and 241 – 250 %, respectively.

- Effect of eccentricity on the strength of the bare steel columns: the strength of the parent steel column decreased by 13 % as eccentricity increased from 17.5 to 35 mm. On the other hand, the strength of the cellular steel columns decreased by 5 – 6 % as eccentricity increased from 17.5 to 35 mm.

- Effect of eccentricity on the strength of the composite columns: the strength of the CES columns decreased by 20 % and 31 % as eccentricity increased from 17.5 to 35 mm and 35 to 70 mm. On the other hand, the strength of the CECS columns decreased by 22 % and 26 – 32 % as eccentricity increased from 17.5 to 35 mm and 35 to 70 mm.

CHAPTER 6
ANALYTICAL MODELS

6.1 Proposed load – axial strain model of cellular steel columns

In this section, equations for predicting the axial stiffness and yield load of the cellular steel columns are proposed.

6.1.1 Yield loads of cellular steel columns

For the prediction of yield loads of the cellular steel columns, the full yielding at the net cross-section area is assumed, as shown in [Section A-A', B-B' and C-C' at hole centerline of the cellular steel columns] Figure 4.1 (a-c), which yield loads:

$$P_{y,ana} = A_{s,net} f_{ys} \tag{6.1}$$

Where

$A_{s,net}$ = net cross-sectional area of structural steel member, Eq. (4.3);

f_{ys} = yield stress of structural steel.

As shown in Table 6.1, Eq. (6.1) overestimated the measured yield loads of the cellular steel columns by 1 %.

6.1.2 Axial stiffnesses of cellular steel columns

The prediction of axial stiffnesses of the cellular steel columns is based on an equivalent cross-section area of structural steel member, as shown in Eq. (6.2).

$$\left(EA/L\right)_{ana} = E_s A_{s,eq}/L \tag{6.2}$$

Where

$A_{s,eq}$ = equivalent cross-sectional area of structural steel member, Eq. (6.9);

E_s = elastic modulus of structural steel;

L = length of column.

As the cellular steel column is the nonprismatic member, the equivalent cross-sectional area ($A_{s,eq}$) can be derived for the prediction of axial stiffness of the cellular steel columns. Refer to Figure 6.1, the total axial deformation of the cellular steel column over the gauge length "S" is

$$\Delta_{total} = \Delta_{solid} + \Delta_{hole} \tag{6.3}$$

$$\frac{PS}{A_{s,eq}E_s} = \frac{P(S-D_o)}{A_{s,g}E_s} + 2\int_0^{D_o/2} \frac{P}{E_s A_s(x)} dx \tag{6.4}$$

$$\frac{PS}{A_{s,eq}E_s} = \frac{P(S-D_o)}{A_{s,g}E_s} + 2\frac{P}{E_s}\int_0^{D_o/2} \frac{1}{A_s(x)} dx \tag{6.5}$$

$$\frac{S}{A_{s,eq}} = \frac{(S-D_o)}{A_{s,g}} + 2\int_0^{D_o/2} \frac{1}{A_s(x)} dx \tag{6.6}$$

$$\frac{1}{A_{s,eq}} = \frac{(S-D_o)}{A_{s,g}S} + \frac{2}{S}\int_0^{D_o/2} \frac{1}{A_s(x)} dx \tag{6.7}$$

Where P is the axial load, consider an integral term in Eq. (6.7)

$$A_s(x) = A_{s,g} - 2t_w\sqrt{\left(\frac{D_o}{2}\right)^2 - x^2} \tag{6.8}$$

Then, Eq. (6.7) becomes

$$\frac{1}{A_{s,eq}} = \frac{(S-D_o)}{A_{s,g}S} + \frac{2}{S}\int_0^{D_o/2} \frac{1}{A_{s,g} - 2t_w\sqrt{\left(\frac{D_o}{2}\right)^2 - x^2}} \, dx \tag{6.9}$$

Eq. (6.8) can also be written in the polar form as

$$A_s(\theta) = A_{s,g} - 2t_w\frac{D_o}{2}\cos(\theta) \tag{6.10}$$

Where

$$x = \frac{D_o}{2}\sin(\theta) \tag{6.11}$$

$$dx = \frac{D_o}{2}\cos(\theta)d\theta \tag{6.12}$$

Then, Eq. (6.7) becomes

$$\frac{1}{A_{s,eq}} = \frac{(S - D_o)}{A_{s,g}S} + \frac{2}{S}\int_0^{\pi/2}\frac{\frac{D_o}{2}\cos(\theta)}{A_{s,g} - 2t_w\frac{D_o}{2}\cos(\theta)}d\theta \tag{6.13}$$

Simplifying Eq. (6.13), the equivalent cross-sectional area ($A_{s,eq}$) can be determined from

$$\frac{1}{A_{s,eq}} = \frac{(S - D_o)}{A_{s,g}S} + \frac{D_o}{A_{s,g}S}\int_0^{\pi/2}\frac{1}{\sec(\theta) - \frac{t_w D_o}{A_{s,g}}}d\theta \tag{6.14}$$

Where

$A_{s,eq}$ = equivalent cross-sectional area of cellular steel member;

$A_{s,g}$ = gross cross-sectional area of cellular steel member (at solid web section);

D_o = hole diameter of cellular column;

E_s = elastic modulus of structural steel;

S = center-to-center hole spacing of cellular column;

t_w = web thickness of structural steel;

Δ_{hole} = axial deformation along the hole section of the cellular steel column;

Δ_{solid} = axial deformation along the solid web section of the cellular steel column;

Δ_{total} = total axial deformation of the cellular steel column.

(a)   (b)
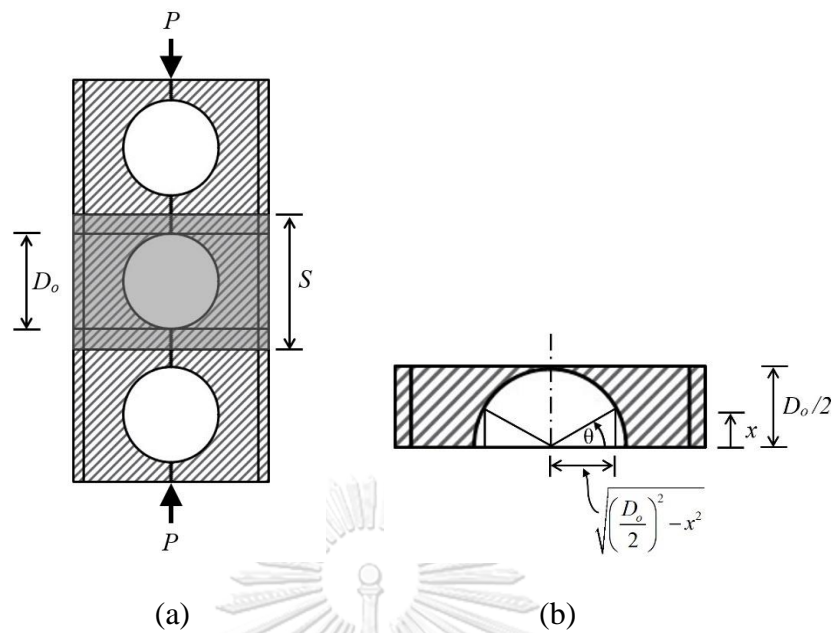
Figure 6.1 Determination of equivalent axial stiffness; (a) cellular steel column;
and (b) nonuniform section.

For the equivalent cross-sectional area of each tested column as shown in Table 6.1, gauge length "S" used the LVDT gauge length. In Table 6.1, Eq. (6.2) underestimated the axial stiffness of cellular steel columns by 6 %.

Table 6.1 Test and predicted results of bare steel columns.

Columns	Section analysis			Experimental results		Comparison	
						Experiment / Analysis	
	Equivalent area	Axial stiffness	Yield load	Axial stiffness	Yield load	Axial stiffness	Yield load
	$A_{s,eq}$	$(EA/L)_{ana}$	$P_{y, ana}$	$(EA/L)_{exp}$	$P_{y, exp}$	$(EA/L)_{exp} \div (EA/L)_{ana}$	$P_{y, exp} \div P_{y, ana}$
	cm^2	MN/m	kN	MN/m	kN	-	-
	[1]	[2]	[3]	[4]	[5]	[4] / [2]	[5] / [3]
ST-W	40.15	4131	1234	4175	1292	1.01	1.05
ST-C1	39.36 [a]	4047	1114	4477	1094	1.11	0.98
ST-C2	39.07 [a]	4016	1103	4114	1099	1.02	1.00
ST-C3	38.35 [a]	3941	1114	4193	1103	1.06	0.99
	Average					1.06	0.99

[a] Based on the actual LDVT gauge.

6.1.3 Proposed load – axial strain model of cellular steel columns

To develop the load – strain curve of the cellular steel column, stress – strain model of steel of Giuffrè and Pinto (1970) was used as a prototype. First, the stress – strain model was transformed into the load – strain model. After that, the equation was revised with the cellular steel columns. The equation was derived as follows, The stress – strain model of steel of Giuffrè and Pinto (1970) is

$$f_s = \frac{E_s \varepsilon_s}{\left[1 + \left(\frac{E_s \varepsilon_s}{f_{y,s}}\right)^R\right]^{\frac{1}{R}}} \tag{6.15}$$

For transform the stress – strain curve to be the load – strain curve, the equation Eq. (6.15) is transformed as follow,

$$P_s = \frac{E_s \varepsilon_s A_s}{\left[1 + \left(\frac{E_s \varepsilon_s}{f_{y,s}}\right)^R\right]^{\frac{1}{R}}} \tag{6.16}$$

The Eq. (6.16) is the equation for predicting load – strain curves of the bare steel columns, as shown in Figure 6.2. For the cellular steel columns, the equation was transformed as follows,

$$P_s = \frac{E_s^* \varepsilon_s A_{s,net}}{\left[1 + \left(\frac{E_s^* \varepsilon_s}{f_{y,s}}\right)^R\right]^{\frac{1}{R}}} \tag{6.17}$$

Where

$$E_s^* = \frac{E_s A_{s,eq}}{A_{s,net}} \tag{6.18}$$

R = parameter ($R = 10$ recommended).

Figure 6.2 shows proposed load – strain curve model of the cellular steel columns. The initial slope of the curve is axial stiffness of the columns. The curve is flat at yield load of the columns.
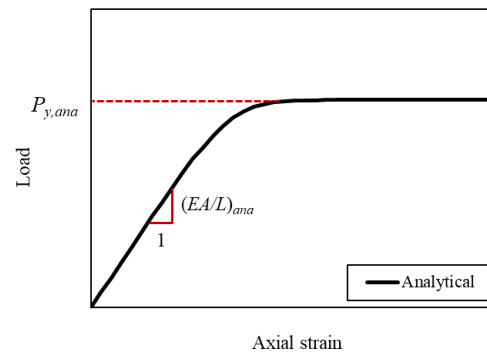
Figure 6.2 Proposed load – strain curve model of cellular steel columns.

(a)

(b)

(c)
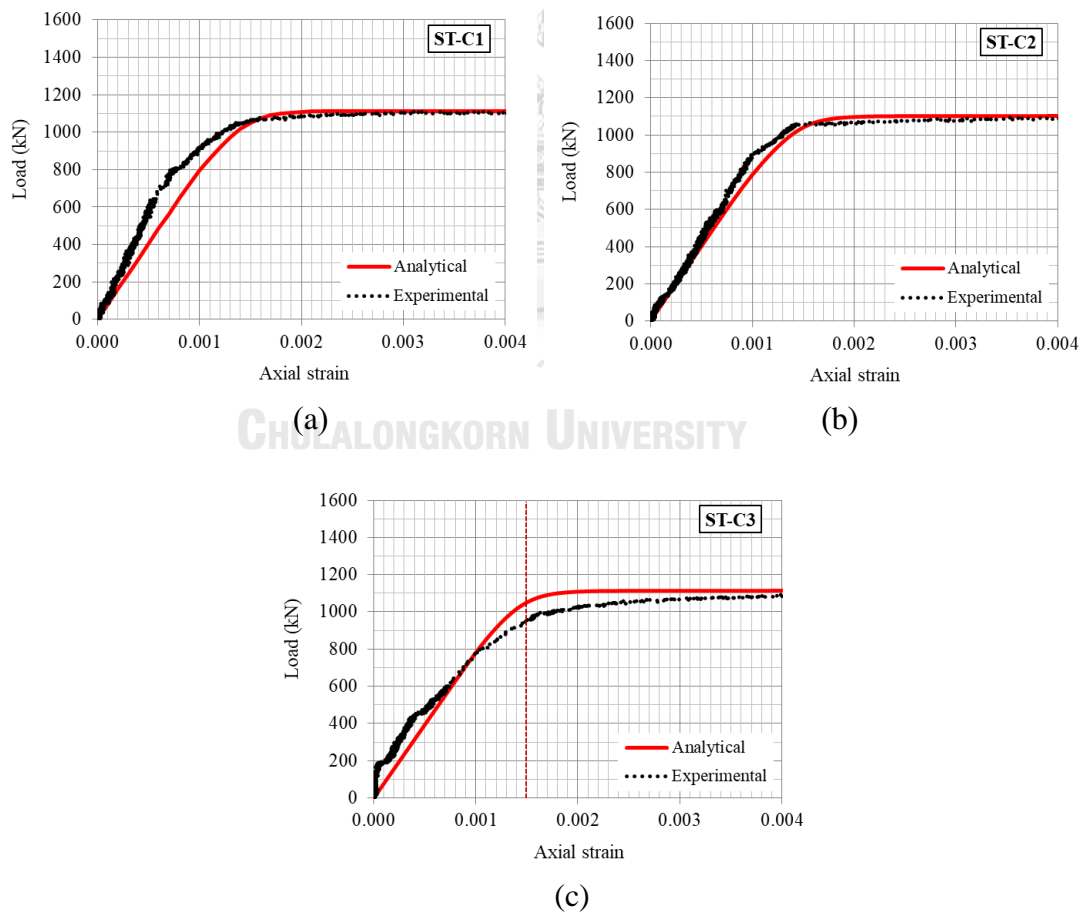
Figure 6.3 Validation of the proposed load – strain curves of tested cellular steel columns; (a) ST-C1; (b) ST-C2; and (c) ST-C3.

The load – strain curves were validated with the tested result (ST-C1, ST-C2, and ST-C3), as shown in Figure 6.3. The verification showed that the model accurately predicts the axial compressive behavior of the cellular steel columns. However, the model should be validated with more cellular steel columns in the future.

6.1.4   Conclusions

In this section, the equations for calculating yield loads, axial stiffnesses, and load – axial strain curve of the cellular steel columns are proposed. The proposed equations and curve were verified with the tested cellular steel columns in this research. However, the model should be validated with more cellular steel columns in the future.

6.2 Proposed analytical model of CES columns

This section proposes analytical model for predicting the axial load – strain relation of the CES columns subjected to concentric loading. This model based on the models of CES columns of Chen and Wu (2017) and Chen and Lin (2006). The design chart for calculating compressive strength of confined concrete, which proposed by Mander et al. (1988), was adopted to predict the confined concrete of the CES columns that contain any doubly-symmetric structural steel shapes. This proposed analytical model considers the concrete confinement effects, which increase the compressive strength of confined concrete and reduce the web strength of structural steel, and the buckling of longitudinal steel reinforcements.

6.2.1   Load – axial strain model

This analytical model predicts the load – axial strain relation of the CES columns based on section analysis method by combining all materials together. The CES column section consists of unconfined concrete, partially confined concrete, highly confined concrete, structural steel and longitudinal bars, as shown in Figure 6.4.
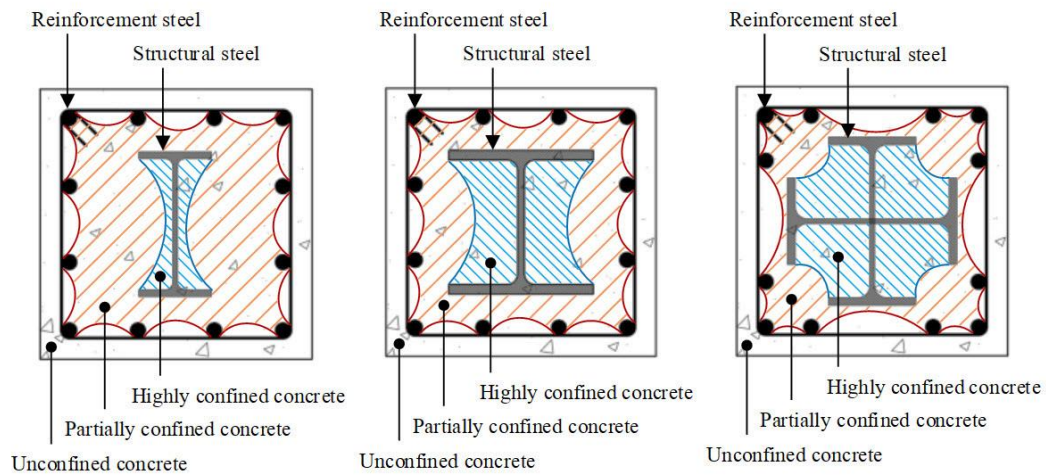
Figure 6.4 Materials in concrete-encased steel columns.

The axial load capacity of all materials is combined to be the capacity of the CES column. An equation for combining the load at each strain is as follows,

$$P_{ana} = f_s A_s + f_{sr} A_{sr} + f_{uc} A_{uc} + f_{pc} A_{pc} + f_{hc} A_{hc} \tag{6.19}$$

Where

A_{hc} = cross-sectional area of highly confined concrete;

A_{pc} = cross-sectional area of partially confined concrete;

A_{uc} = cross-sectional area of unconfined concrete;

f_{hc} = stress of highly confined concrete;

f_{pc} = stress of partially confined concrete;

f_s = stress of structural steel;

f_{sr} = stress of longitudinal rebar;

f_{uc} = stress of unconfined concrete.

Figure 6.5 shows the use of this model to predict the axial load – strain relation of the specimens of Chen and Yeh (1996) and Zhu et al. (2014).

Assumptions of the model are as follows,

1. The axial compressive strain is assumed to be uniform distribution.

2. Load capacity of each materials are calculated based on corresponding uniaxial stress – strain relations.

3. Local buckling of longitudinal bars is assumed.

4. Strength reduction of web of structural steel is caused by expansion of concrete.

5. Concrete confinement effect is caused by structural steel and stirrups.

6. Second-order effect is ignored.

Figure 6.6 shows procedure to calculate the axial load – strain relation of each materials of the CES column. The details to calculate the stress – strain relation of each materials of the CES column is shown in next sections.
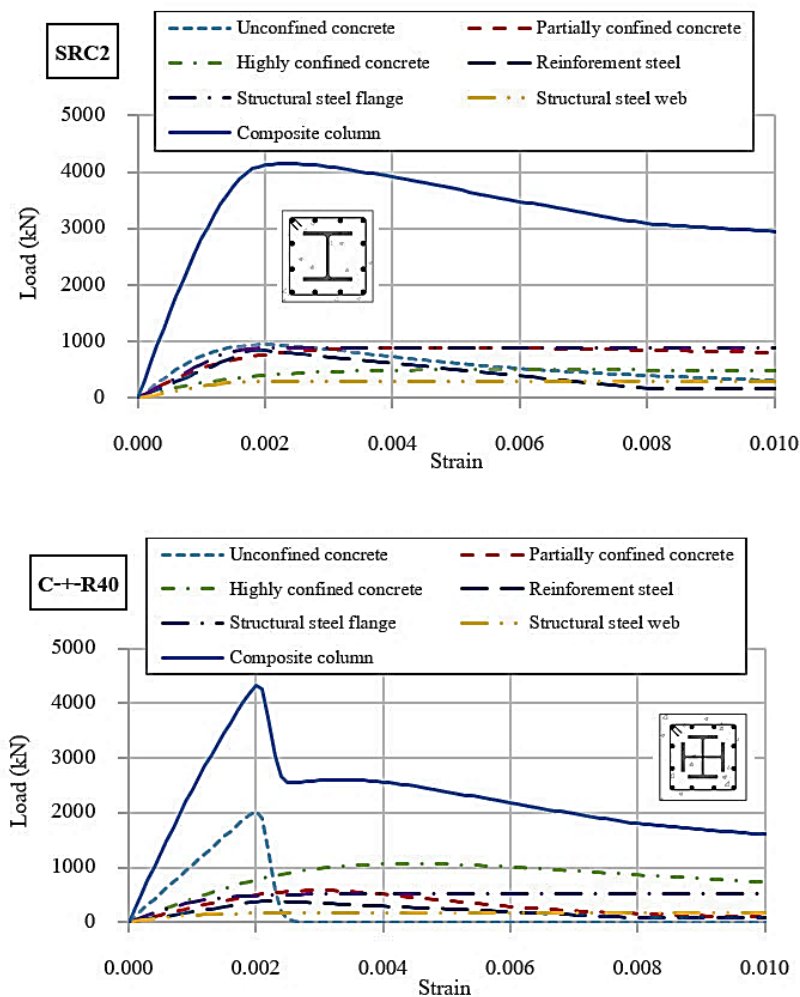
Figure 6.5 Axial load – strain relation of CES columns from (a) Chen and Yeh (1996); and Zhu et al. (2014).
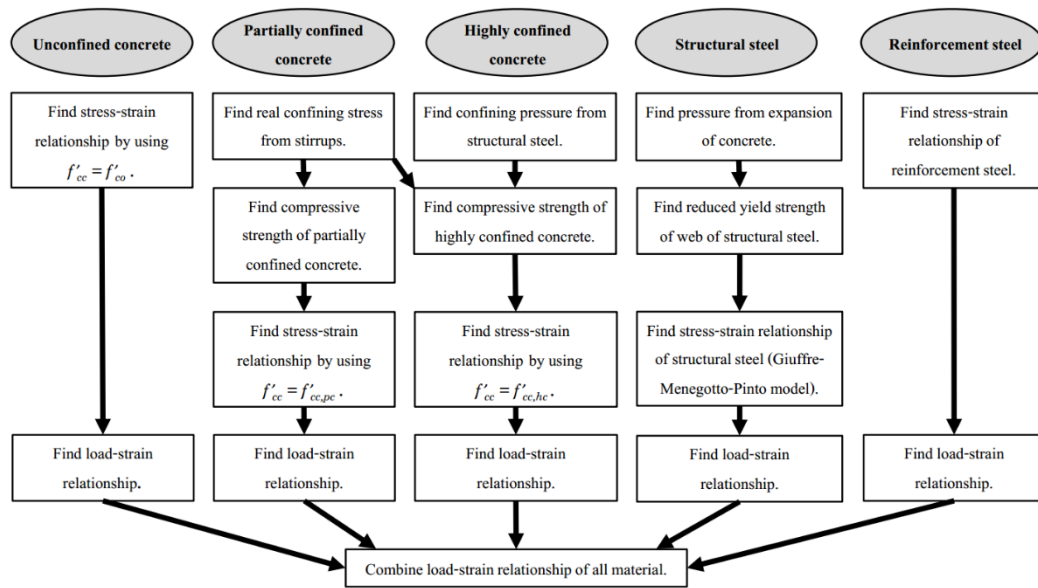
Figure 6.6 Procedure for predicting axial load – strain relation of the CES column.

6.2.2 Constitutive model for concrete

As shown in Figure 6.4, concrete of the CES columns is divided into 3 zones consisting of unconfined concrete, partially confined concrete, and highly confined concrete. The highly confined concrete is the concrete confined by structural steel and stirrups. The partially confined concrete is the concrete confined by stirrups only. The unconfined concrete is outside the stirrups. The stress – strain relation of the concrete, as shown in Figure 6.7, is based on model of Mander et al. (1998) as follows,

$$f_c = \frac{f_{cc}{}'}{r - 1 + X^r} \tag{6.20}$$

$$X = \frac{\varepsilon_c}{\varepsilon_{cc}} \tag{6.21}$$

$$r = \frac{E_c}{E_c - E_{sec}} \tag{6.22}$$

$$E_{sec} = \frac{f_{cc}{}'}{\varepsilon_{cc}} \tag{6.23}$$

$$\varepsilon_{cc} = \varepsilon_{co}\left[1+5\left(\frac{f_{cc}{}'}{f_{co}{}'}-1\right)\right] \tag{6.24}$$

$$\varepsilon_{co} = 0.002 \tag{6.25}$$

$$f_{cc}{}' = f_{co}{}' \quad \text{for unconfined concrete} \tag{6.26}$$

$$f_{cc}{}' = f_{co,p}{}' \text{ for partially confined concrete} \tag{6.27}$$

$$f_{cc}{}' = f_{co,h}{}' \text{ for highly confined concrete} \tag{6.28}$$

Where

E_c =   elastic modulus of concrete;

E_{sec} =   secant modulus of concrete at peak strength of confined concrete;

$f_{cc}{}'$ =   compressive strength of confined concrete;

$f_{co}{}'$ =   compressive strength of concrete cylinder;

ε_c =   corresponding strain of concrete;

ε_{co} =   corresponding strain at compressive strength of concrete cylinder.

For the compressive strength of highly confined concrete ($f_{co,h}{}'$), the strength is calculated using the design chart proposed by of Mander et al. (1988), as shown in Figure 6.8. The design chart, which was proposed for confined concrete of RC columns, is adopted for using with confined concrete of CES columns. The compressive strength is calculated based on lateral confined pressure which it is confined by structural steel and stirrups ($f_{le,h}{}'$), as shown in Eq. (6.29).

$$f_{le,h}{}' = f_{le,r}{}' + f_{le,s}{}' \tag{6.29}$$

Where

$f_{le,r}{}'$ =   lateral confining pressure from stirrups;

$f_{le,s}{}'$ =   lateral confining pressure from structural steel.

For the compressive strength of partially confined concrete ($f_{co,p}'$), the strength is calculated by using model proposed by of Cusson and Paultre (1995). The compressive strength is calculated based on lateral confined pressure which is confined by stirrups only ($f_{le,p}'$), as shown in Eq. (6.30).

$$f_{le,p}' = f_{le,r}' \tag{6.30}$$
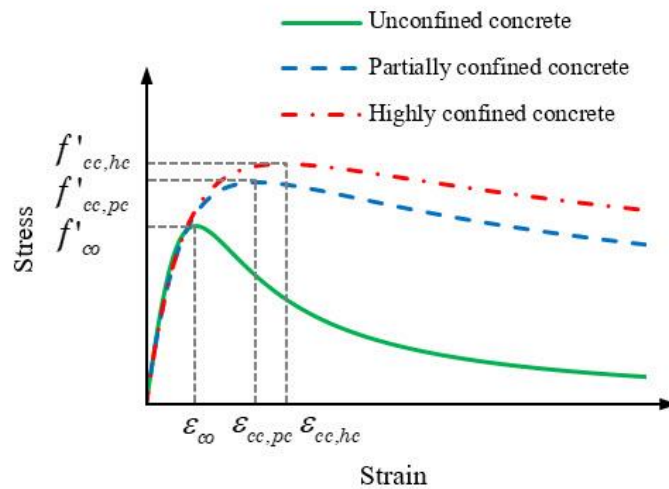
Figure 6.7 Stress – strain relation of unconfined, partially confined and highly confined concrete.
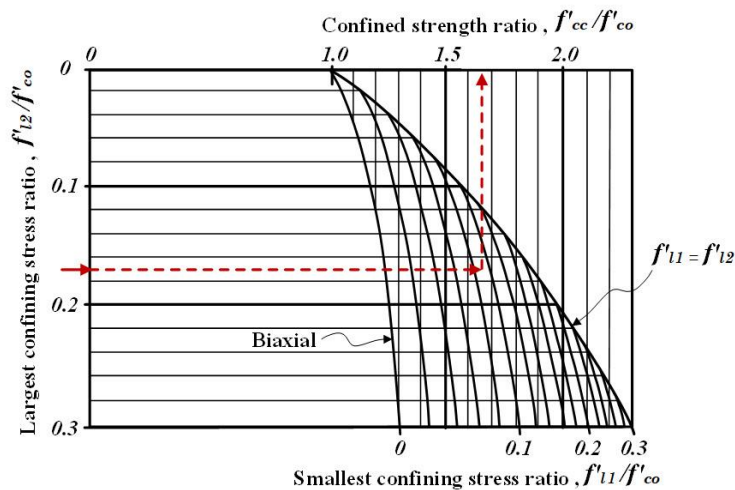
Figure 6.8 Design chart for calculating compressive strength of confined concrete (Mander et al., 1988).

The lateral confining pressure caused by stirrups ($f_{le,r}'$) is referred to the model by Cusson and Paultre (1995). The lateral confining pressure is calculated by using real stress in stirrups (f_{hcc}), as shown in Eq. (6.31). The equation was developed from the model of Mander et al. (1988), which was calculated by assuming yielding of stirrups. Equations for calculating the lateral confining pressure are as follows,

$$f_{le,r}' = \frac{k_{e,p} f_{hcc}}{s} \left(\frac{A_{shx} + A_{shy}}{c_x + c_y} \right) \tag{6.31}$$

$$k_{e,p} = \frac{\left(1 - \dfrac{\sum w_i^2}{6 c_x c_y}\right)\left(1 - \dfrac{s'}{2 c_x}\right)\left(1 - \dfrac{s'}{2 c_y}\right)}{\left(1 - \rho_{cc}\right)} \tag{6.32}$$

$$f_{cc}' = f_{co}' + 2.1 f_{le,r}'^{0.7} f_{co}'^{0.3} \tag{6.33}$$

$$\varepsilon_{cc} = \varepsilon_{co} + 0.21 \left(f_{le,r}' \middle/ f_{co}' \right)^{1.7} \tag{6.34}$$

$$\varepsilon_{hcc} = \nu_c \varepsilon_{cc} - \frac{(1 - \nu_c) f_{le,r}'}{E_{sec}} \tag{6.35}$$

$$f_{hcc} = E_s \varepsilon_{hcc} \tag{6.36}$$

Where

A_{shx} = area of stirrups in the x direction;

A_{shy} = area of stirrups in the y direction;

c_x = concrete core dimension to center line of stirrup in x-direction;

c_y = concrete core dimension to center line of stirrup in y-direction;

E_s = elastic modulus of structural steel;

E_{sec} = secant modulus of concrete at peak strength of confined concrete;

f_{cc}' = compressive strength of confined concrete;

f_{co}' = compressive strength of concrete cylinder;

f_{hcc} = stress in the transverse reinforcement at the maximum strength of confined concrete;

$f_{le,r}'$ = lateral confining pressure from stirrups;

s' = clear longitudinal spacing of stirrup;

w_i' = clear transverse spacing between adjacent longitudinal bars;

ρ_{cc} = ratio of longitudinal reinforcement area to core section area;

ε_{co} = corresponding strain at compressive strength of concrete cylinder;

ε_{cc} = corresponding strain at compressive strength of confined concrete;

v_c = Poisson's ratio of concrete.

For calculating the lateral confining pressure by using the real stress in the stirrups, iterative procedure was used by following the step as follows,

1. Assume real stress of stirrup (f_{hcc}) are to be yield stress of the stirrup (f_y).

2. Find compressive strength (f_{co}') and corresponding strain (ε_{cc}) of confined concrete by using Eq. (6.33) and (6.34).

3. Calculate real strain in the stirrup (ε_{hcc}) by using Eq. (6.35).

4. Calculate real stress in the stirrup (f_{hcc}) by using Eq. (6.36).

5. Calculate the updated lateral confining pressure ($f_{le,r}'$) by using updated real stress in the stirrup (f_{hcc}) by using Eq. (6.31).

6. Repeat the step 2 – 5 until the stress in stirrup is converged to a certain value.

The lateral confining pressure caused by structural steel ($f_{le,s}'$), as shown in Eq. (6.37), is referred to the model by Chen and Wu (2017). The assumption of yielding of steel flange from expansion of concrete was used to calculate the lateral confining pressure, as shown in Figure 6.9. The steel flange, which resembled a cantilever beam, is subjected to expansion forced of concrete. The internal moment (M_u) at support of the cantilever beam is expressed in Eq. (6.39), which assumed nonlinear expansion of concrete occurring at 0.75 of yielding of structural steel. The

maximum expansion force of concrete (q_u), which was parabolic curve, is expressed in Eq. (6.40). In addition, expansion pressure of concrete acting on structural steel ($f_{le,s}{}'$) is expressed in Eq. (6.41).

$$f_{le,s}{}' = k_{e,h} f_{l,s}{}' \qquad (6.37)$$

$$k_{e,h} = \frac{\left(d - 2t_f\right)\left(b - t_w\right) - \dfrac{\left(d - 2t_f\right)^2}{6}}{\left(d - 2t_f\right)\left(b - t_w\right)} \qquad (6.38)$$

$$M_u = \frac{f_{ys} t_f^2}{16} \qquad (6.39)$$

$$q_u = \frac{t_f^2}{4b^2} f_{ys} \qquad (6.40)$$

$$f_{l,s}{}' = \frac{2}{3} q_u \qquad (6.41)$$

Where

b = clear width of steel flange;

d = total depth of steel column;

$k_{e,h}$ = area ratio of effective confined concrete to total concrete;

$f_{le,s}{}'$ = lateral confining pressure from structural steel;

f_{ys} = specified minimum yield stress of structural steel;

q_u = maximum lateral confining pressure;

t_f = flange thickness of structural steel;

t_w = web thickness of structural steel.

In addition, the concrete confinement factor of partially and highly confined concrete are defined as follows,

$$K_p = \frac{f_{cc,p}{}'}{f_{co}{}'} \tag{6.42}$$

$$K_h = \frac{f_{cc,h}{}'}{f_{co}{}'} \tag{6.43}$$

Where

$f_{cc,h}{}' =$ compressive strength of highly confined concrete;

$f_{cc,p}{}' =$ compressive strength of partially confined concrete;

$f_{co}{}' \ =$ compressive strength of concrete cylinder;

$K_h \ =$ confinement factor of highly confined concrete;

$K_p \ =$ confinement factor of partially confined concrete.
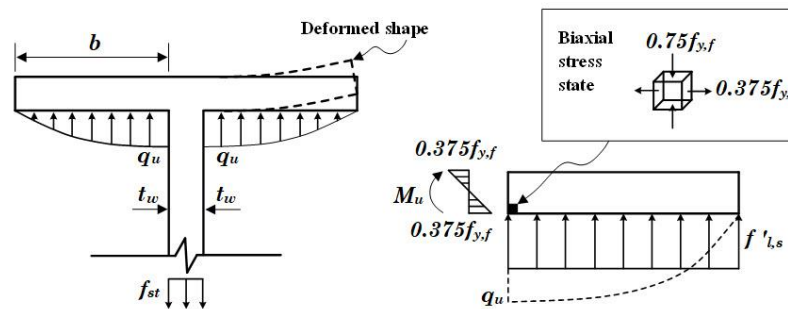
Figure 6.9 Constitutive model for concrete.

6.2.3   Constitutive model for structural steel

For the model of structural steel, Giuffre-Menegotto-Pinto model was used in this study as shown in Figure 6.10, with R to be 10 for hot rolled steel and to be 3 for welded steel and $\varepsilon_{su} = 0.02$.

The structural steel in this model was divided into 2 parts consisting of steel flange and web. The steel web was affected from expansion of concrete. Biaxial Stress Ellipse Theory, as express in Eq. (6.44), was used to reduce the strength of steel web. The expansion force of concrete acted on the steel web is expressed in Eq. (6.45), which was calculated by equilibrium, as shown in Figure 6.9.

$$f_{st}^2 + f_{sv}^2 - f_{st}f_{sv} = f_y^2 \tag{6.44}$$

$$f_{st} = \frac{4b}{3t_w}q_u \tag{6.45}$$

Where

b = clear width of steel flange;

f_{st} = maximum lateral tensile stress in web;

f_{sv} = maximum vertical stress in web;

q_u = maximum lateral confining pressure;

t_w = web thickness of structural steel.
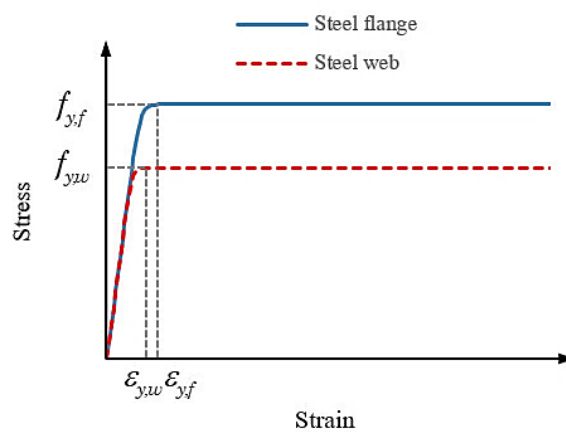
Figure 6.10 Constitutive model for concrete.

In addition, the reduction factor of web of structural steel is defined as follows,

$$K_w = \frac{f_{sv}}{f_{ys}} \tag{6.46}$$

Where

f_{sv} = maximum vertical stress in web;

f_{ys} = specified minimum yield stress of structural steel;

K_w = reduction factor of steel web.

6.2.4 Constitutive model for longitudinal bar

Figure 6.11 shows stress – strain relation of longitudinal bars referring model by Chen and Wu (2017). The curve is linear from origin to yield stress (f_{yr} and ε_{yr}). The stress is to be yield stress until corresponding strain at peak stress of concrete (ε_{co}). After that, the strain reduces linearly to be 20 % of yield stress ($0.2 f_{yr}$) at 4 times of corresponding strain at peak stress of concrete ($4\varepsilon_{co}$).
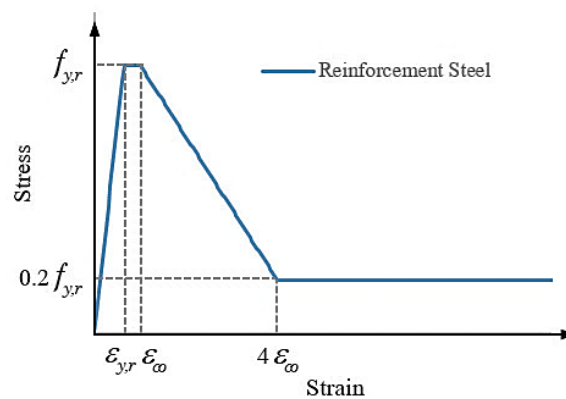
Figure 6.11 Constitutive model for concrete.

6.2.5 Verification of proposed analytical model

The 22 specimens of CES columns subjected to concentric loadings of Chen and Yeh (1999), Tsai et al. (1996), Liang et al. (2014), and Zhu et al. (2014) are used for verification of proposed analytical model.

Chen and Yeh (1999) and Tsai et al. (1996) specimens were 280×280 mm in cross section and 1200 mm in height. Four and twelve 16-mm-diameter bars were used as the longitudinal reinforcements. The 6 and 9 mm-diameter bars were used as the transverse reinforcements (closed stirrups). The structural steel was H-shape, I-shape and cross-shape. The concrete was normal strength concrete.

Liang et al. (2014) specimens were 600×600 mm in cross section and 1200 mm in height. Twelve 29-mm-diameter bars were used as the longitudinal reinforcements. The 13 mm-diameter bars were used as the transverse reinforcements (closed stirrups). The structural steel was cross-shape. The concrete was normal strength concrete.

Zhu et al. (2014) specimens were 200×200 mm in cross section and 600 mm in height. Twelve 10-mm-diameter bars were used as the longitudinal reinforcements. The 6.5 mm-diameter bars were used as the transverse reinforcements (closed stirrups). The structural steel was I-shape and cross-shape. The concrete was high strength concrete.

Figure 6.12 shows cross-sectional of CES columns of Chen and Yeh (1999) and Zhu et al. (2014).

(a)

(b)
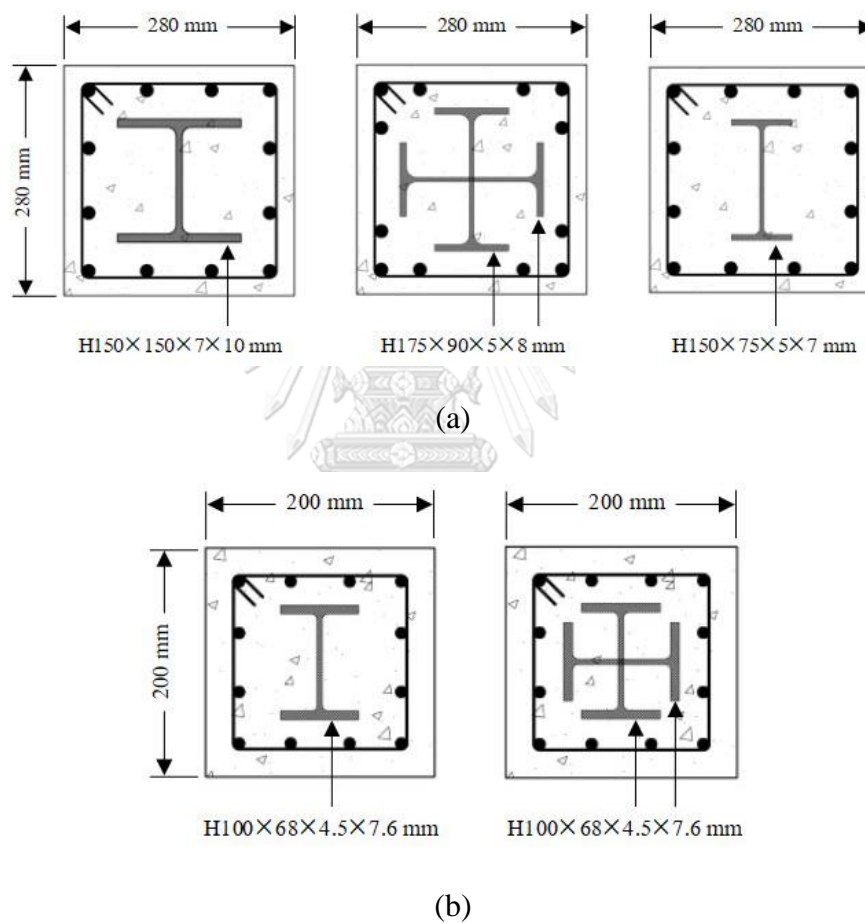
Figure 6.12 Cross-sectional of CES columns of (a) Chen and Yeh (1999); and (b) Zhu et al. (2014).

Figure 6.13 shows comparison of the axial load – strain relation of the analytical model with the experimental results from the literature. The comparison shows that the model accurately predicts axial load – strain curves and axial compressive strength of the CES columns. The comparison ratio of the axial

compressive strength of the model predictions to the experimental results are shown in Table 6.2. The average ratio is 1.00 with standard deviation is 0.05.

Table 6.2 Comparison of axial compressive strength predicted from analytical model and experimental results.

Author	Specimen	Maximum load					
		Experiment	Squash load	Analysis model	Experiment ÷ Squash	Experiment ÷ Analysis	Analysis ÷ Squash
		P_{exp}	P_{squash}	P_{ana}	P_{exp} / P_{squash}	P_{exp} / P_{ana}	P_{ana} / P_{squash}
		(kN)	(kN)	(kN)	-	-	-
		[1]	[2]	[3]	[1] / [2]	[1] / [3]	[3] / [2]
Tsai et al. (1996)	src1	3602	3227	3587	1.12	1.00	1.11
	src2	3502	3202	3567	1.09	0.98	1.11
	src5	3063	2664	2918	1.15	1.05	1.10
	src6	3009	2684	2974	1.12	1.01	1.11
	src8	3088	2703	3000	1.14	1.03	1.11
	src9	3748	3515	3533	1.07	1.06	1.01
Chen and Yeh (1999)	SRC1	4220	3833	4187	1.10	1.01	1.09
	SRC2	4228	3747	4147	1.13	1.02	1.11
	SRC3	4399	3851	4385	1.14	1.00	1.14
	SRC4	4441	4231	4438	1.05	1.00	1.05
	SRC5	4519	4231	4471	1.07	1.01	1.06
	SRC6	4527	4213	4549	1.07	1.00	1.08
	SRC7	3788	3153	3502	1.20	1.08	1.11
	SRC8	3683	3046	3434	1.21	1.07	1.13
	SRC9	3630	3153	3502	1.15	1.04	1.11
	SRC10	3893	3261	3674	1.19	1.06	1.13
Liang et al. (2014)	DH-TI-75	18188	18447	19259	0.99	0.94	1.04
	DH-TI-90	17952	18447	19229	0.97	0.93	1.04
Zhu et al. (2014)	C-I-R40	3809	3685	4088	1.03	0.93	1.11
	C-I-R60	3838	3685	4114	1.04	0.93	1.12
	C-+-R40	3855	3926	4294	0.98	0.90	1.09
	C-+-R60	4010	3926	4317	1.02	0.93	1.10
				Average	1.09	1.00	1.09
				Standard deviation	0.07	0.05	0.03
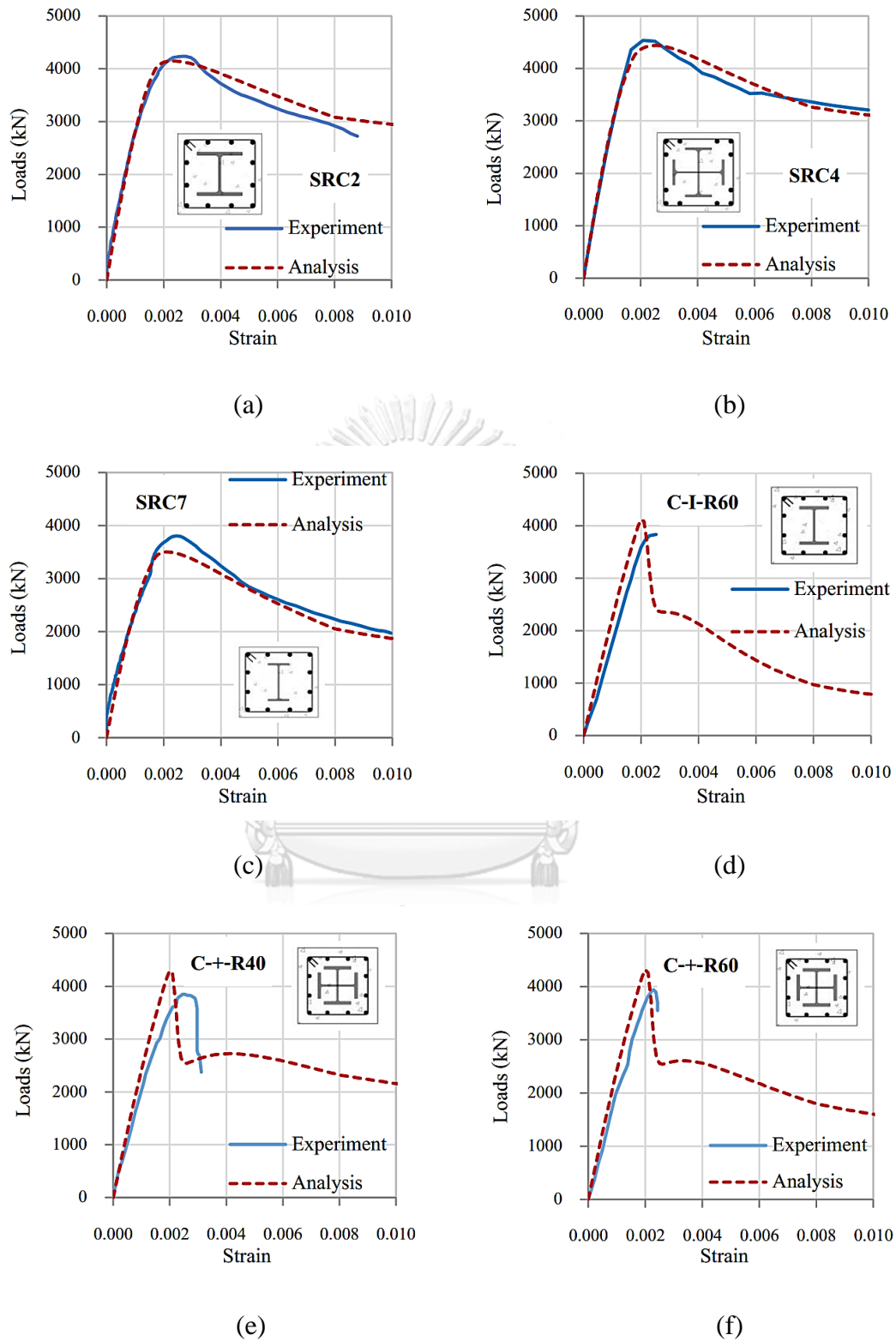
Figure 6.13 Verification of axial load – strain relation with the CES specimens of
(a-c) Chen and Yeh (1999); and (d-f) Zhu et al. (2014).

6.2.6 Squash loads

Squash load equation is a simplified equation for predicting axial compressive strength of composite stub column. The equation combines ultimate strength of all material in the composite column without considering the effect of concrete confinement. The squash load equation for the CES stub column express as follows,

$$P_{Squash} = 0.85 f_{co}' A_c + f_{ys} A_s + f_{ysr} A_{sr} \qquad (6.47)$$

Where

A_c = cross-sectional area of concrete;

A_s = cross-sectional area of structural steel;

A_{sr} = cross-sectional area of longitudinal rebar;

f_{co}' = compressive strength of concrete cylinder;

f_{ys} = yield stress of structural steel;

f_{ysr} = yield stress of longitudinal rebar.

The comparison ratio of the axial compressive strength of the squash load equation to the experimental results is shown in Table 6.2. The average ratio is 1.09 and standard deviation is 0.07. The results showed that the squash load equation underestimate the compressive strength of CES columns from the previous test data.

In addition, the comparison ratio of the axial compressive strength from the analytical model to the squash load equation is shown in Table 6.2. The average ratio is 1.09 and standard deviation is 0.03. The results showed that the axial compressive strength of squash load equation less than the axial compressive strength of the analytical model.

6.2.7 Parametric study

The analysis model is used to study effect of design parameters on maximum loads of CES column and design factors. The design parameters consisted of concrete strength, steel strength, stirrup spacing, flange slenderness ratio, and web slenderness

ratio. The design factors consisted of partially confined factor (K_p), highly confined factor (K_h), and reduction factor of steel web (K_w).

In the parametric study, the properties of SRC2 specimen of Chen and Yeh (1999) were used. The column was 280 × 280 mm in cross section and 1200 mm in height. Twelve 16-mm-diameter bars were used as the longitudinal reinforcements. The 8 mm-diameter bars were used as the transverse reinforcements with spacing of 50 mm. The structural steel was H-shape with total depth 150 mm, flange width 150 mm, flange thickness 10 mm and web thickness 7 mm. The compressive strength of concrete was 30 MPa. The yield stress of structural steel and longitudinal bars were 400 MPa. The yield stress of stirrups was 245 MPa.

Figure 6.14 shows effect of concrete strength on maximum loads and the design factors. The concrete strength varies from 20 to 80 MPa. An increase of concrete strength increased the maximum loads, reduced the partially confined factor and highly confined factor. The increase of concrete strength did not affect the reduction factor of steel web.

(a)　　　　　　　　　　　　　　　　(b)
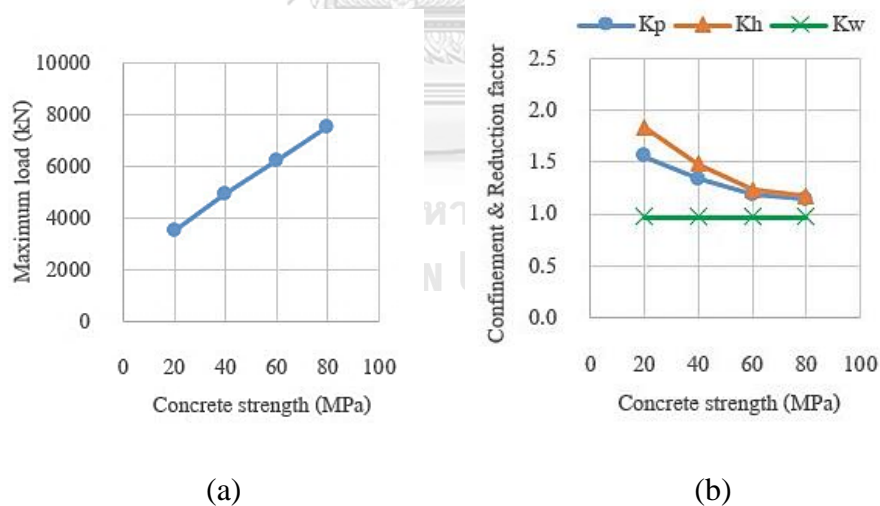
Figure 6.14 Effect of concrete strength on (a) maximum loads of CES column; and (b) partially confined factor, highly confined factor, and reduction factor of steel web.

Figure 6.15 shows effect of steel strength on maximum loads and the design factors. The steel strength varies from 200 to 500 MPa. An increase of steel strength slightly reduced the reduction factor of steel web. The increase of steel strength did not affect the maximum loads, the partially confined factor, and highly confined factor.

(a)   (b)
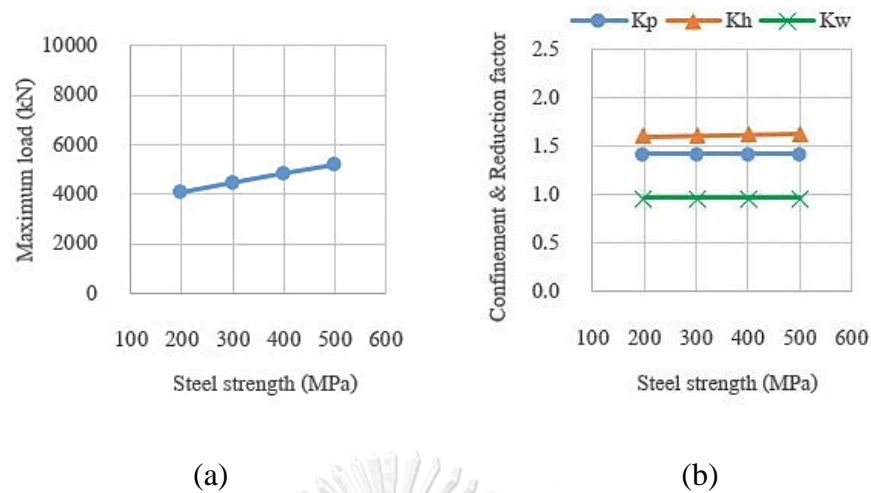
Figure 6.15 Effect of steel strength on (a) maximum loads of CES column; and
(b) partially confined factor, highly confined factor, and reduction factor of steel web.

Figure 6.16 shows effect of stirrup spacing on maximum loads and the design
factors. The stirrup spacing varies from 25 to 200 mm. An increase of stirrup spacing
reduced the partially confined factor and highly confined factor, and slightly reduced
the maximum loads. The increase of stirrup spacing did not affect the reduction factor
of steel web.

(a)   (b)
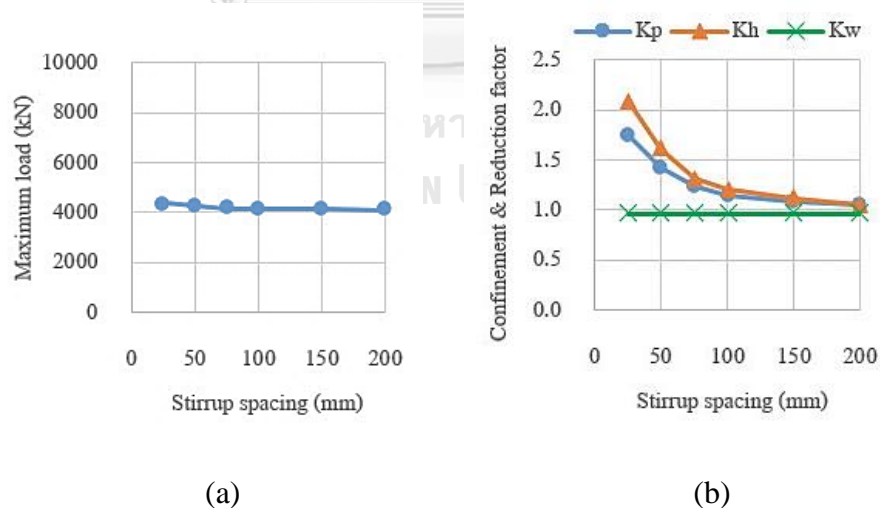
Figure 6.16 Effect of stirrup spacing on (a) maximum loads of CES column; and
(b) partially confined factor, highly confined factor, and reduction factor of steel web.

Figure 6.17 shows effect of flange slenderness ratio on maximum loads and
the design factors. The flange slenderness ratio varies from 4.8 to 14. An increase of

flange slenderness ratio slightly reduced the maximum loads, the partially confined factor and highly confined factor; and the increase of flange slenderness ratio slightly increased the reduction factor of steel web.

(a)   (b)
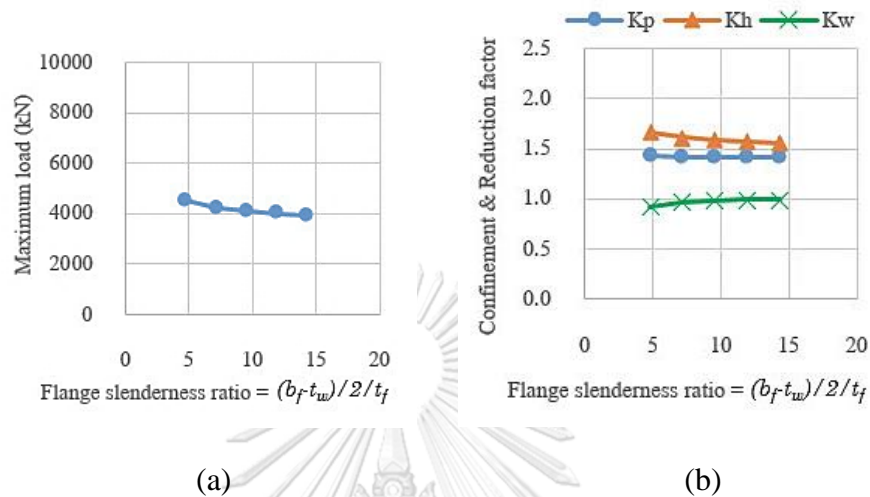
Figure 6.17 Effect of flange slenderness ratio on (a) maximum loads of CES column; and (b) partially confined factor, highly confined factor, and reduction factor of steel web.

Figure 6.18 shows effect of web slenderness ratio on maximum loads and the design factors. The web slenderness ratio varies from 13.7 to 52. An increase of web slenderness ratio slightly reduced the maximum loads, the partially confined factor, highly confined factor, and the reduction factor of steel web.

(a)   (b)
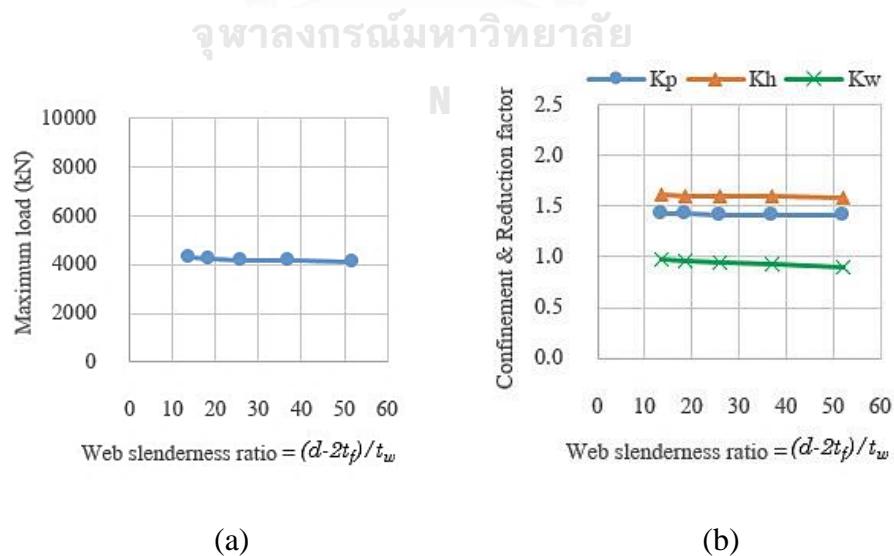
Figure 6.18 Effect of web slenderness ratio on (a) maximum loads of CES column; (b) partially confined factor, highly confined factor, and reduction factor of steel web.

6.2.8 Conclusions

The analytical model which considers the effect of concrete confinement and strength reduction of steel web accurately predicts the axial compressive behavior of the CES columns. The effects of the design parameters on the maximum loads of the CES columns, the partially confined factor, the highly confined factor and the reduction factor of steel web can be summarized as follows,

- Increase of concrete strength increased the maximum loads, reduced the partially confined factor and highly confined factor of the CES columns. The increase of concrete strength did not affect the reduction factor of steel web.

- Increase of steel strength slightly reduced the reduction factor of steel web. The increase of steel strength did not affect the maximum loads, the partially confined factor, and highly confined factor of the CES columns.

- Increase of stirrup spacing reduced the partially confined factor and highly confined factor, and slightly reduced the maximum loads. The increase of stirrup spacing did not affect the reduction factor of steel web.

- Increase of flange slenderness ratio slightly reduced the maximum loads, the partially confined factor, and highly confined factor; and the increase of flange slenderness ratio slightly increased the reduction factor of steel web.

- Increase of web slenderness ratio slightly reduced the maximum loads, the partially confined factor, highly confined factor, and the reduction factor of steel web.

6.3 Proposed modified squash load equation for composite columns

As discussed in section 6.2, the analytical model, which considers concrete confinement effect, accurately predicted the axial compressive strength of tested CES columns from the previous test data; and the squash load equation predicted conservatively the axial compressive strength of the tested CES columns from the previous test data. However, the analytical model and squash load equation

overestimate the axial compressive strength of the tested CES columns in this research.

The predicted squash loads of all tested columns are shown in Table 6.3. A comparison with the test results showed that Eq. (6.47) overestimated the compressive strength for all CES columns. The overestimation was highest at 19% for the largest stirrup spacing and decreased as stirrup spacing decreased. This overestimation was possibly due to the use of total concrete area in Eq. (6.47). In the experiments, the lateral deformation of longitudinal rebars and spalling of concrete cover occurred before the maximum loads. Therefore, Eq. (6.47) is not recommended for the CES or CECS composite columns with low-strength concrete strength, low longitudinal reinforcement ratio, and large stirrup spacing. In addition, the analytical model is also not recommended for the CES and CECS columns in this case, because the early spalling of cover concrete and the concrete confinement effect is not evident in the experiments.

The cover concrete spalling behavior before the maximum loads was also observed in the CES columns with high-strength concrete tested by Zhu et al. (2014) and Lai et al. (2019).

6.3.1 Modified squash loads of CES columns

A modified squash load was proposed by Lai et al. (2019) for high-strength concrete CES columns. All materials were assumed to reach their maximum strength. However; only concrete area enclosed by the stirrup was considered, as given by

$$P_{sq,\mathrm{mod}} = 0.85 f_{co}' A_{c,core} + f_{ys} A_s + f_{ysr} A_{sr} \tag{6.48}$$

Where

$A_{c,core}$ = cross-sectional area of concrete enclosed by the closed stirrups;

A_s = cross-sectional area of structural steel;

A_{sr} = cross-sectional area of longitudinal rebar;

f_{co}' = compressive strength of concrete cylinder;

f_{ys} = yield stress of structural steel;

f_{ysr} = yield stress of longitudinal rebar.

Because the modified squash load equation has not considering strength of cover concrete and effect of concrete confinement; therefore, this equation is appropriate with the experimental results in this research. The predicted compressive strengths by Eq. (6.48) are shown in Table 6.3. A comparison with the test results showed that Eq. (6.48) accurately predicted the strength of the CES columns with low-strength concrete and large stirrup spacing (W-170 (A), W-170 (B), and W-126). However, the Eq. (6.48) underestimated the strength of the CES column with concrete strength in range of AISC specification (W-63). Therefore, Eq. (6.48) is recommended for the CES composite columns with low-strength concrete strength (as low as 21 MPa AISC minimum), low longitudinal reinforcement ratio (as low as AISC minimum), and large stirrup spacing (up to the AISC maximum). It should be noted that the squash load equation conservatively predicts the axial compressive strength of the CES columns in range of AISC specification; and the analytical model is appropriate with the CES columns with small stirrup spacing, which have evident effect of concrete confinement behavior.

Table 6.3 Test and predicted results of CES composite columns.

Composite column	Section analysis			Experimental result		Comparison		
						Experiment / Analysis		
	Axial stiffness	Squash load	Modified squash load	Axial stiffness	Maximum load	Axial stiffness	Squash load	Modified squash load
	$(EA/L)_{ana}$	P_{squash}	$P_{sq,\,mod}$	$(EA/L)_{exp}$	P_{max}	$(EA/L)_{exp}$ $\div$ $(EA/L)_{ana}$	P_{max} $\div$ P_{squash}	P_{max} $\div$ $P_{sq,\,mod}$
	MN/m	kN	kN	MN/m	kN	-	-	-
	[1]	[2]	[3]	[4]	[5]	[4] / [1]	[5] / [2]	[5] / [3]
W-170 (A)	8402	3396	2688	8228	2744	0.98	0.81	1.02
W-170 (B)	8116	3227	2582	7626	2632	0.94	0.82	1.02
W-126	8402	3396	2688	8402	2868	1.00	0.84	1.07
W-63	8822	3660	2853	8807	3469	1.00	0.95	1.22

[a] Based on the actual LDVT gauge.

6.3.2 Axial stiffnesses of CES columns

For the tested CES columns in this research, the axial stiffness was predicted as follows,

$$\left(EA/L\right)_{ana} = \left(E_s A_s + E_{sr} A_{sr} + E_c A_c\right)/L \tag{6.49}$$

Where

A_c = cross-sectional area of concrete;

A_s = cross-sectional area of structural steel;

A_{sr} = cross-sectional area of longitudinal rebar;

E_c = elastic modulus of concrete ($E_c = 5000\sqrt{f_{co}'}$, MPa);

E_s = elastic modulus of structural steel (MPa);

E_{sr} = elastic modulus of longitudinal rebar (MPa).

The predicted axial stiffnesses of the CES columns are shown in Table 6.3. A comparison showed that Eq. (6.49) is applicable for CES columns.

6.3.3 Modified squash loads of CECS columns

For the tested CECS columns with low-strength concrete strength, low longitudinal reinforcement ratio, and large stirrup spacing, the modified squash load of the CES columns with similar properties was used. All materials were assumed to reach their maximum strength. The only concrete area enclosed by the stirrup was considered. The cellular steel members assumed the full yielding at the net cross-section area as shown in [Section A-A', B-B' and C-C' at hole centerline of the cellular steel columns] Figure 4.1 (a-c), is given by

$$P_{sq,\text{mod}} = 0.85 f_{co}' A_{c,core} + f_{ys} A_{s,net} + f_{ysr} A_{sr} \tag{6.50}$$

Where

$A_{s,net}$ = net cross-sectional area of structural steel, Eq. (4.3).

The predicted compressive strengths of the tested CECS columns by Eq. (6.50) are shown in Table 6.4. For the tested CECS columns with low-strength

concrete and largest stirrup spacing as up to the AISC maximum spacing [C1-170 (A), C2-170 (A), C3-170 (A), C1-170 (B), C2-170 (B) and C3-170 (B)], the squash load equation [Eq. (6.47) by using net cross-sectional area of structural steel] overestimated the compressive strength of the CECS columns by 20%. The modified squash load equation accurately predicted the compressive strength of the CECS columns, the highest average error was 2%. The prediction tended to be less accurate, i.e., more conservative, as concrete strength increased and stirrup spacing decreased. Therefore, Eq. (6.50) is recommended for the CECS composite columns with low-strength concrete strength (as low as 21 MPa AISC minimum), low longitudinal reinforcement ratio (as low as AISC minimum), and large stirrup spacing (up to the AISC maximum).

Table 6.4 Test and predicted results of CECS composite columns.

Composite column	Section analysis			Experimental result		Comparison Experiment / Analysis		
	Axial stiffness	Squash load	Modified squash load	Axial stiffness	Maximum load	Axial stiffness	Squash load	Modified squash load
	$(EA/L)_{ana}$	P_{squash}	$P_{sq, mod}$	$(EA/L)_{exp}$	P_{max}	$(EA/L)_{exp} \div (EA/L)_{ana}$	$P_{max} \div P_{squash}$	$P_{max} \div P_{sq, mod}$
	MN/m	kN	kN	MN/m	kN	-	-	-
	[1]	[2]	[3]	[4]	[5]	[4] / [1]	[5] / [2]	[5] / [3]
C1-170 (A)	8346 [a]	3278	2570	8175	2636	0.98	0.80	1.03
C2-170 (A)	8330 [a]	3267	2559	8236	2572	0.99	0.79	1.01
C3-170 (A)	8346 [a]	3278	2570	9151	2637	1.10	0.80	1.03
Average						1.02	0.80	1.02
C1-170 (B)	8059 [a]	3108	2463	7896	2478	0.98	0.80	1.01
C2-170 (B)	8043 [a]	3097	2452	8164	2480	1.02	0.80	1.01
C3-170 (B)	8059 [a]	3108	2463	8095	2493	1.00	0.80	1.01
Average						1.00	0.80	1.01
C1-126	8346 [a]	3278	2570	8974	2809	1.08	0.86	1.09
C2-126	8330 [a]	3267	2559	8601	2782	1.03	0.85	1.09
Average						1.05	0.85	1.09
C3-108	8346 [a]	3278	2570	9319	2906	1.12	0.89	1.13
C1-63	8767 [a]	3543	2736	10250	3307	1.17	0.93	1.21
C2-63	8751 [a]	3532	2725	10644	3270	1.22	0.93	1.20
Average						1.19	0.93	1.20

[a] Based on the actual LDVT gauge.

It should be noted that the squash load equation accurately predicts the axial compressive strength of the CECS columns with concrete strength in range of AISC specification; and concrete confinement effect could be considered in the CECS columns with small stirrup spacing.

6.3.4 Axial stiffnesses of CECS columns

For the tested CECS columns in this research, the axial stiffness was predicted by using the equivalent cross-sectional area of the cellular steel members. The method for predicting the equivalent cross-sectional area of the cellular steel members is proposed in section 6.1.2. The axial stiffness of the tested CECS columns can be expressed as follows,

$$\left(EA/L\right)_{ana} = \left(E_s A_{s,eq} + E_{sr} A_{sr} + E_c A_c\right)\Big/L \tag{6.51}$$

Where

$A_{s,eq}$ =   equivalent cross-sectional area of structural steel, Eq. (6.14).

This equation is based on the assumption of neglect of transfer shear force between the non-prismatic steel member (cellular steel member) and the encased concrete.

The predicted axial stiffnesses of the CECS columns are shown in Table 6.4. A comparison showed that Eq. (6.51) accurately predicted the axial stiffness of CECS columns with high stirrup spacing, and underestimated axial stiffness of CECS columns with closely stirrup spacing.

6.3.5 Conclusions

The proposed modified squash load and axial stiffness equations for predicting the tested CES and CECS columns were investigated in this section. The conclusions of this section are as follows,

Because the analytical model and squash load equation overestimate the axial compressive strength of the tested CES columns in this research. The overestimation of the squash load equation was highest at 19% for the largest stirrup spacing. This overestimation was possibly due to the use of total concrete area. In the experiments,

the lateral deformation of longitudinal rebars and spalling of concrete cover occurred before the maximum load; and the effect of concrete confinement of the tested CES and CECS columns did not evident. Therefore, the modified squash load equations, which proposed by Lai et al. (2019), was used to predict the axial compressive strength of the tested CES columns, and adopted to predict the axial compressive strength of the tested CECS columns. The modified squash load equations accurately predicted the strength of the CES and CECS columns with low-strength concrete and large stirrup spacing. The prediction tended to be less accurate, i.e., more conservative, as concrete strength increased and stirrup spacing decreased. Therefore, the modified squash load equation is recommended for the CES and CECS columns with low-strength concrete strength (as low as 21 MPa AISC minimum), low longitudinal reinforcement ratio (as low as AISC minimum), and large stirrup spacing (up to the AISC maximum). It should be noted that the squash load equation conservatively predicts the axial compressive strength of the CES and CECS columns in range of AISC specification; and the analytical model is appropriate with the CES columns with small stirrup spacing, which have evident effect of concrete confinement behavior.

For the axial stiffnesses, the equation to predict the axial stiffnesses of the CECS columns was proposed by using the equivalent cross-sectional area of the cellular steel members. The proposed equation accurately predicted the axial stiffness of CECS columns with high stirrup spacing, and underestimated axial stiffness of CECS columns with closely stirrup spacing.

CHAPTER 7
STRENGTH INTERACTION DIAGRAM

7.1 Strength interaction diagrams of cellular steel columns

7.1.1   Plastic stress distribution method

For the plastic stress distribution method, the neutral axis is assumed on the cross-section of the cellular steel column, as shown in Figure 7.1. The steel is assumed to reached a yield stress (f_y) in either tension or compression. Axial force and bending moment are computed over centroid of the section.
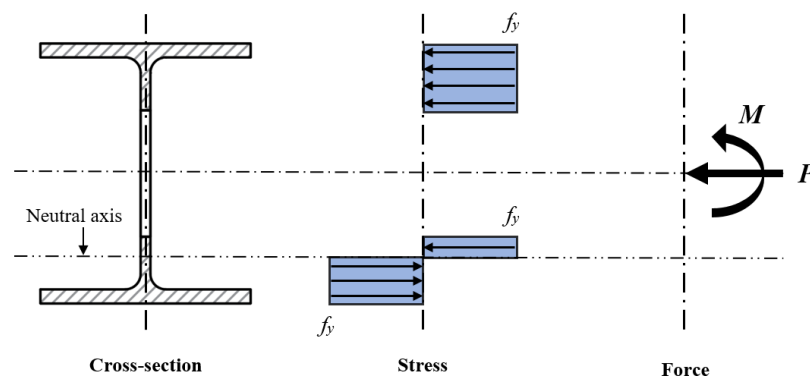
Figure 7.1 Determination of P-M interaction based on plastic stress distribution method.

To develop an interaction diagram, the axial force and bending moment are computed as the neutral axis shifts along cross-section of the cellular steel column. For the cellular steel columns, an interaction diagram was developed by using over 300 coordinates of axial force and bending moment, as shown in Figure 7.2. It should be noted that the Vierendeel bending failure is not considered in this method.

Figure 7.3 shows comparison between the interaction diagram developed by plastic stress distribution method and the experimental results of bare steel columns subjected to concentric and eccentric loadings. The comparison shows that this method accurately predicts the interaction diagram with the test results. For the parent steel columns, this method slightly underestimated the interaction diagram compared with the test results. For the cellular steel columns, this method overestimated the interaction diagram in some load cases.
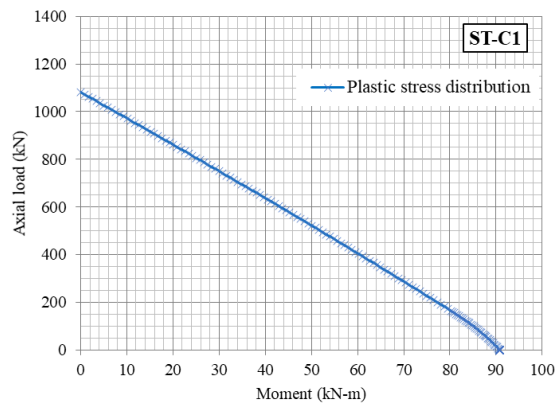
Figure 7.2 Strength interaction diagram of cellular steel column by plastic stress distribution method.
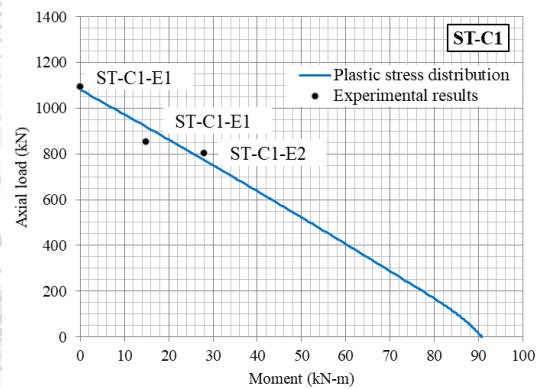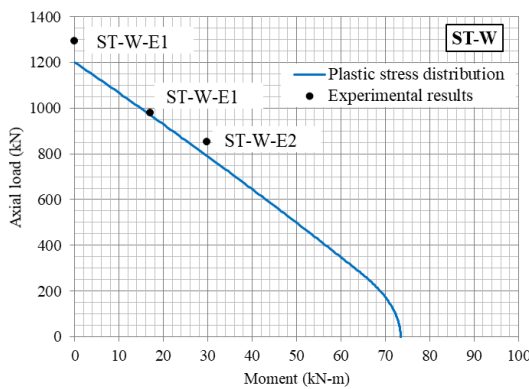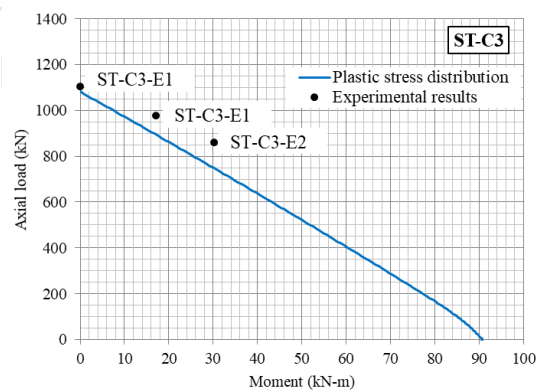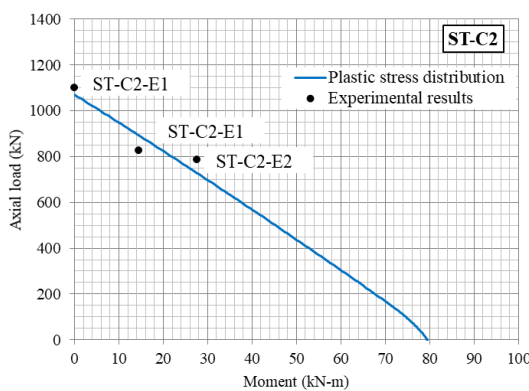
Figure 7.3 Comparison of the strength interaction diagram of cellular steel columns between plastic stress distribution method and experimental results; (a) ST-W; (b) ST-C1; (c) ST-C2; and (d) ST-C3.

Figure 7.4 shows comparison of unit interaction diagrams of the bare steel columns. The comparison shows that the interaction diagram of the cellular steel columns (Plastic stress distribution – ST-W) is different from the interaction diagram of the parent steel columns (Plastic stress distribution – ST-C1). The unit interaction diagram of specimen ST-C3 is similar to that of specimen ST-C1; and the unit interaction diagram of specimen ST-C2 is very close to the interaction diagram of specimen ST-C1.
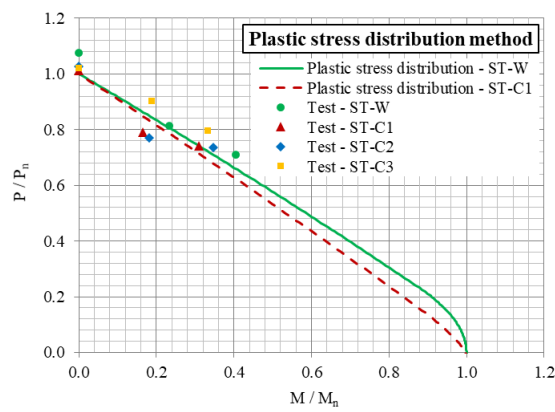
Figure 7.4 Comparison of the strength interaction diagram of cellular steel columns between plastic stress distribution method and experimental results.

7.1.2 Modified AISC 360-16 (Chapter H) method

The modified method proposes an interaction diagram based on the interaction diagram in Chapter H1.1 of AISC 360-16 (2016), which is proposed for double and single symmetric members subjected to flexure and compression, is expressed as follows,

When $\dfrac{P_r}{P_c} \geq 0.2$

$$\frac{P_r}{P_c} + \frac{8}{9}\left(\frac{M_{rx}}{M_{cx}} + \frac{M_{ry}}{M_{cy}}\right) \leq 1.0 \tag{7.1}$$

When $\dfrac{P_r}{P_c} < 0.2$

$$\frac{P_r}{2P_c} + \left(\frac{M_{rx}}{M_{cx}} + \frac{M_{ry}}{M_{cy}} \right) \leq 1.0 \tag{7.2}$$

Where

P_r = required axial strength;

P_c = available axial strength;

M_r = required flexural strength;

M_c = available flexural strength;

x = subscript relating symbol to major axis bending;

y = subscript relating symbol to minor axis bending.

When assuming required flexural strength of minor axis bending is to be zero, the Eq. (7.1) and (7.2) are expressed as follows,

When $\dfrac{P_r}{P_c} \geq 0.2$

$$\frac{P_r}{P_c} + \frac{8}{9}\frac{M_{rx}}{M_{cx}} \leq 1.0 \tag{7.3}$$

When $\dfrac{P_r}{P_c} < 0.2$

$$\frac{P_r}{2P_c} + \frac{M_{rx}}{M_{cx}} \leq 1.0 \tag{7.4}$$

For the available axial strength (P_c), the proposed yield load equation as shown in section 6.1.1 [Eq. (6.1)] is used to predict the axial strength of cellular steel columns. The prediction of yield load of the cellular steel columns assumed the full yielding at the net cross-section area.

For the available flexural strength (M_c), flexural strength of overall beam and Vierendeel bending of tees are considered. For flexural strength of overall beam, the maximum moment equations of steel beam with web openings, which is proposed in steel design guide 2 (AISC Design guide 2: Design of steel and composite beams with

web openings, 1990), is applied. For Vierendeel bending of tees, the method to check the Vierendeel bending failure, which is proposed in steel design guide 31 (AISC Design guide 31: Castellated and cellular beam design, 2016), is applied. Because of load condition, web post buckling, horizontal shear and vertical shear are not considered in this research. Because this research focused on stub columns only, lateral torsional buckling is not considered in this research.

For flexural strength of overall beam, the equations to predict flexural strength of the cellular steel columns, which is proposed in the steel design guide 2, are as follows,

$$M_n = M_{pl} \left[1 - \frac{A_{s,hole}\left(\dfrac{D_o}{4}\right)}{Z_{s,g}} \right] \tag{7.5}$$

Where

$A_{s,hole} = D_o t_w$;

$M_{pl} = f_{ys} Z_{s,g}$;

D_o = hole diameter of cellular column;

t_w = web thickness of structural steel;

f_{ys} = specified minimum yield stress of steel;

$Z_{s,g}$ = plastic section modulus of gross section about x axis.

For Vierendeel bending failure, this failure is caused by combining of the shear force across the openings (global shear) and the rate of change of bending along the beam (global moment). This failure occurred from plastic hinge at four location around the openings. To check this failure, three steps for checking the Vierendeel bending failure, which is proposed in steel design guide 31, are carry out as follows,

1. Calculate a require axial force (due to the global moment) and Vierendeel moment (due to the global shear) on top and bottom tees at each opening, as shown in section 3.8.1.

2. Calculate axial tensile and compressive strength of the tees using Chapter D and E of AISC360-16 and calculate flexural strength of the tee section using Chapter F of AISC360-16, as shown in section 3.8.2 – 3.8.4.

3. Check the failure of combined axial force and Vierendeel moment using Chapter H of AISC360-16, as shown in section 3.8.5.

Because this research is focused on the columns subjected to concentric and eccentric loadings, the global shear is assumed to be zero. Therefore, the Vierendeel moment (due to the global shear) of top and bottom tees at each opening is to be zero. From checking the Vierendeel bending failure for all specimens, this failure is not controlled in this research.

After calculating the available axial strength (P_c) and the available flexural strength (M_c), the interaction diagram by the modified AISC 360-16 (chapter H) method is developed based on Eq. (7.3) and Eq. (7.4), as shown in Figure 7.5.

Figure 7.6 shows comparison between the interaction diagram developed by the modified AISC 360-16 (chapter H) method and the experimental results of bare steel columns subjected to concentric and eccentric loadings. The comparison shows that this method accurately predicts the interaction diagram with the test results. For the parent steel columns, this method slightly underestimated the interaction diagram compared with the test results. For the cellular steel columns, this method overestimated the interaction diagram in some load cases.
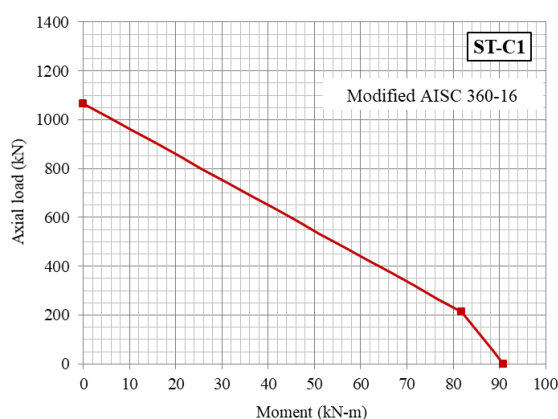
Figure 7.5 Strength interaction diagram of cellular steel columns by modified
AISC 360-16 (Chapter H) method.
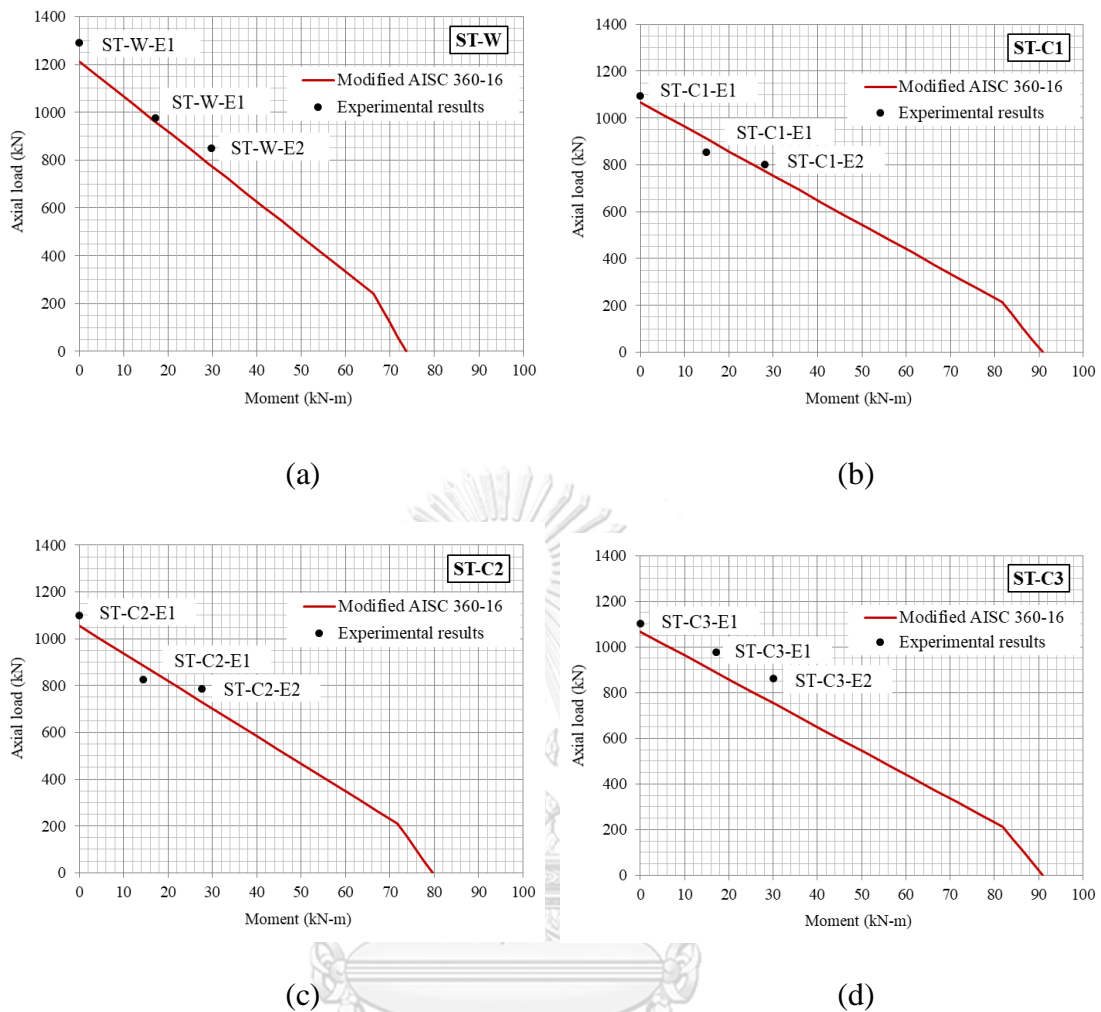
Figure 7.6 Comparison of the strength interaction diagram of cellular steel columns between modified AISC 360-16 (Chapter H) method and experimental results; (a) ST-W; (b) ST-C1; (c) ST-C2; and (d) ST-C3.

Figure 7.7 shows comparison of unit interaction diagrams of the bare steel columns. The comparison shows that the unit interaction diagrams of the cellular steel columns are similar to the unit interaction diagram of the parent steel column. The unit interaction diagram predicted conservatively for most of the bare steel columns, and predicted unconservatively for some of the cellular steel columns.
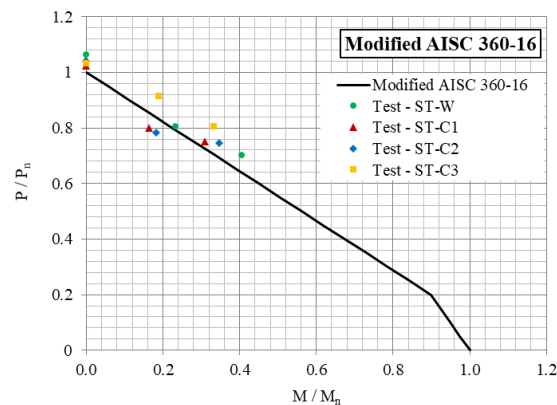
Figure 7.7 Comparison of the strength interaction diagram of cellular steel columns between modified AISC 360-16 (Chapter H) method and experimental results.

7.1.3 Comparison of different methods

Figure 7.8 shows comparison of the strength interaction diagram of cellular steel columns between plastic stress distribution method and modified AISC 360-16 (Chapter H) method. For the parent steel columns, the plastic stress distribution method predicts conservatively compared with the modified AISC 360-16 (Chapter H) method. For the cellular steel columns, the plastic stress distribution method predicts un-conservatively compared with the modified AISC 360-16 (Chapter H) method.

In addition, a methodology of comparing analytical result with test result is proposed by Lai et al. (2019) as shown in Figure 7.9. The vector R_{test} and $R_{analysis}$ (vector from origin to coordinate of test results and interaction diagrams) were defined. Ratio of $R_{analysis}$ and R_{test} is used to evaluate the accuracy of this method.

The comparison of the ratio of $R_{analysis}$ and R_{test} is shown in Table 7.1. The comparison shows that the modified AISC 360-16 (Chapter H) method has similar accuracy to the plastic stress distribution method when comparing the specimens in this research.
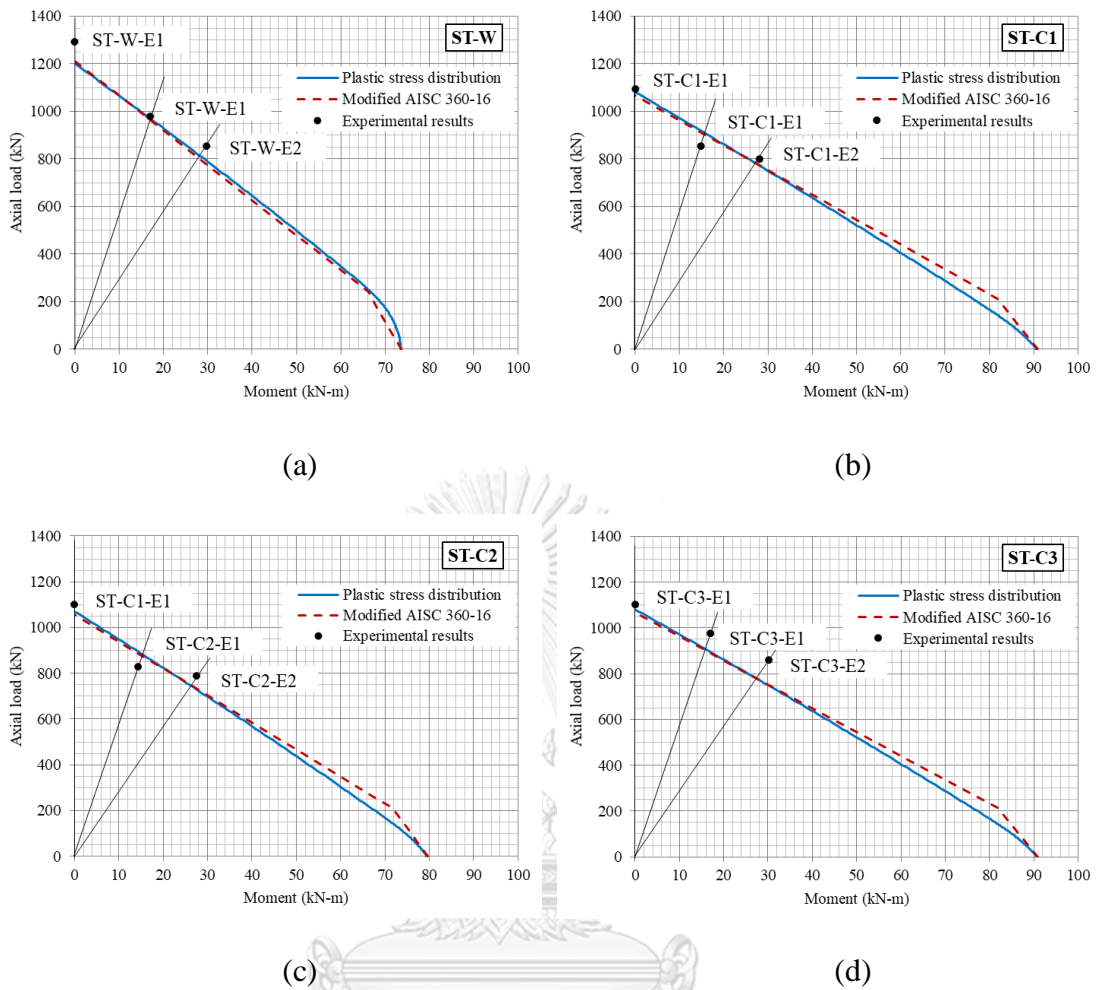
Figure 7.8 Comparison of the strength interaction diagram of cellular steel columns between plastic stress distribution method and modified AISC 360-16 (Chapter H) method; (a) ST-W; (b) ST-C1; (c) ST-C2; and (d) ST-C3.
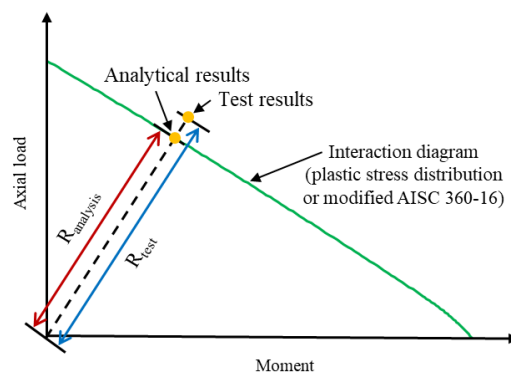
Figure 7.9 Methodology of comparing analytical result with test result by Lai et al. (2019).

Table 7.1 Comparison between plastic stress distribution method and AISC 360-16 (chapter H) method.

Specimen	Experimental results			Plastic stress distribution			AISC 360-16 (Chapter H1.1)		
	e	P	M	P_n	M_n	$R_{analysis} \div R_{test}$	P_n	M_n	$R_{analysis} \div R_{test}$
	mm	kN	kN-m	kN	kN-m	-	kN	kN-m	-
ST-W	0.0	1292	0.0	1201	0.0	0.93	1212	0.0	0.94
ST-W-E1	17.5	978	17.1	972	16.9	0.99	965	16.9	0.99
ST-W-E2	35.0	851	29.8	815	28.1	0.96	801	28.0	0.94
					Average	0.96		Average	0.96
					Standard deviation	0.03		Standard deviation	0.03
ST-C1	0.0	1094	0.0	1081	0.0	0.99	1067	0.0	0.98
ST-C1-E1	17.5	853	14.9	907	16.0	1.06	902	15.8	1.06
ST-C1-E2	35.0	801	28.0	778	27.5	0.97	781	27.4	0.98
ST-C2	0.0	1099	0.0	1070	0.0	0.97	1056	0.0	0.96
ST-C2-E1	17.5	826	14.5	878	15.7	1.06	876	15.3	1.06
ST-C2-E2	35.0	787	27.5	749	25.9	0.95	748	26.2	0.95
ST-C3	0.0	1103	0.0	1081	0.0	0.98	1067	0.0	0.97
ST-C3-E1	17.5	976	17.1	907	16.0	0.93	902	15.8	0.92
ST-C3-E2	35.0	861	30.1	778	27.5	0.90	781	27.4	0.91
					Average	0.98		Average	0.98
					Standard deviation	0.05		Standard deviation	0.05

7.1.4 Parametric study

For parametric study of the cellular steel columns, the modified AISC 360-16 (chapter H) method was used. The design parameters consist of hole diameter to depth of parent ratio (D_o / d) and hole spacing to hole diameter ratio (S / D_o). The column properties consist of depth of cellular steel column to depth of the parent steel column ratio (d_g / d), plastic section modulus of cellular steel column to the parent steel column ratio ($Z_{x,cellular} / Z_{x,parent}$), loss of the cellular column (as shown in Figure 4.2) to depth of the parent steel column ratio ($loss / d$), and cross section area of cellular steel column (at center of hole) to the parent steel column ratio ($A_{cellular} / A_{parent}$). The hot-rolled wide flange steel columns with flange width 150 mm, total depth 150 mm, flange thickness 10 mm and web thickness 7 mm were chosen for parametric study. Yield stress and elastic modulus are 300 MPa and 210000 MPa.
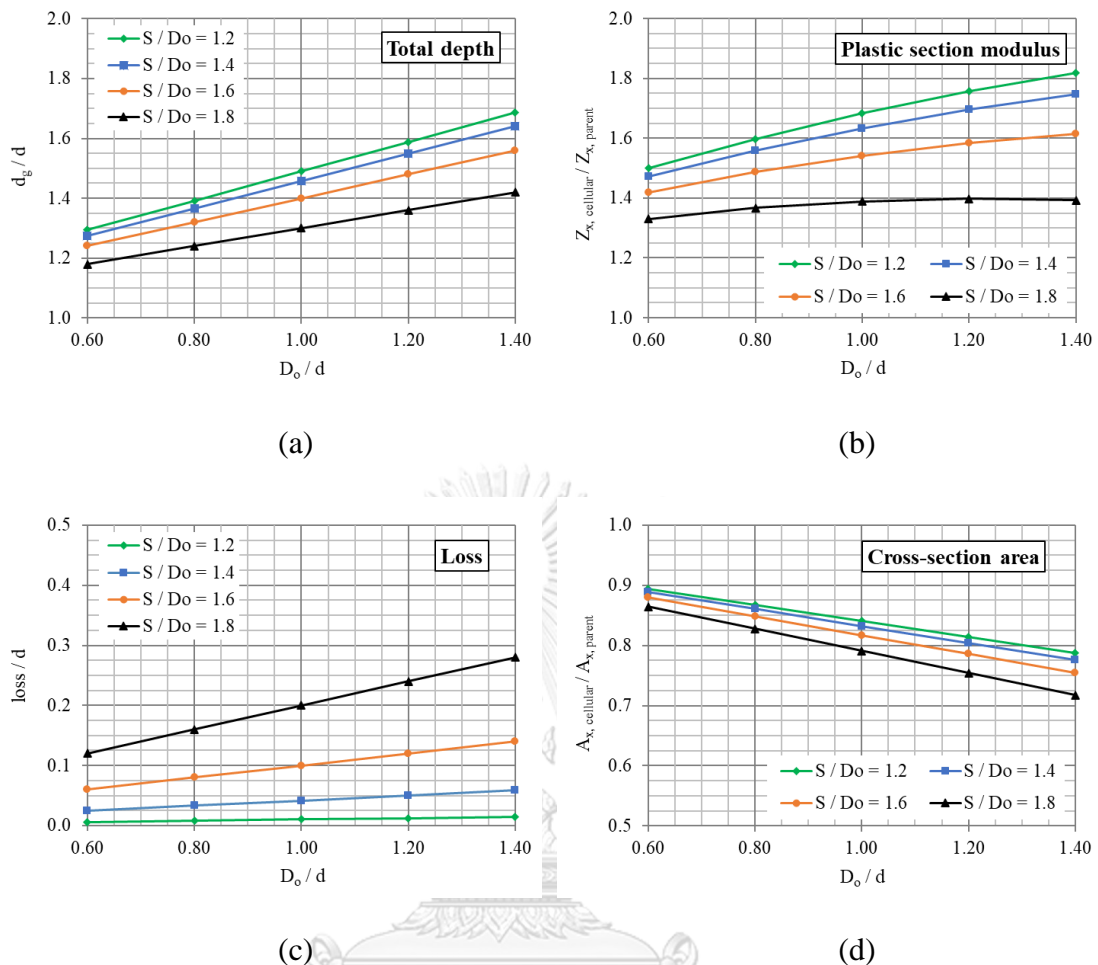
Figure 7.10 Effect of design parameters on properties of cellular steel columns;
(a) d_g / d; (b) $Z_{x,cellular} / Z_{x,parent}$; (c) $loss / d$; and (d) $A_{cellular} / A_{parent}$.

As shown in Figure 7.10, the study of the effect of design parameters on the column properties shows that an increase of the hole diameter to depth of parent ratio (D_o / d) linearly increases d_g / d and $loss / d$, nonlinearly increases $Z_{x,cellular} / Z_{x,parent}$ ratio, and linearly decreases $A_{cellular} / A_{parent}$. The study of hole spacing to hole diameter ratio (S / D_o) shows that an increase of S / D_o decreases d_g / d, $Z_{x,cellular} / Z_{x,parent}$, and $A_{cellular} / A_{parent}$; and, an increase of S / D_o increases $loss / d$.

From the study effect of design parameters on the column properties, it was concluded that the smallest value of S / D_o should be chosen, because of the highest saving of the loss and the highest value of d_g / d, $Z_{x,cellular} / Z_{x,parent}$ and $A_{cellular} / A_{parent}$.

Figure 7.11 shows the effect of hole diameter to depth of parent ratio (D_o / d) on strength interaction diagrams of cellular steel columns. The study shows that an increase of D_o / d decreases axial capacity (the maximum reduction is less than 30 %), but increases bending capacity (the maximum increase is more than 50 %) of the cellular steel columns.
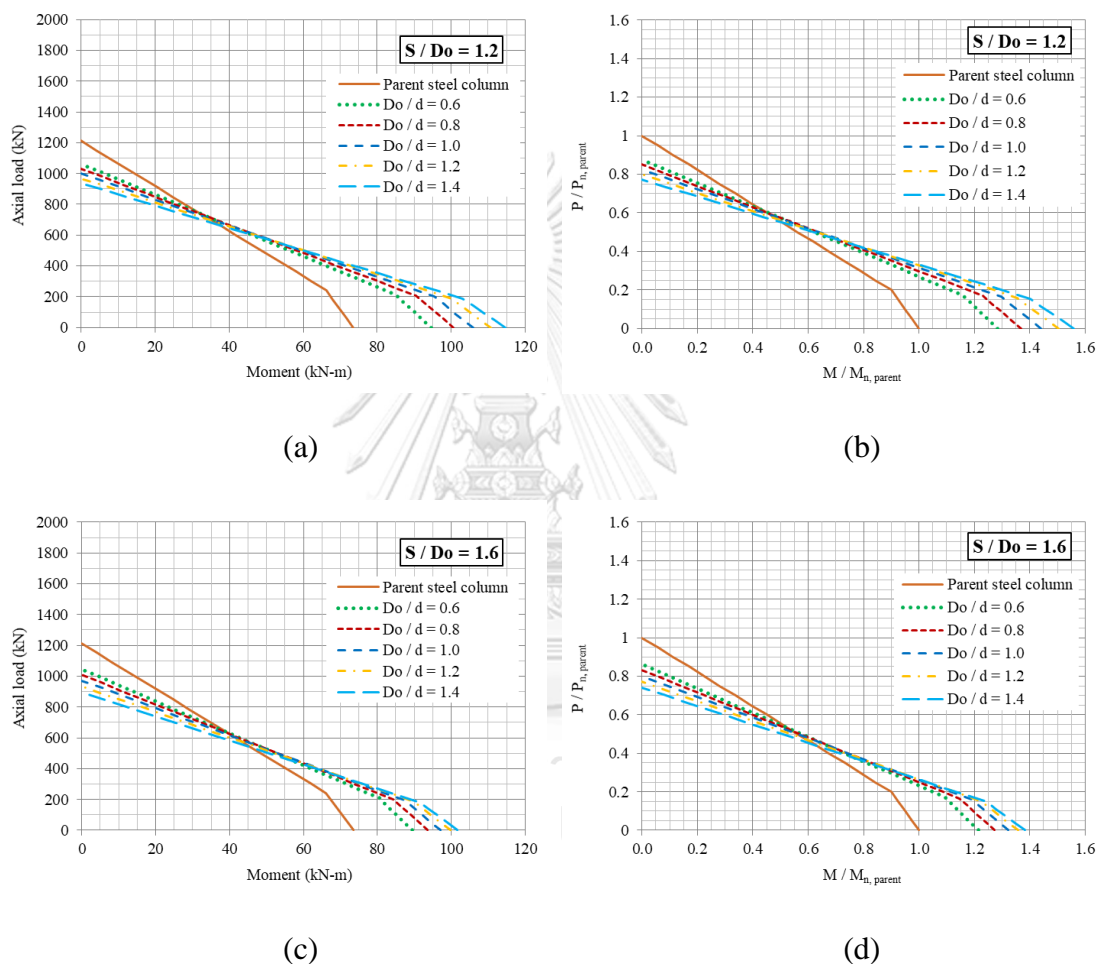
Figure 7.11 Effect of hole diameters on strength interaction diagrams of cellular steel columns; (a-b) $S / D_o = 1.2$; and (c-d) $S / D_o = 1.6$.

Figure 7.12 shows the effect of hole spacing to hole diameter ratio (S / D_o) on strength interaction diagrams of cellular steel columns. The study shows that an increase of S / D_o decreases both axial capacity and bending capacity of the cellular steel columns.

(a)

(b)

(c)

(d)
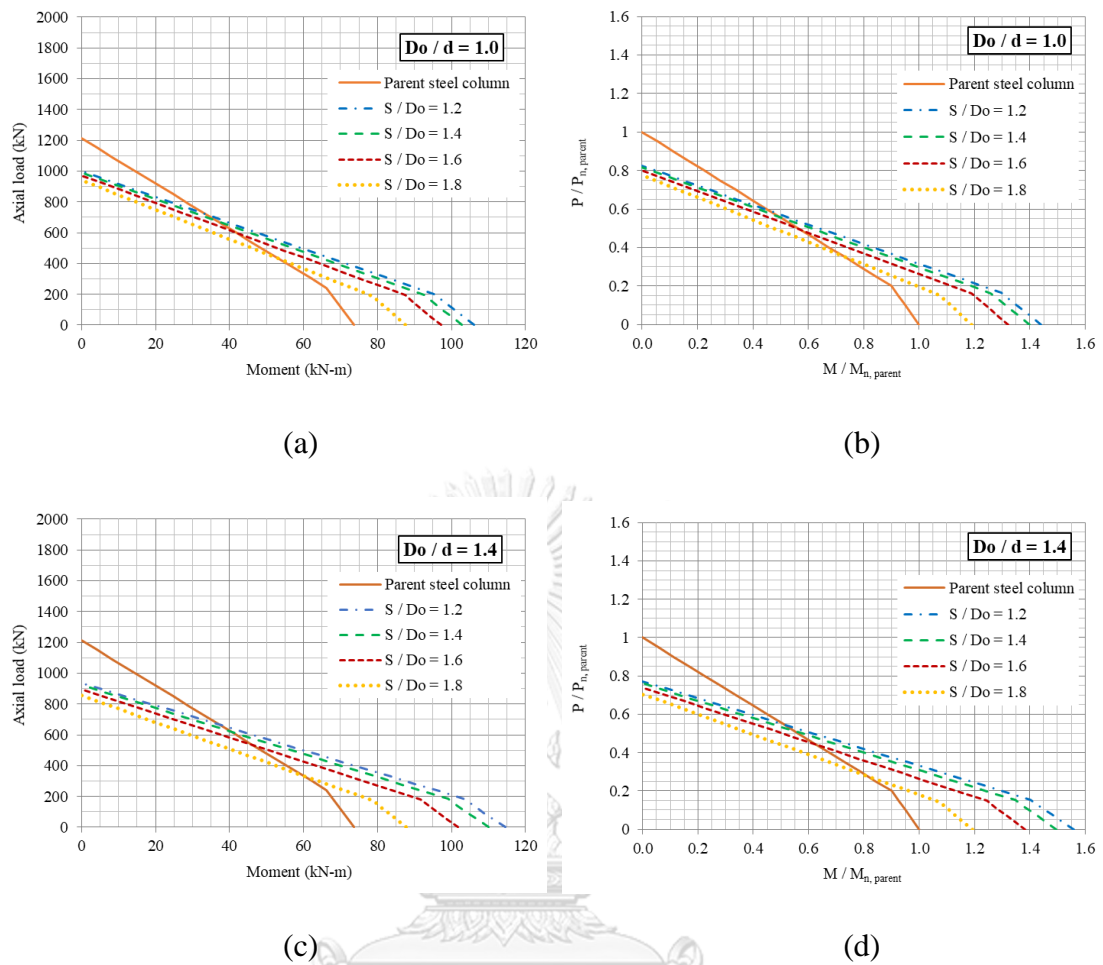
Figure 7.12 Effect of hole spacings on strength interaction diagrams of cellular steel columns; (a-b) $D_o / d = 1.0$; and (c-d) $D_o / d = 1.4$.

7.1.5 Conclusions

The study on strength interaction diagram of the cellular steel columns can be summarized as follows,

- The plastic stress distribution method and modified AISC 360-16 (chapter H) method is applicable to develop the strength interaction diagrams of cellular steel columns.

- From the study of effect of design parameters on the column properties, it was concluded that the smallest value of S / D_o should be chosen, because of the highest saving of the loss and the highest value of plastic section modulus and cross-section area of cellular steel columns.

- Increase of hole diameter to depth of parent ratio (D_o / d) decreases axial capacity, but increases bending capacity of the cellular steel columns.

- Increase of hole spacing to hole diameter ratio (S / D_o) decreases both axial capacity and bending capacity of the cellular steel columns.

7.2 Strength interaction diagrams of CECS columns

7.2.1 Plastic stress distribution method

For the plastic stress distribution method, the neutral axis is assumed on the cross-section of the cellular steel column, as shown in Figure 7.13. The structural steel and longitudinal bars are assumed to have reached a yield stress (f_y) either tension and compression. The concrete in compression is assumed to reached a stress of 0.85 of compressive strength of concrete cylinder ($0.85 f_{co}'$); and, the concrete in tension is ignored. Axial force and bending moment are computed over centroid of the section.
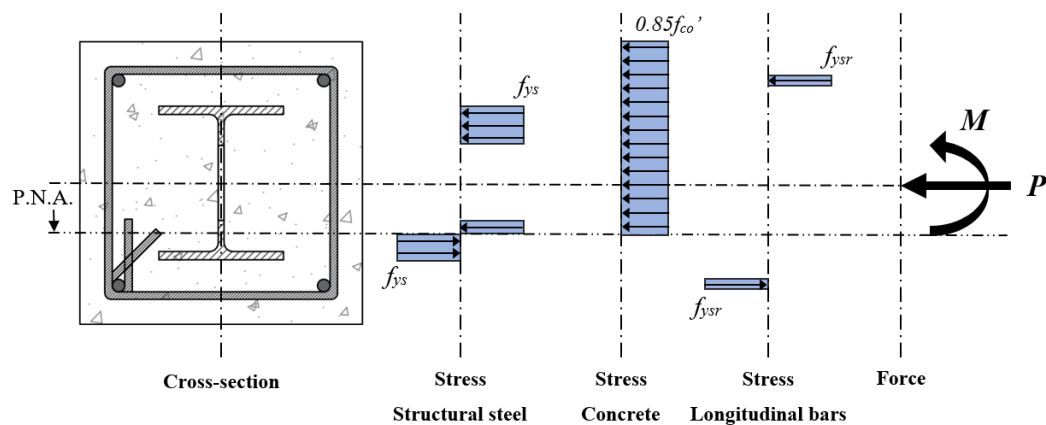
Figure 7.13 Determination of P-M interaction based on plastic stress distribution method.

To develop an interaction diagram, the axial force and bending moment are computed as the neutral axis shifts along cross-section of the cellular steel column. For the cellular steel columns, an interaction diagram was developed by using over 30 coordinates of axial force and bending moment over 30, as shown in Figure 7.14. It should be noted that the Vierendeel bending failure is not considered in this method.
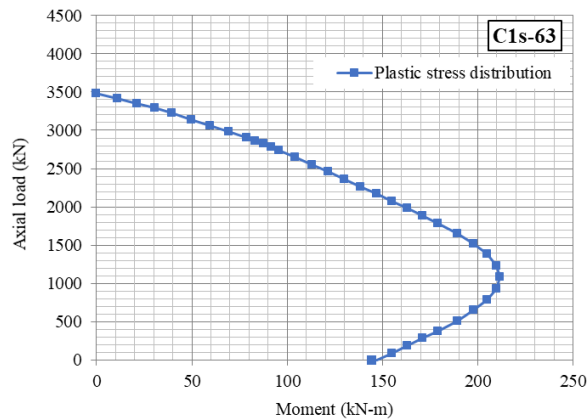
Figure 7.14 Strength interaction diagram of composite column by plastic stress distribution method.

Figure 7.15 shows comparison between the interaction diagram developed by plastic stress distribution method and the experimental results of composite columns subjected to concentric and eccentric loadings. The comparison shows that this method accurately predicts the interaction diagram with the test results. For the columns subjected to concentric loads, this method predicts slightly unconservatively. For the columns subjected to eccentric loading (E1, $e/B \approx 0.1$), this method predicts slightly conservatively. For the columns subjected to eccentric loading (E2, $e/B \approx 0.2$), this method predicts slightly unconservatively.

(a)

(b)

(c)
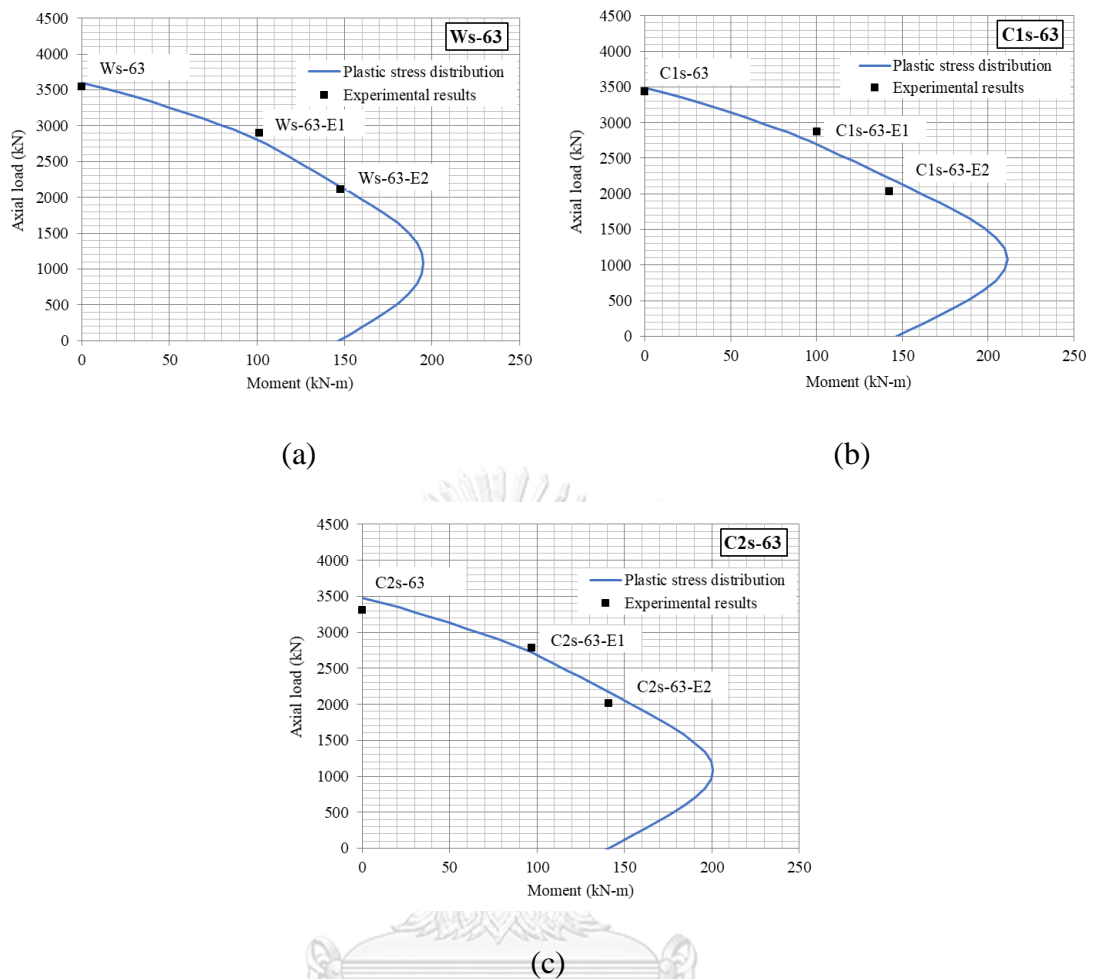
Figure 7.15 Comparison of the strength interaction diagram of composite columns between plastic stress distribution method and experimental results; (a) Ws-63; (b) C1s-63; (c) C2s-63.

7.2.2 Simplified plastic stress distribution method

The simplified plastic stress distribution method proposed on AISC 360-16 (Chapter I1.2) was used to propose the interaction diagrams of the CECS columns. The simplified plastic stress distribution method used plasticity material properties based on the plastic stress distribution, as shown in section 7.2.1. A conservative linear relation between four points (point A, B, C, and D) was used to develop an interaction diagram, as shown in Figure 7.16. It should be noted that the Vierendeel bending failure is not considered in this method.
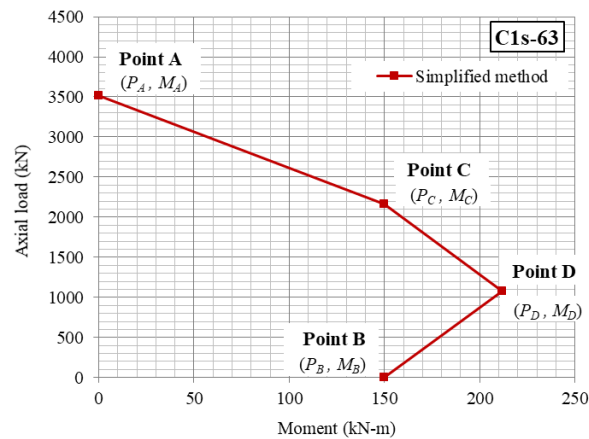
Figure 7.16 Strength interaction diagram of CECS column by simplified plastic stress distribution method method.

The method to calculate the coordinates (P, M) of point A, B, C, and D of the CECS columns are express as follows,

Figure 7.17 shows stress distribution and axial force – moment relation of point A of the CECS columns. The equation of axial force (P_A) and moment (M_A) is expressed as follows,

$$P_A = 0.85 f_{co}' A_c + f_{ys} A_{s,net} + f_{ysr} A_{sr}$$ (7.6)

Where

A_c = cross-sectional area of concrete;

$A_c = BD - A_{s,net} - A_{sr}$;

$A_{s,net}$ = net cross-sectional area of structural steel, Eq. (4.7);

A_{sr} = cross-sectional area of longitudinal rebar;

B = total width of cross-section area of column;

D = total depth of cross-section area of column;

f_{co}' = compressive strength of concrete cylinder;

f_{ys} = yield stress of structural steel;

f_{ysr} = yield stress of longitudinal rebar.

$$M_A = 0$$ (7.7)
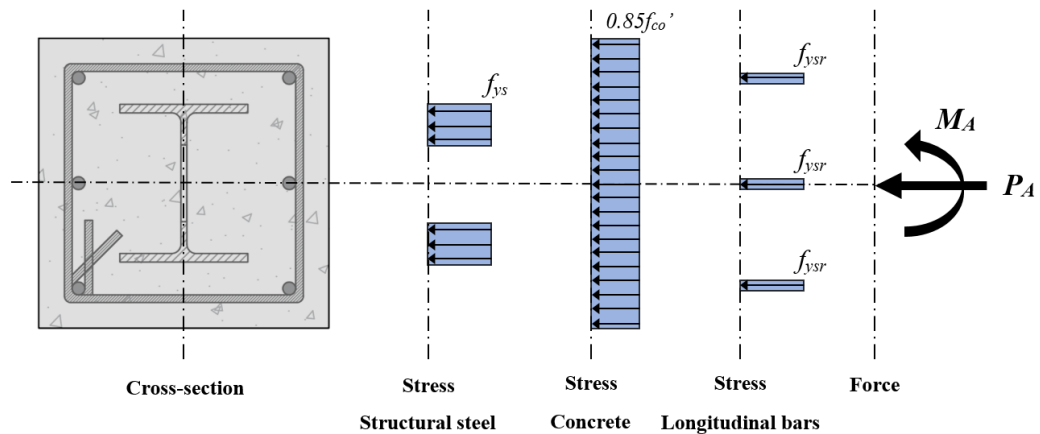
Figure 7.17 Determination of P-M interaction of point A of simplfied plastic stress distribution method of CECS columns.

Figure 7.18 shows stress distribution and axial force – moment relation of point B of the CECS columns. The equation of axial force (P_B) and moment (M_B) is expressed as follows,

$$P_B = 0 \tag{7.8}$$

$$M_B = M_D - Z_{sn}F_y - Z_{cn}\left(0.85f_{co}{}'\right)/2 \tag{7.9}$$

$$Z_{cn} = Bh_n{}^2 - Z_{sn} \tag{7.10}$$

When $h_n \leq \dfrac{d_g}{2} - t_f$

$$h_n = \frac{\dfrac{0.85f_{co}{}'A_c}{2} - 0.85f_{co}{}'t_w\dfrac{D_o}{2} + 2f_{ys}t_w\dfrac{D_o}{2} - f_{ysr}A_{srs}}{2f_{ys}t_w + 0.85f_{co}{}'\left(B - t_w\right)} \tag{7.11}$$

$$Z_{sn} = t_w\left(h_n - \frac{d_g}{2}\right)\left(h_n + \frac{d_g}{2}\right) \tag{7.12}$$

When $\dfrac{d_g}{2} - t_f < h_n \leq \dfrac{d_g}{2}$

189

$$h_n = \frac{0.85 f_{co}{}'\left(A_c + A_{s,net} - d_g b_f + A_{srs}\right) - 2f_{ys}\left(A_s - d_g b_f\right) - 2f_{ysr}A_{srs}}{2\left[0.85 f_{co}{}'\left(B - b_f\right) + 2f_{ys}b_f\right]} \tag{7.13}$$

$$Z_{sn} = Z_s - b_f\left(\frac{d_g}{2} - h_n\right)\left(\frac{d_g}{2} + h_n\right) \tag{7.14}$$

When $h_n > \dfrac{d_g}{2}$

$$h_n = \frac{0.85 f_{co}{}'\left(A_c + A_{s,net} + A_{srs}\right) - 2f_{ys}A_{s,net} - 2f_{ysr}A_{srs}}{2\left(0.85 f_{co}{}'B\right)} \tag{7.15}$$

$$Z_{sn} = Z_{s,net} \tag{7.16}$$

Where

A_{srs} = cross-sectional area of longitudinal rebar at centerline of column section;

b_f = flange width of cellular steel member;

d_g = total depth of cellular steel member;

h_n = distance between plastic neutral axis to centerline of column section;

t_f = flange thickness of cellular steel member;

t_w = web thickness of cellular steel member;

$Z_{s,net}$ = plastic section modulus at net section about x axis.
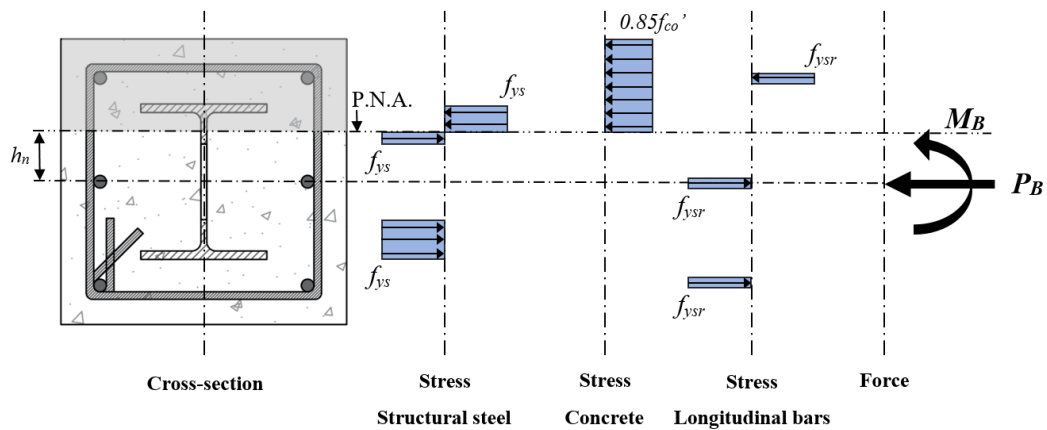
Figure 7.18 Determination of P-M interaction of point B of simplfied plastic stress distribution method of CECS columns.

Figure 7.19 shows stress distribution and axial force – moment relation of point C of the CECS columns. The equation of axial force (P_C) and moment (M_C) is expressed as follows,

$$P_C = 0.85 f_{co}' A_c \tag{7.17}$$

$$M_C = M_B \tag{7.18}$$
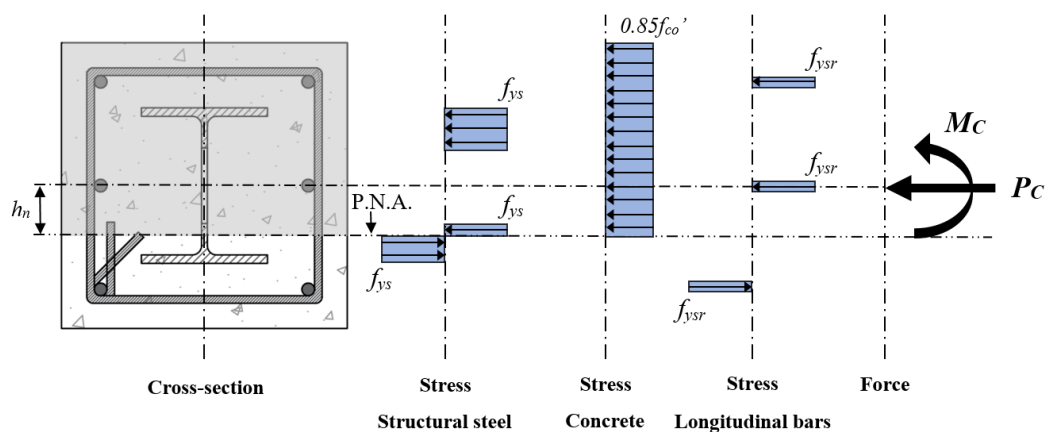
Figure 7.19 Determination of P-M interaction of point C of simplfied plastic stress distribution method of CECS columns.

Figure 7.20 shows stress distribution and axial force – moment relation of point D of the CECS columns. The equation of axial force (P_D) and moment (M_D) is expressed as follows,

$$P_D = \frac{0.85 f_{co}' A_c}{2} \tag{7.19}$$

$$M_D = Z_{s,net} f_{ys} + Z_r f_{ysr} + \frac{Z_c (0.85 f_{co}')}{2} \tag{7.20}$$

$$Z_c = \frac{BD^2}{4} - Z_{s,net} - Z_r \tag{7.21}$$

$$Z_r = (A_{sr} - A_{srs}) \left(\frac{D}{2} - c \right) \tag{7.22}$$

Where

c =   concrete covering.
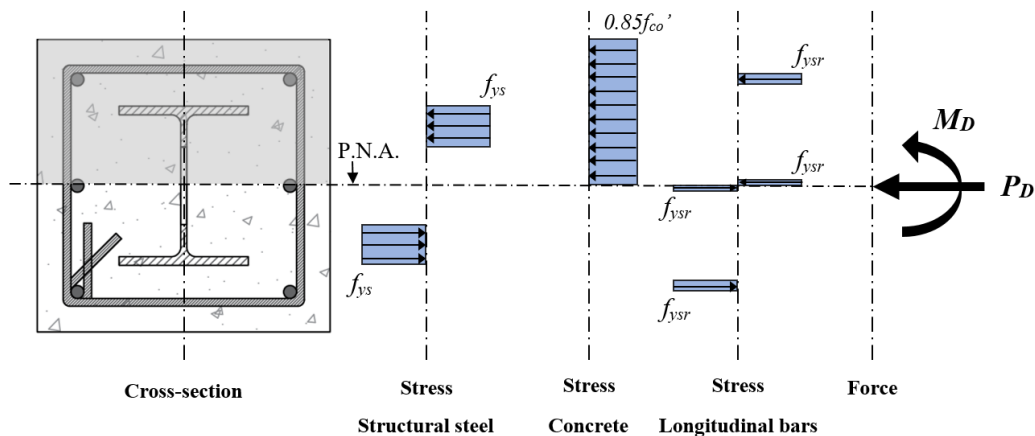
Figure 7.20 Determination of P-M interaction of point D of simplified plastic stress distribution method of CECS columns.

     Figure 7.21 shows comparison between the interaction diagram developed by simplified plastic stress distribution method and the experimental results of composite columns subjected to concentric and eccentric loadings. The comparison shows that this method accurately predicts the interaction diagram with the test results. For the columns subjected to concentric loads, this method predicts unconservatively. For the columns subjected to eccentric loading (E1, $e/B \approx 0.1$), this method predicts conservatively. For the columns subjected to eccentric loading (E2, $e/B \approx 0.2$), this method predicts unconservatively.
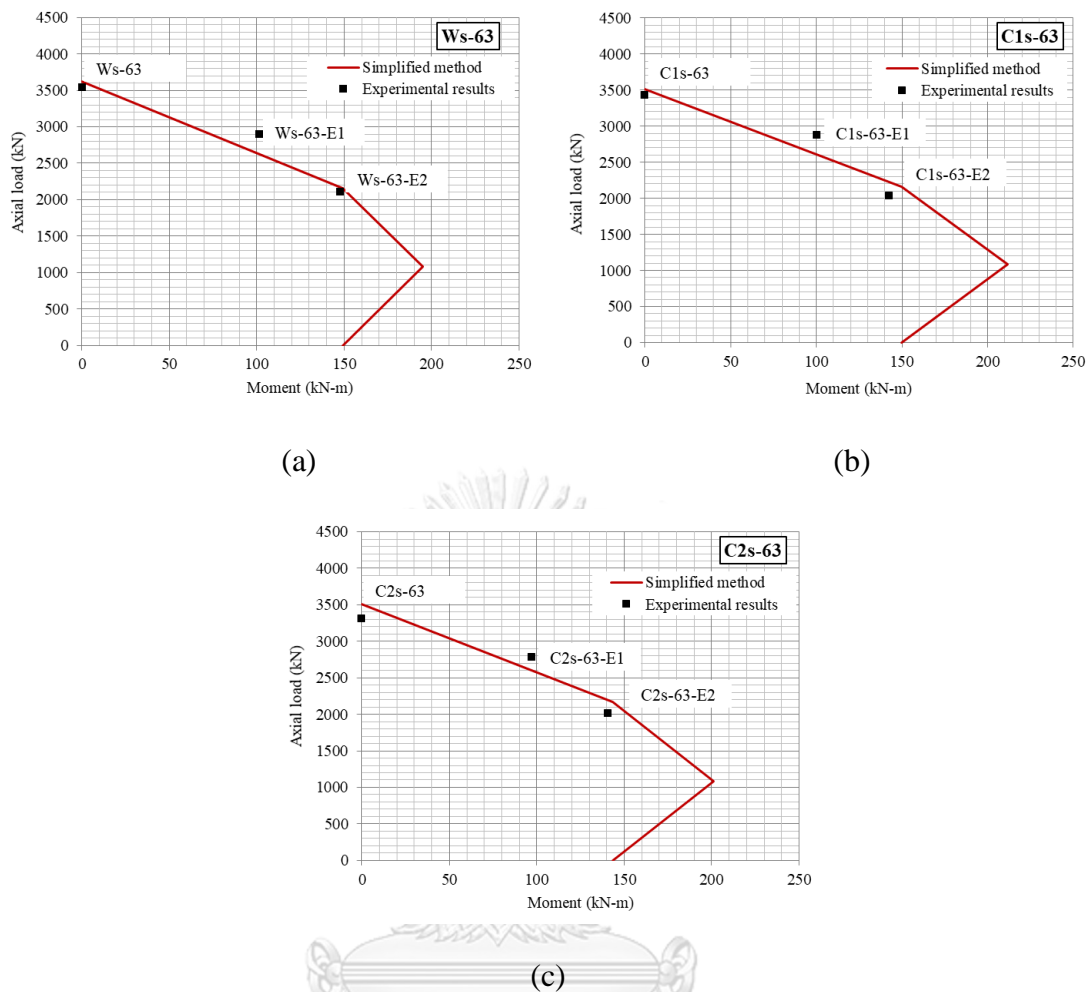
Figure 7.21 Comparison of the strength interaction diagram of CES and CECS columns between simplified plastic stress distribution method and experimental results; (a) Ws-63; (b) C1s-63; and (c) C2s-63.

7.2.3 Comparison of different methods

Figure 7.22 shows comparison of the strength interaction diagram of CECS and CES columns between plastic stress distribution method and simplified plastic stress distribution method [AISC 360-16 (Chapter H) method]. The comparison shows that the plastic stress distribution method is more accurately predict the strength interaction diagram than the simplified method. However, the simplified method is easier for calculation than the plastic stress distribution method.
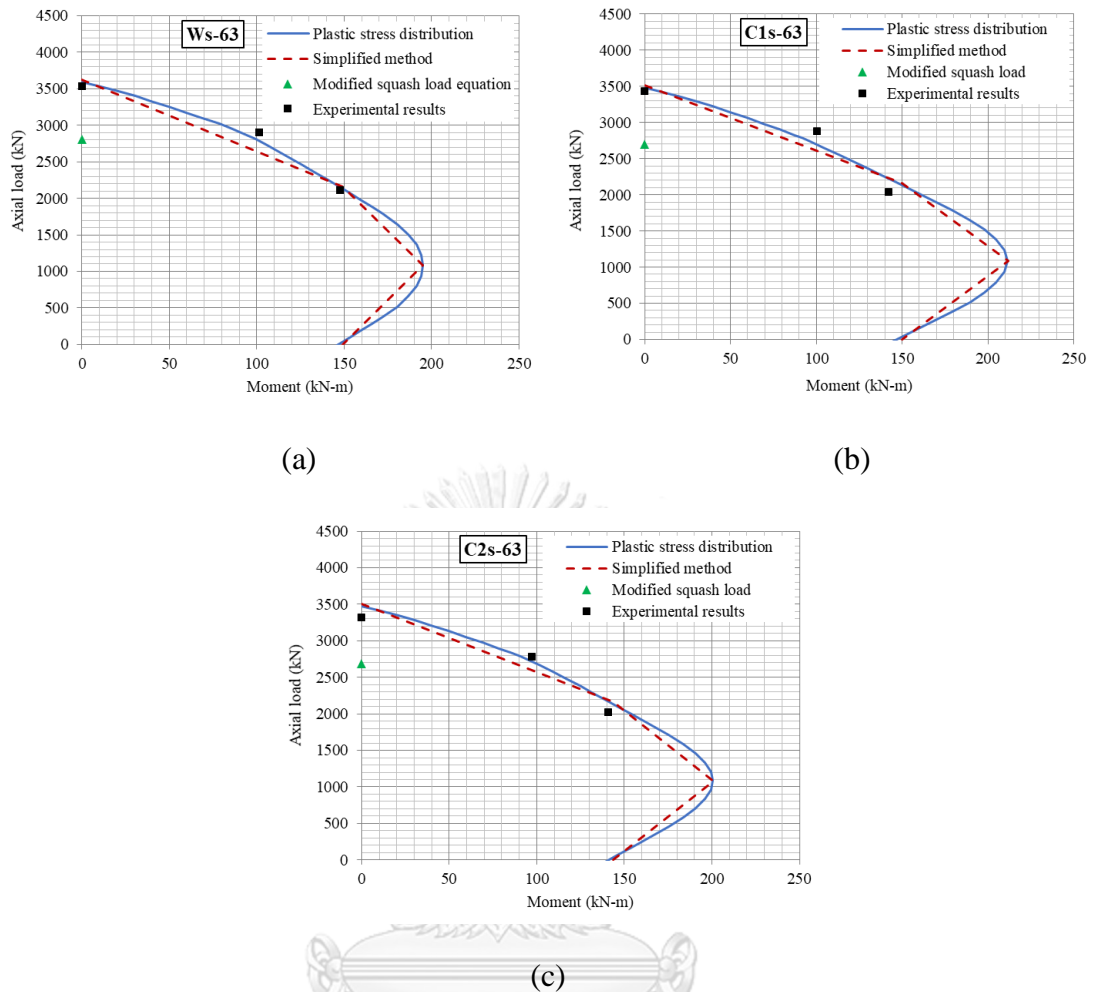
Figure 7.22 Comparison of the strength interaction diagram of composite columns between plastic stress distribution method and simplified plastic stress distribution method; (a) Ws-63; (b) C1s-63; and (c) C2s-63.

7.2.4 Parametric study

Figure 7.23 shows the comparison of strength interaction diagrams between the CECS and CES columns tested in this research by the plastic stress distribution method and the simplified plastic stress distribution method. The comparison shows that the CECS columns have higher strength than CES columns in low axial load and high moment condition.

(a)   (b)
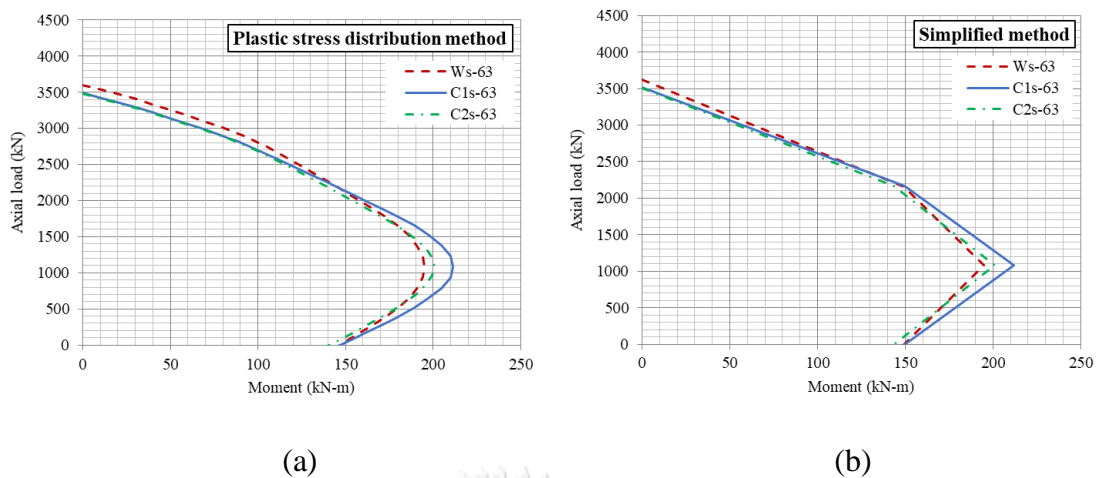
Figure 7.23 Comparison of strength interaction diagrams between CECS and CES
columns by; (a) plastic stress distribution method; and (b) simplified method.

Figure 7.24 shows properties of the CES and CECS columns, which was used
to study the effect of design parameters on the strength interaction diagrams. The
interaction diagrams were performed by the simplified plastic stress distribution
method. The design parameters consist of hole diameter to depth of parent ratio
(D_o / d) and hole spacing to hole diameter ratio (S / D_o). The dimensions of the
columns were 340×400 mm in cross section and 1100 mm in height. Four 15-mm-
diameter round bars (RB15) were used as the corner longitudinal reinforcements. The
compressive strength of concrete cylinders was 21 MPa. For the structural steel
member, flange width, total depth, flange thickness, and web thickness were 150 mm,
150 mm, 10 mm, and 7 mm, respectively. Yield stress and elastic modulus of
structural steel and reinforcement steel were 300 MPa and 210000 MPa.

Figure 7.25 shows the effect of hole diameter to depth of parent ratio (D_o / d)
on strength interaction diagrams of CECS columns. The study shows that increase of
D_o / d decreases the axial capacity (the maximum reduction is less than 10 %), but
increases bending capacity (the maximum increase is more than 20 %) of the CECS
columns.

Figure 7.26 shows the effect of hole spacing to hole diameter ratio (S / D_o) on
strength interaction diagrams of CECS columns. The study shows that increase of
S / D_o decreases both axial capacity and bending capacity of the CECS columns.
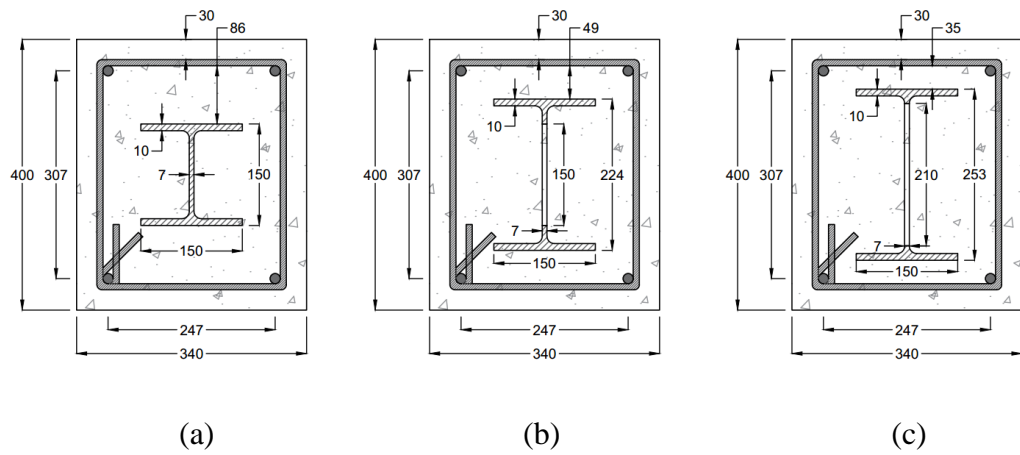
Figure 7.24 (a) CES column; (b) CECS column with $D_o / d = 1.0$ and $S / D_o = 1.2$; and (c) CECS column with $D_o / d = 1.4$ and $S / D_o = 1.2$ for parametric study.
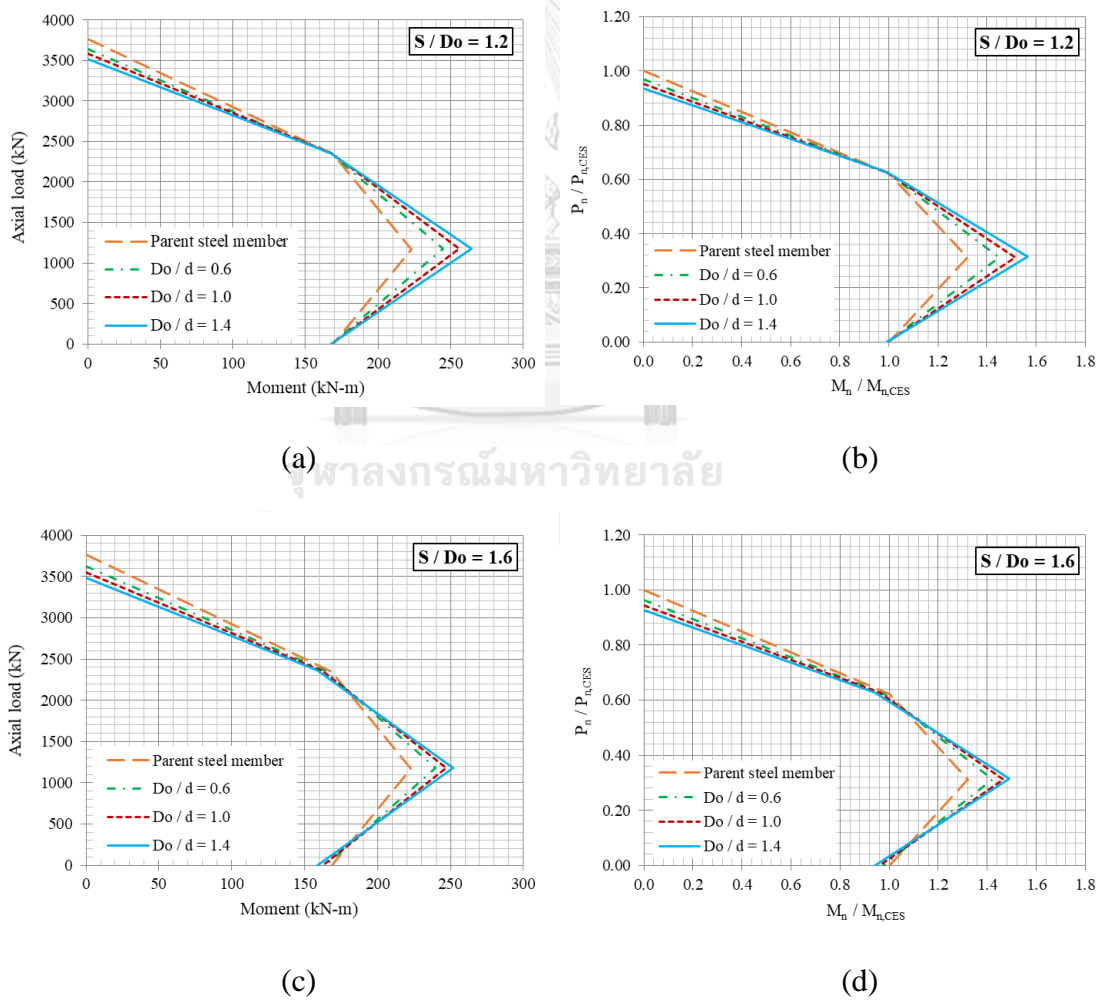
Figure 7.25 Effect of hole diameters on strength interaction diagrams of CECS and CES columns; (a-b) $S / D_o = 1.2$; and (c-d) $S / D_o = 1.6$.

(a)

(b)

(c)

(d)
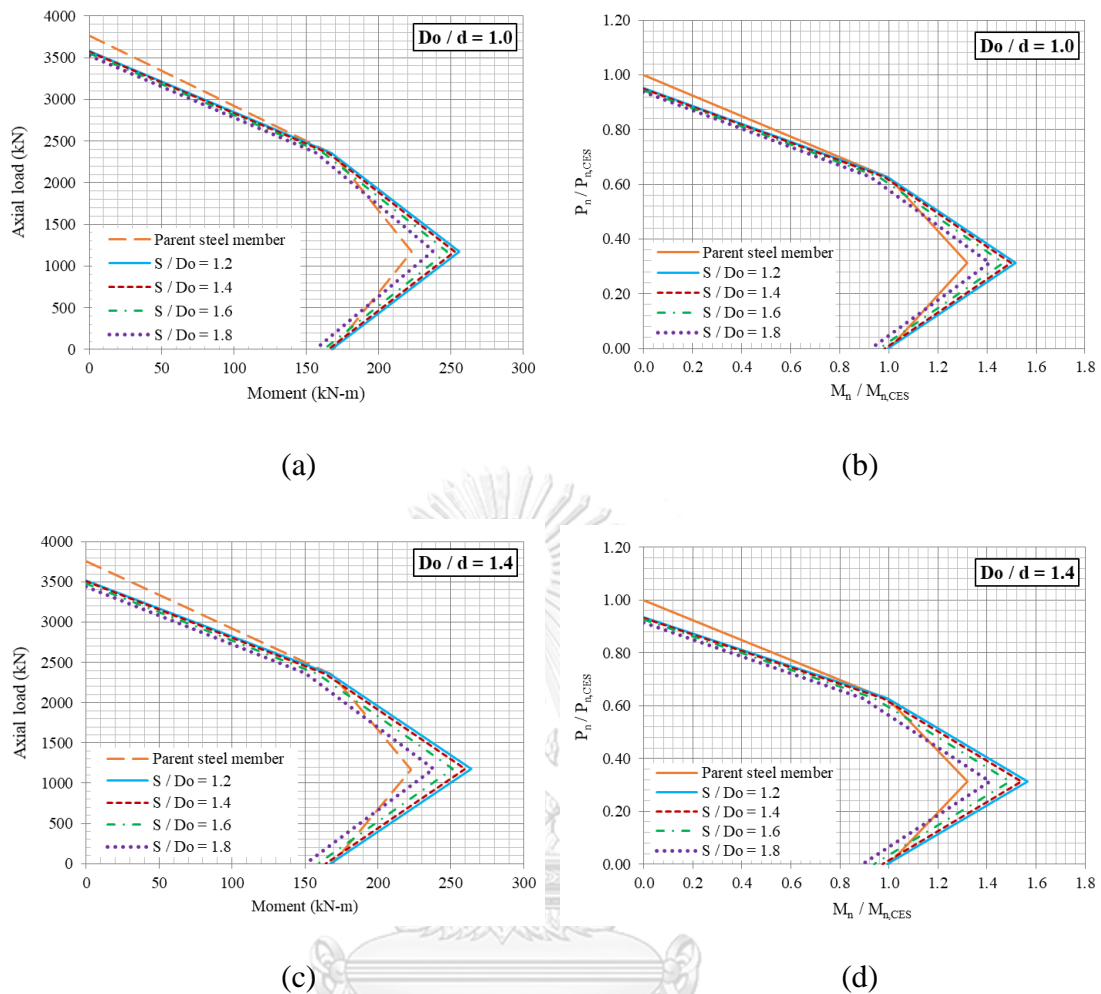
Figure 7.26 Effect of hole spacings on strength interaction diagrams of CECS and CES columns; (a-b) $D_o / d = 1.0$; and (c-d) $D_o / d = 1.4$.

7.2.5 Conclusions

The conclusions of strength interaction diagram of the CECS and CES columns are as follows,

- The plastic stress distribution method and simplified plastic stress distribution method are applicable to develop the strength interaction diagrams of CECS and CES columns.

- The plastic stress distribution method predicts the strength interaction diagram more accurately than the simplified plastic stress distribution method. However, the simplified method is easier calculation than the plastic stress distribution method.

- The comparison of strength interaction diagrams between CECS and CES columns shows that the CECS columns have higher strength than CES columns in low axial load and high moment condition.

- Increase of hole diameter to depth of parent ratio (D_o / d) decreases axial capacity (the maximum reduction is less than 10 %), but increases bending capacity (the maximum increase is more than 20 %) of the CECS columns.

- Increase of hole spacing to hole diameter ratio (S / D_o) decreases both axial capacity and bending capacity of the cellular steel columns.

CHAPTER 8
CONCLUSIONS

8.1 Conclusions

This research investigates the cellular steel columns and the concrete-encased cellular steel (CECS) columns. This research is divided into three main parts. The experimental studies of the cellular steel and CECS columns were proposed in first part. The analytical models and the simplified equation to predict the axial compressive strength of the cellular steel and CECS columns were proposed in second part. Using the existing method and modifying the AISC 360-16 method to develop the strength interaction diagram of the cellular steel and CECS columns was discussed in third part.

In the first part, the experimental study of the cellular steel columns and the CECS columns subjected to concentric and eccentric loadings was conducted in the laboratory.

For the experimental study of the cellular steel columns subjected to concentric loadings, all cellular steel columns exhibited yielding and hardening behavior. However, the hardening behavior became less obvious as hole size increased. Axial stiffness of the cellular steel columns is close to the axial stiffness of the parent steel column. The cellular columns had the averaged proportional limit, yield and maximum loads less than the corresponding values of the parent column by 17, 15, and 17 %, respectively. Failure mode of the cellular steel columns is both web and flange local buckling occurred at the hole section. The local buckling occurred at the strain reached yield stress. No failure of weldment was observed.

For the experimental study of the CECS columns subjected to concentric loadings, axial stiffness of the CECS columns is close to the axial stiffness of the CES column. The CECS columns had the averaged maximum loads less than the CES column by 3 – 6 %. Failure of the CECS columns in this research was cover concrete spalling and buckling of the longitudinal rebars at maximum loads, which was similar to the CES columns in this research. With similar stirrup spacing, the load – deformation curves of the CECS columns are similar to the CES columns. For the load – axial strain curves, the curve can be divided into three stages: (1) linear elastic stage (from origin to the proportional limit) where the initial slope was the axial rigidity. (2)

nonlinear elastic stage (from the proportional limit to the maximum load). At the maximum loads, the strain in structural steel almost achieved the coupon yield strain. Meanwhile, the strain in reinforcement bars did not achieve the yield strain of rebars; and (3) post-peak stage (beyond the maximum load), the strain in structural steel suddenly dropped. But the columns were capable of sustaining 80% of the maximum loads until steel strain at about 0.004. The measured ductility indexes of the CECS columns was about 3 similarly to the CES columns. For parametric study, effect of increase concrete strength or decreasing stirrup spacing of CECS columns are increase strength of the CECS columns. In addition, the concrete confinement behavior of the composite columns was not captured by the strain gauges installed in transverse direction.

For the experimental study of the cellular steel columns subjected to eccentric loadings, the cellular columns had the averages yield and maximum loads less than the parent column by 16 and 10 %, respectively, for eccentricity 17.5 mm and by 4 and 4 %, respectively, for eccentricity 35 mm. All cellular steel columns exhibited yielding and slight hardening behaviors. Failure mode of the cellular steel columns are both compression web and compression flange local buckling occurred at the hole section. No failure of weldment was observed. In addition, the load – axial deformation curves and the load – axial strain curves of the cellular columns are similar to the curves of the parent steel columns.

For the experimental study of the CECS columns subjected to eccentric loadings, the CECS columns had slightly less compressive strength values than the CES columns with the average ratio of 0.96, 0.94, and 0.97 for concentric loadings, eccentric loadings E1 (35 mm) and eccentric loadings E2 (70 mm), respectively. Failure mode of the composite columns subjected to eccentric loads E1 (35 mm) was crushing of concrete occurred on the compression side at mid-height of the columns. After that, transverse crack expanded rapidly from the compression side to the tension side; and, transverse crack occurred on the tension side. Failure mode of the composite columns subjected to eccentric loads E2 (70 mm) was concrete crushing occurred on the compression side and large transverse crack occurred on the tension side at the same time. For the axial strain contribution, the strain distribution across the section remain linear up to over 80 % of maximum loads. The hypothesis plane-section remain plane is satisfied.

In the second part, the analytical models to predict the load – strain relation of the cellular steel columns and the CES columns are proposed. In addition, the equations to predict the yield load and axial stiffness of the cellular steel columns, the maximum loads, and axial stiffness of the CECS columns are proposed.

For the cellular steel columns, an analytical model to predict load – strain curve of the cellular steel columns was proposed and validated with the experimental results. The model accurately predicts the yield loads and axial stiffnesses of the tested cellular steel columns in this research. However, the model should be validated with more tested cellular steel columns in the future.

For the CES columns with concrete confinement behavior, a modified analytical model based on Chen and Wu (2017) model was proposed, which modified by using a design chart for calculating compressive strength of confined concrete of Mander et al. (1988). The modified model is applicable for the CES columns with the cross section of structural steel as I-shape, H-shape or cross-shape. The modified model accurately predicts the load – axial strain curves and the axial compressive behavior of the CES columns. In addition, the effects of the design parameters on the maximum loads of the CES columns, the partially confined factor, the highly confined factor and the reduction factor of steel web were investigated in this research. Increase of concrete strength increased the maximum loads, reduced the partially confined factor and highly confined factor of the CES columns. Increase of steel strength slightly reduced the reduction factor of steel web. Increase of stirrup spacing reduced the partially confined factor and highly confined factor, and slightly reduced the maximum loads. Increase of flange slenderness ratio or increase of web slenderness ratio slightly reduced the maximum loads, the partially confined factor, and highly confined factor; and the increase of flange slenderness ratio slightly increased the reduction factor of steel web.

For the CES and CECS columns with early spalling of cover concrete and did not have the concrete confinement behavior, the analytical model and squash load equation overestimate the axial compressive strength of the tested CES columns in this research. The overestimation of the squash load equation was highest at 19 % for the largest stirrup spacing. This overestimation was possibly due to the use of total concrete area. Therefore, the modified squash load equations, which was proposed by Lai et al. (2019), was used to predict the axial compressive strength of the tested CES columns,

and adopted to predict the axial compressive strength of the tested CECS columns. The modified squash load equations accurately predicted the strength of the CES and CECS columns with low-strength concrete and large stirrup spacing. The prediction tended to be less accurate, i.e., more conservative, as concrete strength increased and stirrup spacing decreased. Therefore, the modified squash load equation is recommended for the CES and CECS columns with low-strength concrete strength (as low as 21 MPa AISC minimum), low longitudinal reinforcement ratio (as low as AISC minimum), and large stirrup spacing (up to the AISC maximum). It should be noted that the squash load equation conservatively predicts the axial compressive strength of the CES and CECS columns in range of AISC specification; and the analytical model is appropriate with the CES columns with small stirrup spacing, which have evident effect of concrete confinement behavior. In addition, the equation to predict the axial stiffnesses of the CECS columns was proposed by using the equivalent cross-sectional area of the cellular steel members. The proposed equation accurately predicted the axial stiffness of CECS columns with high stirrup spacing, and underestimated axial stiffness of CECS columns with closely stirrup spacing.

In the third part, the plastic stress distribution method and the modified AISC 360-16 methods are used to develop the strength interaction diagram of the cellular steel columns and the CECS columns.

For the cellular steel columns, the plastic stress distribution method and modified AISC 360-16 (chapter H) method is applicable to develop the strength interaction diagrams of cellular steel columns. From the parametric study, increase of hole diameter to depth of parent ratio (D_o / d) decreases axial capacity, but increases bending capacity of the cellular steel columns. Increase of hole spacing to hole diameter ratio (S / D_o) decreases both axial capacity and bending capacity of the cellular steel columns. From the study of effect of design parameters, it was concluded that the smallest value of   should be chosen.

For the CECS steel columns, the plastic stress distribution method and simplified plastic stress distribution method are applicable to develop the strength interaction diagrams of CECS and CES columns. The plastic stress distribution method predicts the strength interaction diagram more accurately than the simplified plastic

stress distribution method. However, the simplified method is easier in the calculation than the plastic stress distribution method. The comparison of strength interaction diagrams between CECS and CES columns shows that the CECS columns have higher strength than CES columns at low axial load and high moment condition. For the parametric study, increase of hole diameter to depth of parent ratio (D_o / d) decreases axial capacity (the maximum reduction is less than 10 %), but increases bending capacity (the maximum increase is more than 20 %) of the CECS columns. Increase of hole spacing to hole diameter ratio (S / D_o) decreases both axial capacity and bending capacity of the cellular steel columns.

8.2 Recommendation for future works

8.2.1 Recommendation for experimental study in the future works

- Experimental study of the cellular steel columns and the CECS columns subjected to combining of low axial load and high moment should be investigated, because this research found that the cellular steel columns and the CECS columns are stronger than the parent steel columns and CES column, respectively, in this load condition.

- Experimental study of the cellular steel columns and the CECS columns with high hole diameter to depth ratio should be investigated, because this research investigated the cellular steel columns and the CECS columns with low hole diameter to depth ratio.

8.2.2 Recommendation for numerical study in the future works

- Finite element analysis of the cellular steel columns and the CECS columns subjected to concentric and eccentric loadings should be investigated.

- Analytical models for predicting axial load – strain relation of the CECS and CES columns with cover concrete spalling before the columns reached maximum loads should be investigated.

NOMENCLATURE

A_c cross-sectional area of concrete;

$A_{c,core}$ cross-sectional area of concrete core bounded by closed stirrup;

$A_{cellular}$ cross-sectional area of cellular steel column at net section;

A_e effective area of confined concrete;

A_g total cross-sectional area;

A_{hc} cross-sectional area of highly confined concrete;

A_o cross-sectional area of cellular steel member at center of opening;

A_{pc} cross-sectional area of partially confined concrete;

A_s cross-sectional area of structural steel member;

$A_{s,eq}$ equivalent cross-sectional area of cellular steel member;

$A_{s,g}$ gross cross-sectional area of cellular steel member (at solid web section);

$A_{s,parent}$ cross-sectional area of parent steel column;

A_{shx} area of stirrups in the x direction;

A_{shy} area of stirrups in the y direction;

$A_{s,net}$ critical cross-sectional area of cellular steel member (at critical section, i.e., double tee section at hole middle, of cellular steel member);

A_{sr} cross-sectional area of longitudinal rebars;

A_{srs} cross-sectional area of longitudinal rebar at centerline of column section;

A_{sx} area of stirrups in the x direction;

A_{sy} area of stirrups in the y direction;

A_{tee} area of tee-section of cellular steel member at opening section;

A_{uc} cross-sectional area of unconfined concrete;

B total width of cross-section of column;

b clear width of steel flange;

b_c diameter of stirrups in x direction;

b_f flange width of structural steel;

c concrete covering;

c_x concrete core dimension to center line of stirrup in x-direction;

c_y concrete core dimension to center line of stirrup in y-direction;

D total depth of cross-section of column;

D_o hole diameter of cellular column;

DI ductility index;

d total depth of steel column;

d_g total depth of cellular steel column;

d_s diameter of spiral;

d_{sh} diameter of stirrup;

d_{tee} depth of tee section;

E_c elastic modulus of concrete;

E_s elastic modulus of structural steel;

E_{sec} secant modulus of concrete at peak strength of confined concrete;

E_{sr} elastic modulus of reinforcement bars;

EA_{ana} axial rigidity (analytical prediction);

EA_{exp} axial rigidity (experiment);

EI_{eff} effective flexural rigidity;

e load eccentricity;

F_{cr} critical stress;

F_e elastic buckling stress;

f_{hcc} real stress in stirrup;

f_c stress of concrete;

$f_{cc}{}'$ compressive strength of confined concrete;

$f_{cc,\mathrm{h}}{}'$ compressive strength of highly confined concrete;

$f_{cc,\mathrm{p}}{}'$ compressive strength of partially confined concrete;

$f_{cc,u}{}'$ compressive strength of unconfined concrete;

f_{co}'	compressive strength of concrete cylinder;
f_{hc}	stress of highly confined concrete;
f_{hcc}	stress in the transverse reinforcement at the maximum strength of confined concrete;
f_l	lateral pressure;
f_l'	effective lateral pressure;
$f_{le,r}'$	lateral confining pressure from stirrups;
$f_{le,s}'$	lateral confining pressure from structural steel;
f_{pc}	stress of partially confined concrete;
f_s	stress of structural steel;
f_{sr}	stress of longitudinal rebar;
f_{st}	maximum lateral tensile stress in web;
f_{sv}	maximum vertical stress in web;
f_{rh}	real stress in stirrups;
f_{uc}	stress of unconfined concrete;
f_y	specified minimum yield stress of steel;
f_{ys}	specified minimum yield stress of structural steel;
f_{ysh}	specified minimum yield stress of stirrup;
f_{ysr}	specified minimum yield stress of longitudinal rebar;
h	clear height of steel web;
h_n	distance between plastic neutral axis to centerline of column section;
I_c	moment of inertia of concrete section about elastic neutral axis of composite section;
I_s	moment of inertia of structural steel section about elastic neutral axis of composite section;
I_{sr}	moment of inertia of longitudinal rebars about elastic neutral axis of composite section;

I_{sx} moment of inertia about x-axis;

$I_{sx,cellular}$ moment of inertia about x-axis of cellular steel column;

K_h confinement factor of highly confined concrete;

K_p confinement factor of partially confined concrete;

K_w reduction factor of steel web;

k_e area ratio of effectively confined area of partially confined concrete;

k_{ea} confinement effectiveness coefficient;

k_{es} stress effectiveness coefficient;

L column length;

$loss$ loss from fabrication of cellular steel column;

M_c available flexural strength;

$M_{o,pl}$ plastic bending moment capacity of cross-section at center of opening;

M_{pl} plastic bending moment capacity of cross-section;

M_r required flexural strength;

M_{sd} reduced plastic bending moment capacity;

M_y yield bending moment capacity of cross-section;

$N_{o,pl}$ plastic axial compressive capacity of cross-section at center of opening;

N_{pl} plastic axial compressive capacity of cross-section;

N_{sd} axial compressive force;

P assumed axial load;

P_c available axial strength;

P_{max} maximum loads (experiment);

P_{no} nominal strength of CES and CECS column;

P_r required axial strength;

P_{squash} squash load for CES and CECS column (analytical prediction);

$P_{sq,mod}$ modified squash load for CES and CECS column (analytical prediction);

P_p load at proportional limit (experiment);

$P_{y,ana}$ load at yield point (analytical prediction);

$P_{y,\exp}$ load at yield point (experiment);

q_u maximum lateral confining pressure;

r_x radius of gyration about x axis;

r_y radius of gyration about y axis;

S center-to-center hole spacing of cellular column;

S_x elastic section modulus about x-axis;

S_y elastic section modulus about y-axis;

s longitudinal spacing of stirrup;

s' clear longitudinal spacing of stirrup;

t_f flange thickness of structural steel;

t_w web thickness of structural steel;

W_s weight per length of steel column;

$W_{s,cellular}$ weight per length of cellular steel column;

w_i' clear transverse spacing between adjacent longitudinal bars;

x subscript relating symbol to major axis bending;

y subscript relating symbol to minor axis bending;

$Z_{s,g}$ plastic section modulus of gross section about x axis;

$Z_{s,net}$ plastic section modulus of net section about x axis;

$Z_{s,o}$ plastic section modulus of cross-section at opening about x axis;

Z_x plastic section modulus about x axis;

$Z_{x,cellular}$ plastic section modulus about x axis of cellular steel column;

$Z_{x,parent}$ plastic section modulus about x axis of parent steel column;

Z_y plastic section modulus about y axis;

ρ_{cc} ratio of longitudinal reinforcement area to core section area;

ρ_c density of concrete;

ρ_s density of steel;

ρ_{sh} effective volume ratio of stirrups;

ρ_{sr} ratio of stirrups volume to concrete core volume;

ε_{hcc} real strain in stirrup;

ε_c corresponding strain of concrete;

ε_{C50C} longitudinal strain of confined concrete at 50% of the maximum compressive stress;

ε_{C50U} longitudinal strain of unconfined concrete at 50% of the maximum compressive stress (= 0.004);

ε_{co} corresponding strain at compressive strength of concrete cylinder;

ε_{cc} corresponding strain at compressive strength of confined concrete;

ε_{max} corresponding strain at maximum load;

ε_p corresponding strain at proportional limit load;

ν_c Poisson's ratio of concrete;

ν_s Poisson's ratio of steel;

Δ_{hole} axial deformation along the hole section of the cellular steel column;

Δ_{solid} axial deformation along the solid web section of the cellular steel column;

Δ_{total} total axial deformation of the cellular steel column;

REFERENCES

ACI. (2014). Building code requirements for structural concrete (ACI 318-14). In. Farmington Hills, Michigan: American Concrete Institute.

Ahmad, S., Masri, A., and Saleh, Z. A. (2017). Analytical and experimental investigation on the flexural behavior of partially encased composite beams. *Alexandria Engineering Journal, 57*(3), 1693-1712.

AISC. (1990). Steel design guide 2: Design of steel and composite beams with web openings. In. Chicago, Illinois: American Institute of Steel Construction.

AISC. (1992). Steel design guide 6: Load and resistance factor design of W-shapes encased in concrete. In. Chicago, Illinois: American Institute of Steel Construction.

AISC. (2016a). Specification for structural steel buildings (ANSI/AISC 360-16). In. Chicago, Illinois: American Institute of Steel Construction.

AISC. (2016b). Steel design guide 31: Castellated and cellular beam design. In. Chicago, Illinois: American Institute of Steel Construction.

Al-Shahari, A. M., Hunaiti, Y. M., and Ghazaleh, B. A. (2003). Behavior of lightweight aggregate concrete-encased composite columns. *Steel and Composite Structures, 3*(2), 97-110.

Begum, M., Driver, R. G., and Elwi, A. E. (2007). Finite-element modeling of partially encased composite columns using the dynamic explicit method. *Journal of Structural Engineering, 133*(3), 326-334.

Begum, M., Driver, R. G., and Elwi, A. E. (2013). Behaviour of partially encased composite columns with high strength concrete. *Engineering Structures, 56*, 1718-1727.

Chen, C., and Lin, N. (2006). Analytical model for predicting axial capacity and behavior of concrete encased steel composite stub columns. *Journal of Constructional Steel Research, 62*(5), 424-433.

Chen, S., and Wu, P. (2017). Analytical model for predicting axial compressive behavior of steel reinforced concrete column. *Journal of Constructional Steel Research, 128*, 649-660.

Chicoine, T., Massicotte, B., and Tremblay, R. (2003). Long-term behavior and strength of partially encased composite columns made with built-up steel shapes. *Journal of Structural Engineering, 129*(2), 141-150.

Chicoine, T., Tremblay, R., Massicotte, B., Ricles, J. M., and Lu, L. (2002). Behavior and strength of partially encased composite columns with built-up shapes. *Journal of Structural Engineering, 128*(3), 279-288.

Cusson, D., and Paultre, P., (1995). Stress-strain model for confined high-strength concrete. *Journal of Structural Engineering, 121*(3), 468-477.

El-Sawy, K. M., Sweedan, A. M. I., and Martini, M. I. (2009). Major-axis elastic buckling of axially loaded castellated steel columns. *Thin-Walled Structures, 47*, 1295-1304.

Elghazouli, A. Y., and Elnashai, A. S. (1993). Performance of composite steel/concrete members under earthquake loading. Part II: Parametric studies and design considerations. *Earthquake Engineering & Structural Dynamics, 22*(4), 347-368.

Ellobody, E., and Young, B. (2011). Numerical simulation of concrete encased steel composite columns. *Journal of Constructional Steel Research, 67*(2), 211-222.

Ellobody, E., Young, B., and Lam, D. (2011). Eccentrically loaded concrete encased steel composite columns. *Thin-Walled Structures, 49*(1), 53-65.

Elnashai, A. S., and Elghazouli, A. Y. (1993). Performance of composite steel/concrete members under earthquake loading. Part I: Analytical model. *Earthquake Engineering and Structural Dynamics, 22*(4), 315-345.

Elnashai, A. S., Takanashi, K., Elghazouli, A. Y., and Dowling, P. J. (1991). *Experimental behavior of partially encased composite beam-columns under cyclic and dynamic loads*. Proceedings of the Institution of Civil Engineers.

Farajpourbonab, E., Kute, S., and Inamdar, V. (2017). An experimental study on the strength of cft columns reinforced with castellated cruciform steel sections. *Asian Journal of Civil Engineering (BHRC), 18*(2), 271-284.

Gu, J., and Cheng, S. (2016). Shear effect on buckling of cellular columns subjected to axially compressed load. *Thin-Walled Structures, 98*, 416-420.

Hunaiti, Y. M., and Fattah, B. A. (1994). *Design considerations of partially encased composite columns*. Proceedings of the Institution of Civil Engineers - Structures and Buildings.

Jamkhaneh, M. E., Ahmadi, M., and Sadeghian, P. (2020). Simplified relations for confinement factors of partially and highly confined areas of concrete in partially encased composite columns. *Engineering Structures, 208*, 110303.

Jamkhaneh, M. E., Kafi, M. A., and Kheyroddin, A. (2018). Behavior of partially encased composite members under various load conditions: Experimental and analytical models. *Advances in Structural Engineering, 22*(1), 94-111.

Junus, M., Herman, P., Jonie, T., and Rudy, D. (2015). *Behavior of castellated beam column due to cyclic loads*. Conference on Advances in Civil and Structural Engineering.

Kato, B. (1996). Column curves of steel-concrete composite members. *Journal of Constructional Steel Research, 39*(2), 121-135.

Kim, C., Park, H., Chung, K., and Choi, I. (2012). Eccentric axial load testing for concrete-encased steel columns using 800 MPa Steel and 100 MPa Concrete. *Journal of Structural Engineering, 138*(8), 1019-1031.

Ky, V. S., Tangaramvong, S., and Thepchatri, T. (2015). Inelastic analysis for the post-collapse behavior of concrete encased steel composite columns under axial compression. *Steel and Composite Structures, 19*(5), 1237-1258.

Lai, B., and Liew, J. Y. R. (2020). Axial-moment interaction of high strength concrete encased steel composite columns: Design recommendation. *Journal of Constructional Steel Research, 170*, 106136.

Lai, B., Liew, J. Y. R., and Hoang, A. L. (2019c). Behavior of high strength concrete encased steel composite stub columns with C130 concrete and S690 steel. *Engineering Structures, 200*, 109743.

Lai, B., Liew, J. Y. R., and Wang, T. (2019d). Buckling behaviour of high strength concrete encased steel composite columns. Journal of Constructional Steel Research, 154, 27-42.

Lai, B., Liew, J. Y. R., and Xiong, M. (2019b). Experimental study on high strength concrete encased steel composite short columns. *Construction and Building Materials, 228*, 116640.

Lai, B., Liew, J. Y. R., Hoang, A. L., and Xiong, M. (2019a). A unified approach to evaluate axial force-moment interaction curves of concrete encased steel composite columns. *Engineering Structures, 201*, 109841.

Lai, B., Liew, J. Y. R., Venkateshwaran, A., Li, S., and Xiong, M. (2020). Assessment of high-strength concrete encased steel composite columns subject to axial compression. *Journal of Constructional Steel Research, 164*, 105765.

Mander, J. B., Priestley, M. J. N., and Park, R. (1988). Theoretical stress-strain model for confined concrete. *Journal of Structural Engineering, 114*(8), 1804-1826.

Marinopoulou, A. A., Balopoulos, V. D., and Kalfas, C. N. (2007). Simulation of partially encased composite steel–concrete columns with steel columns. *Journal of Constructional Steel Research, 63*, 1058-1065.

Mirza, S. A., Hyttinen, V., and Hyttinen, E. (1996). Physical tests and analyses of composite steel-concrete beam-columns. *Journal of Structural Engineering, 122*(11), 1317-1326.

Mirza, S. A., and Skrabek, B. W. (1991). Reliability of short composite beam-column strength interaction. *Journal of Structural Engineering, 117*(8), 2320-2339.

Mirza, S. A., and Skrabek, B. W. (1992). Statistical analysis of slender composite beam-column strength. *Journal of Structural Engineering, 118*(5), 1312-1332.

Najafi, M., and Wang, Y. C. (2017). Behaviour and design of steel members with web openings under combined bending, shear and compression. *Journal of Constructional Steel Research, 128*, 579-600.

Panedpojaman, P., Thepchatri, T., and Limkatanyu, S. (2019). Elastic buckling of cellular columns under axial compression. *Thin-Walled Structures, 145*, 106434.

Pereira, M. F., Nardin, S. D., and EI Debs, A. L. H. C. (2016). Structural behavior of partially encased composite columns under axial loads. *Steel and Composite Structures, 20*, 1305-1322.

Piquer, A., and Hernandez-Figueirido, D. (2016). Protected steel columns vs partially encased columns: Fire resistance and economic considerations. *Journal of Constructional Steel Research, 124*, 47-56.

Ricles, J. M., and Paboojian, S. D. (1994). Seismic performance of steel-encased composite columns. *Journal of Structural Engineering, 120*(8), 2474-2494.

Serror, M. H., Hamed, A. N., and Mourad, S. A. (2016). Numerical study on buckling of steel web plates with openings. *Steel and Composite Structures, 22*, 1417-1443.

Sonck, D., and Belis, J. (2016). Weak-axis flexural buckling of cellular and castellated columns. *Journal of Constructional Steel Research, 124*, 91-100.

Sonck, D., Boissonnade, N., and Impe, R. V. (2012). *Instabilities of cellular members loaded in bending or compression.* Proceeding of the Annual Stability Conference.

Sonck, D., Impe, R. V., and Belis, J. (2014). Experimental investigation of residual stresses in steel cellular and castellated members. *Construction and Building Materials, 54*, 512-519.

Sonck, D., Impe, R. V., Belis, J., and Vandebroek, M. (2011). *Buckling failure of compressed cellular members.* Proceedings IABSE-IASS.

Song, Y., Wang, R., and Li, J. (2016). Local and post-local buckling behavior of welded steel shapes in partially encased composite columns. *Thin-Walled Structures, 108*, 93-108.

Sweedan, A. M. I., and El-Sawy, K. M. (2011). Elastic local buckling of perforated webs of steel cellular beam–column elements. *Journal of Constructional Steel Research, 67*, 1115-1127.

Sweedan, A. M. I., El-Sawy, K. M., and Martini, M. I. (2009). Identification of the buckling capacity of axially loaded cellular columns. *Thin-Walled Structures, 47*, 442-454.

Task Group 20, S. S. R. C. (1979). A specification for the design of steel-concrete composite columns. *Engineering Journal, American Institute of Steel Construction, 16*, 105-115.

Uy, B. (2001). Local and postlocal buckling of fabricated steel and composite cross sections. *Journal of Structural Engineering, 127*(6), 666-677.

Wang, Y. C. (1999). Tests on slender composite columns. *Journal of Constructional Steel Research, 49*, 25-41.

Weng, C. C., and Yen, S. I. (2002). Comparisons of concrete-encased composite column strength provisions of ACI code and AISC specification. *Engineering Structures, 24*, 59-72.

Yuan, W., Kim, B., and Li, L. (2014). Buckling of axially loaded castellated steel columns. *Journal of Constructional Steel Research, 92*, 40–45.

Zhu, W., Jia, J., Gao, J., and Zhang, F. (2016). Experimental study on steel reinforced high-strength concrete columns under cyclic lateral force and constant axial load. *Engineering Structures, 125*, 191-204.

APPENDIX A
REINFORCEMENT DETAIL OF SPECIMENS

Figure A.1 – A.17 presents reinforcement details of all tested composite and reinforced concrete columns in this research. The tested composite and reinforced concrete columns were 340×340 mm in cross section and 1100 mm in height. Four 15-mm-diameter round bars (RB15) were used as the corner longitudinal reinforcements. The 9-mm-diameter round bars (RB9) were used as the transverse reinforcements (closed stirrups). In the composite columns, the flange width, web thickness and flange thickness of structural steel were 150 mm, 7 mm and 10 mm, respectively.

(a)   (b)
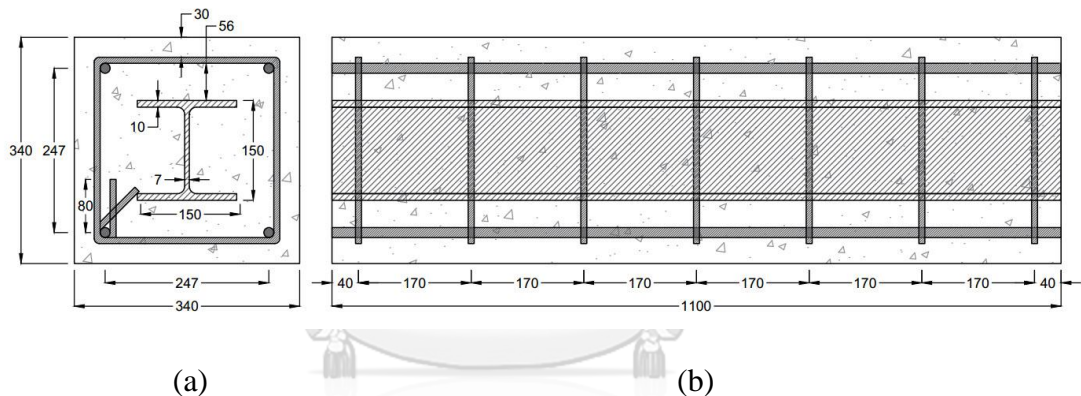
Figure A.1 Reinforcement details of W-170 (A) and W-170 (B) columns;
(a) cross-section; and (b) longitudinal section (dimensions in mm).

(a)   (b)
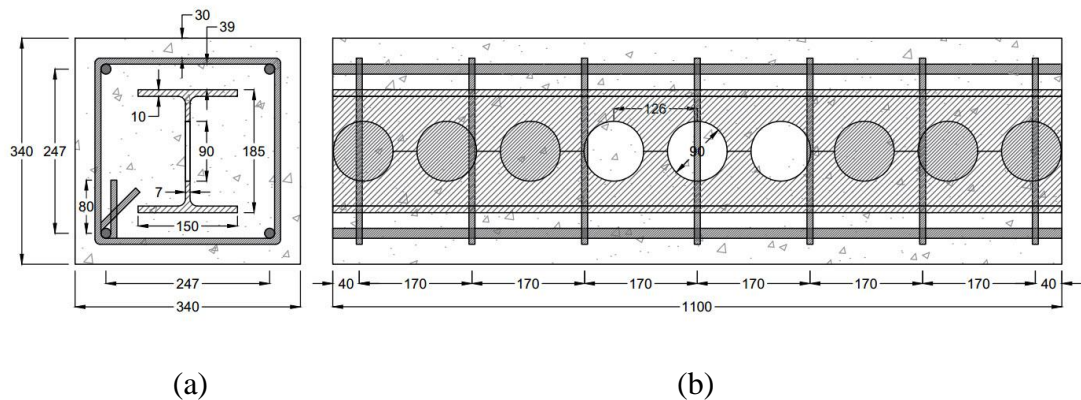
Figure A.2 Reinforcement details of C1-170 (A) and C1-170 (B) columns;
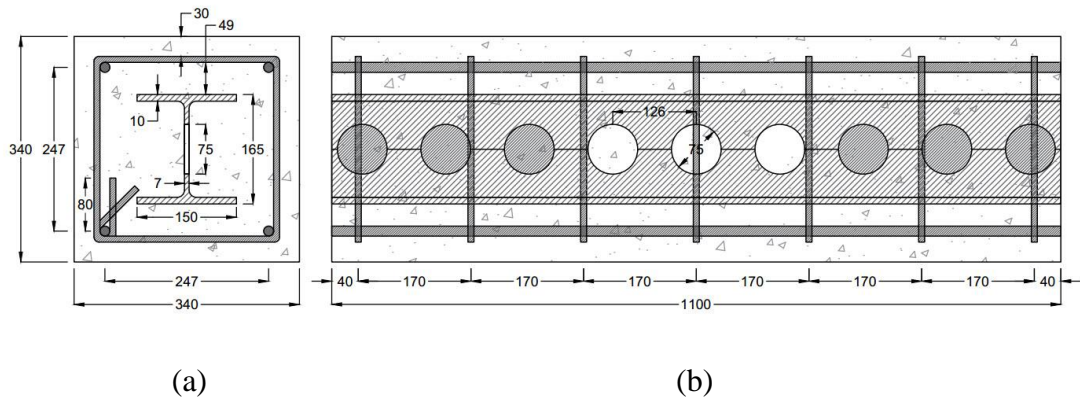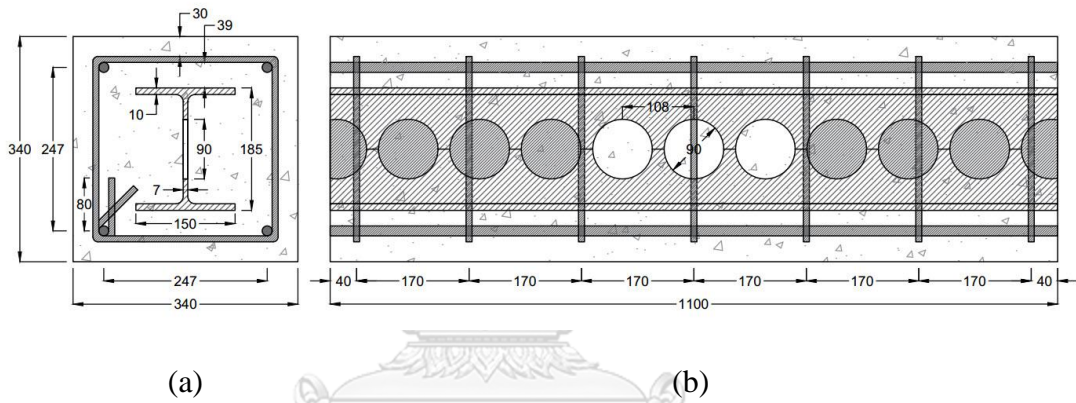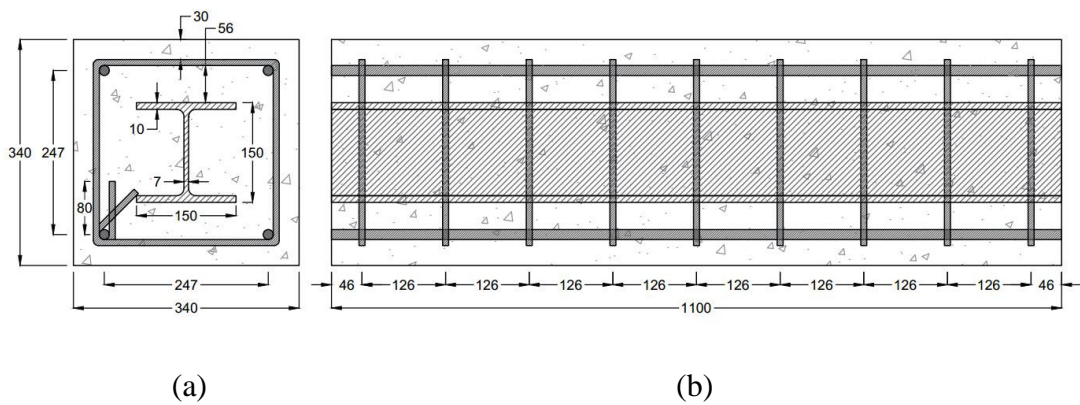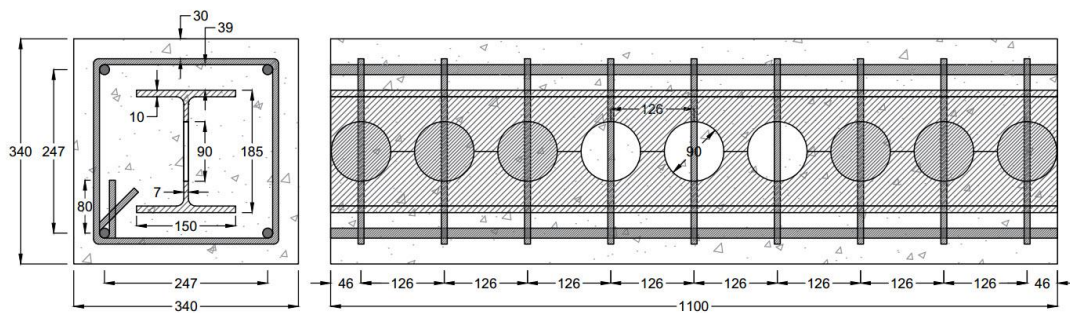(a) cross-section; and (b) longitudinal section (dimensions in mm).

(a)   (b)

Figure A.3 Reinforcement details of C2-170 (A) and C2-170 (B) columns;
(a) cross-section; and (b) longitudinal section (dimensions in mm).

(a)   (b)

Figure A.4 Reinforcement details of C3-170 (A) and C3-170 (B) columns;
(a) cross-section; and (b) longitudinal section (dimensions in mm).

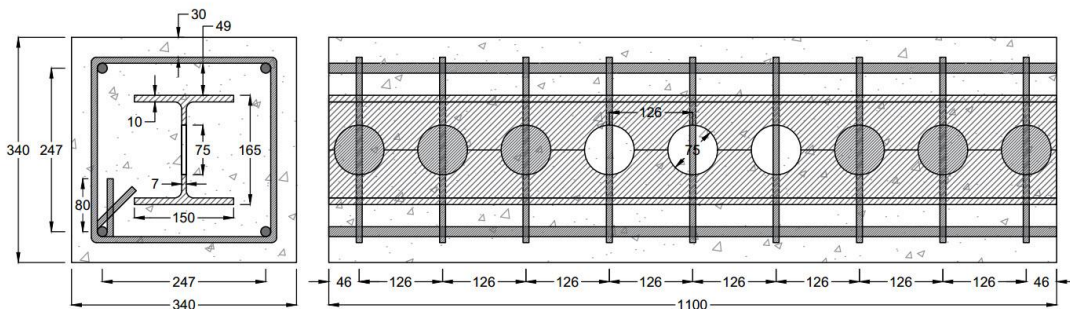(a)   (b)

Figure A.5 Reinforcement details of W-126 column;
(a) cross-section; and (b) longitudinal section (dimensions in mm).

(a)   (b)
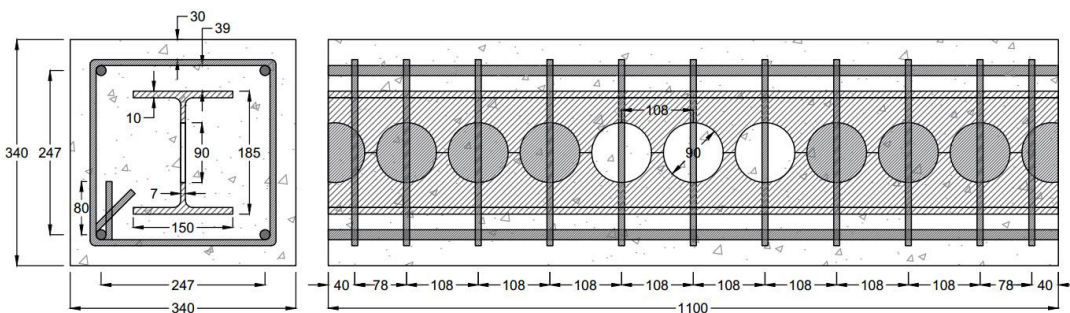
Figure A.6 Reinforcement details of C1-126 column;
(a) cross-section; and (b) longitudinal section (dimensions in mm).

(a)   (b)

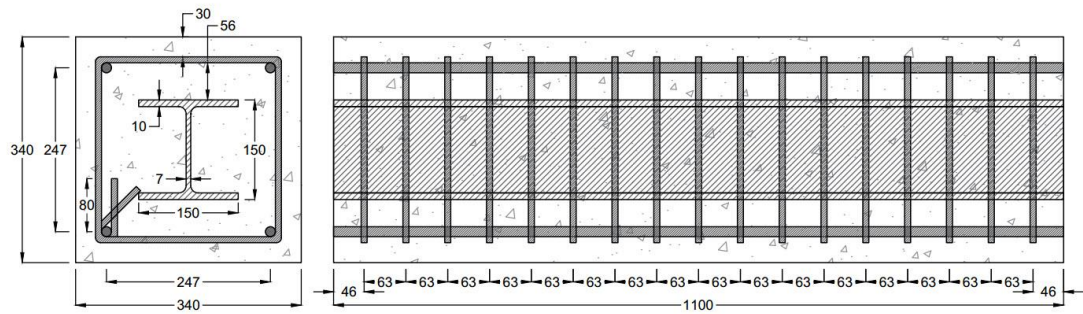Figure A.7 Reinforcement details of C2-126 column;
(a) cross-section; and (b) longitudinal section (dimensions in mm).
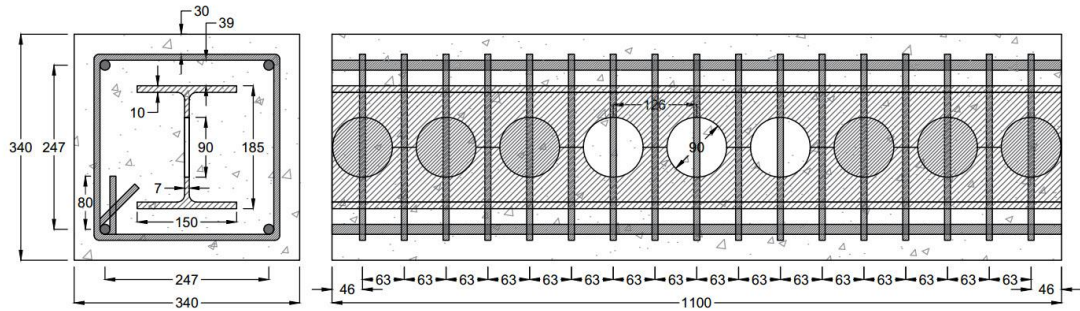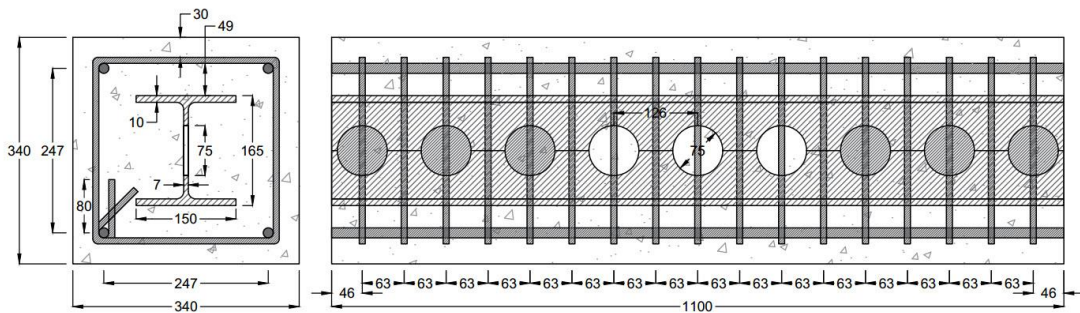

(a)   (b)

Figure A.8 Reinforcement details of C3-108 column;
(a) cross-section; and (b) longitudinal section (dimensions in mm).

Figure A.9 Reinforcement details of W-63 column;
(a) cross-section; and (b) longitudinal section (dimensions in mm).

Figure A.10 Reinforcement details of C1-63 column;
(a) cross-section; and (b) longitudinal section (dimensions in mm).

Figure A.11 Reinforcement details of C2-63 column;
(a) cross-section; and (b) longitudinal section (dimensions in mm).

(a)   (b)
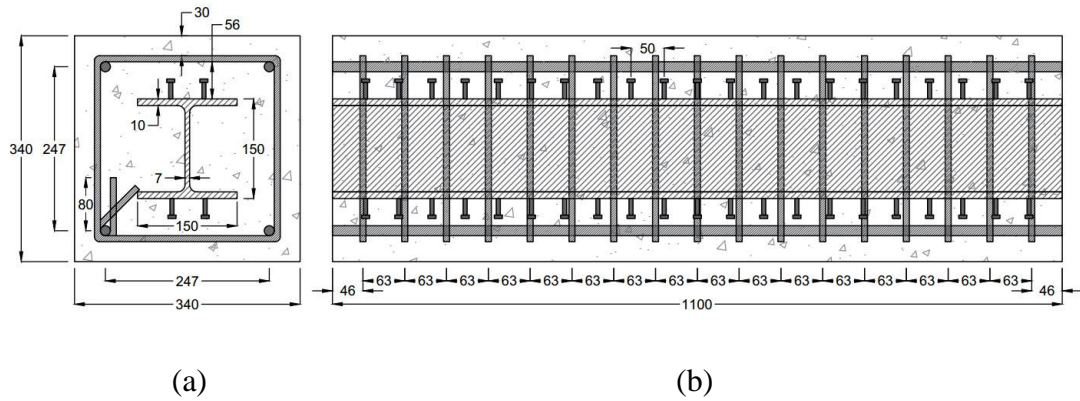
Figure A.12 Reinforcement details of Ws-63, Ws-63-E1 and Ws-63-E2 columns;
(a) cross-section; and (b) longitudinal section (dimensions in mm).

(a)   (b)

Figure A.13 Reinforcement details of C1s-63, C1s-63-E1 and C1s-63-E2 columns;
(a) cross-section; and (b) longitudinal section (dimensions in mm).

(a)   (b)

Figure A.14 Reinforcement details of C2s-63, C2s-63-E1 and C2s-63-E2 columns;
(a) cross-section; and (b) longitudinal section (dimensions in mm).

(a)   (b)

Figure A.15 Reinforcement details of RC-170 column;
(a) cross-section; and (b) longitudinal section (dimensions in mm).

(a)   (b)

Figure A.16 Reinforcement details of RC-126 column;
(a) cross-section; and (b) longitudinal section (dimensions in mm).
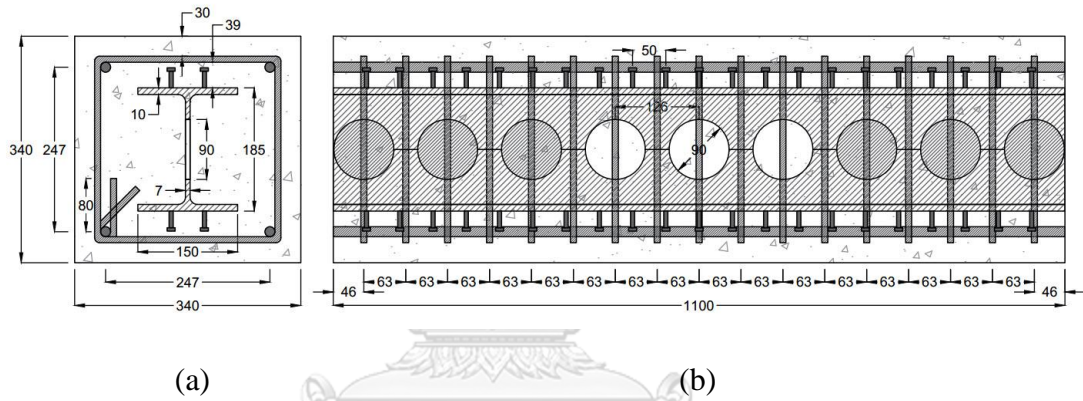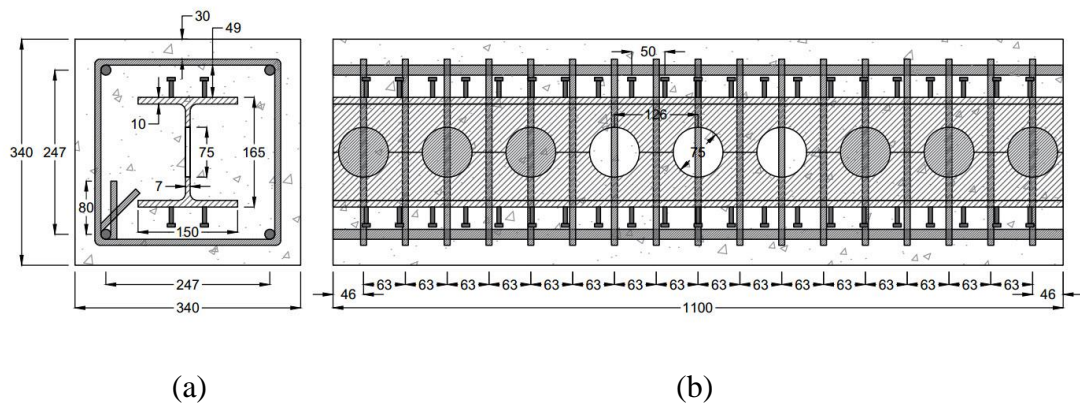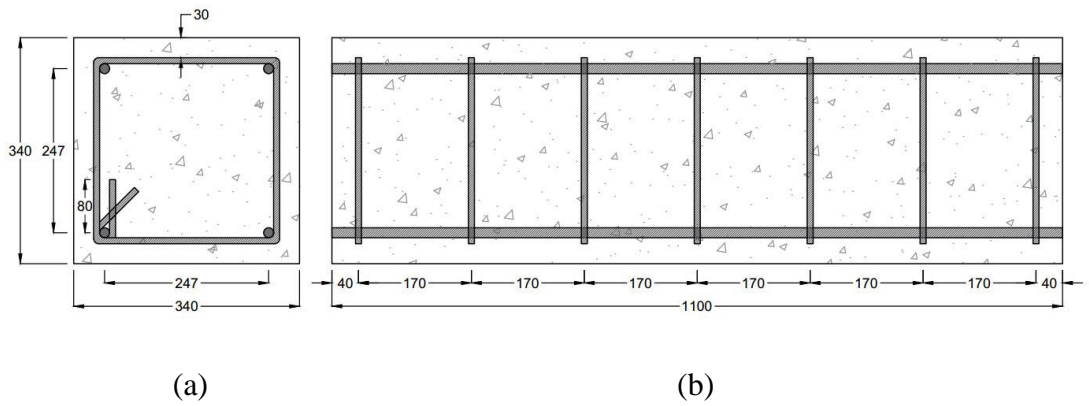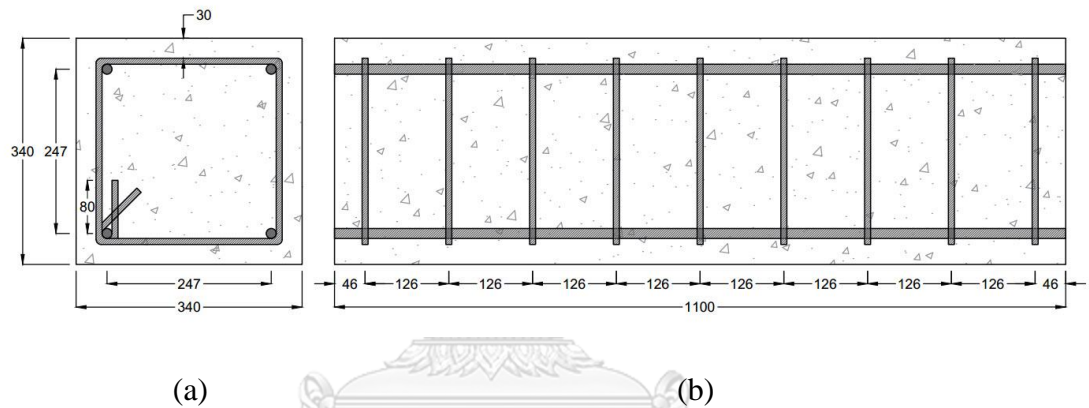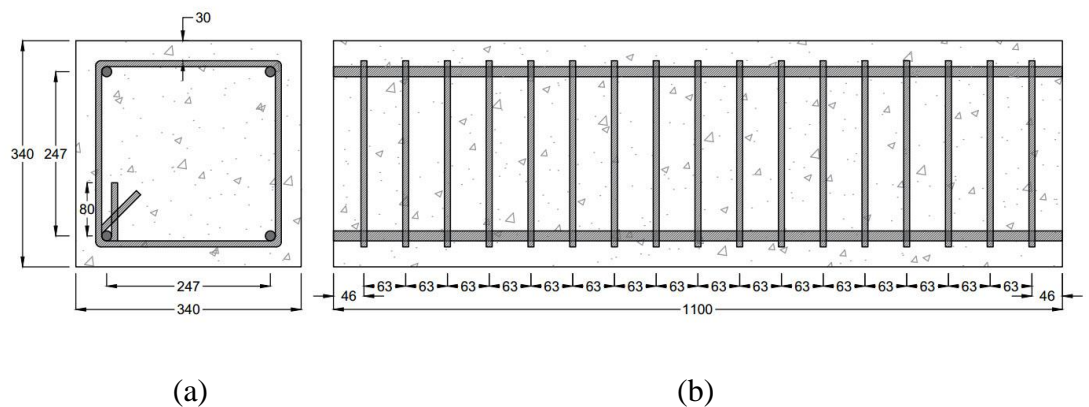

(a)   (b)

Figure A.17 Reinforcement details of RC-63 column;
(a) cross-section; and (b) longitudinal section (dimensions in mm).

APPENDIX B
EXPERIMENTAL RESULTS OF RC COLUMNS

Experimental results of RC-170, RC-126, RC-63 and added RC columns [RC-63 (2)] are reported in this section. Properties of the RC-63 (2) column is similar with RC-63 column. However, the RC-63 (2) used strain gauges in longitudinal direction (SG 1) which it's installed on the surface of concrete. Failure of all tested RC columns are a combination of concrete spalling and buckling of longitudinal rebars, as shown in Figure B.1. The results shown that the failure of the tested RC columns is similar to the failure of tested composite columns in this research. Load – deformation curves, load – axial strain curves and load – transverse strain curves of tested RC columns show in Figure B.2 – B.4, respectively. The maximum loads of RC-170, RC-126, RC-63 and RC-63 (2) are 1355 kN, 1673 kN, 2265 kN and 1954 kN, respectively. The proportional limit loads of RC-170, RC-126, RC-63 and RC-63 (2) are 1161 kN, 1255 kN, 1775 kN and 1558 kN, respectively.

(a)   (b)   (c)

Figure B.1 Failure of RC columns (a) RC-170; (b) RC-126; and (c) RC-63.
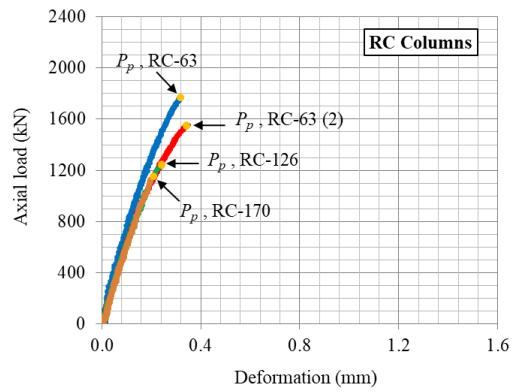
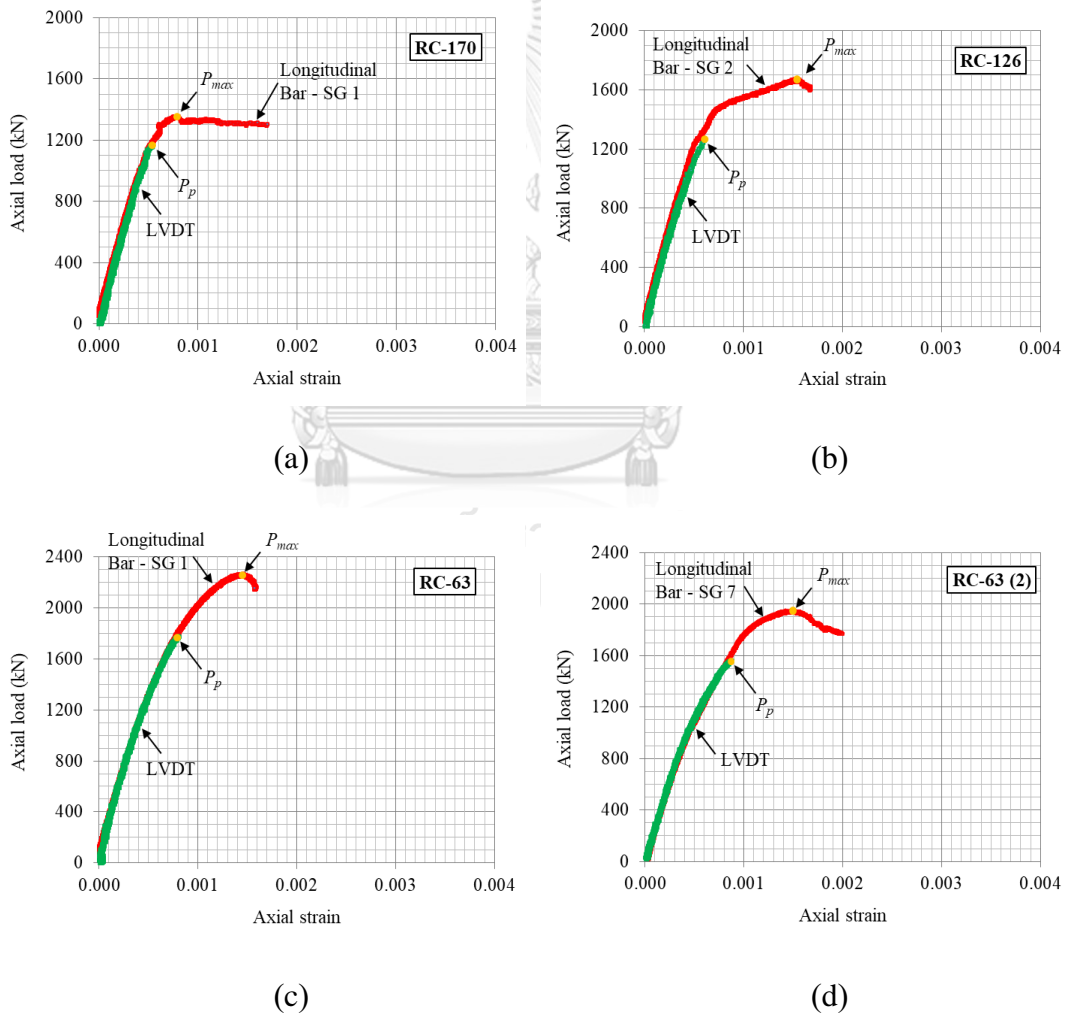Figure B.2 Load – deformation curves of RC columns.

Figure B.3 Load – axial strain curves of RC columns (a) RC-170; (b) RC-126;
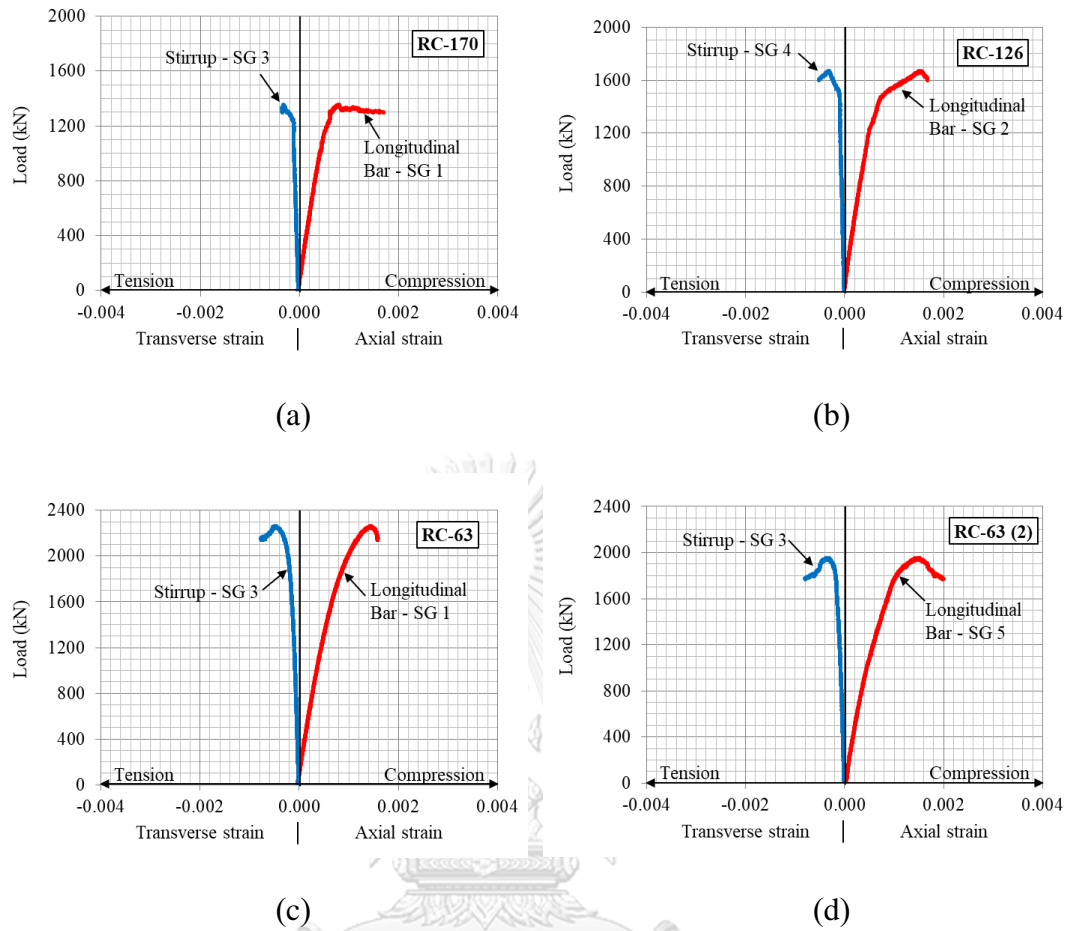(c) RC-63; and (d) RC-63 (2).

Figure B.4 Load – transverse strain curves of RC columns (a) RC-170; (b) RC-126;
(c) RC-63; and (d) RC-63 (2).

<div align="center">**VITA**</div>

NAME   Worakarn Anuntasena

DATE OF BIRTH   29 October 1991

PLACE OF BIRTH   Bangkok

HOME ADDRESS   29/8 Moo 3, Sao Thong Hin, Bangyai, Nonthaburi
                      11140